University of Strathclyde
Glasgow

3D-PRINTED PHOTOACOUSTIC SPECTROSCOPY FOR INDUSTRIAL PROCESS CONTROL

METIN ILKE

Centre for Microsystems and Photonics
Department of Electronic and Electrical Engineering
University of Strathclyde

A thesis presented in fulfilment of the requirements for the degree of Doctor of Philosophy

May 1, 2022

This thesis is the result of the author's original research. It has been composed by the author and has not been previously submitted for examination which has led to the award of a degree.

The copyright of this thesis belongs to the author under the terms of the United Kingdom Copyright Acts as qualified by University of Strathclyde Regulation 3.50. Due acknowledgement must always be made of the use of any material contained in, or derived from, this thesis.

Signed:

Date: May 1, 2022

METIN ILKE

Acknowledgements

input and support whenever needed.

Thank you to my parents, Vecdi and Hülya. I wouldn't be who I am without your support and love.

Finally and most importantly, Emine; my soulmate, the source of my happiness and motivation. Your contribution to the completion of this PhD is unfathomable, thank you for giving me all you have and always being by my side during the hardest times of this journey.

Abstract

Photoacoustic spectroscopy (PAS) is a well-established technique for trace gas sensing reaching above parts-per-quadrilion levels. This technique consists of the generation and detection of an acoustic signal from a gas sample using sensitive microphones, by the interaction of the gas with a modulated laser beam at an optical wavelength coinciding with a spectral feature of the target gas molecule. Over the past decades, many PAS techniques and sensors have been developed and deployed for applications such as: environmental monitoring, medical applications and life science applications. However, PAS applications in industrial uses was dwarfed by other gas sensing techniques, due to its requirement for frequent re-calibration for changing environmental conditions and input light power fluctuations limiting its deployment for on-site, long-term remote applications and limitations in simultaneous multi-gas measurement. The work presented here aims to present 3D-printed longitudinal resonant PAS cells that can be constructed in 4 hours with a robust, miniaturised form factor (volume $< 20,000$ mm^3) which can address these two main drawbacks of PAS technique: calibration and multi-gas measurement.

To address the calibration problem, the development of theory and application of a calibration-free wavelength modulation photoacoustic Spectroscopy (CF-WM-PAS) technique using quantum cascade lasers operating at 8.65 µm wavelength is presented. The CF-WM-PAS technique was mainly developed for measurement of SO$_2$ gas in industrial desulphurisation process. This method uses 2f/1f calibration technique, where the second harmonic (R_{2f}) component which is dominated by laser-gas interaction and optical intensity, is normalised by the first harmonic (R_{1f}) component dominated by a newly discovered DC offset in PAS called cell dependent absorption signal (CDAS) found to be originating from laser-resin interaction, in order to isolate the output from changes in the gas matrix, optical intensity and electrical gain. The normalisation technique is confirmed for changes in laser modulation frequency, gas concentration and attenuation in input light intensity. A normalized noise equivalent absorption

(NNEA) of 1.37×10^{-8} Wcm^{-1}Hz$^{-1/2}$ for calibration-free R_{2f}/R_{1f} measurements is demonstrated, reaching sensitivity of $\sigma = 232$ ppb for SO$_2$ gas. Using the same PAS sensor and setup, the effect of different types of acoustic sensors, (an electret microphone (ECM) and a micro-electromechanical system (MEMS) microphone) on the PAS signal was also investigated, and it was concluded that ECM can result in higher sensitivities owing to their broader variant types allowing a simpler assembly process. Using calculated NNEA values for both microphones, 70 % superior performance was found with the ECM compared to the MEMS microphone.

To address PAS multi-gas measurement, a fiber optic based, 3D-printed, miniaturised PAS sensor capable of measuring two gases simultaneously, operating at telecommunications wavelength range, is also developed as a part of this work. The multi-gas PAS gas sensor employs a double-resonator for measuring CO and CO$_2$ in near-infrared range was developed using two DFB lasers, as an alternative to gas chromatography technique. Using the resonators operating at 10.25 kHz and 13.8 kHz resonant frequencies, the simultaneous gas measurement was demonstrated using erbium doped fibre amplifiers (EDFA), resulting in CO$_2$ sensitivities of 2,032 ppm at 26 s and 13,008 ppm at 81 s for resonators 1 and 2 respectively. The corresponding NNEA values are 1.52×10^{-7} Wcm^{-1}Hz$^{-1/2}$ and 2.89×10^{-6} Wcm^{-1}Hz$^{-1/2}$ for resonators 1 and 2 respectively, demonstrating the possibility for multi-gas sensing measurement that would have normally required two sensors, which results in overall reduction of cost, compactness and complexity.

Contents

Contents

Contents

Contents

Contents

Contents

Chapter 1

Introduction

1.1 Motivation and Applications of Gas Sensors

The increasing demand for gas measurements to monitor and control environmental emissions, industrial processes, and human health has resulted in significant interest in the further development of gas sensors with higher sensitivity and improved ruggedisation [1]. Gas sensing technologies were originally developed for regulating hydrocarbon build-up in the mining, oil and gas industries, but are now employed in a wide variety of sectors for measuring a large number of gaseous species.

Initially, gas sensing focused on the measurement of a specific gas above a certain threshold. However, modern gas sensing requires the measurement of multiple species at concentrations below the parts-per-billion (ppb) levels, as a part of intelligent control and monitoring systems. There is, therefore, a drive for sensing techniques that can provide in-situ information of gas concentration, temperature, pressure, flow velocity, and spatial distribution to ensure optimal efficiency, safety and control in many industrial processes. These measurements need to be produced in real-time, continuously and for numerous species, and each individual application has a list of varying requirements of sensitivity, compactness, cost and durability, which can vary in each sector. Examples of key sectors where gas sensing research is focused are industrial process control [2][3][4], healthcare

[5][6][7] [8][9], environmental monitoring [10][11], air quality [12][13], agriculture [14] and national security [15].

Industrial process control is required to carefully monitor physical or chemical processes to maintain optimal conditions and minimise output waste within a controlled feedback mechanism. Hence, these sensors require high accuracy and reliability, with an ability to be operated continuously. However, due to the extreme environmental conditions (temperature and pressure) and difficulties in differentiating similar waste molecules, such as in the petrochemical industry, the costs of sensors operating in the industry can be high. An example of such systems is the monitoring of the exhaust gases emitted by internal combustion engines in automotive and aeronautics industries to control the fuel injection and emitted pollutants, which in turn increases the engine efficiency [2], leading to more environmentally conscious technology. Similarly, industrial gas sensors are used as a safety tool for the detection of toxic exhaust gases [3] or built up hazardous explosive gases, particularly in the hydrocarbon industry [4].

Healthcare applications are mainly focused on medical diagnoses of illnesses by measuring the characteristic bio-marker gases of certain diseases. Breath analysis is used for disease detection as it presents a noninvasive, simple, and mobile diagnostic tool compared to other laboratory based diagnostic techniques [5]. Examples of this include: the detection of ammonia gas in exhaled breath from Helicobacter pylori, indicating the possibility of stomach ulcers [6]; early stages of asthma can be diagnosed through detection of nitrogen oxide, which is an indicator of inflamed airways [7][8]; cancer diagnosis via detection of volatile organic compounds (VOCs) in breath [9].

Environmental gas sensing can be divided into atmospheric and air quality measurements [7]. Atmospheric gas monitoring focuses particularly on greenhouse gases, which play a central role in global climate change [10][11]. Air quality measurements can be divided into two, depending on the location of the measurement. Outdoor air quality (OAQ) measurements include quantifying urban air quality, typically monitoring of automobile exhaust emissions [12]

and industrial sources affecting the environment and life quality in large cities. Indoor air quality (IAQ) sensors gained importance in recent years with the demonstration of the detrimental effects of various pollutants found in our households, particularly when temperature and humidity is high and ventilation is limited. Pollutants such as VOCs (emitted by paint, lacquer, glue, and plywood), asbestos, dust, radon gas, solvents and mould can lead to various short-term and long-term adverse health problems, including cancer and birth defects [13]. This has increased the demand for IAQ sensors as an addition to carbon monoxide sensors already installed in many homes and work environments. The main challenges for IAQ sensors are: versatility, as there are multiple different pollutants that need to be monitored to assess indoor air quality; cost, as sensors need to be at low cost due to the requirement for a large amount of sensors in large offices; sensitivity and cross talk, as low cost sensors typically have reduced selectivity and accuracy.

In the agriculture sector, one main area of interest is the detection of exhaled methane gas by livestock to monitor efficiency in which animal feed is digested to maximise conversion of calories into meat and dairy and minimise its environmental impact [14].

Another major area where gas sensing has seen significant interest is national security, with applications including the detection of explosives, and other chemical or biological hazardous substances, for example, ammonia as a signature of TNT explosives [15].

1.2 Overview of Gas Sensing Technologies

The first modern gas sensor was based on the principle of catalytic combustion, and was developed in 1926 for the detection of combustible gases in fuel storage tanks. The technique was based on combustion of a sample of air inside an isolated combustion chamber. However, the lack of selectivity and the limitations of continuous operation have seen this sensor becoming obsolete for most applications [16].

The gas sensing market is currently dominated by technologies based on gas chromatography [17], pellistors [18], electro-chemical sensors [19], semiconductor devices [20], and optical absorption [1]. Although alternative techniques are available, these are either still in the development stage or are only suited towards highly specialised applications. The choice of a particular gas sensor type is based on its performance parameters [15] listed as:

- sensitivity

- selectivity

- response time

- energy consumption

- reversibility

- fabrication cost

- stability of operation

Gas chromatography (GC) is a sensitive technique reaching up to ppb measurement levels [21], and is based on the adsorption of different gases at different rates when they pass through a column made up of an adsorbing material. However, GCs require sample preparation leading to an increased response time, they cannot be operated in-situ, have a large footprint, and are cost ineffective. A number of GC devices also require water vapour to be removed prior to measurement to prevent measurement errors. Hence, it is not possible to make real-time continuous measurements or in-situ measurements.

Pellistors are often used in oil and gas industry for accurate detection of hydrocarbon concentrations between their lower and upper explosive limits, with limited species selectivity [18]. In pellistor-based sensors, gas concentration is measured by comparing the increase in filament resistance during the oxidation of the target gas as the filament is heated to a reference resistance. There are several disadvantages of this technique, particularly its vulnerability to permanent deterioration by contaminants. Similarly, electrochemical devices heat up and

oxidise specific gases, such as oxygen or toxic gases on an electrode and the change in current passing through the electrode is measured. This current depends on the target gas concentration. As with pellistors, electrochemical sensors have low lifetimes due to electrode poisoning and they are also prone to cross-talk issues.

Semiconductor devices can be sensitive up to ppm levels [1], can be used in a variety of applications, and are long-lived, even in extreme ambient conditions. The main operating principle of these sensors is the change in the resistance of a sensitive metal oxide film layer when the target gas molecules react with it. The main disadvantage of these sensors is their poor selectivity and high power consumption.

Compared to the alternatives, optical gas sensing is attractive as it can compensate for the majority of shortfalls and disadvantages. Optical gas sensing techniques can offer real-time, in-situ, and non-invasive measurements to detect gaseous species with high sensitivity and selectivity. In addition, optical gas sensing techniques are not limited to a specific type of gas, such as pellistors being limited to only combustible gases, and can be used to detect any gas molecule with accessible spectral features. Because the method is based on taking a measurement of a molecule's absorption at specific wavelengths, the drift is minimal. Also, as the incident light intensity can be determined, measurements are self-referenced, making them inherently reliable [1]. Hence, as quoted by Hodkingson et al. [1], "... optical gas sensing fills an important gap between lower cost sensors with inferior performance and high end laboratory equipment.". However, optical spectroscopic techniques also have limitations, such as the requirement for complex and large setups for high sensitivity and limitations of power input into photodetectors [15]. In the next section, a more detailed description of various optical gas sensing techniques will be presented.

1.3 Optical Gas Sensing Techniques

Almost all optical gas sensing techniques are based on spectroscopy: examining the interaction of the matter with the electromagnetic radiation. The frequency

of the electromagnetic radiation at which it is absorbed is defined by the energy states of electrons or molecular bonds, which are excited to higher energy levels by the absorption of photons. Each specific atom or molecule has a unique 'spectral fingerprint' defining the frequencies at which light will be absorbed. Hence, by utilising light at frequencies/wavelengths of absorption for a known gaseous species it is possible to identify the presence of a specific gas with certainty. The wavelength of interrogation must be selected carefully to avoid misidentifying with non-target gases with overlapping spectral absorption lines. Commonly, molecular absorption is quantified by measuring the transmitted light through the gas sample using optical detectors, where the higher level of absorption at the characteristic optical frequency indicates a higher gas concentration of the target gas, as described by Beer-Lambert law as:

$$I_{out} = I_{in}e^{-\alpha C\ell} \tag{1.1}$$

where I_{in} and I_{out} are incident and transmitted intensity, ℓ is the path length, α is the absorption coefficient and C is the gas concentration. This law is also illustrated simply in figure 1.1 below:
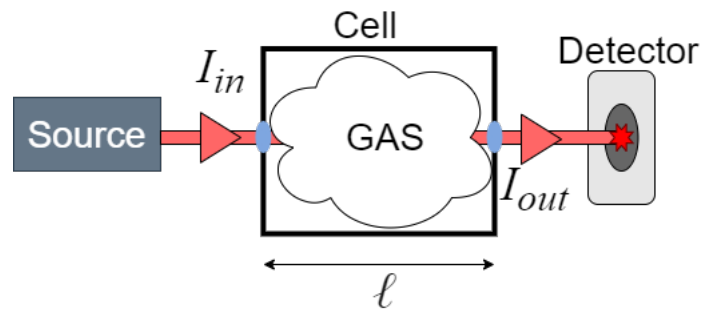
Figure 1.1: A simple schematic displaying the concept of quantifying molecular absorption through a gas with ℓ path length. The gas is confined in a chamber called 'cell' with entry and exit windows for electromagnetic radiation.

Over the years, optical gas sensing branched out to a number of distinct techniques to measure gas concentration and other related parameters, for example: non-dispersive infrared radiation (NDIR) [22], correlation spectroscopy

(CS) [1], tunable diode laser spectroscopy (TDLS) [23], cavity ring-down spectroscopy (CRDS) [24] and photoacoustic spectroscopy (PAS) [25]. A comparison of these techniques is shown in table 1.1, including the type of gas interrogated, wavelength, input power, path length and resulting sensitivity for each technique.

NDIR is based on the detection of broadband infrared light using a cheap optical detector and narrow band optical (100 - 200 nm) filters for gas selectivity. Typically, a reference filter targeting a zero absorption wavelength region is also used for system calibration. Correlation spectroscopy is commonly considered as an improved NDIR technique, where the reference filter is replaced by a reference gas cell containing a defined concentration of the target gas, to normalise the signal and improve selectivity [1]. Although, NDIR techniques are often low cost and simple to implement, they are often limited when there is spectral interference from other gases.

One method which addresses the low selectivity and slower response time of NDIR based techniques is TDLS. TDLS uses a narrow linewidth laser source that can be wavelength scanned across an isolated spectral absorption line. The reduced linewidth of the laser provides higher selectivity and sensitivity and allows fast recovery (< 0.2 s) of absorption spectra due to fast modulation rates (> 1 MHz) of modern semiconductor diode lasers, as shown in table 1.1. A baseline for normalising the signal is provided by the zero absorption on either side of the absorption peak. However, in regions of very high optical noise, or significant bunching and overlapping of spectral features intensity normalisation becomes much more difficult, resulting in large overall errors. Another major limitation of TDLS is the high cost of targeting strong fundamental mid-infrared (MIR) absorption lines which can have 10-100 times higher absorption cross section compared to near-infrared (NIR) [1] , due to the prohibitive expensive cost of optical detectors operating in this region. This is the main reason why TDLS devices commonly operate in NIR wavelengths using cheaper distributed feedback lasers (DFB) and InGaAs photodetectors[26].

CRDS is a multi-path technique that enhances the sensitivity of TDLS, and is based on measuring the exponential decay time of light in a high finesse cavity of two mirrors enclosing the sample gas. The high finesse cavity increases the laser-gas interaction path length to the kilometer scale, providing sensitivities in the parts-per-quadrillion (ppq) range [27]. Normalisation is complex, and the recovered exponential signal has to be compared to a spectral baseline or a reference measurement to identify spectral information about the target gas. Causes of error include the reduction of mirror reflectivity, optical misalignment, and even scatter from dust. However, one important advantage of this technique is immunity to input power fluctuations, as decay time is measured rather than the changes in light intensity [28]. However, CRDS devices are highly sensitive to environmental changes, making it difficult to maintain long-term stability [1]. In addition, the high cost and complexity of CRDS limits its use for in-situ applications.

PAS is a hybrid gas sensing technique that combines TDLS with acoustic sensing, and is able to provide a higher sensitivity than TDLS, and a comparative sensitivity to CRDS techniques, but at a superior selectivity and reduced complexity. In PAS, the laser-gas interaction is measured indirectly via a pressure wave, generated through localised heating and cooling in a periodically excited gas sample [29]. As both PAS and TDLS measurement sensitivities are linearly proportional to the input optical power, and photoreceivers are often limited in the level of power detection, the use of higher power lasers in PAS systems can achieve higher overall measurement sensitivities [1]. Secondly, the photoreceiver is replaced by a cheap, small-scale acoustic transducer allowing MIR laser sources to be used without incurring the high cost of MIR photoreceivers. The main limiting factors of PAS are the difficulties in filtering external acoustic noise, which reduces the sensitivity, and the requirement to re-calibrate the sensor frequently as the gas sample density, input light intensity and transducer responsivity changes. Photoacoustic detection is the main focus of this thesis, and is further detailed in the next section.

Table 1.1: Comparison of performance indicators for optical detection of different gases.

Detection	Gas	λ [nm]	I_{in} [mW]	ℓ [m]	Sensitivity
NDIR [30]	N_2O	2,189	2	76	350 ppt at 1s
CS [30]	CO_2	300	>0.001	0.19	400 ppb at 60 s
TDLS [31]	C_2H_2	3,369	10	580	560 ppt at 290 s
CRDS [27]	CO_2	4,500	100	5,200	5 ppq at 2 hr
PAS [32]	HF	2,476	950	0.095	650 ppq at 32 min

1.4 Photoacoustic Spectroscopy

1.4.1 Background

The photoacoustic (PA) effect of solids was first reported by Alexander Graham Bell in the 19th century, when he found out that a rubber diaphragm emitted an audible sound if periodically interrupted sunlight was focused onto it[33]. Using a device he invented called the 'Photophone', where light passed through the holes of a rotating disc, he also noticed that the sound can be amplified if the sample is confined into a selenium cell. In the same year, John Tyndall discovered the PA effect in gases and proposed that this effect was caused by the effects of radiant heat [34]. After some initial work by Mercadier [35], Preece [36], Röntgen [37] and Lord Rayleigh [38], the excitement around the photoacoustic effect faded due to the difficulties in signal quantification, as it was subjectively based on researcher's hearing through the photophone tubes and the lack of suitable, directional light sources [39].

In 1938, the interest in the PA effect was revived for a short period, particularly with the work of Veingerov [40] who developed the first PAS based spectrometer using capacitive microphones as acoustic sensing elements and intense infrared blackbody sources for the detection of CO_2 gas with a minimum sensitivity of 0.2 %. During this period, PAS was also used to measure the relaxation rates and energy transfer rates of gases and vapours [41][42][43], providing an understanding of the underlying processes of the PA effect. However, the interest in the implementation of PAS faded again after the development of gas chromatography, which had a superior sensitivity and accuracy compared to PAS at the time.

Finally, in the 1960s, after the invention of the first laser sources offering high intensity, low-bandwidth, highly stable, and collimated beams, increasingly more sensitive acoustic transducers and lock-in amplification techniques, a new era of discovery and applications began for PAS studies. In 1968, Kerr and Atwood [44] were the first to describe an 'absorptivity spectrophone' to obtain the spectra of small molecules using a chopper modulated CO_2 laser. Kreuzer [45] managed to reach 10 ppb CH_4 sensitivity using a HeNe laser and an electret microphone. In the 1970's, resonant cells started to be utilised in PAS as a way of amplifying the signal, initially through the work of Max and Rosengren [46], where optical modulation (ω) was set to be equal to the acoustic resonance of a carefully designed cell (ω_r).

Since the 1970's, a wide variety of optical sources, cell types, and acoustic transducers have been investigated in the field. PAS has now become a commercialised, accessible, and highly sensitive technique reaching below part-per-trillion (ppt) level detection limits [32]. These sensitivity limits are comparable to path length enhanced gas sensing techniques, such as cavity-enhanced absorption spectroscopy (CEAS). However, PAS has the advantage of not requiring the same high stability or expensive equipment that limits CEAS techniques.

PAS is now being applied to many applications that require high sensitivity, high selectivity, short response time, and portability, including;

- Life science: CH_4, H_2O and CO_2 emissions from small insects [47]; monitoring of large caged mammals [48].

- Environmental monitoring: exhaust emission by cars in traffic [49][50]; water vapour in the upper atmosphere [51]; the effect of N_2O on the ozone layer [52].

- Medical diagnostics: NO monitoring to analyse for asthma patients [53]; NH_3 in human breath [54].

- Industrial control: NO in industrial chimney stack emissions [55]; gas release

during manufacturing of optical fibres [56].

1.4.2 Basic Principles of PAS

1.4.2.1 PA Cell

In other optical spectroscopy techniques the cell has only one function: to confine the measured sample. However, in PAS the cell can be carefully designed to amplify the PA signal through resonance. The most common targeted resonance is the first longitudinal mode of a cylindrical resonator. In resonant cells, the laser frequency is aimed to be matched with the cell's resonance frequency, $(\omega = \omega_r)$, to amplify the PAS signal by the amplification factor (Q-factor) of the resonator. If the modulation frequency of the laser, typically $\omega < 100$ Hz, is much lower than the resonant frequency of the cell, $(\omega \ll \omega_r)$, the operation is said to be non-resonant [57]. Low modulation frequency, non-resonant operation allows the use broadband sources and arc lamps which can be effectively modulated using external modulation techniques such as choppers but have limited modulation frequencies using current modulation. However, non-resonant PAS systems have a major disadvantage: low signal-to-noise ratio (SNR) as the low modulation frequency generates increased 1/f noise and increased flow noise during gas sampling [58]. Thus, resonant PAS cells are commonly superior to non-resonant designs in terms of sensitivity, response time and versatility, and are more popular for PAS trace gas sampling.

A unique and widely utilised feature of PAS gas sensing using longitudinal cells is the increase in the generated pressure wave by a reduction in cell volume, which allows the miniaturisation of PAS cells into compact devices. Miniaturisation of gas sensors implies compact sensors, and reduced sample sizes, and is highly desirable for many industrial applications. The use of new fabrication techniques, particularly high resolution 3D-printing technology, allows cells with low volume and intricate internal geometries to be manufactured, compared to traditional methods of fabrication, thus providing a high overall sensitivity [59].

1.4.2.2 Acoustic Transducer

PAS signals are traditionally detected via a sensitive microphone. Recently, alternative transducers with miniaturised form factors, i.e., quartz tuning forks (QTFs) [60], optimised capacitive microelectromechanical systems (MEMS) microphones [61] or cantilevers [62] have been demonstrated. Quartz enhanced photacoustics (QEPAS) uses a high Q-factor (8,000 - 20,000) and high resonance frequency ($\omega_r = 32{,}768$ Hz) piezoelectric quartz tuning fork. It has become an important tool in PAS, due to reduced background noise resulting from the high resonance frequency. Many studies have also been published that have integrated QTFs with a micro-resonator to increase the interaction region and reached a normalised noise equivalent absorption (NNEA) of 1.21×10^{-8} Wcm^{-1}Hz$^{-1/2}$ using a quantum cascade laser (QCL) [63]. However, particularly the on-beam QEPAS setups, where laser beam is aligned through the prongs of a QTF, are generally more expensive, requiring high beam quality and complex optical alignment, and are also extremely sensitive to changes in pressure, due to its high Q-factor. Recently, high frequency resonant piezoelectric crystal-based transducers have also been introduced to PAS, which produced sensitivities reaching to parts-per-quadrillion level through the production of an optical grating that moves at the speed of sound through the gas [64].

Cantilever enhanced PAS (CEPAS) include micro-cantilevers that show large percentage of deformity under small acoustic pressure. The displacement of the lever can be registered optically using a reflected laser beam or an interferometer [1]. These transducers can be included in miniaturised gas sensors and can reach to NNEA of 4.6×10^{-9} Wcm^{-1}Hz$^{-1/2}$ using optical parametric oscillators (OPO) using 2.476 µm wavelength lasers [65].

MEMS microphones based on micro-fabrication using bonded silicon wafer stacks or miniature milling have been demonstrated recently as PAS transducers [61] [66]. These microphones have a negligible volume of air adjacent to the diaphragm, hence they do not contribute towards the total resonance of the gas cells. In addition, their overall sizes are small, contributing to the overall

compactness compared to other acoustic transducers and are very cheap ($< £ 1.5$ per unit in 2022). An NNEA of 4.5×10^{-9} Wcm^{-1}Hz$^{-1/2}$ has been reached for CH_4 gas using MEMS transducers using Raman amplified DFB [66].

1.4.2.3 Optical Source

Any radiation source for PAS applications for sensitive and selective detection must exhibit the following characteristics: (i) high optical intensity; (ii) narrow linewidth; (iii) single mode beam; (v) high stability; (vi) compact form factor [67].

Many years of extensive work in telecommunications applications (1490 - 1625 nm) resulted in the development of DFBs, reaching powers up to hundreds of milliwatts, providing standardised optical fibers and stable optical devices for highly sensitive and selective optical gas measurements [1]. However, as the strong fundamental ro-vibrational transitions of many molecules appear in mid-infrared range (> 2 µm), and PAS systems have reduced cost due to signal detection via cheap acoustic transducers instead of expensive MIR receivers, recent PAS developments have focused in the MIR. The investigated MIR sources for this purpose include OPOs, lead-salt diode lasers, external cavity diode systems (ECDL), quantum cascade and interband cascade lasers (ICL) [67]. Among these sources, the most versatile choice is the quantum cascade lasers, due to their high optical powers (> 1 W) [68] and large frequency tuning ranges (3.5 - 24 µm) using external cavity arrangements [69].

Semiconductor lasers have become invaluable tools for PAS, conforming with all requirements of a selective and sensitive PAS radiation source. Semiconductor lasers are wavelength tunable, rapidly modulating their output via modulation of the injection current, allowing higher sensitivity measurements at reduced 1/f noise.

The modulation techniques for semiconductor lasers can be divided into two schemes: wavelength modulation (WM) and intensity modulation (IM). IM is based on the direct control of the laser's output radiation by using an external

modulation such as a mechanical chopper or an acousto-optic modulator [58] or switching the laser on and off as the injection current is modulated above and below the laser's threshold current [67].

In WM, the current modulation of the laser is used to tune the wavelength over a spectral feature of interest. For applications in PAS, WM provides a better suppression of the ambient noise and is a more efficient technique overall as suggested by Schilt et al. [48]. However, in a WM scheme a small amount of IM will always be present, which is commonly called a residual amplitude modulation, RAM, leading to undesirable effects such as signal distortion and wall noise [58]. To allow WM spectroscopy, a dual current modulation is applied to the laser, with a slow frequency ramp waveform to scan over the targeted rotational-vibrational transition and a higher frequency sinusoidal modulation that generates laser-gas interaction signals at the harmonics of the modulation frequency. The PA signal can then be extracted from the harmonics of this modulation using phase-sensitive, lock-in amplification (LIA) producing output harmonic signals, where the nth derivative of the absorption lineshape corresponds to n^{th} harmonic.

1.4.3 Limitations of Traditional PAS

One key disadvantage of resonant PAS measurements is the requirement for calibration of the cell resonance, to ensure the laser modulation frequency is correct ($\omega = \omega_r$). Environmental parameters such as temperature (T), pressure (P), gas flow velocity ($\dot{V}$) and changes in gas density $\Delta\rho$ are continuously variable in a real measurement environment. Hence, changes in these parameters need to be monitored frequently to be related to changes in ω_r or alternative methods need to be used to overcome this issue. In addition, as with all PAS systems, there is also a requirement to calibrate for the input optical power and the acoustic transducer responsivity.

In addition to environmental parameters, PAS signals are also highly sensitive to instantaneous or gradual changes in the sensor setup. In harsh environments, the

incident laser intensity can be highly unstable due to vibrations, beam steering, scattering, particulate absorption such as soot or window fouling. In prolonged sensor applications, errors in signal calibration can also arise due to drift in laser intensity, laser wavelength and acoustic transducer responsivity.

In recent years various techniques have been presented to overcome the problem of calibration in PAS, such as the intermittent scanning of the modulation frequency to measure the cell's resonant frequency [70], continual measurement of the temperature [71] and multi-frequency excitation [72].

Frequent characterisation of the cell resonance is achieved by intermittent sequential acquisition of the PAS signal amplitude as a function of frequency, providing an accurate measurement of the resonance frequency and quality factor. The scan can be performed by either changing the laser's modulation frequency or the frequency applied to a calibrated speaker placed on the acoustic resonator [70]. However, this method has a slow response time as the acquisition takes a certain period of time and cannot account for short-term changes in sample gas temperature and pressure. Methods such as short square pulse [73] or chirped modulation [74] have faster response times, and both are based on the excitation of multiple frequencies simultaneously. The normalised Fourier transform of the acoustic response at the laser's multiple drive frequencies is used to extract the acoustic resonance curve. However, this method can only be applied to systems with relatively high PAS signal amplitudes and with high Q-factors. This technique is also complex and cannot be used to compensate for rapid fluctuations in external system parameters, such as temperature and pressure. There are also PAS calibration techniques that monitor the phase of the generated PAS signal using phase sensitive detection. As the phase of the resonant signal is in phase with the drive signal, any measured phase variation can be compensated for by varying the laser drive frequency [75] [76]. The disadvantage of phase monitoring is the lack of compensation for any changes in sensor performance i.e. microphone output drift. It is also possible to actively measure the ambient pressure and temperature, allowing acoustic compensation algorithms to estimate

the shift in the resonant frequency and Q-factor after the measurement [77] [50]. However, these methods generally require extensive pre-deployment calibration and increases complexity.

There are also calibration techniques exclusively developed for certain types of acoustic transducers. Beat frequency QEPAS (BF-QEPAS) has been specifically developed to be used in conjunction with QTF sensors. In this technique, the laser modulation frequency is shifted by $\Delta\omega_q$ from the resonance frequency of QTF, ω_r. This leads to a formation of beat signal with a period equalling $\Delta\omega_q$ which can be detected when the laser wavelength is scanned over the target spectral line with a high frequency ramp and demodulated at the laser's modulation frequency[78]. This allows the Q-factor, resonance frequency and target gas concentration to be identified by analysing the beat signal between the laser modulation and the instantaneous QTF resonance frequency. However, this technique is not suitable for conventional PAS systems with lower response time, frequency, and Q-factor.

1.5   Thesis Aims and Objectives

The primary aim of this thesis is to develop 3D-printed, miniaturised photoacoustic sensors to measure trace gases for real world applications with variable environmental conditions such as industrial process control. The two main topics of research is the measurement of SO_2 gas in desulphurisation process and measurement of CO_2 and CO gases simultaneously using one sensor.

The three main objectives of this thesis can be listed as follows:

- Comparing the differences of PAS cells using different types of acoustic sensors: electret-condenser (ECM) and MEMS microphones.

- Developing a calibration-free PAS-WMS technique for various changing gas parameters such as gas concentration, light intensity and flow rate for detection of SO_2.

- Developing a fiber optic based dual-resonator PAS cell for measuring two gases simultaneously for detection of CO_2 and CO.

1.5.1 Natural Gas Desulphurisation

Natural gas has multiple components with varying percentages (CH_4, C_2H_6, C_3H_8, CO_2 and SO_2) depending on the specific extraction location [79]. The purification of the natural gas is a priority for both the petrochemical industry and the fuel cell industry, and is achieved by removing unwanted components, commonly made up of SO_2 and CO_2 [80].

SO_2 is an important component of polluting flue gas and it is a major air pollutant leading to the formation of sulphuric acid when combined with water. Sulphuric acid in the atmosphere is the main source of highly corrosive acid rains which is highly dangerous to the environment and human health.

Due to these concerns, emission of SO_2 from power plants are highly regulated, often requiring the process of 'desulphurisation' in order to minimise SO_2 in natural gas. The measurement of the concentration of SO_2 gas in natural gas before and after desulphurisation is highly important [81]. For this reason, a high precision, reliable and durable gas sensor is required during this operation.

Industrial solid oxide fuel cells were originally developed to run off hydrogen obtained via steam reforming of natural gas. In this process, the reaction of methane from natural gas and the high temperature steam produces CO_2 and hydrogen. The hydrogen is then used in the fuel cell to generate electricity via oxidation. However, the low levels of sulphur oxide species in the natural gas also have to be removed prior to entering the fuel cell to ensure there is no oxidation of the sulphur species at the cathode, resulting in sulphur poisoning.

Currently there are multiple different types of SO_2 gas sensors used in the desulphurisation process [82][83]. As most of these sensors are often expensive and bulky, the development of inexpensive sensors with reduced form factor, high precision and capable of operating in harsh, variable conditions has been a priority for the detection of SO_2 gas in petrochemical industry [84][85]. An alternative, which suits the required specifications, is the use of PAS based sensors using a newly developed calibration-free measurement technique which is presented

within this thesis.

1.5.2 PAS as an Alternative to Gas Chromatography for Industrial Process Control

Gas chromatography has been discussed in section 1.2. For the purpose of industrial process control, PAS provides advantages over GC such as: continuous online monitoring, cost effectiveness and ability to be miniaturised. In addition, PAS allows the measurement of wider variety of gases as only volatile and thermally stable gases can be measured with the GC technique. However, one obvious advantage of GC over conventional PAS technique based sensors is the ability to measure multiple gases at same time with one device. This is mostly achieved by increasing the GC column length, which allows for the separation of increasingly complex samples with high resolution.

One suggestion to increase the detection capability of PAS sensors to multiple gas detection simultaneously is the use of multiple acoustic resonators that can be excited by different lasers targeting different gases [67]. For this purpose, a novel multi-resonator PAS cell is presented in this work, allowing multi-gas measurement with all existing advantages of PAS over GC for the measurement of CO_2 and CO for measurements in fuel cells.

1.5.3 Thesis Organisation

In this chapter a brief introduction to the fundamentals of gas sensing has been presented. The applications and principles of major gas sensing techniques are discussed along with their advantages and disadvantages under certain conditions. The focus of this thesis, photoacoustic spectroscopy, is discussed briefly, as well as the main limitations of conventional PAS hindering its use in a wider fields of use. In addition, two main topics investigated in this work are introduced in chapter 1, as well as application of PAS in these topics using the sensors designed in this work.

In chapter 2, an overview to principles of laser spectroscopy and photoacoustics is

provided. The fundamentals of spectroscopy such as energy levels, line broadening mechanisms, molecular absorption is discussed in detail. In addition, extraction of gas parameters including various lineshape functions and HITRAN database is explained in chapter 2.

The photoacoustic effect is described in detail in chapter 3. The principles of this effect in gases and solids are described along with the details of the construction of PAS cells, different radiation sources, transducers and resonator designs. The newly discovered technique of 2f/1f calibration in PAS is described mathematically along with the justification for the development of this technique.

Chapter 4 describes the design criteria employed in cell manufacture as well as fabrication and assembly of the 3D-printed PAS cells used in this study.

Chapter 5 describes the experimental methods and techniques in detail and the experimental components are characterised thoroughly. An experimental comparison on the use of two different types of acoustic transducers in PAS is presented in detail.

Chapter 6 is the main experimental results chapter of this thesis for 2f/1f technique. In this chapter, the technique which enables calibration-free measurements is investigated in great detail and 2f/1f calibration technique in PAS is investigated in depth under various changing environmental conditions. Finally, Allan-Werle variance analysis is used to reveal ultimate sensor performance.

In chapter 7, fiber based 3D-printed PAS cells are introduced. The fabrication and COMSOL simulations of the PAS cells are presented along with the procedure of characterisation. A dual-resonator cell, capable of simultaneous measurement of different gases, is also introduced and its performance is investigated in depth.

Finally, in chapter 8 conclusions of the thesis are summarised and potential scope of further work is suggested.

Chapter 2

Introduction to Principles of Laser Spectroscopy

2.1   Introduction

This chapter presents a brief introduction on the theory of molecular spectroscopy. Initially, there is a discussion of absorption spectroscopy, focusing on the rotational-vibrational energy levels of diatomic molecules using the simple harmonic oscillation model. Subsequently, the spectral line broadening mechanisms, line intensity and Beer-Lambert law are described. In addition, spectral modelling is explained along with the influence of pressure, temperature and concentration on the line-shape. As only a simple introduction to this topic is presented in this chapter, more comprehensive descriptions can be found in the following publications [86][87][88].

2.2   Molecular Absorption and Spectroscopy

When electromagnetic energy is absorbed or emitted by an atom, it undergoes a change in its total internal energy, E. For atoms, a change in total energy is associated with changing configuration of its electronic energy levels, E_e, as electrons are excited between allowed energy levels in the atom. In molecules,

the energy transition can also be manifested as its vibrational, E_v and rotational energy states, E_r, both corresponding to discrete, allowed energy levels. Hence, total energy of a molecule can be expressed as:

$$E = E_e + E_v + E_r \tag{2.1}$$

Each of these energy components require a different amount of energy for excitation, corresponding to different parts of the electromagnetic spectrum, as discussed further in section 2.3. Absorption and emission processes only take place between discrete, 'quantised', energy levels, ΔE, defined by Planck's law:

$$\Delta E = h\nu \tag{2.2}$$

where h is Planck's constant and ν is the frequency of the absorbed or emitted electromagnetic radiation. This mechanism of energy transfer is shown in figure 2.1, where ΔE corresponds to the difference between two energy states E_2 - E_1.
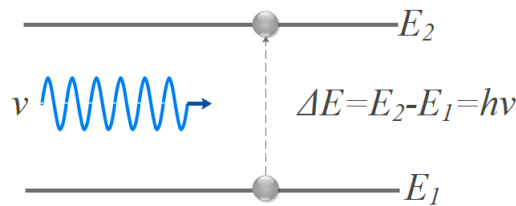
Figure 2.1: Absorption of electromagnetic radiation with photon frequency ν as energy level is excited from E_1 to E_2.

As the incident light is only absorbed when its frequency ν corresponds to the energy difference between the two energy states, as shown in figure 2.1, there is attenuation of the transmitted light at this particular frequency.

2.3   Energy Levels

As previously discussed, excitation by different parts of electromagnetic spectrum correspond to different types of energy transitions. The spectrum of

electromagnetic radiation with high energy photons ($\lambda < 1$ µm) are commonly associated with rearrangement of electronic energy levels, E_e. As the EM wavelength increases towards the infrared (IR) region ($\lambda > 1$ µm) the photon energy reduces, therefore allowing access to the ro-vibrational (rotational + vibrational) energy levels of molecules. The IR region is a particularly active area of work, due to the availability of tunable distributed feed-back diode lasers in the NIR and MIR.

2.3.1 Rotational and Vibrational Energy Levels

At a given energy state, a molecule can vibrate relative to its mean position and rotate around its own axes, leading to vibrational and rotational energy levels respectively. For these transitions the dipole moment of the molecule needs to be changed, leading to absorption in the IR. When considering the behaviour of vibrating atoms within a molecule an an-harmonic oscillator model can be used. Using this model, the relationship between the potential energy, E_p, and the inter-nuclear distance, r_n is given by the Morse function as:

$$E_p = E_d(1 - e^{\alpha_c(r_n - r_{eq})}) \tag{2.3}$$

where E_d is the bond dissociation energy, α_c is the molecular constant and r_{eq} is the equilibrium distance. In figure 2.2, the potential energy modelled using the Morse function resulting from the vibration of two atoms in a molecule is shown. When Schrodinger's equation is solved for this function, quantised energy levels for vibrational energy levels are obtained as:

$$E_v = \left(1 - \chi_e(v + \frac{1}{2})\right)\left(v + \frac{1}{2}\right)\omega_e \tag{2.4}$$

where χ_e is the anharmonicity constant, ω_e is the vibrational frequency and v is the vibrational quantum number. The resulting selection rule for the discrete, allowable transition energies is given by:

$$\Delta v = \pm 1, \pm 2, \pm 3 .... \tag{2.5}$$

The intensity of a transition is dependent on the probability of the excitation process and the populations of the initial states, given by Boltzmann distribution. The strongest transition is between $v = 0 \to v = 1$ and is known as the fundamental transition. This equates to wavelengths in the mid-infrared region (3 - 20 µm). The weaker transition between $v = 0 \to v = 2$ is known as an overtone transition, and is exhibited in the near-infrared (0.74 - 3 µm). As the surrounding temperature is increased, the population of states at $v = 1$ is increased, and absorption related to transitions from this state become stronger, leading to observation of so called 'hot lines'.
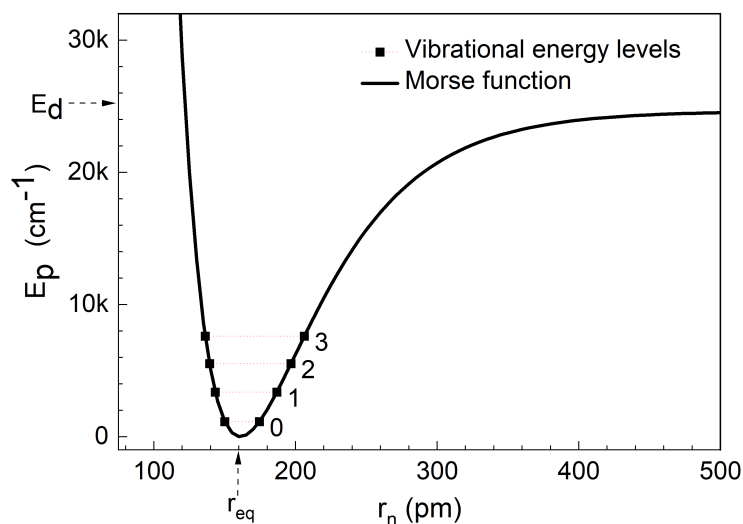
Figure 2.2: Molecular potential energy versus inter-nuclear distance, modelled by Morse function given in equation 2.3. The dissociation energy E_d, equilibrium distance r_{eq} and first four transitions from $v = 0$ to $v = 3$ is also marked on the figure.

The vibrational eigenfrequency model for diatomic molecules given above in figure 2.2 is relatively simple. However, the model becomes highly complex when applied to poly-atomic molecules. The number of degrees of vibrational freedom is dependent on the number of atoms in a molecule, N_m, and molecular linearity or non-linearity. A linear molecule has $3N_m$ - 5 degrees of freedom, whereas a

non-linear molecule has $3N_m$ - 6. The main target gas used in this work, methane, is a non-linear molecule and consequently has 9 degrees of freedom. The methane molecule is also a spherical top molecule with cubic symmetry, which leads to some modes carrying the same energy or degeneracy. As a result of this degeneracy, two states are triple degenerate and another state is double degenerate.

Vibrating molecules can also undergo rotations simultaneously. As the timescales for rotational motion are shorter than vibrational motion, the Born-Oppenheimer approximation can be used and E_r and E_v are considered separately. For two atom molecules with an assumption of rigid bonds between them, the energy levels of a rotation are given by:

$$E_r = \frac{h^2}{8\pi^2 I_M} J(J+1) \tag{2.6}$$

where I_M is the moment of inertia of the molecule and J is the rotational quantum number. Similar to the vibrational motion, angular momentum is quantised, leading to a selection rule for radiative transitions between rotational energy levels. For methane molecules, where the moment of inertia is the same in all three orthogonal axes, the selection rule is given by:

$$\Delta J = 0, \pm 1 \tag{2.7}$$

For rotational transitions, each of these three allowed states, -1, 0, 1, are commonly denoted using the letters P, Q and R respectively. For asymmetric molecules, such as H_2O, as the moment of inertia along each orthogonal axis is different, there is no solution to the Schrodinger equation and the rotational spectra is highly complex.

2.4 Spectral Line Broadening Mechanisms

The absorption features of gases are commonly called 'lines' where they are assumed to be of infinitely sharp spectral width. However, in reality this is

not the case and, due to various broadening mechanisms, absorption features have an associated width that can be expressed by its full width at half maximum (FWHM), $\Delta\nu$. The broadening is a consequence of three main broadening mechanisms: natural, Doppler and pressure broadening, along with their respective lineshape functions. In addition, when high power optical sources are used power broadening is also an important broadening mechanism.

2.4.1 Natural Broadening

Natural line broadening originates from Heisenberg's uncertainty principle, where line broadening $\Delta\nu_{nat}$ is related to the ΔE by:

$$\Delta E t_{sp} = t_{sp} h c \Delta\nu_{nat} \geq \hbar \tag{2.8}$$

where $\hbar$ is reduced Planck's constant $(h/(2\pi))$ and t_{sp} is the lifetime of spontaneous transition $(1/e)$ of the total energy states from E_2 to E_1. Hence, as t_{sp} is not infinite this will result in an uncertainty in energy levels ΔE, which leads to an uncertainty or spread in the frequency of photons, $\Delta\nu_{nat}$.

Natural broadening affects all molecules in gas homogeneously and results in a Lorentzian lineshape distribution.

2.4.2 Doppler Broadening

Doppler broadening is a direct consequence of the distribution of the thermal velocity of gas molecules, which induces an uncertainty in the frequency of emitted/absorbed photons via the Doppler effect. The apparent shift in frequency, $\Delta\nu_d$ is expressed as:

$$\Delta\nu_d = \nu(1 \pm \frac{v_m}{c}) \tag{2.9}$$

where v_m is the molecule velocity with respect to the beam direction and c is the speed of light. If a molecule moves towards the beam direction of beam, $-v_m$,

the photon frequency is increased, or blue-shifted. On the other hand, if molecule is moving along the beam direction, $+v_m$, the absorbed frequency is reduced, or red-shifted.

It must be noted that, unlike natural broadening, Doppler broadening is an inhomogeneous process, as at thermal equilibrium gas molecules have a Maxwell distribution of velocities, leading to different broadening effects. The resulting broadening, $\Delta\nu_D$ is modelled using a Gaussian profile given by:

$$\Delta\nu_D = \frac{\nu}{c}\sqrt{\frac{2RTln(2)}{M}} \tag{2.10}$$

where R is the ideal gas constant, T is the temperature and M is the molar mass.

It must be noted that Doppler broadening only gains prominence at lower pressures (< 0.2 atm) and increased temperatures where the influence of other broadening mechanisms are diminished due to decreased collisions.

2.4.3 Pressure Broadening

Pressure or collisional broadening is the dominant spectral broadening mechanism at pressure levels above atmosphere. In a gas sample, the molecules collide with each other at all times due to their random thermal motion, which leads to energy exchange. The energy exchange commonly leads to the redistribution of energy levels of the molecules in collision, leading to collisional frequency broadening ΔV_L. As the name suggests, pressure broadening is proportional to gas pressure, as increased pressure leads to increased probability of molecular collisions. The temperature also affects the lineshape width, but has a smaller influence than pressure, as shown in [28]:

$$\Delta V_L = d\nu(296K)P\left(\frac{T_0}{T}\right)^{n_T} \tag{2.11}$$

where $d\nu(296K)$ is the broadening coefficient, P is pressure, T_0 is 296 K and n_T is the temperature dependence coefficient between 0.5 - 0.8 [89]. Similar to

natural broadening, collisional broadening is a homogeneous mechanism and the resulting spectral feature can be modelled using Lorentzian shape.

2.4.4   Power Broadening

Spectral linewidth is also affected by the intensity of the incident radiation, particularly when continuous wave (cw) lasers are used in steady-state excitation mode [90]. As the power is increased, the spectral line width is also increased. Power broadening is another homogeneous broadening source, hence it can be modelled using Lorentzian lineshape, and given by [91]:

$$\Delta \nu_P = \Delta \nu \left(1 + \frac{I}{I_{sat}} \right)^{1/2} \qquad (2.12)$$

where

$$I_{sat} = \frac{\pi h c}{3 \lambda^3 \tau} \qquad (2.13)$$

where I_{sat} is the saturation intensity and τ is the lifetime of the excited state. As can be seen from equation 2.12, linewidth broadening is dependent on the square-root of the instantaneous intensity of the light source used.

2.5   Line Intensity

The spectral line intensity is dependent on the transition probability of photon absorption and the population of the lower state.

The transition probability is the likelihood of a molecule transitioning between two energy levels ($E_2 \rightarrow E_1$). In section 2.3.1, these probabilities for rotational and vibrational transitions were already discussed. Referring back to Planck's law in equation 2.2, allowed transitions have a higher transition probability than forbidden transitions, hence, their spectral line intensity is much stronger. For example, the selection rule for rotational transition can be $\Delta J = 0, \pm 1$, which

means the probability of transition outside this rule is zero and will not lead to an observable spectral feature. The mathematical description of probabilities is beyond the scope of this work, for more detail excellent resources are available in references [92].

The intensity of spectral lines from a transition between two energy levels, is directly proportional to populations of these energy levels. The populations of a set of energy levels are given by the Boltzmann distribution. For a transition from energy level E_2 to E_1, the ratio of populations is given by:

$$\frac{N_2}{N_1} = e^{\frac{-\Delta E}{k_B T}} \tag{2.14}$$

where N_2 and N_1 represent the populations of the upper and lower energy levels respectively and k_B is the Boltzmann constant. Hence, it is deducted that ΔE and subsequently spectral line intensity is increased for increased ratio of N_2/N_1.

2.6   Beer-Lambert Law

The Beer-Lambert law is used to describe the relationship between the incident intensity, and the transmitted intensity, through an absorbing medium with path length, and gas concentration, often described as percentage of molar fraction. The law is the basis of understanding gas spectroscopy and it is given by:

$$I_{out} = I_{in}e^{-\alpha C\ell} = I_{in}(1 - \alpha C\ell) \tag{2.15}$$

where α is the molar absorption coefficient (cm^{-1}).

The absorption coefficient is directly related to two factors affecting line intensity, which were previously explored in section 2.5 by:

$$\alpha = N_d\sigma(\nu) \tag{2.16}$$

where N_d is the number density of target gas and σ is the absorption cross section

which defines the transition probability, and is expressed by:

$$\sigma(\nu) = Sg(\nu) \tag{2.17}$$

where S is the line-strength and $g(\nu)$ is the normalised lineshape function, which is discussed further in section 2.7.1.

2.7   Extraction of Gas Parameters

The recovered experimental signals are meaningless unless they are related or calibrated to known data. One way of obtaining gas parameters from an acquired signal is fitting and comparing it with theoretical lineshape models using least-squares fit algorithms. When using this approach some physical parameters are particularly important for the fit: temperature, concentration and pressure. In some cases, concentration may be the known parameter but temperature or pressure is aimed to be extracted, alternatively in most cases temperature and pressure are tracked using external sensors, while concentration is targeted for extraction. However, as more information is known about the other parameters, the speed and accuracy of the fit is increased. The other essential parameters for accurate lineshape fit are line-strength and broadening coefficients which can be obtained from spectroscopic databases such as HITRAN. Although these databases, obtained from multiple spectroscopy experiments and theoretical analyses, can contain minor inaccuracies, they are a good approximation for most applications.

2.7.1   Lineshape Functions

Three main types of line-shape fitting profiles: Lorentzian, Gaussian and Voigt are discussed in next subsections.

2.7.1.1   Lorentzian Profile

As previously discussed, homogeneous broadening mechanisms, such as natural and pressure broadening, are modelled by a Lorentzian line shape. The normalised profile for Lorentz shape, Φ_L, is given by:

$$\Phi_L = \frac{1}{\pi} \frac{\gamma_L}{(\nu - \nu_0)^2 + \gamma_L^2} \tag{2.18}$$

where ν_0 is the central laser operation frequency and γ_L is the Lorentzian HWHM, for species j, given by:

$$\gamma_L = P \sum_j C_j \gamma_j \tag{2.19}$$

where C_j is the concentration of each gas species j in the gas sample being investigated, as non-target gas species also contributes to pressure broadening.

The peak height of the Lorentzian profile is given by the equation:

$$\Phi_{L-PEAK} = \frac{1}{\gamma_L \pi} \tag{2.20}$$

2.7.1.2   Gaussian Profile

The Gaussian lineshape fitting is given by:

$$\Phi_G = \frac{2}{\Gamma_G} \sqrt{\frac{ln(2)}{\pi}} exp\left[-4ln(2)\left(\frac{\nu - \nu_0}{\Gamma_G}\right)^2 \right] \tag{2.21}$$

where Γ_G is the Gaussian FWHM given by:

$$\Gamma_G = \nu_0 \sqrt{\frac{8k_B T ln(2)}{mc}} \tag{2.22}$$

where m is the molecular mass.

2.7.1.3 Voigt Profile

As previously mentioned, pressure broadening begins to dominate Doppler and natural broadening at increased pressure, starting from $\sim$ 200 mbar. Hence, the effective lineshape can be approximated by a Lorentzian lineshape as the pressure is increased. However, at atmospheric pressure ($\sim$ 1 bar), where all experiments in this work are carried out, the spectral lines are best represented using a Voigt profile, Φ_V, which represents a convolution of the two dominant broadening mechanisms, Gaussian and Lorentzian. The convolution is expressed as:

$$\Phi_V = \int_{-\infty}^{+\infty} \Phi_G(\nu')\Phi_L(\nu - \nu')d\nu' \tag{2.23}$$

It is non-trivial to find an analytical solution to this convolution. Hence, most Voigt models use numerical approximations such as the algorithm of McLean [93]. By using McLean's approximation, multiple absorption features from various gas species can be simulated, without high computational processing power. The McLean Voigt profile is given by:

$$\Phi_V = \frac{2\sqrt{ln(2)}}{\gamma_G\sqrt{\pi}}V(X,Y) \tag{2.24}$$

where γ_G is the Gaussian HWHM and $V(X,Y)$ is given by:

$$V(X,Y) = \sum_{i=1}^{4} \frac{C_i(Y - A_i) + D_i(X - B_i))}{(Y - A_i)^2 + (X - B_i)^2} \tag{2.25}$$

The coefficients A_i, B_i, C_i and D_i are given in table 2.1.

X and Y are given by:

$$X = \frac{2\sqrt{ln(2)}}{\gamma_G}(\nu - \nu_0) \tag{2.26}$$

$$Y = \frac{\gamma_L\sqrt{ln(2)}}{\gamma_G} \tag{2.27}$$

Table 2.1: McLean's Voigt model coefficients for Voigt profile.

i	A_i	B_i	C_i	D_i
1	-1.215	0.3786	-0.3085	0.021
2	-1.3509	0.3786	0.5906	-1.1858
3	-1.215	-1.2359	-0.3085	-0.021
4	-1.3509	-0.3786	0.5906	1.1858

The FWHM of a Voigt profile can be approximated to:

$$\gamma_V = 0.5346\gamma_L + \sqrt{0.2166\gamma_L^2 + \gamma_G^2} \tag{2.28}$$

2.7.2   HITRAN Database

The HITRAN database is commonly used for obtaining spectral parameters for optimising fitting algorithms. In the HITRAN 2016 database parameters of 32 different species and their isotopologues [94] are provided. HITRAN is particularly useful for applications under atmospheric conditions. For accurate transitions at increased temperatures (> 1000 K), the HITEMP database is used. The most essential parameters for basic spectral models are: transition line position in wavenumber, line-strength, air and self broadening HWHM, temperature dependence coefficient and air pressure shift. A HITRAN based spectral model using these parameters, previously developed by Bain [26], is presented in appendix C.

In addition to obtaining spectral details during the extraction of gas parameters, the HITRAN database is also an invaluable tool when designing spectroscopy setups. HITRAN is commonly used to identify strong spectral regions, regions of potential interference with other gases and temperature dependencies of the target gas(es) before the acquisition of lasers and optical components.

It must be noted that, there are occasional discrepancies between actual measurement and the HITRAN data, however, HITRAN is still a valuable tool

before and during the testing.

2.7.3 Extraction of Gas Concentration

Typically, extraction of certain gas parameter involves assumptions or estimations about the remaining parameter. For instance, gas concentration and temperature might be known while pressure is unknown. In this study, temperature and pressure are known and monitored using external sensors and regulators, while gas concentration is the unknown parameter.

PAS systems are often based on the use of calibration scales, determined using extensive preliminary tests. The PAS signal amplitude, $S_A(Pa)$, registered using a sound transducer, is dependent on the gas concentration with the following relationship:

$$S_A(Pa) \propto K_m(Pa)C \tag{2.29}$$

where $K_m(Pa)$ is the sensitivity of the microphone which is dependent on the sound pressure level, SPL. Hence, for a measurement with negligible maximum SPL variation, a linear relationship calibration curve is obtained between the sound transducer amplitude and gas concentration. In addition, once $K_m(Pa)$ is also characterised at a range of SPL levels, this data can also be used to normalise the PAS calibration curve.

2.8 Summary

In this chapter, an overview of the underlying principles of spectroscopy has been introduced. Throughout this introductory chapter, methane gas was discussed under every relevant subsection, as it is the main gas specie used throughout this thesis.

In the first section, the relationship between the spectroscopy and molecular absorption has been introduced. Subsequently, energy levels were discussed

with an emphasis on ro-vibrational energy levels. Then, the spectral line broadening mechanisms: Doppler, pressure and natural, as well as their resultant lineshape functions (Lorentzian, Gaussian and Voigt) were described in detail and discussed mathematically. The factors determining line intensity such as transition probability and population of states was also discussed, as well as the main principle of absorption spectroscopy: Beer-Lambert law. Finally, the HITRAN database and methods for extracting relevant information from a recovered absorption spectra was reported.

Chapter 3

The Photoacoustic Effect

3.1 Introduction

This chapter addresses the fundamental principles of the photoacoustic effect for different states of matter, and its implementation for the detection of gases in photoacoustic spectroscopy.

A description of the PAS signal generation process will be presented, providing details on different cell structural designs to target different resonant conditions and modulation techniques. The prevailing problems with the implementation of PAS in industrial applications are discussed, such as the requirement to frequently re-calibrate the sensor for changing environmental conditions. Finally, our proposed calibration technique is presented theoretically.

3.2 Photoacoustic Signal Generation

Photoacoustic signal generation from a material illuminated with a modulated optical source can be simply described as a four-step process:

- Sample absorbs electromagnetic energy and is excited to higher ro-vibrational energy levels

- Heat generation as energy is lost to molecular motion, leading to increased

pressure

- Acoustic wave generation due to rapid, localised heating and cooling

- Measurement of the acoustic wave via a suitable transducer confined within a resonant cell, used to isolate and amplify the PAS signal

In next two subsections the physical process of photoacoustic generation in gaseous and solid media will be presented respectively.

3.2.1 Photoacoustic Signal Generation in Gaseous Media

As described in section 2.2 of chapter 2, photons from the optical source at a target wavelength will be absorbed by the target molecules within a gas sample, resulting in excitation of the target species to a higher energy state. The energy acquired by a gaseous species during ro-vibrational absorption is then lost through a combination of radiative de-excitation and non-radiative processes, each with differing lifetimes.

At standard temperature and pressure, STP, the non-radiative energy transfer processes typically have time constants of τ_{nr} (10^{-6} s - 10^{-9} s), which is significantly faster than the radiative time constants τ_r (10^{-1} s - 10^{-3} s) [95]. This implies that the majority of the optical energy is released as kinetic energy i.e. thermal expansion. The total generated energy density in the sample material is dependent on the optical intensity of the beam and the absorption coefficient of the target gas. However, as the system pressure reduces to < 100 mbar, the radiative emission contribution begins to dominate.

In a closed system, the thermal expansion generated in a single laser pulse results in a subsequent pulse of increased pressure, i.e. an acoustic pulse. Periodic generation of the transient localised heating and cooling by a pulsed or modulated optical signal leads to an acoustic wave. The generation of acoustic wave signal is described by combination of fluid mechanics and thermodynamics. The main laws involved are energy, momentum and mass conservation laws, thermodynamic state equations and Navier-Stokes for fluids, and additional longitudinal elastic

wave equation for solid samples [29]. These six laws are solved to generate six quantities describing the PA signal generation: temperature, pressure, density and three-dimensional particle velocities. The process of solving this complex problem is beyond the scope of this work and given in detail in external sources [56][28][29].

During the detection of the PAS signal, the use of a closed system for the PA generation provides acoustic isolation and enhancement of the SNR via resonant amplification using specially designed gas cells. In such systems, the optical modulation frequency, is set to be equal to the acoustic resonance frequency of the gas cell ($\omega_r = \omega$), allowing amplification of the PA signal by the Q-factor, defined in section 3.4.

If it is assumed that the PAS signal is being generated in a rigid cylindrical gas cell of length l and radius r, the solution to the wave equation is:

$$S_r(\omega_r) = \frac{(\gamma_a - 1)P_{g-abs}K_m(\omega_r)QF}{V\omega_r} \qquad (3.1)$$

where Q-factor defines the system losses, γ_a is the adiabatic constant, $K_m(\omega_r)$ describes the microphone response at ω_r, V is the volume of the gas chamber $V = \pi r^2 l$, F is the optical excitation-resonator overlap integral and P_{g-abs} is total optical power absorbed by the gas and can be calculated using the Beer-Lambert law:

$$P_{g-abs} = P_L(1 - e^{-S(T)\phi(\nu,T,P)P\chi l}) \qquad (3.2)$$

where P_L is the incident optical power, ϕ is the line-shape function of the targeted spectral feature respectively, χ is the target species mole fraction, and l is the laser-gas interaction path length inside the resonator. An important note is that the PAS signal has no phase lag with respect to the heating of the gas as long as $\omega\tau_{nr} \ll 1$ and ω is in the kHz range. However, the phase relationship of the laser's injection current is dependent only on τ_{nr}, and will be discussed in detail

in chapter 6.

3.2.2   PAS in Solids

In solids the most dominant de-excitation process is the generation of phonons within the material. In this case, the Navier-Stokes equation is replaced with a wave equation describing longitudinal waves within solid materials. The phonons created on the solid surface transfer energy to heat up gas around the vicinity of the surface. According to the Rosencwaig-Gersho model [96], the depth of this thin layer of coupled gas, L_B, is dependent on the frequency of the generating thermal excitation process, given by [97]:

$$L_B = \frac{2\pi}{a_g} = \frac{2\pi}{\sqrt{2\alpha_g/\omega}} \tag{3.3}$$

where α_g is the thermal diffusivity of a gas. For a 100 Hz modulation, the boundary layer of about 1 mm is observed for air [96] and this boundary layer becomes thinner as the modulation frequency is increased. The periodic heating of the surface gas acts like a gas piston, creating pressure waves in the sample cell [98]. This acoustic signal is amplified in a similar manner to the gas PAS signal when using resonant acoustic structures at ω_r resonance frequency. Therefore, PAS signals generated using solid materials can be described by the equation:

$$S_s(\omega_r) = \frac{P_s K_m(\omega_r) Q A_s l_c F}{V \omega_r} \tag{3.4}$$

where P_s is the optical power incident on the solid surface, A_s is the probability of absorption by the solid material and l_c is the length of interaction within the solid material along the beam-path. For interaction of a light beam with the walls of cylinder such a longitudinal resonator, l_c equals the resonator length l. It should be noted that A_s is dependent on the wavelength of the incident radiation, and for polymer materials used in this work the probability of absorption is much higher in the MIR, than in the NIR, visible and UV regions. Optical absorption in solids is mathematically described by using the Beer-Lambert law to define the

total power absorbed by the material, P_{s-abs} as:

$$P_{s-abs} = P_s(1 - e^{\sigma_s(\lambda)N_a l_c}) \qquad (3.5)$$

where $\sigma_s(\lambda)$ is the absorption cross section of the solid material and N_a is the absorber density. The probability of absorption is defined here by $A_s = \sigma N_a$.

3.3   Defining   and   Designing   Resonant Structures

A conventional PAS cell has four main functions:

- isolate the gas sample

- minimise the noise from the environment

- act as an anchor point for sensor parts such as a microphone and a window

- amplify the acoustic signal by utilising an optimised geometry to create resonances

In addition, optional additions to cell design can be used in various ways for different PAS measurement purposes, such as: the addition of buffer regions; differential measurement designs for noise filtering; and multi-pass cells to increase the overall sensitivity of the sensor.

In PAS research there are two types of resonator designs that are commonly used, Helmholtz and cylindrical resonators. In this section a brief description of each resonator type will be provided, along with their advantages and disadvantages for different applications.

3.3.1   Cylindrical Resonators

A cylindrical shaped cell generates three different types of resonant modes, longitudinal, radial and azimuthal, that can be described using the equation:

$$f_{jmq} = \frac{c_s}{2} \left[\left(\frac{\alpha_{jm}}{r} \right)^2 + \left(\frac{q}{l} \right)^2 \right]^{1/2} \tag{3.6}$$

where the angular frequency of each resonance is $\omega_{jmq} = 2\pi f_{jmq}$, c_s is the speed of sound, j, m, q are non-negative index integers used for identification of eigenmodes and α_{jm} is the mth zero of the derivative of the jth order Bessel function divided by π. When only one of these index numbers is non-zero, the resonant mode is classified as pure longitudinal $(q \neq 0)$, azimuthal $(j \neq 0)$ or radial $(m \neq 0)$. Simulated spatial pressure distributions of the fundamental mode of each resonance, calculated using the COMSOL pressure-acoustic module, are shown in figure 3.1, for a cylindrical resonator filled with 100 % CH_4.

The spatial distribution of the eigenfrequencies for multiple mixed modes is complex, have a lower magnitude and are commonly unpractical for uses in PAS. Hence, cylindrical cells are commonly designed to utilise only one type of resonance.

Typically, the fundamental harmonic modes are selected for a cell design, as they are at the lowest frequencies and have the highest acoustic amplitudes, and the cell is designed according to the l and r given by equation 3.6, constrained within manufacturing limits. As can be seen from figures 3.1b and 3.1c, the ω_r difference between the radial and longitudinal fundamental modes is 2.4 kHz, which can potentially lead to cross-talk between the separate modes as both will be excited. The overlap integral, F, introduced in equation 3.1, is different for each mode of a resonator. For this reason, by changing the path of the optical beam through the cell, the overlap of a specific mode can be maximised $(F \Rightarrow 1)$ while other resonances are minimised $(F \Rightarrow 0)$. For example, when the laser path is through the central axis of a cylindrical resonator, longitudinal modes are efficiently excited, whereas azimuthal modes are suppressed, which require off-axis optical input for optimum excitation.

(a)

(b)

(c)
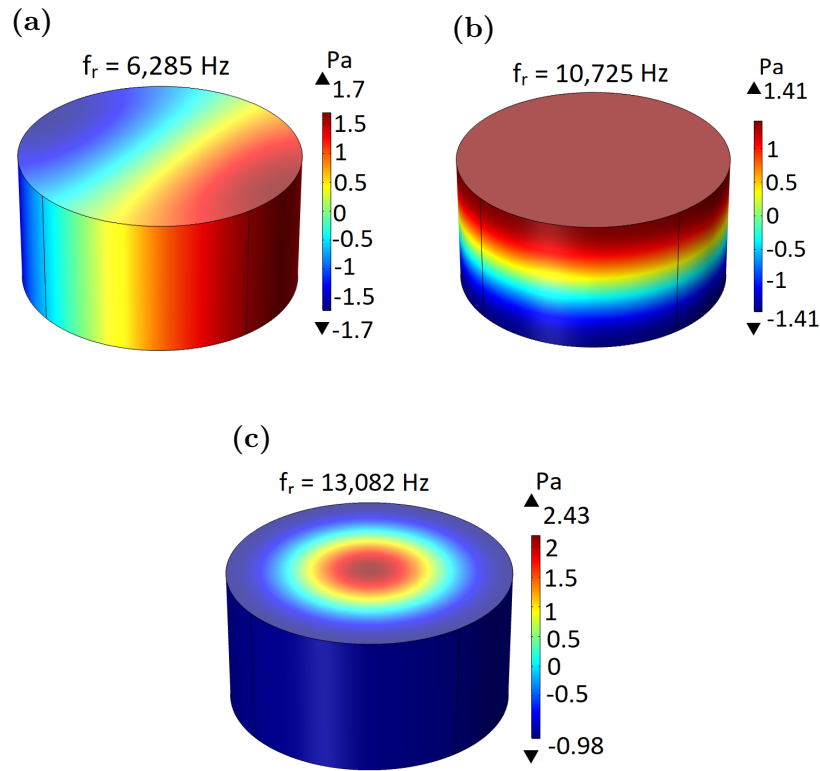
Figure 3.1: Pressure distributions of (a) Azimuthal (100), (b) Longitudinal (001), (c) Radial (010) fundamental eigenmodes of a cylindrical cell - simulated using the finite element modelling (FEM) software COMSOL.

As evidenced from equation 3.6, cell length is not an important consideration for fundamental azimuthal and radial cell designs, as ω_r is dependent on $1/r$. These cells commonly have higher Q-factors and resonance frequencies, but have lower F values due to their larger volumes and requirement for off-axis laser path for excitation. The fundamental azimuthal resonant mode has a node in the middle of the cell and two anti-nodes located at the top and bottom extremities of the cylinder centre. By placing two microphones at these two extremities, a certain amount of common-mode noise cancellation can be achieved as the generated pressure wave is π out of phase at the node and anti-node. The subtraction of the signals from the two microphones removes any in-phase background noise, whilst adding together the acoustic PAS signals. In must also be noted that high Q-factors imply that these cells are more susceptible to the signal deterioration due to resonance frequency drift - more detail is presented in section 3.8.

For longitudinal cells l is the determining factor for ω_r. These cells commonly have a lower Q-factor compared to azimuthal and radial modes. However, for purely longitudinal modes the acoustic pressure can be increased by decreasing the total cell volume, which is commonly achieved by the reduction of r - this will be discussed in detail in section 3.5. These cells offer the highest F values and as can be seen from the figure 3.1 the fundamental longitudinal mode offers the highest frequency resonance compared to azimuthal and radial modes, reducing the 1/f noise. In addition, again seen from the figure 3.1, spatial separation of the anti-nodes is largest in longitudinal modes, leading to better isolation of the acoustic signal and reduced cross-talk at the point of measurement. Unlike radial and azimuthal cells, longitudinal cell designs allow the addition of $\Lambda/4$ length buffer regions for effective acoustic noise filtering, discussed in more detail in section 4.2.3.

Due to the potential for miniaturisation, ease of efficient beam coupling and acoustic filtering, purely longitudinal cells have been used throughout this study.

3.3.2 Helmholtz Resonators

Helmholtz resonators have a more complex geometry than cylindrical cells and consist of two larger volumes V_a and V_b, called vessels, connected by at least one neck, defined as the capillary and having a length l_{cap} and cross-section A_{cap}. In these resonator designs the PAS signal is amplified by the periodic movement of the gas from one vessel to another via the capillaries, which is equivalent to a simple harmonic motion in mechanics. For maximum amplification, the laser beam passes through the central axis of one of the vessels and is modulated at the Helmholtz resonance frequency, which is defined in equation 3.7:

$$\omega_r = \frac{c_s}{2\pi}\sqrt{\frac{A_{cap}}{V_{eff}l_{cap}}} \tag{3.7}$$

where V_{eff} is the effective volume given by:

$$\frac{1}{V_{eff}} = \frac{1}{V_a} + \frac{1}{V_b} \tag{3.8}$$

The simulated pressure distribution of a Helmholtz resonance for 100 % N_2 gas is shown in figure 3.2. The small cylinders placed in the centre of the capillaries are the positions of the gas inlets and outlets. The PAS signal in a Helmholtz cell is detected via microphones placed at the centre of vessels.
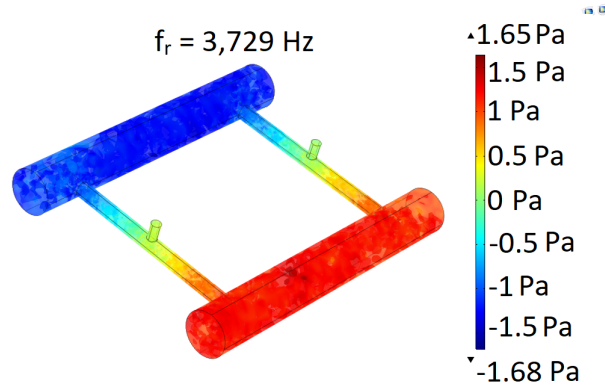
Figure 3.2: Pressure distribution at resonance frequency of a Helmholtz resonator simulated using finite element modelling software COMSOL.

Although Helmholtz cell arrangements are as sensitive as cylindrical cells for PAS measurement, it has particularly important advantages for specific measurement needs. When two capillaries are used, the pressure waves in each duct are out of phase by π degrees, potentially allowing differential measurements to increase the SNR. Also, as the signal is not dependent on an overlap integral of the optical source and the acoustic mode, Helmholtz cells can be used effectively with divergent, incoherent sources [99]. One further interesting advantage of Helmholtz cells is their ability to be used at gas temperatures much higher or lower than the operating range of microphones, as the microphone can be kept away from the excitation vessels [100].

3.4 Signal Losses in PAS and the Effect on the Q-factor

When a system is set to operate in resonance, the generated signal amplitude is amplified by the quality factor (Q-factor) of the resonant mode, which is proportional to the ratio of stored energy in the system per cycle, E_{stored}, to the energy lost to various processes that cause broadening of the resonant shape, E_{lost}, and can be described mathematically as:

$$Q = 2\pi \frac{E_{stored}}{E_{lost}} = \frac{\omega_r}{\Delta\omega_r} \tag{3.9}$$

where $\Delta\omega_r$ is the frequency difference between two points on a frequency response curve that correspond to the amplitude values that are $1/\sqrt{2}$ of the peak amplitude i.e. full width at half maximum power.

As the Q-factor describes the losses in a resonant system, the total loss in a system, Q_T is the summation of all the different loss mechanisms within the system and can be defined as:

$$\frac{1}{Q_T} = \sum_j \frac{1}{Q_j} \tag{3.10}$$

where Q_j is each type of loss mechanism. For longitudinal mode based PAS cell designs there are three loss mechanisms that need to be considered, the surface, volumetric and radiation losses.

3.4.1 Surface Losses

Surface losses are due to the interaction of the acoustic standing wave with the surfaces within the cell. They can be split into the following dissipation processes [101]: wave scatter at obstructions such as microphone inlets, losses at elastic resonator surfaces, viscous and thermal losses and losses at the microphone diaphragm surface.

Energy losses due to wave scatter at obstructions and wave confinement issues due to surface elasticity can be minimised, and assumed to be negligible, by a careful design process of the resonator and the selection of a rigid fabrication material to prevent damping.

The quantification of surface losses at the microphone diaphragm is more complex, since energy transfer to the diaphragm is essential for the generation of an electrical signal at the microphone output and will be dependent on the microphone characteristics. For PAS cells with small diaphragm surface area compared to the total surface area of the resonator this dissipation process can be neglected as well [102]. However, during simulation of acoustics of miniaturised PAS cells, with comparable resonator surface area to the microphone diaphragm, this energy loss must be taken into account.

Thermal surface losses originate from the assumption in equation 3.1 given in section 3.2.1 that a fluid behaves adiabatically. In actuality, when heat is exchanged with compression and rarefaction regions the sound wave cannot be contained in a standing wave efficiently, leading to thermal losses.

Viscous surface losses originate from the loss of energy when sound travels at different velocities in the vicinity of the resonator surface, leading to sheer stress. Although thermal and viscous losses are commonly limited, they become the dominant sources of loss for PAS cells with smaller form factors. The loss due to viscosity and thermal effects is given by the equation [56]:

$$\frac{1}{Q_s} = \frac{\sqrt{2\mu} + (\gamma_a - 1)\sqrt{2\kappa M/C_p}(1 + 2r/l)}{r\sqrt{\rho f_{jmq}}} \tag{3.11}$$

where μ is the dynamic viscosity, κ is thermal conductivity, C_p is the heat capacity and ρ is the gas density.

Surface losses are commonly the most dominant acoustic energy loss source for longitudinal modes of cylindrical cells.

3.4.2   Volumetric Losses

Volumetric losses originate from processes of homogeneity establishment in the pressure wave [101], such as relaxation, diffusion effects and free-space viscous and thermal losses.

Losses due to diffusion and relaxation are commonly negligible under normal operating conditions of PAS cells [29]. However, under low pressure operation, or in presence of certain poly-atomic molecules such as water vapour which affect relaxation processes with τ_{nr} relaxation time, relaxation losses can make a significant contribution.

Free-space viscous and thermal losses originate from the energy dissipation of the acoustic wave as it travels along the cell volume to thermal conduction and viscosity due to thermal gradients [103]. As the characteristic length is too small for many target gas molecules, this loss source only becomes significant after the acoustic wave travels large distances [103] and can therefore can be ignored for miniaturised PAS cell designs.

Q-factor related to volumetric losses in a PAS cell, Q_V, is given by the Stokes-Kirchoff equation [58]:

$$\frac{1}{Q_v} = \frac{f_{jmq}}{2c_s^2} \left(4/3\frac{\mu}{\rho} + (\gamma_a - 1)\frac{\kappa}{\rho C_p} + \frac{\mu}{\rho} \right) \tag{3.12}$$

3.4.3   Radiation Losses

Radiation losses are defined as the acoustic energy lost through unsealed crevices and inlets of the PAS cell. For a closed PAS cell, the radiation loss through the optical input port and microphone port can be neglected, due to high acoustic reflectivity coefficient at windows. However, the losses through other openings, such as inlet/outlet piping, buffer volumes and unsealed microphone ducts and windows, cannot be neglected without careful design and fabrication. Losses due to unsealed sections can be eliminated by the use of an appropriate fabrication procedure to achieve acoustic isolation, whereas, other losses can

be minimised by increasing the acoustic impedance of these openings to reduce acoustic transmission through the boundaries [104]. In cases where these losses can not be eliminated or minimised, multi-physics simulation tools, such as the software package COMSOL, can be used to account for losses or eigenfrequency shifts caused by design features.

3.5   Miniaturisation

An interesting and widely utilised feature of PAS gas sensing using longitudinal cells is the increase in the generated pressure wave by a reduction in cell volume, which allows miniaturisation of PAS cells into compact devices. Miniaturisation in gas sensors leads to lower power consumption, compact sensors and reduced sample sizes and is highly desirable for many industrial applications.

Considering the dominant Q-factor source for surface losses in equation 3.11 for cylindrical resonators with $l \gg r$ and equation 3.1 for signal generation in longitudinal cells ($\alpha_{jm} = 0$), it can be shown that the PAS signal is dependent on the resonator dimensions as:

$$S_r(\omega_r) \propto \frac{1}{r}\sqrt{l} \qquad (3.13)$$

Equation 3.13 clearly shows that increasing the resonator length or reducing the resonator diameter will increase $S_r(\omega_r)$. However, the volume reduction is typically realised through radius reduction, as evidenced from equation 3.6, as a reduction in resonator length leads to lower resonance frequencies, which results in increased 1/f noise.

The maximum $S_r(\omega_r)$ signal achievable by the reduction in r is limited by the fabrication techniques and the Q-factor. For fabrication by 3D-printing this limit is defined by the printing resolution as compared to the resonator radius. As the radius tends toward the printer resolution the Q-factor inherently tends to 0. In addition, it can be seen from equation 3.11 that for long cylindrical resonators with $l \gg r$, the surface Q-factor is dependent on cell dimensions with the relation

$Q_s \propto \sqrt{r}/l$, which implies any reduction in r also leads to a larger surface area to volume ratio. This will also reduce the overall quality factor of the resonance. So there is a trade-off between the achievable Q-factor, the amplitude of the generated acoustic pressure and the resonator frequency.

In recent years, the use of new fabrication techniques, particularly high resolution 3D-printing technology allows cells with low volume and intricate internal geometries to be manufactured, compared to traditional methods of fabrication such as steel and glass, thus providing a high overall sensitivity [59].

3.6   Radiation Sources for PAS

During the development of the PAS technique in early 1970s, broadband sources were replaced by infrared gas lasers such as CO_2 and CO lasers, owing to their superior spectral power densities, coherence and ability to be tuned to strong ro-vibrational spectral features of some gases [29]. Although, these gas lasers are still being used in some applications requiring high radiation power, there is now a well established and growing dominance of semiconductor lasers in all areas of spectroscopic trace gas sensing including PAS. In addition, the field of PAS closely followed and implemented new developments in this laser technology such as OPOs [105] and ECDLs [106].

The optical sources for selective and sensitive PAS applications must have features such as:

- high power output

- narrow linewidth

- single mode beam

- long term stability and reliability

In addition to these features, small form factor and low cost can also be required.

Due to their extensive development infrared semiconductor lasers became invaluable tools for PAS, conforming with all the requirements of a selective

and sensitive PAS radiation source. In addition, semiconductor lasers can cover an extensive spectral range from visible to far-infrared, presenting additional versatility. However, the most peculiar advantage of semiconductor lasers is the ease of rapidly modulating their output via modulation of the injection current allowing higher sensitivity measurements at reduced 1/f noise. This is commonly achieved by modulating the laser using an external current injection modulation method using a high-frequency signal, which is then used to demodulated the PAS signal using lock-in amplification.

The modulation techniques for semiconductor lasers can be divided into two schemes: wavelength modulation and intensity modulation, as previously introduced in in section 1.4.2.3.

For applications in PAS, WM presents a better suppression of the ambient noise and is a more efficient technique overall as suggested by Schilt [48]. However, in a WM scheme a small amount of IM will always be present accompanying the WM, which is commonly called a residual amplitude modulation, leading to undesirable effects such as signal distortion and wall noise in PAS [56].

The effects of noise can be further reduced by the use of harmonic detection in conjunction with WM. In harmonic detection of WM spectroscopy, a dual current modulation is applied to the laser, with a slow frequency ramp waveform (< 10 Hz) to scan over the targeted rotational-vibrational transition and a higher frequency sinusoidal modulation (> 1 kHz) that generates laser-gas interaction signals at the harmonics of the modulation frequency [48]. The PA signal can then be extracted from the harmonics of this modulation using a phase-sensitive lock-in amplifier, where the nth derivative of the absorption lineshape corresponds to the nth harmonic. This WMS technique can also be applied to PAS to increase the signal sensitivity in a similar way. The theoretical description of the harmonic WM detection for PAS is explained in detail in section 3.9.

3.7 Transducers

The generated acoustic signal is converted into an electric signal by the use of transducers. Traditionally, various types of microphones were used, such as electret and condenser transducers. However, other transducers have been gaining prominence and will also be discussed briefly below.

Electret condenser microphones are capacitor-based microphones made up of a rigid back plate and a thin metal electret diaphragm, which creates an electric signal as the diaphragm oscillates due to an acoustic wave. Unlike traditional condenser microphones, electret microphones do not require a high external polarization voltage on the diaphragm. Although these microphones are very low in cost, sensitivity of the microphone is directly proportional to diaphragm surface area, which means a reduced compactness. In addition, there is also a trade-off between the sensitivity and frequency bandwidth.

An alternative to these bulky microphones is the use of MEMS microphones, which are also very low cost, can offer a wide range range of acoustic detection (up to ultra-sound) but at a much reduced form factor. This reduced form factor is also highly advantageous for PAS applications requiring overall compactness.

An optical cantilever microphone system is made up of a flexible pressure-sensitive, silicon cantilever and an optical interferometer unit [107]. As the cantilever oscillates due to the external acoustic wave, the optical interferometer detects motion of the cantilever, which is subsequently converted into a voltage signal. The main advantages of this system is detection via EM radiation rather than electrical detection and their high response at low frequency. Unfortunately, the manufacturing process of cantilevers and their attachment to PAS cells is highly complex and overall costs are high.

Quartz tuning forks [60] used in quartz-enhanced PAS have resonant frequencies, $\omega_r = 32.75$ kHz, with a Q-factor reaching up to 10,000. The main advantage of QTFs are reduced 1/f noise due to high ω_r, small form factor, and low cost. However, QTF's require a complicated and highly accurate alignment process,

particularly for multi-pass arrangements [75], as well as lasers with tight focus due to the small gap of the tuning fork leading to increased total cost and reduced ruggedness.

3.8   Justification for PAS Calibration Requirements

One key disadvantage of the traditional resonant PAS techniques is the requirement for the re-determination of the cell resonance frequency ω_r, which varies as a function of various physical parameters, and to calibrate the sensor to obtain signals at the re-calibrated resonance frequency. In this section, the influence of there various parameters on ω_r is discussed in detail.

The parameters affecting ω_r can be classified into two: fabrication and environmental parameters:

1. fabrication parameters:

   - (QTF's) prong length (L_q), width (W_q), separation (g_q), thickness (T_q) and Young's modulus (E) and quartz density (ρ_q)

   - (Cylindrical cells) length and radius

2. environmental parameters

   - temperature , pressure , gas flow velocity and changes in gas density

In general, after sensor fabrication the fabrication parameters are assumed to be fixed. However, environmental parameters are continuously variable in a real measurement environment. Hence, changes in these parameters need to be monitored frequently to be related to changes in ω_r or alternative methods need to be used to overcome this issue. Once the drifted resonance frequency of the PA cell is re-determined, the PAS sensor can resume measurements, as long as the profile of the frequency curve remains unchanged.

3.8.1 Influence of Changes in Temperature And Gas Composition

The resonant frequency of a PAS cell is proportional to the speed of sound in the gas sample. Therefore, it is dependent on the local environmental parameters, including the gas composition, temperature and humidity. For an ideal gas the speed of sound is defined as:

$$c_s = \sqrt{\frac{\gamma_a k_B T}{m}} \tag{3.14}$$

As evidenced from equation 3.14, the localised pressure does not effect c_s for a specific gas mixture. For an ideal gas, where $PV = N_T k_B T$ with V being the volume of gas and N_T being the total number of gas molecules, any change in P will be compensated by change in density, $\rho = N_T/V$, by the same factor. However, changes in P can also influence the generated PAS signals directly, which will be discussed in section 3.8.3.

Figure 3.3 shows the influence of gas composition and temperature on resonance frequency and the speed of sound for the first longitudinal mode of a 16 mm long cylindrical resonator. The physical constants used for this simulation are given in table 3.1. As expected from equation 3.14, the resonance frequency and the speed of sound increase with the square root of temperature. However, the relationship between the gas composition and the speed of sound is not inverse square root relationship for this particular case. The difference arises from CH_4 being a polyatomic molecule with $\gamma_a = 1.304$ and N_2 being a diatomic molecule with $\gamma_a = 1.4$. Commonly, molecules with lower number of atoms have lowered degrees of freedom and lower adiabatic constants (monoatomic - $\gamma_a = 5/3$, diatomic - $\gamma_a = 7/5$, polyatomic - $\gamma_a \approx 4/3$), which effectively leads to higher speed of sound at the same molar mass.
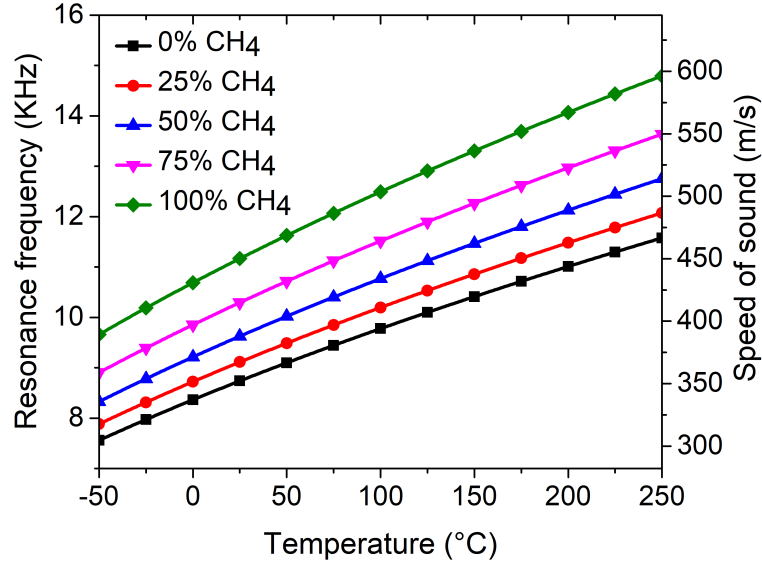
Figure 3.3: Theoretical change in the resonance frequency, f_r (left y-axis) and speed of sound, c_s (right y-axis) as a function of the gas temperature at varying CH_4/N_2 ratios. In calculation of f_r the first longitudinal mode (100) of cylindrical resonator with 16 mm length is used.

Table 3.1: Physical gas parameters of N_2 and CH_4 used in simulations.

Physical parameters	CH_4	N_2
Molar mass, M [g/mol]	16	28
Density, ρ [kg/m^3]	0.717	1.25
Adiabatic constant, γ_a	1.304	1.401
Heat capacity at constant pressure, C_p [J/(kg K]	2220	1040
Heat capacity at constant volume, C_v [J/(kg K]	1700	743
Thermal Conductivity, κ [W/(m.K)]	0.0341	0.026
Viscosity, η [Pa.s]	1.10×10^{-5}	1.76×10^{-5}

Gas composition also has a profound effect on the efficiency of photoacoustic signal generation. The temporal behaviour of the non-radiative deexcitation process, described in chapter 3.2.1, is dependent on the molecular collision process. Variations in the vibrational energy states of the target molecules, and other species within the gas mixture, can lead to variation of τ_{nr} from 10^{-3}

to 10^{-8} s at 1 atm pressure [108]. Therefore, the introduction of fast relaxing molecules into a sample of a slow relaxing target species will increase the PAS signal amplitude. It was observed that the introduction of 4 % SF_6 gas with very short relaxation times to buffer gas during PAS measurement of CO_2 with slow relaxation time can dramatically increase the sensitivity to 7 pbbv at 4.23 µm using a 20 mW OPO [109]. As H_2O is also a fast relaxing molecule compared to N_2, PAS sensitivity increases in more humid atmospheric conditions.

Temperature variation also varies the performance of commonly used acoustic transducers, such as QTF's, electret microphones and MEMS microphones.

For a QEPAS sensor the generated noise is proportional to $\sqrt{T}$ [110], and the resonant frequency has been shown to vary with -0.04 $\times$ 10^{-6} Hz/$^\circ$C ^{2} whereas the Q-factor scales with a coefficient $(\Delta Q/Q)/\Delta T$ = -0.4 %/$^\circ$C [111]. For standard microphones, temperature response varies depending on the type of microphone. For instance, a MEMS microphone may vary by 0.5 dB over their operating ranges [112], whilst an electret condenser microphone can vary by ± 4 dB.

3.8.2   Influence of Changes in Gas Flow Velocity

The acoustic resonance frequency of an open ended cylindrical resonator can shift dramatically at high gas flux rates [113]. This phenomenon arises from the Doppler shift caused by the flowing gas. The detected fundamental longitudinal resonance frequency, f_{rD}, can be derived from the principles of Doppler shift and is given by [113]:

$$f_{rD} = f_{r0}(1 - Ma^2) = \frac{c_s}{2l}(1 - Ma^2) \tag{3.15}$$

where f_{r0} is resonance frequency in the case of no gas flow and Ma is the Mach number (the ratio of the gas flow velocity to the speed of sound). Figure 3.4 shows the variation in resonant frequency of a 16 mm long longitudinal resonator at normal temperature and pressure for a 10 % CH_4 - 90 % N_2 gas mixture for flow velocity ranging from 0 Ma (no gas flow) to 1 Ma, which equates to a flow

rate of 354 m/s or 37.8 l/min for a 0.75 mm cylindrical radius.
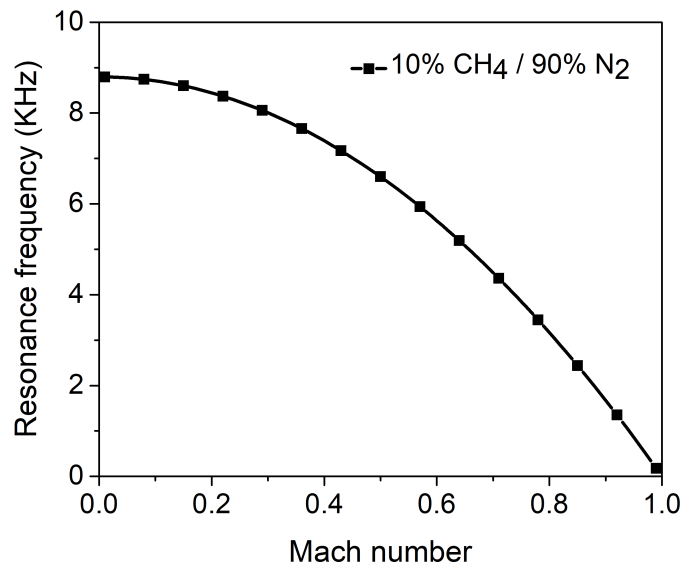
Figure 3.4: Simulated resonance frequency against Mach number.

It is clear from figure 3.4, that variation in flow rate has a significant effect on the resonant frequency. In addition, at higher gas flux rate, the flow becomes turbulent and adds to the noise detected at the acoustic element.

3.8.3   Influence of Changes in Pressure

Microphone sensitivity and Q-factor are also dependent on pressure [113]. Commercially available microphones are ideally designed to operate in air at normal temperature and pressure (NTP), and any deviation from these conditions changes microphone sensitivity. Electret microphone responsivity has been shown to reduce for pressures below 1 bar, both theoretically and experimentally [57]. Webber [114] have shown an increase in Q-factor of 81.25 % for a pressure increase from 0.06 bar to 0.2 bar. However, theses studies are all for individual microphone types, and sensitivity variation and Q-factor trends shown by both of these studies for Q-factor and microphone sensitivity could be reversed or different in pressures above 1 bar, for other gas mixtures and different types of microphones. However, PAS setups operated at lowered pressures will always benefit from increased selectivity due to the reduced pressure broadening of spectral lines.

Pressure also plays a major role in the efficiency of the photoacoustic signal generation, as the non-radiative lifetime is inversely proportional to the pressure [113]. In fact, when the non-radiative lifetime becomes comparable or smaller than the optical modulation frequency the PAS signal amplitude decreases and its phase is reversed [108].

3.8.4   Influence of Changes in Input Radiation

Generated photoacoustic signals are also directly proportional to the input optical power, as evidenced in equation 3.1. Therefore, any optical variation will cause variation in the generated PAS signal. This includes short term variations, such as particulate contamination, and long term optical drift, due to input beam misalignment or laser performance degradation.

3.9   Theoretical   Description   of   PAS-WMS Signal Generation

In TDLS-WMS, a high frequency modulation is superimposed on the low frequency wavelength tuning used to interrogate a spectral feature. Lock-in amplification is then used to demodulate gas dependent signals generated at the harmonics of the high frequency drive signal. The PAS-WMS technique was originally adapted from this optical counterpart. The application of WMS in PAS allowed higher sensitivities to be achieved than in TDLS-WMS, and also allowed access to a large number of a large number of IR active species not available with high power pulsed lasers originally used in PAS research.

One of the interesting features of TDLS-WMS is the measurement of the direct intensity modulation from the laser, which is present even in absence of laser-gas interaction, and is known as the RAM. At low gas absorption the RAM is the dominant signal output at the first (fundamental) modulation frequency (1f) and has been used in a number of calibration-free WMS techniques. Originally, the RAM was seen as an undesirable signal component, which saturates the detector

and analog-to-digital (ADC) inputs and caused unwanted signal distortion. This led many researchers to avoid 1f detection, and to focus on the second-harmonic, or 2f detection.

It is the RAM effect that presents the major difference between TDLS-WMS and PAS-WMS. As the RAM is a direct measurement of the laser intensity modulation output, and involves no optical absorption, it does not generate an acoustic signal. Hence, PAS is an intrinsically zero-background gas sensing technique, and this is often seen as one of the main advantages of PAS-WM.

The theory of TDLS-WM, and PAS-WM, has been developed over a number of years [48][115][116] [117][118] [119] [120][121][122]. In this work a derivation for PAS-WMS based on an adaptation of the derived signals obtained from WMS presented by Rieker [123] is presented. It should be noted that the PAS-WMS signals derived in this section are valid for any optical thickness, modulation amplitude, type of acoustic detector, target gas species, target gas concentration, temperature and pressure.

As PAS-WMS is based on optical absorption, rather than transmitted power, the use of total optical power absorbed by the gas, P_{g-abs} is used rather than the transmitted power. P_{g-abs} can still be obtained using the Beer-Lambert given in equation 3.2.

Equation 3.2 is used to describe the low frequency interrogation of the targeted spectral region. To describe the high frequency modulation applied to the laser at the cell resonance the incident optical power can be presented as:

$$P_L = P_0(\nu_0) + \Delta P cos(\omega_r t) \tag{3.16}$$

where $P_0(\nu_0)$ is the laser power output at line centre, and ΔP is the power modulation amplitude that is related to current modulation amplitude via the laser's power tuning rate, ξ_P. Substituting equation 3.16 and 3.2 into equation 3.1 describes the PAS signal generation with IM as:

$$S_r(\omega_r) = G\left[P_0(\nu) + \Delta P cos(\omega_r t)\right]\left[1 - e^{-\kappa l}\right] \tag{3.17}$$

where G is the overall gain of the system including resonant amplification and microphone response given by $G = ((\gamma_a - 1)K_m(\omega_r)QF)/(V\omega_r)$, and $\kappa = S(T)\phi(\nu, T, p)p\chi$.
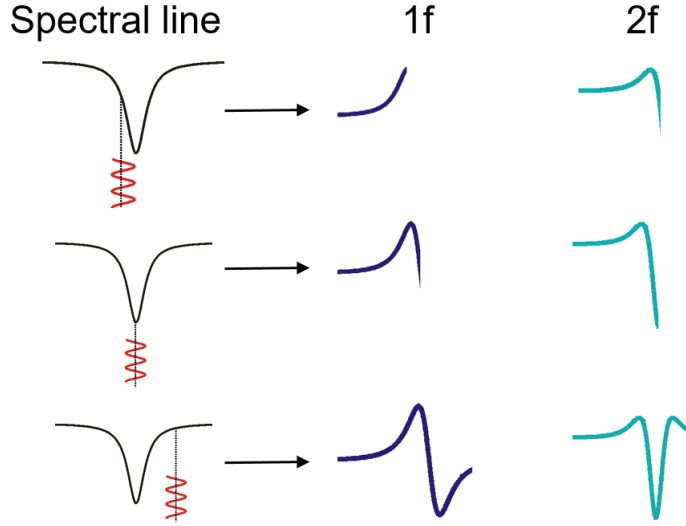
Figure 3.5: Illustration for the generation of 1f and 2f signals using wavelength modulation spectroscopy (WMS).

It is also necessary to consider the frequency/wavelength modulation output from the laser, which can be described as:

$$\nu = \nu_0 + \delta\nu cos(\omega_r t + \psi) \tag{3.18}$$

where $\delta\nu$ is the frequency/wavelength modulation amplitude (FM or WM), which is related to the current modulation amplitude via the laser's wavelength tuning co-efficient, ξ_ν, and ψ is the phase delay of the FM with respect to the IM. The FM-gas interaction process generates harmonic signals that can be described by a Fourier series expansion of the Beer-Lambert law:

$$1 - e^{-\kappa l} = 1 - \sum_{k=0}^{k=\infty} H_k(\nu, \delta\nu)cos(k\theta_T) \tag{3.19}$$

where H_k are the Fourier coefficients defined by Rieker et al. [123] and $\theta_T = \omega_r t - \psi$. The H_k terms are given as:

$$H_0(T, P, \nu, \delta\nu) = \frac{1}{\pi} \int_0^{2\pi} e^{-\kappa l} d\theta_T \tag{3.20}$$

$$H_1(T, P, \nu, \delta\nu) = \frac{2}{\pi} \int_0^{2\pi} e^{-\kappa l} cos(k\theta_T) d\theta_T \tag{3.21}$$

Using a theoretical Fourier Matlab model, given in appendix A for the following conditions: 1 atm pressure, 16 mm interaction length, and 10 % CH$_4$ gas concentration; H$_0'$, H$_1$, H$_2$ and H$_3$ are shown in figure 3.6 where $H_0' = 1 - H_0$, and describes the gas dependent IM signal without the WMS RAM background.

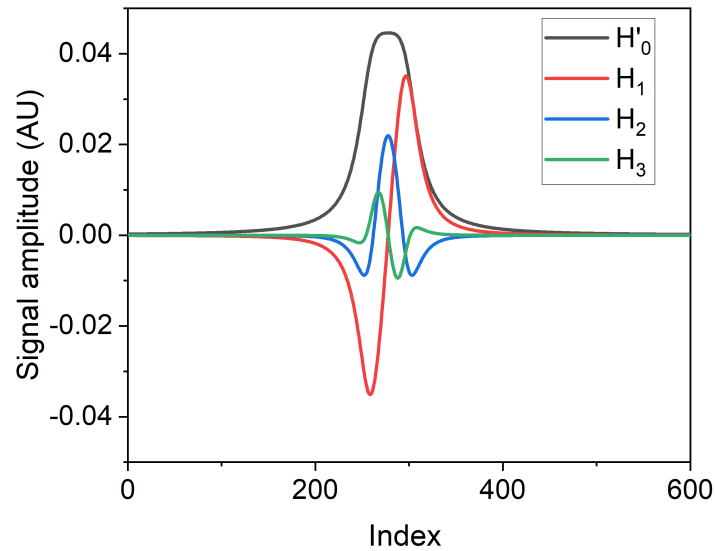Figure 3.6: Theoretical H$_0'$, H$_1$, H$_2$ and H$_3$ for 1 atm pressure, 18 mm interaction length, and 10 % CH$_4$ gas concentration.

Substituting equation 3.19 into equation 3.17 leads to a final expression for the generated photoacoustic signal as:

$$S_r(\omega_r) = G\left[P_0(\nu) + \Delta P cos(\omega_r t)\right]\left[H_0' - H_1 cos(\omega_r t - \psi) - H_2 cos(2\omega_r t - 2\psi)\right.$$
$$\left. - H_3 cos(3\omega_r t - 3\psi).....\right]$$

$$(3.22)$$

This can be expanded further and separated into the harmonics detectable by the LIA as:

$$S = G \begin{cases} P_0(\nu)H_0' - \frac{\Delta P}{2}cos(-\psi)H_1, & \mathbf{0}^{th}\ \textbf{Harmonic} \\\\ \Delta P cos(\omega_r t)H_0' - P_0 H_1 cos(\omega_r t - \psi) & \\ +\frac{\Delta P}{2}cos(\omega_r t - 2\psi)H_2, & \mathbf{1}^{st}\ \textbf{Harmonic} \\\\ \frac{\Delta P}{2}cos(2\omega_r t - \psi)H_1 - P_0 H_2 cos(2\omega_r t - 2\psi) & \\ +\frac{\Delta P}{2}cos(2\omega_r t - 3\psi)H_2, & \mathbf{2}^{nd}\ \textbf{Harmonic} \end{cases} \quad (3.23)$$

The components in form of $GP_0 H_k cos(k(\omega_r - \psi))$ in each harmonic are commonly defined as the derivative terms, they represent the kth derivative of the spectral lineshape for small amplitude modulation [122]. Components of the form $G\Delta P cos(k\omega_r t - (k\pm 1)\psi)H_{k\pm 1}$ represent the intensity modulation-gas interaction terms for each kth harmonic. In fact, the terms in equation 3.23 correspond to the TDLS-WMS Fourier terms defined by Rieker [123], except that each term has an opposite sign as PAS is an absorption based technique.

The photoacoustic signal generated according to equation 3.23 is measured by an acoustic transducer and the electrical output from the transducer is passed to a LIA. The LIA multiplies the input signal with a reference cosine and sine wave of the targeted k^{th} harmonic i.e. $Acos(k\omega_r t)$ and $Asin(k\omega_r t)$. Essentially, the LIA applies the trigonometric identities $cos(x)cos(y) = 1/2\big(cos(x-y) + cos(x+y)\big)$ and $cos(x)sin(y) = 1/2\big(sin(x-y) + sin(x+y)\big)$. A low-pass filter is then used to obtain the generated DC components from the LIA multiplication process, where

the DC components obtained from the cos term are defined as the X and and sin multiplication results in the Y components of the LIA output at k^{th} harmonic.

If the high frequency modulation and the LIA reference frequency are both equal to ω_r, the X_{1f} and Y_{1f} components are:

$$X_{1f} = G\Delta P H_0' - GP_0 cos(\psi)H_1 - \frac{G\Delta P}{2}cos(2\psi)H_2 \tag{3.24}$$

$$Y_{1f} = -GP_0 sin(\psi)H_1 - \frac{G\Delta P}{2}sin(2\psi)H_2 \tag{3.25}$$

To generate a PAS signal that can be recovered at the second harmonic of the PAS requires the high frequency laser modulation to be halved to $\omega_r/2$. If the LIA reference is kept at ω_r and $\psi_{LIA} = 0$ the X_{2f} and Y_{2f} components are:

$$X_{2f} = -GH_2 P_0 cos(2\psi) - \frac{G\Delta P}{2}\left[H_1 cos(\psi) + H_3 cos(3\psi)\right] \tag{3.26}$$

$$Y_{2f} = -GH_2 P_0 sin(2\psi) - \frac{G\Delta P}{2}\left[H_1 sin(\psi) + H_3 sin(3\psi)\right] \tag{3.27}$$

The magnitude of each harmonic R_{1f} or R_{2f} can be found by adding the orthogonal components in quadrature as $R = \sqrt{X^2 + Y^2}$.

Unlike the TDLS-WMS case [123], equations 3.24, 3.25, 3.26 and 3.27 contain no background RAM terms. Therefore, the first harmonic signal is targeted as it has the largest magnitude, thus leading to greater sensitivity.

An important factor that requires consideration in any WMS technique is the modulation index, m-value, which is defined as:

$$m = \frac{\delta\nu}{\gamma} \tag{3.28}$$

where γ is the half width at half maximum (HWHM) of the spectral line of

interest. The m-value defines the amplitude of the each of the H components, which causes significant distortion in the derivative-like FM signals, and is dependent on the FM modulation amplitude and the spectral linewidth. Figure 3.7, shows the effect of different m-values on the peak-to-peak amplitude of H_1 Fourier term for 100 % CH_4 gas at 1 atm and 296 K, for a Lorentzian dominated broadening scheme ($\gamma_L/\gamma_D \approx 8$), including the signal shapes at 0.5, 2 and 6 m-values.
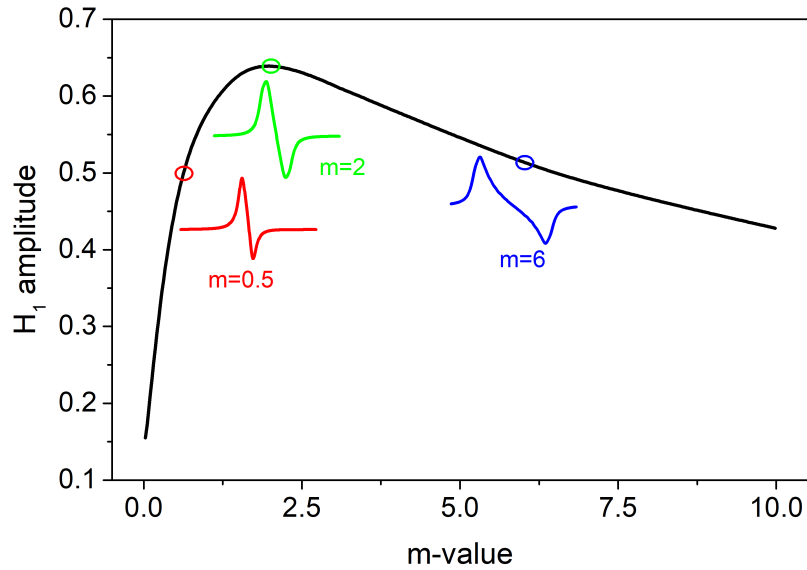
Figure 3.7: H_1 Fourier component peak-to-peak amplitude at various m-values, obtained using a Matlab model for a Lorentzian broadening dominated scheme . The peak signal is obtained when m = 2. The H_1 signal shapes at m-values 0.5, 2 and 6 are also shown.

As shown in figure 3.7, the maximum signal for the H_1 component is obtained for an m-value of approximately of 2. The optimal m-value varies for each harmonic, and is approximately equal to 2.2 for the second harmonic. At increased m-values, non-linear intensity and wavelength modulation terms (third term in equation 3.24 and second terms in equations 3.25, 3.26 and 3.27) becomes more significant, leading to distortion of the R_{1f} and R_{2f} signals. Hence, at increased modulation dept, these terms must also be considered to improve the model accuracy.

3.10 Calibration-Free PAS-WMS Model

In sections 3.2.1 and 3.2.2, the generation of photoacoustic signals in solids and gases were introduced, and in section 3.9 the theory for PAS generation using WMS in gases was further described. In this section, the generation of acoustic signals by the cell walls of the resonant gas cell is introduced. Furthermore, if the optical power absorbed by the cell wall generates acoustic signals that are comparable to, or greater than, the WMS gas signals described in 3.9, a new signal is introduced, which can be defined as the cell dependent absorption signal (CDAS). The CDAS signal is described by equation 3.4.

In this work, polymer materials have been used to fabricate the PAS cells, which are broadband absorbers at the wavelength of interest i.e. in the MIR, and other materials or other types of polymers may not be suitable to generate CDAS. This is particularly the case for NIR or visible wavelengths, where polymers are known to be weak absorbers. The WM signals generated by a broadband absorbing solid material are essentially negligible, as the m-value tends to zero. Therefore, a polymer material interacting with an intensity and wavelength modulated MIR source only generates an IM term at the first harmonic, which is similar to the direct RAM term in TDLS-WMS. The solid PAS signal can then be described as:

$$S_r(\omega_r) = G[P_s + \Delta P_s cos(\omega_r t)]A_s l \tag{3.29}$$

The solid PAS extended forms of the components X_{1f}, Y_{1f}, previously described in equations 3.24, 3.25, are:

$$X_{1f} = G\Delta P H_0' - GP_0 cos(\psi)H_1 - \frac{G\Delta P}{2}cos(2\psi)H_2 + G\Delta P_s A_s l \tag{3.30}$$

$$Y_{1f} = -GP_0 sin(\psi)H_1 - \frac{G\Delta P}{2}sin(2\psi)H_2 \tag{3.31}$$

Whilst the X_{2f} and Y_{2f} terms remain as

$$X_{2f} = -GH_2P_0cos(2\psi) - \frac{G\Delta P}{2}\left[H_1cos(\psi) + H_3cos(3\psi)\right] \qquad (3.32)$$

$$Y_{2f} = -GH_2P_0sin(2\psi) - \frac{G\Delta P}{2}\left[H_1sin(\psi) + H_3sin(3\psi)\right] \qquad (3.33)$$

The addition of the solid PAS IM leads to a $G\Delta P_s A_s l$ term in the X-component of the first harmonic signal when the LIA reference phase is set to $\psi_{LIA} = 0$. This CDAS term represents a DC offset generated by the PAS signal from the solid cell material, and is similar to the DC offset RAM signal in TDLS-WMS.

As described in section 3.9, the RAM signal in TDLS-WMS can be used as a normalisation term, as evidenced in the 2f/1f technique [123]. This allows accurate signal recovery of spectra that are already normalised for incident optical intensity and system gain. Hence, with the introduction of the CDAS component in PAS-WMS the same normalisation technique can be applied to compensate for optical power drift and system gain i.e. all the issues discussed in section 3.8.

If the optical power absorbed by the cell walls is greater than WM terms in the first harmonic signal then $R_{1f}(\omega_r)$ will tend to:

$$R_{1f}(\omega_r) \approx G\Delta P_s A_s l \qquad (3.34)$$

whereas, if the gas dependent IM terms are assumed to be significantly smaller than the second harmonic WM term then $R_{2f}(\omega_r)$ is expressed by:

$$R_{2f}(\omega_r) = GH_2P_0 \qquad (3.35)$$

assuming $\Delta P/2 << P_0$ and $\omega = \omega_r/2$, where $\omega_m = \omega_r/2$ for 2f for the recovery of $R_{2f}(\omega_r)$.

The division of equation 3.35 by equation 3.34 results in a final normalised PAS signal of:

$$\frac{R_{2f}(\omega_r)}{R_{1f}(\omega_r)} = \frac{GH_2P_0}{G\Delta P_s A_s l} = \frac{H_2P_0}{\Delta P_s A_s l} \tag{3.36}$$

The importance of equation 3.36 is the removal of all dependencies on resonant frequency, microphone responsivity and the total gain of the system. The only components left in the relationship are the gas absorption dependent H_2 term, and the ratio of the incident optical power to the optical power absorbed by the PAS cell $P_0/(\Delta P_s A_s l)$.

Using a theoretical WMS-PAS model in Matlab, given in appendix A, R_{1f}, R_{2f} and R_{2f}/R_{1f} for 10 % CH_4, 18 mm interaction length and 1 atm gas pressure is shown in figure 3.8. To approximate the CDAS signal, a perturbation, *io*, with an amplitude in accordance with the experimental observations has been added to the calculation of first and second harmonics. The H components used to simulate these plots were previously given in figure 3.6.
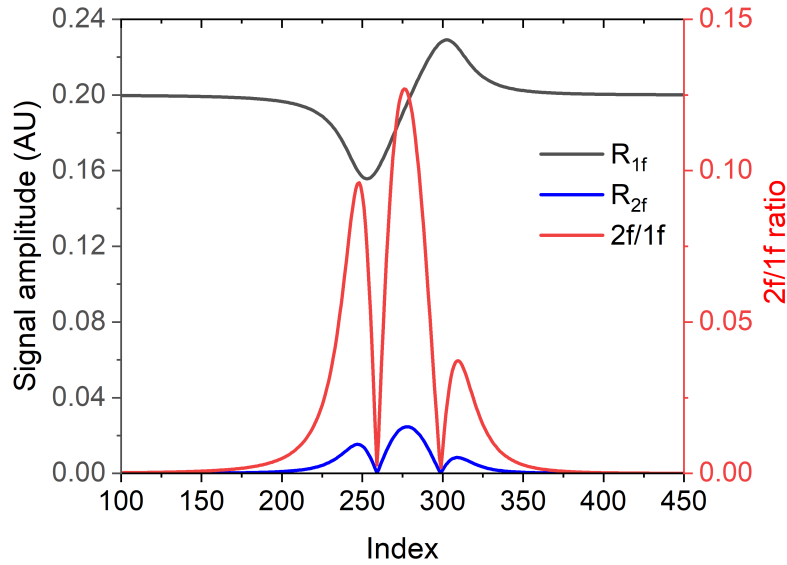

Figure 3.8: Results of theoretical model for WMS-PAS showing R_{1f}, R_{1f} and R_{2f}/R_{1f}.

As shown in figure 3.8, the addition of perturbation results in the expected DC level in R_{1f}, while R_{2f} and R_{2f}/R_{1f} signals are based on the x-axis without any DC background.

To obtain the first and second harmonic signals the laser has to be modulated

at two different frequencies, and the signals cannot be recovered simultaneously. Instead, they have to be recovered alternately as described in the experimental setup section of chapter 5. Therefore, this normalisation technique for PAS does not have the same common mode noise cancellation advantage of TDLS-WM 2f/1f. It must also be noted that the ratio of optical powers must be kept constant for the normalisation process. Therefore, any optical power variation between the recovery of the first and second harmonic signals cannot be normalised. Furthermore, the power ratio may be prone to long-term drift without careful consideration of cell and setup design.

However, this calibration technique provides a suitable normalisation process for resonant PAS systems, making it possible to compensate for varying temperature and pressure conditions and both the degradation in laser and acoustic transducer performance, and also allows measurement of gas concentrations over a wide range with varying gas densities without the requirement to monitor the variation in the resonant frequency.

3.11   Summary

In this chapter, an overview of the underlying principles of the photoacoustic spectroscopy technique upon the calibration-free measurements presented in next chapters is based on, is introduced.

Sections 3.2 and 3.3, aimed to present the fundamentals of PAS in solid and gas samples, including the two types of resonator cells commonly used in PAS applications. This section was supported with the introduction of all the sources of energy losses limiting the sensitivity of PAS measurements in section 3.4. Section 3.5, aimed to provide a rigorous mathematical justification for the advantages and disadvantages of miniaturising PAS cells. In section 3.6, a short introduction to the types of radiation sources used in PA trace gas sensing was outlined. Particular focus was directed to semiconductor lasers and their modulation techniques. On the other hand, in section 3.7 transducers used in PAS studies are introduced. In section 3.8, the major disadvantage of PAS for long

term, in-situ deployment is discussed - need to calibrate the resonant frequency, ω_r for changes in gas matrix and optical input. Finally sections 3.9 and 3.10, the PAS-WMS model presented previously in section 3.6, is expanded to include the simultaneous absorption and PA signal generation from the target gas and a DC level signal in first harmonic signal from the solid cell material, allowing the use of 2f/1f calibration technique to normalise for variables affecting the signal.

Chapter 4

Design and Manufacture of PAS cells

4.1   Introduction

This chapter presents an introduction on the design of the PAS cells used in this work. The criteria for the selection of the resonator and buffer volume dimensions are given, supported with relevant COMSOL simulations. In addition, the details of the fabrication process and assembly of the sensor are discussed in detail.

4.2   Design of a PAS Cell

A photoacoustic cell has four main functions: to contain the sample gas without leakage; to provide a platform to attach the required parts of the assembly; to increase the sensitivity by minimising external noise; and to amplify the acoustic signal.

Often, PAS cell designs are optimised according to the requirements of a particular application, such as the target gas species, the required sensitivity and the location of the sensor (defining the operation range of temperature and pressure). However, for industrial application on a large scale the priorities for the design are:

- Ruggedness

- Lifetime

- Compactness

- Cost

- Ability to measure multiples gases simultaneously

- Ability to work in high noise environments

As can be seen from equation 3.1, for a specific laser source the sensor sensitivity can only be influenced by parameters dependent on physical design, such as the volume, V, the overlap integral, F_n, the angular resonant frequency, $\omega_r = 2\pi f_r$, and the quality factor. However, as shown in chapter 3, Q and ω_r are also dependent on the dimensional parameters of the resonator. Therefore, the resonator design must be carefully considered to ensure maximum sensitivity, for targeted operating conditions of the optical source and the acoustic transducer. In this section, the design methodology used for the construction of longitudinal PAS cells used in this work will be described in detail. Each design criteria will be assessed and optimised and the results of advanced acoustic finite element modelling using software package COMSOL will be shown.

4.2.1 Criteria for Design Process

The selection of a free-space, water cooled, continuous-wave quantum cascade laser operating at 8650 nm imposes the use of a free space optical setup for a PAS sensor. Hence, the fibre coupled PAS cell designs developed in our previous studies [61][66] were modified for free-space systems. In this work, the main target gas was CH_4, which has been used instead of SO_2 due to its easier handling within the laboratory, but the sensor will also support potential SO_2 monitoring in future. At low concentration SO_2 gas is an irritant to the respiratory tract, eyes, mucous membranes, and skin, at higher concentration exposure can lead to pulmonary oedema and bronchial inflammation. On the other hand, CH_4 is a relatively safer gas to handle with similar spectral features to SO_2, which will be

discussed in detail in section 5.3.

The target absorption range of measurement is set to be between 1.53×10^{-5} to 1.53×10^{-9} corresponding to concentration ranges of 10 % and 10 ppm of CH_4 gas and 237 ppm to 2 ppb of SO_2 gas, for the specific spectral lines being considered for this work (presented in chapter 5). Subsequently, the designed sensor is required to have a large linear dynamic range. On the other hand, as the main application is the monitoring of the desulphurisation process in industrial plants, noise immunity, ruggedness and compact form factor ($< 60{,}000$ mm^3 sample volume) are also essential features of the PAS cell design.

One major design constraint is the use of 3D-printing as the fabrication method in this work. Hence fabrication is limited by the printer's resolution(43 μm X-Y and 25 μm Z for the printer used in this study) and the ability to clean residue in the thin ducts during post-processing.

4.2.2 Resonators

Longitudinal cylindrical resonators open at both ends are used for PAS cells throughout this work.

The relationship between ω_r and cell dimensions was given previously in equation 3.6 for cylindrical cells and also shown in figure 4.1 below for 10 % CH_4 gas.

The range of r and l were selected to be $r = 0$ - 2.5 mm and $l = 0$ - 30 mm for the analysis below, corresponding to a sample volume less than 60,000 mm^3, in compliance with the design criteria given section 4.2.1. The gas parameters used to calculate the resonant frequencies in figure 4.1 were provided previously in table 3.1 in chapter 3. Further consideration has to be given to pressure node shifting into the buffer volumes, located at both ends of the open-open cylindrical resonator. In this case, the resonator length l is replaced by an effective length approximation l_{eff} given by [101]:
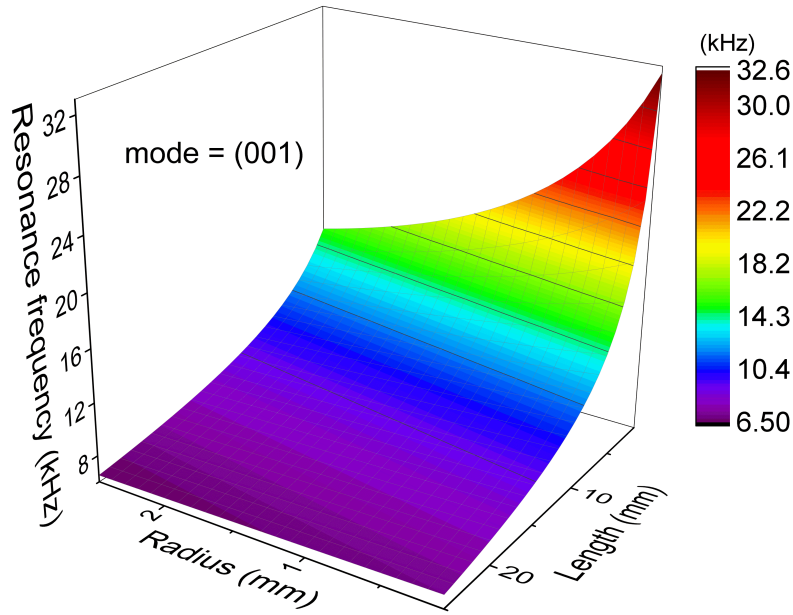
$$l_{eff} = l + \frac{16}{3\pi}r \qquad (4.1)$$

Figure 4.1: Theoretical dependence of the fundamental longitudinal resonance (001) frequency, f_r, on resonator radius r and length l at 20 °C 1 atm and 10 % CH_4 target with N_2 buffer gases.

As can be seen from the figure 4.1 and equation 3.6, the dependence of f_r on r becomes more significant as l_{eff} tends to zero, i.e. when the correction term, $\frac{16}{3\pi}r$ in equation 4.1 becomes a larger proportion of the overall cell dimensions. However, as l is increased the resonant frequency reduces, leading to a poorer SNR due to the increase in 1/f noise and environmental noise.

The resonance frequency, is also limited by the chosen microphone performance parameters. Commercial microphone responsivity is typically designed to operate in the human audible range i.e. up to 15 - 20 kHz. They are also designed to have a linear gain response over this frequency range. However, at frequencies above the linear operational range the responsivity varies greatly, which sets an lower limit for the resonator length dimension. There is also a lower frequency limit for the resonator radius, set by the laser beam waist. The QCL laser beam waist used in this work was measured as 1.204 mm in sagittal and 0.586 mm in tangential directions using a knife-edge method, which is reported in greater detail in chapter 5. Hence, to minimise power loss, and thus improve signal sensitivity, during optical coupling into the resonator requires a minimum resonator diameter greater than 1.204 mm.

The surface Q-factor, Q_s is also dependent on the resonator dimensions, as evidenced in figure 4.2 for 10 % CH_4, which shows the Q_s in a cylindrical cell for different radii and lengths. During the design process only Q_s was considered as the low volume of the miniaturised designs targeted in this work implies that the volumetric losses, Q_v, are orders of magnitude smaller than Q_s [58]. However, for non-miniaturized cells, where the ratio of the surface area to the volume is reduced, Q_v must also be considered during the design process.
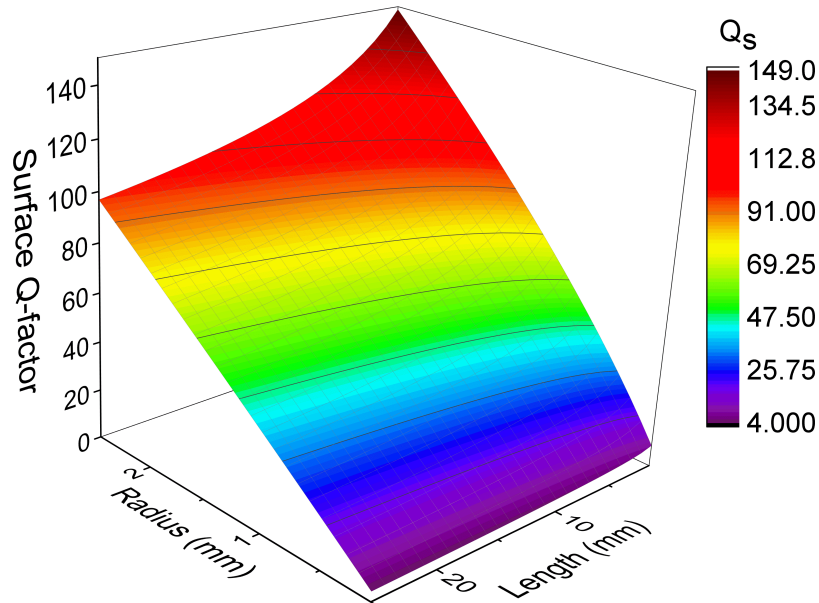

Figure 4.2: Theoretical dependence of the surface Q-factor, Q_s, for longitudinal resonances of a resonator with radius r and length l, at 20 °C 1 atm using 10 % CH_4 target with N_2 buffer gas.

As expected, figure 4.2 shows that Q_s is mainly influenced by r as $Q_s \propto r/\sqrt{l}$, previously described in equation 3.11.

When making a decision on the optimal Q-factor, consideration must also be given to the sensing environment and its effect on the overall Q-factor. For high-Q resonators, small changes in the gas matrix will lead to significant variation in Q-factor, resulting in a large decrease in PA signal compared to low-Q sensors. Hence, for applications where large changes in gas concentration, temperature, flow or pressure are expected, such as the conditions within the scope of this work, a lower Q-factor design may be preferential.

Finally, for this work, the cell length was chosen to be 16 mm. The range of theoretical resonance frequencies at this length is 7.820 - 8.750 kHz for the range of radii considered (0.1 mm to 2.5 mm) which is in the optimal sensitivity range of the microphones considered for this work (< 15 kHz). As this range is above 5 kHz, it leads to reduced 1/f noise, while l is kept long enough to allow sufficient laser-gas interaction. The Q-factor estimations were not considered when selecting the length, as frequency of operation is more important.

The resonator radius is selected as 0.75 mm, allowing the laser beam to pass to through the resonator with extra 0.145 mm tolerance on both sides of the beam, minimising any potential energy loss during coupling. Although smaller resonator radius could have been selected for miniaturisation, this will lead to reduced Q-factor as the surface losses are increased, as shown in figure 4.2. For these chosen dimensions, a theoretical resonant frequency of $f_r = 8.480$ kHz and a Quality Factor, Q = 33.13 are obtained from figures 4.1 and 4.2 for 10 % CH_4.

The beam waist plot through half cross section of a cell at these dimensions is shown in figure 4.3. The beam waist plot presented here is explained further in chapter 5. At the selected cell radius, 95.82% of the beam enters into the resonator, while the beam passing through the resonator interacts with the resonator walls. The importance of this beam-resonator interaction is detailed in chapter 6. Hence, from the figure 4.3, it can be concluded that selected cell dimensions allows the maximum overlap integral at the optimal operation frequency.
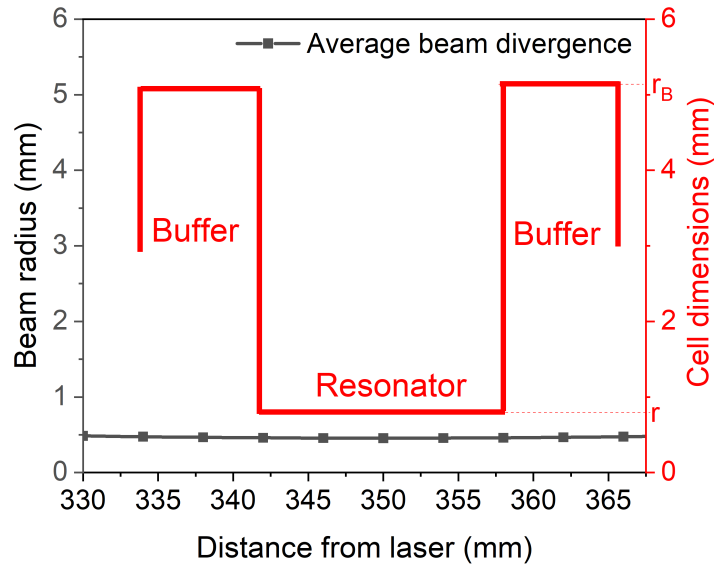
Figure 4.3: The divergence of laser beam for when resonator centre is placed at beam waist and half cross section of the cell. In this figure the resonator mid-point is positioned at the beam waist.

4.2.3 Buffer Sections

A buffer volume is added to each end of the open-open resonator design to aid the suppression of gas flow noise, and noise generated by optical absorption into the optical coupling windows of the cell. The noise suppression is achieved by the abrupt change in acoustic impedance, resulting in a high acoustic reflectivity coefficient. The gas flow noise originates from turbulence created as the gas sample passes through the cell, with increased noise being generated at increased flow rates. The majority of this noise can be removed by the lock-in amplification process. However, if the flow rate is too high this noise source can saturate the output from the acoustic transducer. More importantly, optical absorption into the windows causes them to vibrate at the laser drive frequency. The added buffer volumes on longitudinal cylindrical resonators act like silencers at either end of the resonator, suppressing this window noise.

The gas inlet/outlets and windows are attached to these buffer volumes. However, it must be noted that these buffer volumes will not remove any noise generated outside of the cell.

The buffer regions also act as high acoustic impedance reflectors, ensuring efficient acoustic reflection at the ends of the resonator and providing valid boundary conditions. It has been shown that the most suitable buffer regions have a length of $\Lambda/4$, where Λ is the acoustic wavelength [124]. For cells targeting the qth longitudinal harmonic, the length of buffer region l_B is found by [28]:

$$l_B = (2q + 1)\frac{\Lambda}{4} \tag{4.2}$$

The theoretical effect of different buffer region dimensions on the fundamental longitudinal resonant frequency and the generated acoustic pressure of a 16 mm long resonator with 0.75 mm radius are shown on figures 4.4 and 4.5 respectively. For this simulation, a hard wall boundary cell was filled with 100 % N_2 gas and the pressure-acoustic module of COMSOL was used with a parametric eigenfrequency study. In figure 4.4 it can be seen that as buffer radius and length, r_B and l_B reduce, f_r shows a sharp increase as the resonator approaches the case of a closed-closed resonator. In this case, the fundamental longitudinal resonance is at a significantly higher frequency. In addition, when the buffer length approaches the 16 mm length of the resonator, where $l_B = \Lambda/2$, the boundary condition is not supported, and f_r reduces from the expected value of 9,488 Hz for the given resonator dimensions.
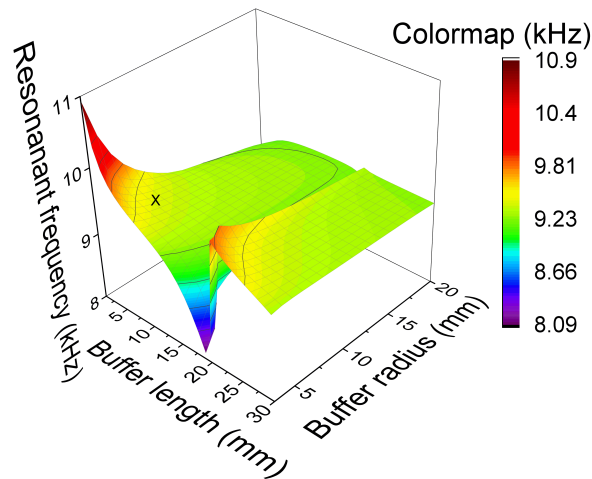

Figure 4.4: COMSOL simulation showing dependence of the first longitudinal resonant frequency on the length and radius of buffer regions on either side of a cylindrical resonator.
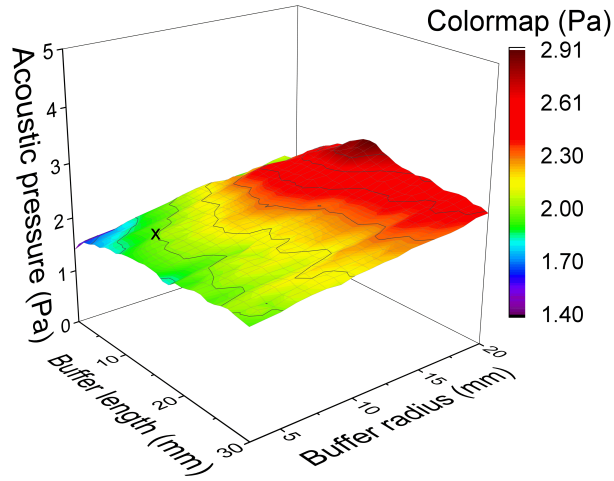
Figure 4.5: COMSOL simulation showing dependence of the acoustic signal generated on the length and radius of buffer regions on either side of a cylindrical resonator.

Figure 4.5, shows that there is a reduction in peak sound pressure at the anti-node as the buffer length and radius approach zero. Similar to the plot of resonant frequency variation shown in figure 4.4, but not as profound, a small drop in the generated pressure as l_B approaches the resonator length is also observed in this figure. This is again caused by invalidity of the boundary conditions, as buffer length approaches the resonator length. Another interesting feature of figure 4.5 is the increase in acoustic pressure as l_B approaches 13 mm in length and the radius increases to 20 mm. Although designing a cell at this peak dimensions (l_B = 13 mm and r_B = 20 mm) will theoretically increase the registered PAS signal, the large buffer region radius will reduce the potential for miniaturising cells. It should also be noted that this data was modelled for noiseless media where gas flow is non-existent. Hence, in real conditions the trends shown in figures 4.5 and 4.4 may not be valid.

A symbol 'x' has been located on both figures 4.4 and 4.5 where the optimal buffer design has been chosen for the specified resonator (at l_B = 8 mm and r_B = 5.25 mm).

The choice of this l_B is mainly affected by consideration of acoustic boundary conditions and required form factor. The boundary conditions for open-open resonator if l_B is at half integer values of resonator length, given by the following

equation:

$$l_B = (t+1)\frac{l}{2} \qquad (4.3)$$

where t is integers starting from zero. In order to satisfy this condition, t=0 was selected resulting in a l_B value with the smallest available form factor. This is also evidenced from the resonant of the point 'x' in figure 4.4 having the same resonant frequency as the largest dimension simulated (at $l_B = 30$ mm and $r_B = 20$ mm), signifying at $l_B = 8$ mm, the resonators can be regarded as being connected to an infinitely large volume of gas, satisfying the optimal boundary conditions. Hence, the dimensions at point 'x' results in optimal boundary conditions at the smallest possible dimensions for miniaturisation purposes.

The r_B is selected as 7 times the size of resonator radius at $r_B = 5.25$ mm. As previously mentioned for figure 4.4, as r_B is reduced, a sharp increase in f_r is observed. For this reason, this region of the plot must be avoided to minimise unexpected results due to potential inaccuracies in fabrication process. The r_B at position 'x' in the figure 4.4 is well outside this region of instability and still small enough to satisfy the miniaturisation criteria of this work.

4.3 Fabrication by 3D-Printing

Recent advances in 3D-printing technology has allowed the manufacture of components that are cost effective and allow rapid prototyping in the early stages of development. Traditional PAS cells are manufactured of metal or glass and there are multiple steps involved in their manufacture, such as moulds, cutting and drilling, which can lead to potential inaccuracies. However, 3D-printing is a single-step manufacturing process that produces smooth surface quality even without polishing, particularly with stereolitographic methodologies. In addition, prototypes are developed in-house providing confidence in the manufacture process and confidentiality of innovation. Furthermore, the 3D-printing of PAS cells allows a variety of materials to be used, such as those with resistance

to elasticity, heat, UV and impact, as well as materials that are chemically non-reactive to the gases being sampled.

In this work, the gas cell was fabricated using HTM140 V2 polymer and a 3D stereolithography printer (EnvisionTec Aureus Desktop), with a 43 µm X-Y resolution and 25 µm Z resolution. HTM140 V2 is a high temperature material with a quoted heat deflection temperature of 140 °C without any heat treatment, and high flexural strength of 115 MPa, which is the maximum load capability of a material without undergoing any permanent deformation. Both of these properties makes this material highly suitable for sensor applications in harsh environments [125].

Each part of the gas cell is initially designed using Autodesk Inventor, before being transferred to the Perfactory suite software for the Aureus printer. For the printing process, the part is oriented at 30° to the horizontal plane, and structural supports are added to the design to provide improved detail and tensile strength and to prevent print failure. The improved detail is achieved because of the higher printing resolution in the Z-axis, at the cost of an increased printing time. The angle also ensures that parallel grains from consecutive layers are avoided, therefore the printed shape is stronger. Finally, the added supports reduces the risk of print failure, particularly of overhanging parts such as extruding pipe inlets and outlet. The design with with added supports is shown in figure 4.6.
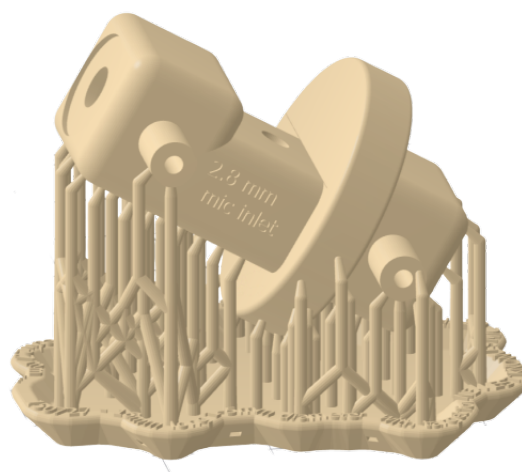

Figure 4.6: Prepared design for printing with 30° to horizontal plane with supports.

The total printing time for cells of this design is typically around 3 hrs and 30 mins. Once printing has been completed the part is removed from the build platform and submerged in 100 % Isopropanol (IPA) solution to rinse away excess resin trapped in the internal chambers and pipes. After approximately 5 mins the part is submerged into fresh 100 % IPA solution and ultrasonic bathed for another 10 mins. Any remaining resin and IPA is then thoroughly cleaned away using pressurised nitrogen, before the supports are removed using cutting pliers. If the part is left within IPA for longer than 10 mins it can become brittle leading to small cracks, and if left in IPA for a significant period of time the walls will begin to thin or may entirely dissolve.

4.4   Final Assembly

The cross sections of PAS sensors for use with an electret condenser microphone and a MEMS microphone are shown in figures 4.7 and 4.8 respectively. The figure also shows all the other components required to manufacture the sensor, including the acoustic transducer, gas inlet/outlet pipes and the optical windows. The construction of the final components must be conducted with the utmost care to avoid pressure leaks.
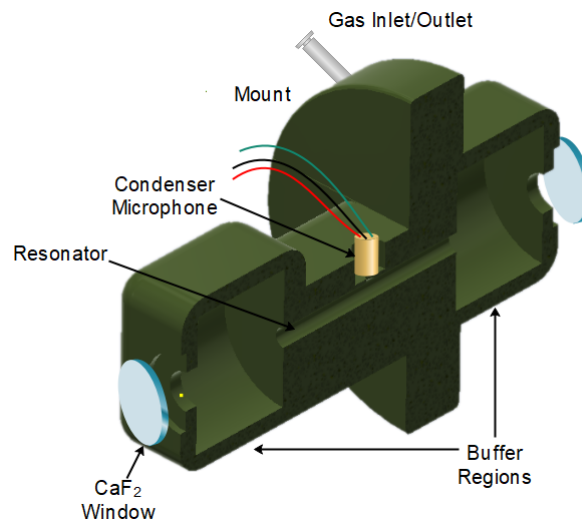

Figure 4.7: The schematic for the cross section of the 3D-printed PAS cell and assembly of the other components with an ECM.
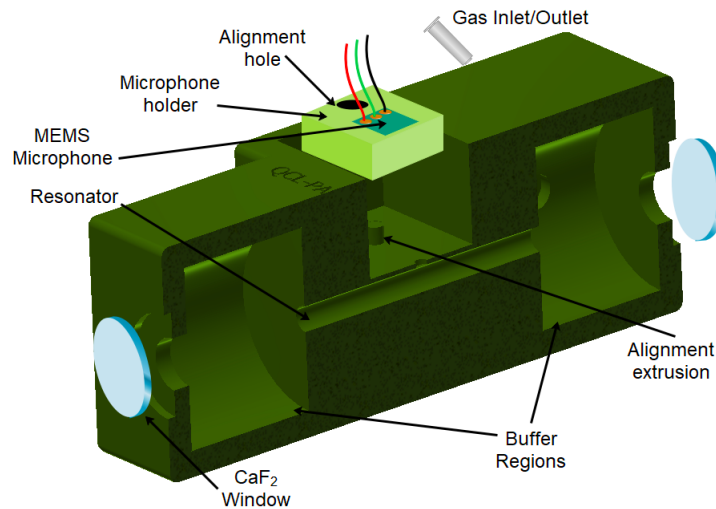
Figure 4.8: The schematic for the cross section of the 3D-printed PAS cell and assembly of the other components with a MEMS.

The most critical component in the assembly process is the alignment of the microphone inlet hole, of diameter < 0.79 mm, with the cell acoustic outlet hole, of diameter 0.74 mm and depth of 0.25 mm (located at the centre of the resonator). Two different types of miniaturised microphones have been used in this work: a top port MEMS microphone (Wolfson WM7133) and an electret condenser microphone (Knowles FG-23742-D36), with acoustic sensitivities of 12.6 mV/Pa and 7.1 mV/Pa respectively. Although the internal cell design is the same for both microphones, the alignment with the resonator centre has different methodologies.

The condenser microphone, shown in figure 4.7, is a cylindrical canister shaped microphone with pre-soldered wire leads. Therefore, an empty slot with the same radial dimensions is simply added above the resonator centre to ensure an accurate alignment when the microphone is located. It must be noted that the length of the slot is kept 1 mm shorter than the microphone length to enable the removal of the microphone if needed.

The MEMS microphone is initially attached to a custom built 3D-printed MEMS microphone holder, shown in figure 4.9, and electrical wires are then soldered directly onto the microphone terminals. It is possible to purchase a

commercial MEMS evaluation board, which presents an easy substitute, however, the 3D-printed MEMS microphone holder is more cost-effective, and the same design can be used by multiple microphones. Furthermore, the microphone can be located closer to the outlet of the resonator, thus reducing the probability of forming a duct between the microphone and the resonator outlet. The 3D-printed holder also allows the MEMS microphone to be attached onto the exterior of the resonator centre by inserting an alignment hole to a cylindrical extrusion printed on the cell, as shown in figure 4.8, located 0.89 mm above the resonator centre. This distance was selected carefully to ensure the alignment of the MEMS sound hole. Furthermore, the cylindrical design also allows rotation around the alignment extrusion if needed during the alignment process.
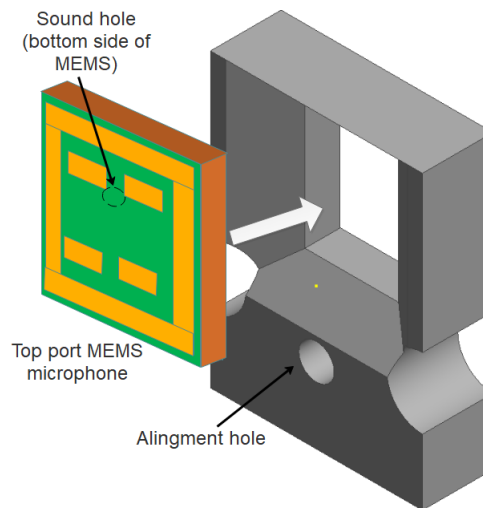

Figure 4.9: A schematic for MEMS microphone holder.

When the microphone is aligned it is initially glued in place using three layers of nail polish, to ensure the microphone can be removed easily if misalignment is detected. Then a thick layer of epoxy resin is applied over the whole microphone structure to ensure there is no gas leakage. During the gluing process there is pressure applied to the microphone to avoid an air gap forming between the resonator and the microphone. This air gap causes an acoustic cavity generating an undesirable Helmholtz resonance, resulting in a reduction of the achievable Q-factor and therefore the PAS signal amplitude. Figure 4.10 shows the frequency response of a PAS cell during different stages of construction: pressure applied and

epoxied, pressure applied but no epoxy, neither epoxied nor pressure applied. As expected, when the microphone is fixed in place and glued to ensure no leaks the resonator produces the maximum acoustic signal. The gluing process increases the signal by a factor of 227 % as compared to when the microphone is fixed but not glued and a factor of 515 % higher than when the microphone is neither fixed nor glued. The Q-factor is also the highest at 6.4, compared to 5.0 in fixed microphone and 5.7 in not fixed case.
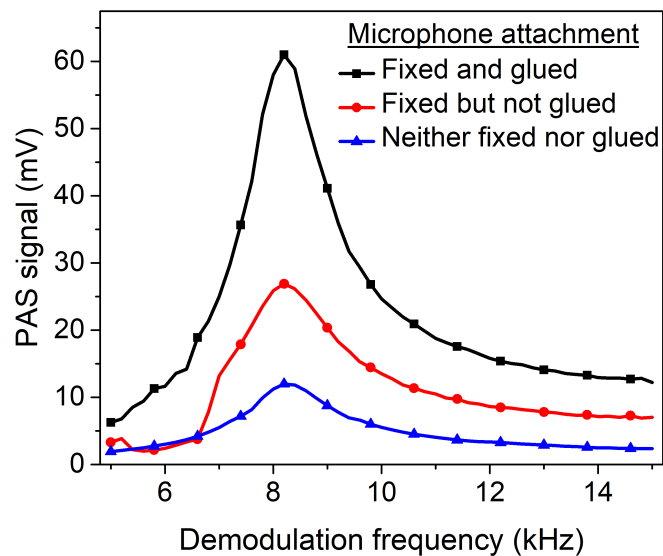

Figure 4.10: Frequency characterisation of the same PAS cell during different phases of assembly. An ECM type microphone was used in this comparison.

The gas inlet and outlet pipes have been designed to allow either 1.6 mm diameter steel pipes for sensitive and fixed installations, or 4.3 mm diameter PTFE pipes for rugged, indoor and outdoor uses. The chosen pipes are attached to the extrusions on the sides of the buffer sections, and fixed in place using epoxy. Finally, 0.5 mm thick CaF_2 windows (Crystran - CAFP10x0.5) are installed to the ends of each buffer region using standard super glue. The windows have 95 % transmission at 8.6 µm wavelength. In this study, cells have been constructed that use either 6 mm and 10 mm diameter windows, depending on the applications presented in chapter 5.

4.5 Summary

In chapter 4, design and manufacture process of PAS cells throughout this thesis has been introduced. In section 4.2, criteria for the design process was described with a particular emphasis on main components of a cell: resonator and buffer regions, both supported by mathematical arguments and COMSOL simulations. Then 3D-printer based manufacture process of the cells are discussed in detail in section 4.3 and the assembly of all components of a cell is reported in section 4.4.

Chapter 5

Experimental Apparatus and Sensor Characterisation

5.1 Introduction

This chapter aims to describe the details of the experimental set-up for PAS, with an emphasis on data acquisition and processing techniques for PAS used for this work. In addition, the quantum cascade laser used in this work is characterised in detail and a comparison of different acoustic transducers used in PAS cells is presented.

5.2 Experimental Setup

In this section two experimental setups used throughout this work are presented. The first set-up uses a commercial lock-in amplifier based measurement system, commercial signal generators for laser control, and data acquisition via an oscilloscope and general purpose interface bus (GPIB) communications. The second system uses a National Instruments (NI) PXIe board that was capable of carrying out all control and data acquisition.

5.2.1 Lock-in Amplifier Based Measurement System

The experimental setup for the LIA based PAS experiments is illustrated in figure 5.1.
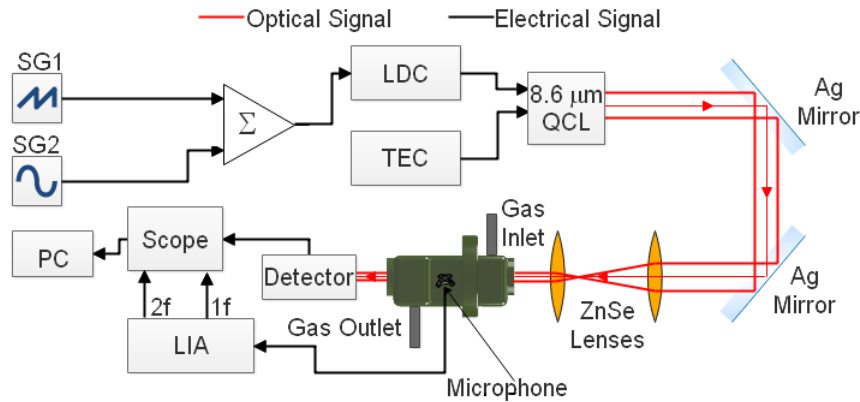

Figure 5.1: The schematic for the experimental setup. Abbreviations: SG1 - signal generator 1 (low frequency), SG2 - signal generator 2 (high frequency), LDC - laser diode controller, TEC - thermoelectric controller, LIA - lock-in amplifier and Σ - summing amplifier.

The laser is controlled using an LDC210C laser diode controller (Thorlabs) and a ITC4005QCL thermo-electric controller (TEC - Thorlabs). A TEC, allows coarse tuning of the wavelength, then fine tuned with the LDC to the central wavelength of the desired spectral feature.

The spectral feature of interest can be measured by applying a 5 Hz saw-tooth current ramp using a signal generator (Aim-TTi TGA1242), whilst simultaneously applying a high frequency laser current modulation equal to the resonant frequency of the PAS cell using a second signal generator (Aim-TTi TGA1242). The two voltage outputs from the signal generators are summed using a custom-built summing amplifier circuit (figure 5.2), before passing to the laser current controller. Further details about the laser operation is also available in section 5.4.

The 5 Hz ramp used for the calibration free PAS work used had a 700 mV$_{pk-pk}$, leading to a current sweep of 70 mA using the LDC 210. The modulation current frequency and amplitude is set according to the measured resonance frequency of a PAS cell and required modulation index value respectively.
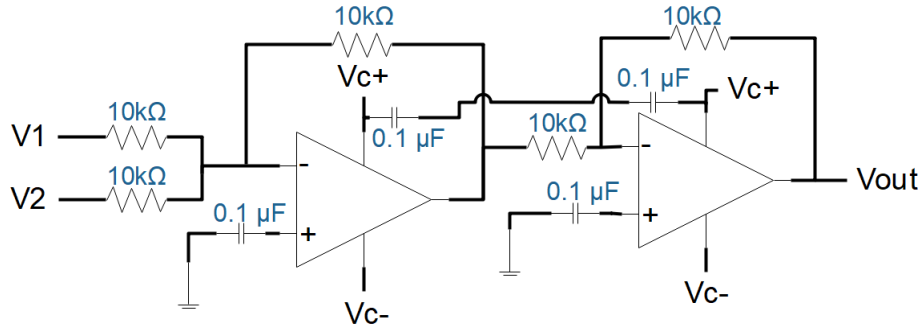
Figure 5.2: Custom built circuit diagram for summing amplifier used to multiplex high frequency sinusoid - f_r and low frequency positive ramp - 5 Hz signals for laser modulation. LM358 op-amp is the main component of this circuit.

The output from the laser is directed towards the PAS cell using two silver coated mirrors and a pair of 25.4 mm diameter, bi-convex ZnSe lenses (7-12 µm AR coated, 99 % transmission at 8.65 µm wavelength - Thorlabs) located within a 45 cm long cage mount. The first lens has a focal length of $f_1 = 75$ mm, and the second lens has a focal length of $f_2 = 25.4$ mm, allowing control over the beam size and divergence, achieved by changing the effective focal length, f_T, of the optical system via changing lens separation, d_L, given by equation:

$$\frac{1}{f_T} = \frac{1}{f_1} + \frac{1}{f_2} - \frac{d_L}{f_1 f_2} \tag{5.1}$$

The PAS cell has been designed with a 25.4 mm surrounding disc, allowing it to also be contained within the cage mounting and maintaining alignment of the optical beam after the lenses.

The optical beam output from the cell is measured using a photodetector (PVI 2TE8), whose output is displayed on an oscilloscope (TDS3014B Tektronix) and recorded via GPIB.

The acoustic signals generated during the laser gas interaction are fed into a LIA (Stanford Research SR830) with a 300 µs time constant and 260 Hz noise bandwidth. The X and Y components of the demodulated signals at the first harmonic frequency or second harmonic frequency are displayed on the oscilloscope and recorded via GPIB. The first harmonic PAS signals are obtained

when the LIA reference signal is set to be equal to the resonant/modulation frequency, f_r, of the PAS cell. The second harmonic signals are obtained when the LIA reference signal is set to double the modulation frequency, whilst the laser is still modulated at the cell's resonant frequency.

The gas flow through the cell is provided by a set of mass flow controllers (Bronkhorst EL-quoted error of ± 1 %). The target gas used throughout this study was CH_4. Two 200 bar gas cylinders were used, one of 10 % and one of 0.1 %, both with an N_2 buffer gas (BOC - 5 % quoted supplier uncertainty). Varying gas concentrations from 10 % to 0.01 % CH_4 were obtained using two mass flow controllers; one supplying either 10 % or 0.1 % CH_4, whilst the second supplied 100 % N_2.

5.2.2 PXIe Board Based Measurement System

The experimental setup for PAS, described in section 5.2, requires simultaneous equipment control using multiple pieces of laboratory equipment. This process is laborious and prone to errors, particularly for experiments requiring large sets of data. In addition, different harmonics of the PAS signal can only be obtained separately by changing the settings on the LIA and the modulation frequency on the signal generator. Hence, R_{2f}/R_{1f} ratios obtained using this setup have a significant time lag between the collection of the R_{1f} and R_{2f} measurements due to the requirement for the user recording data, resetting of the oscilloscope and varying the settings on the on the LIA. For 128 averaging, this lag in measurement time is at least half a minute. To improve control and data acquisition the entire operation was carried out using an automated custom made LabVIEW programme using a NI PXIe-6361 data acquisition board.

As can be seen, the PXIe setup, shown in figure 5.3, is similar to the manual data acquisition setup except for the replacement of signal generators, LIA and scope with a multi-function I/O module.
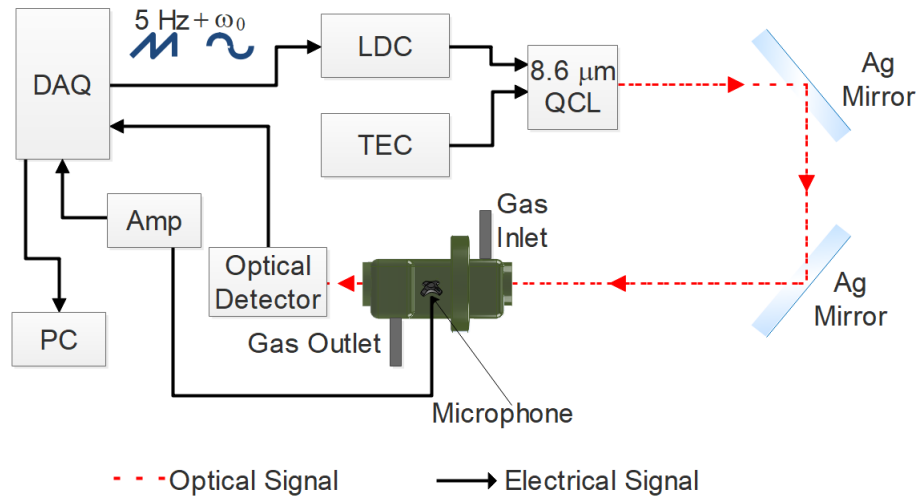
Figure 5.3: A schematic of the experimental setup with data acquisition (DAQ) board and femtoamplifier (Amp). ZnSe lenses were left out of this experimental setup, as the setup can also be used without these lenses for certain applications such as modifying the quantity of CDAS signal.

The PXIe-6361 data acquisition board has a sampling rate of 2 MSs^{-1} with 16 analog inputs (IO), 24 digital inputs/outputs (DIO), 2 analog outputs (AO). The ADC resolution is 16-bits.

For the laser drive signal, two high frequency sinusoid signals at frequencies f_r and $f_r/2$ were generated and added to a positive ramp saw-tooth signal at 5 Hz frequency in alternating periods of the saw-tooth signal. The resulting signal is shown in figure 5.4, with an arbitrary high frequency modulation $f_r = 1,000$ Hz.

Once the PAS signal has been detected using the microphone, the resulting signal is amplified using a current amplifier (Femto Messtechnik DHPCA-100) with a transimpedance gain of 20, in order to amplify the signal above detection limits of the PXIe inputs. The amplifier output is then recorded using an ADC input of the 6361 module at and a digital LabVIEW lock-in amplifier sub-VI is used to demodulate the recorded signals.
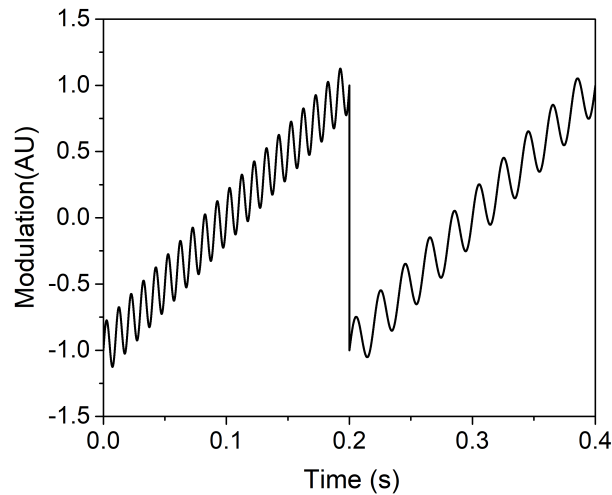
Figure 5.4: A section of the generated output signal to laser from the LabVIEW code. Saw-tooth signal with 5 Hz is added alternately with and $f_r = 1,000$ Hz and $f_r/2 = 500$ Hz in order to generate 1f and 2f signals periodically.

The custom built LIA sub-VI is used to demodulate at only f_r, resulting in the recovery of the first and second harmonics in alternating cycles of the saw-tooth ramp. These are then separated into X and Y components by the sub-VI. Similar to the setup in section 5.2, the sub-VI LIA time constant was set to 300 µs equating to a 260 Hz noise bandwidth. The LabVIEW front panel is programmed to display the averaged (averaging number depending on the specific application) and real time R_{1f}, R_{2f} and R_{2f}/R_{1f}, as well as a fast Fourier transform (fft) of the microphone output, as shown in figure 5.5.
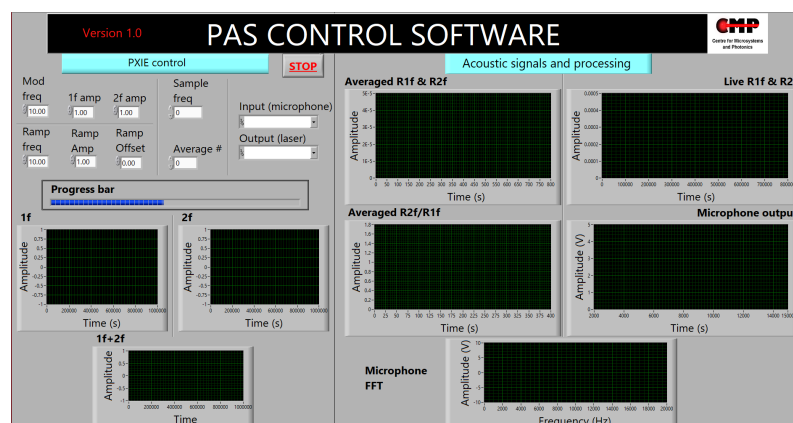

Figure 5.5: LabVIEW front panel for the PAS control VI used to drive electronics, acquire and process PAS signals.

5.3   Targeted Methane Line

To demonstrate the 2f/1f PAS normalisation technique, optimal spectral features of SO_2 and CH_4 within the wavelength range of the MIR laser being used are determined using HITRAN database.

The spectral features of SO_2, H_2O and CH_4 at different wavelength ranges in figure 5.6 below. All of these spectra were simulated using 100 % concentration gas, 1 bar pressure, 20 °C temperature and a 1 cm path length. The simulations were performed using a Matlab code, given in appendix C, using line strength data from the HITRAN 2016 database [94].
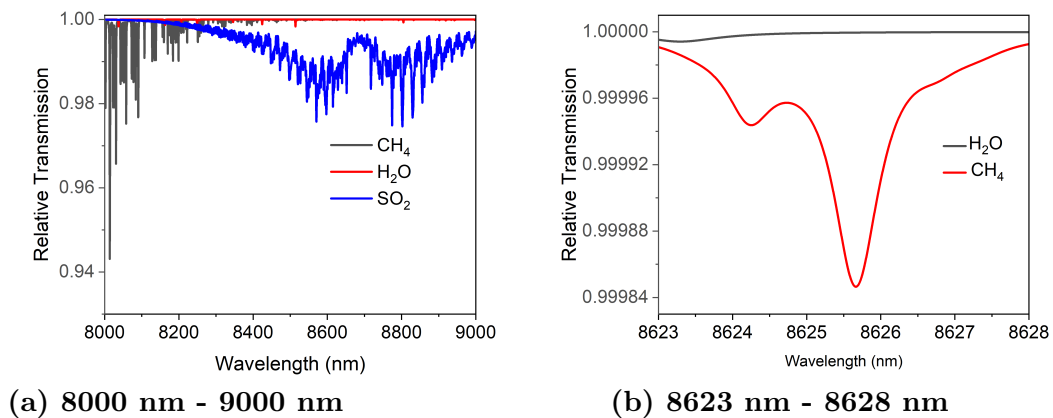

(a) 8000 nm - 9000 nm   **(b) 8623 nm - 8628 nm**

Figure 5.6: Simulated relative transmission of CH_4, H_2O and SO_2 at different wavelength ranges for 1 bar pressure, 20 °C temperature and over 1 cm path length. CH_4 and SO_2 gases were simulated at 100 % concentration, whereas H_2O was simulated at 4 % concentration.

Figure 5.6a shows the spectra of SO_2, H_2O and CH_4 gases at a wavelength range 8 µm to 9 µm, a region where highly strong absorption lines of gases are observed. As mentioned in 4.2.1, CH_4 is used instead of SO_2 throughout this work even though within the laser's wavelength range (8604 nm to 8634 nm), SO_2 lines are on average 420.7 times stronger than CH_4 features. The selected feature of CH_4 for the 2f/1f calibration work, at 8625.55 nm line centre is shown in comparison to water vapour in figure 5.6b. As can be seen from this figure, the selected line is well isolated from the adjacent features, free of any potential interference from the water vapour and one of the strongest lines in the region within laser's wavelength range.
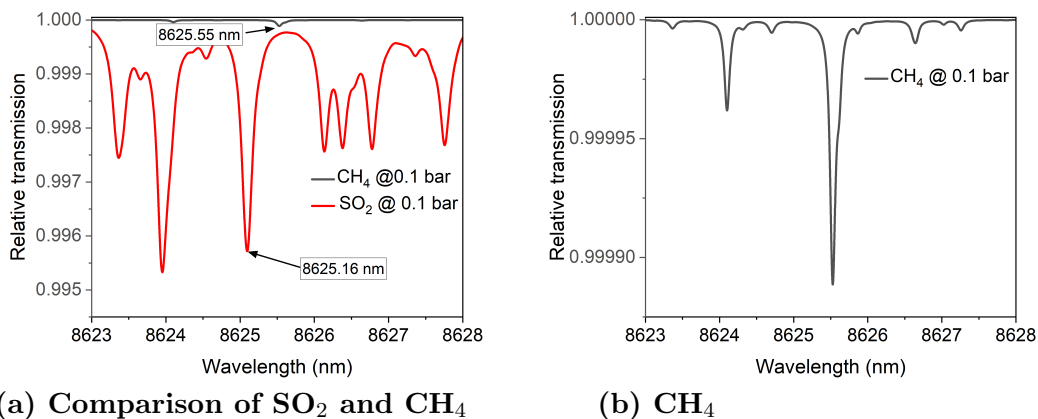
(a) **Comparison of SO₂ and CH₄**   (b) **CH₄**

Figure 5.7: Simulated relative transmissions of gases at a wavelength range of 8623 nm to 8628 nm for 100 % concentration, 0.1 bar pressure, 20 °C temperature over 1 cm path length.

SO_2 gas has been excluded from the figure 5.6b as at 1 bar pressure its features can not be distinguished properly due to broadening. This is another reason for not using SO_2 throughout this work as gas needs to be reduced to at least 0.1 bar to resolve its features, as shown in figure 5.7. The selected line of CH_4 is marked on the plot with a box named '8625.55 nm' and a potential line to be used in further studies with SO_2 is marked with '8625.16 nm'. This line of SO_2 is 38.9 times stronger than the selected CH_4 line, which indicates ~ 38.9 times expected sensitivity increase in further studies using SO_2 gas. The selected methane line is also shown on its own in figure 5.7b, showing that the feature observed at 1 bar in figure 5.6b, is actually a combination of strong and a weaker neighbouring spectral features centred 8625.55 nm and 8624.09 nm respectively. The fact the this feature is a combined spectral line at atmospheric pressure has no effect on the 2f/1f PAS normalisation technique.

5.4 Laser Characterisation and Parameters

The choice of laser is based on the expected spectral absorption features of CH_4 and SO_2 determined using HITRAN 2016 database in MIR range, shown in section 5.3.

The laser source used in these experiments is a continuous wave Thorlabs

distributed feedback QCL (model number-QD8650CM1) with 8.65 µm central emission wavelength, 54 mW average output power and with sub-1 MHz linewidth as stated by the supplier data-sheet. The QCL is packaged in a vertical high heat load (HHL) casing with collimated, single spatial mode, single longitudinal mode output.

For stable operation at a particular central wavelength and power output, temperature control of the laser diode via Peltier element within the laser packaging is also essential along with current control. The laser diode temperature was controlled using a Thorlabs TEC unit (ITC4005QCL) and an external water cooler. The water cooler system (from Alphacool) made up of a water tank filled with distilled water, water pump and a radiator with fans was placed away from the optical bench in an isolated box to minimise vibrations affecting the PAS measurements. The laser's heat sink base was attached to a custom designed aluminium optical mount, and the copper plate of the water cooling unit was attached to the opposite side of the mount to maximise heat transfer.

5.4.1 Beam Diameter and Divergence

The characterisation of the beam diameter and divergence is crucial for the positioning of a PAS cell and for controlling the percentage of input laser interacting with gas and the cell. A simple but effective way of coarsely determining the beam profile is the knife-edge technique: placing a black-painted razor blade attached to a XYZ precision linear translation stage and measuring the power of the clipped beam as the blade edge is scanned across the beam. For a Gaussian beam, a Gaussian error function (erfc) fit is expected from a plot of power versus knife-edge position, as shown in figure 5.8, for the horizontal axis. The detected power, $P(r)$ at position r is given by the equation:

$$P(r) = \frac{P_0}{2}\text{erfc}\left[\frac{\sqrt{2}(r - r_0)}{\omega_r(z)}\right] \tag{5.2}$$

where P_0 is the power detected for an unobstructed beam, z is the axial position,

r_0 is the radial position when the output power is halved $P(r_0) = P_0/2$, and $\omega_r(z)$ is the beam radius given by:

$$\omega_r(z) = \omega_0 \sqrt{1 + \left(\lambda \frac{z}{\pi \omega_0^2}\right)^2} \tag{5.3}$$

where ω_0 is the beam waist and λ is the laser's central wavelength. The beam waist is also dependent on other beam parameters as:

$$\omega_0 \theta_i = \frac{\omega_0^2}{z_0} = \theta_i^2 z_0 = M^2 \frac{\lambda}{\pi} \tag{5.4}$$

where θ_i is the half beam divergence, z_0 is the Rayleigh length and M^2 is the laser radiation quality. In the ideal case, $M^2 = 1$ and the beam has a Gaussian profile. However, this is rarely the case due to non-homogeneity and diffraction losses.
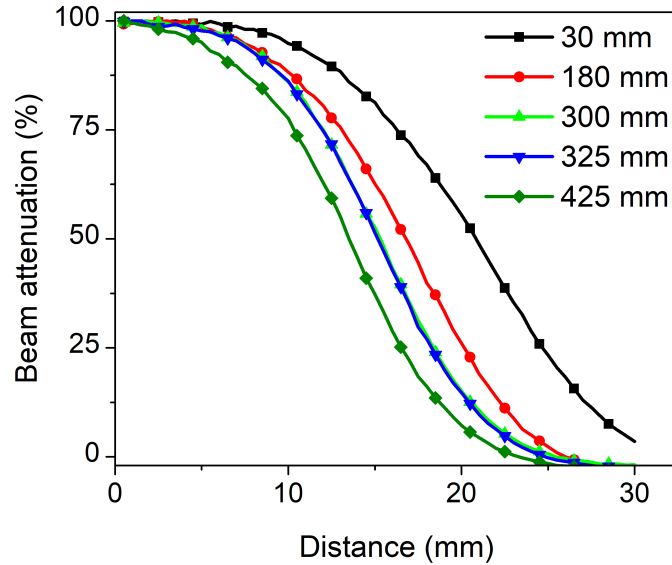

Figure 5.8: Beam attenuation against the knife edge position for horizontal axis at different distances of knife from the laser front end.

The plots in figure 5.8, represent the mathematical integral of the beam distribution, starting with 100 % total beam power and diminishes to 0 % power as knife blade fully blocks the beam. The beam radius, is defined as the

distance between 10 % and 90 % attenuation percentages. Previous studies have shown that the 10/90 knife-edge width measurement is a successful technique for estimating $1/e^2$ width of the intensity of the Gaussian distribution [126].

By repeating this process for multiple axial distances from the laser, the beam radius with respect to distance can be fitted with equation 5.3 and ω_0 is calculated. The plot beam radius as a function of axial distance from the laser for horizontal and vertical axes is shown in figure 5.9.

Using the relationship given in the equation 5.3, $\omega_r(z)$ with respect to distance is found and shown in figure 5.9. The horizontal beam waist, ω_{0x}, is 0.292 mm at 35.7 cm distance from the laser, whereas, the vertical beam waist, ω_{0y}, is 0.602 mm at 32.3 cm from the laser. This means that the optimal position of a PAS cell for minimal optical attenuation by the cell walls is at a distance between 32.3 cm and 35.7 cm from the front end of the laser. Using graphical analysis the overall beam waist is at $\sim$ 350 mm from the laser front end.
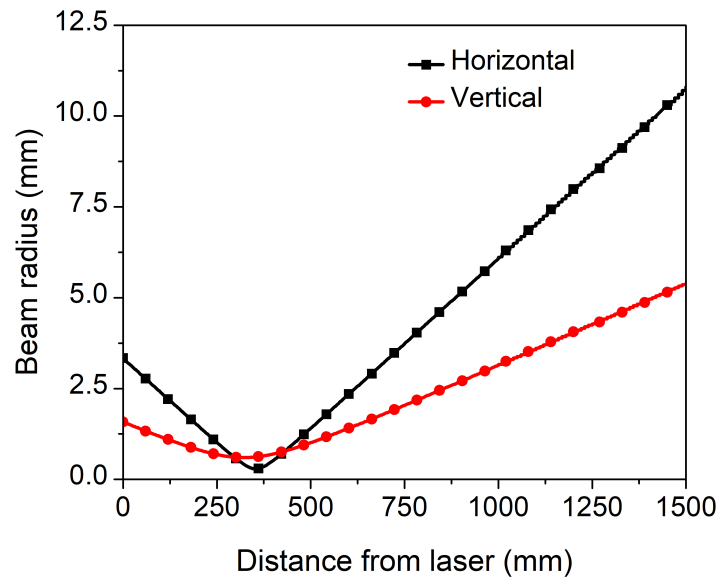
Figure 5.9: The divergence of laser beam for horizontal and vertical axes from laser's front end to a distance of 1.5 m with 2 mm increments.

5.4.2 3D Beam Characterisation

To determine the optical power entering an aperture such as the front end of a resonator, a knife-edge analysis or simple measurement with photodetectors are often inadequate. The main reason for this inadequacy for this study is the size of the available photo detector's (PVI 2TE8) pinhole input (0.25 mm × 0.25 mm) limiting the detection of the non-Gaussian beam shape features. For this reason the actual laser beam shape was captured using a 3D-scanning setup. For the purpose of measuring beam shape, the detector was attached to a 2-axis (Y and X) mounted motorised stage with 100 mm arm length in each axis. The 3D intensity heat map was obtained as shown in figure 5.10. The X and Y axes slice of the peak point is shown in figure 5.11.

Figure 5.10: X-axis and Y-axis slice of the peak intensity of the laser beam.
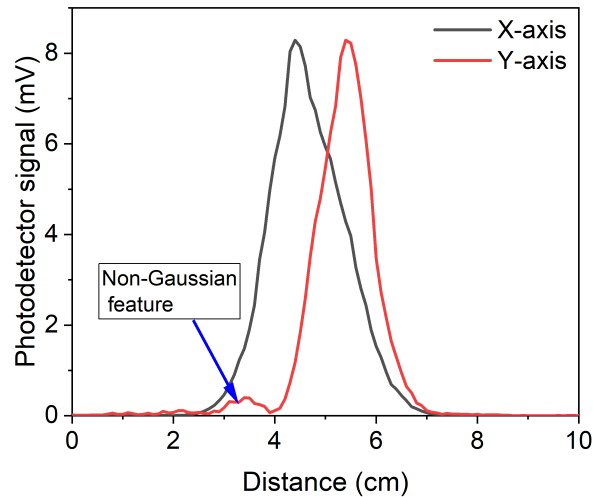
Figure 5.11: X-axis and Y-axis slice of the peak intensity of the laser beam.

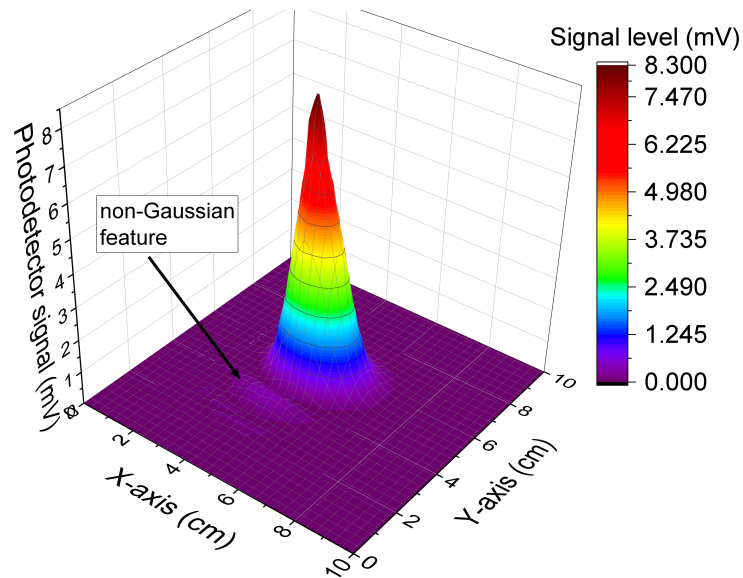One interesting feature of the heat map in figure 5.10 is the increase in power detected between 0.5 cm and 4.0 cm range of the Y-axis, most likely diffraction at the output of the laser package. The two dimensional integration of this plot represents the total power at the output of the sensor device. The percentage of the laser power deposited outside the central Gaussian shape due to diffraction can be calculated as a ratio of the two-dimensional integration in the diffracted region to the whole beam shape as 5.7 %. This Gaussian beam-shape and two-dimensional integration method will be used in the next chapter for determining the amount of laser power entering through apertures such as resonators and pinholes.

5.4.3 Power Output Characterisation

The laser's power output for injection currents between 300 mA and 900 mA, and TEC temperature settings ranging from 0 °C to 40 °C are shown in figure 5.12. The laser output at the beam waist was measured using a 3A-SH bolometer (OPHIR Optronics). As can be seen from figure 5.12, the laser efficiency improves as the temperature decreases, as laser threshold reduces at lower temperatures.
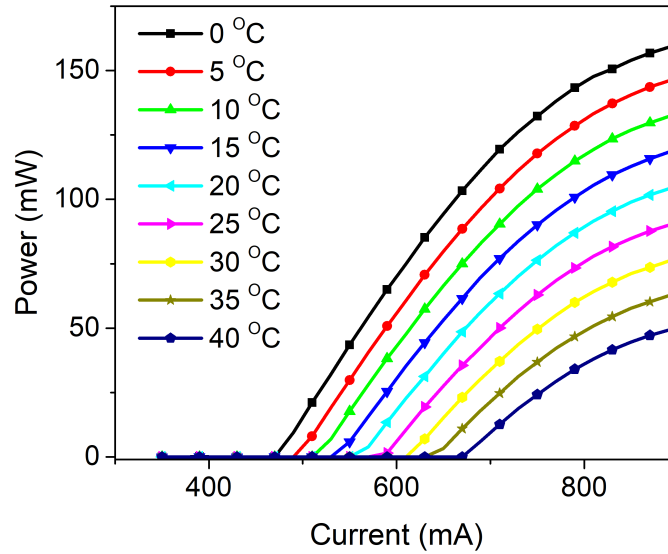
Figure 5.12: QCL power output against current at TEC temperatures ranging from 0 °C to 40 °C.

5.4.4   Wavelength Output Characterisation

The laser's central wavelength output was measured as a function of TEC temperature settings ranging from -0.8 °C to 39.7 °C, at a fixed injection current 795.5 mA as shown in figure 5.13. The central wavelength was found by tuning the TEC temperature until known spectral features of CH_4 is at the centre of the scanned region, indicating central laser wavelength matching with the spectral feature peak. As the TEC is scanned between -0.8 °C to 39.7 °C, a wavelength scan of 8605.94 nm to 8634.832 nm is obtained. From the plot, tunability is obtained as 0.715 nm/°C. Due to the repeatable wavelength tuneablility of the lasers, the wavelength modulation of the laser output is commonly performed using current tuning.
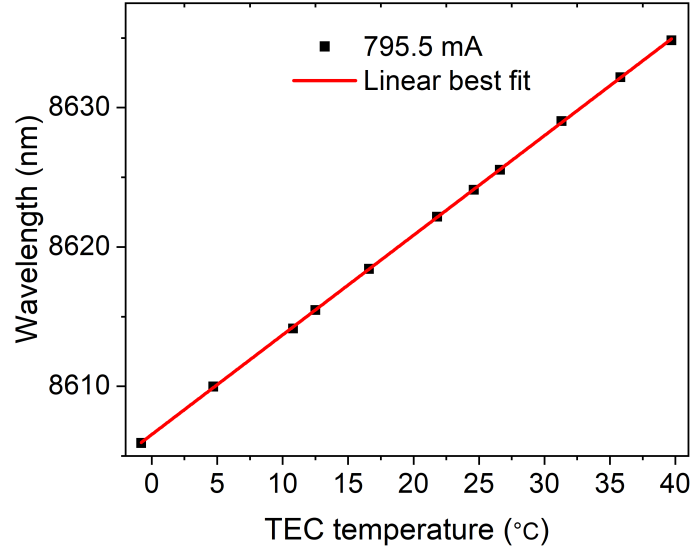
Figure 5.13: QCL central wavelength vs TEC temperatures ranging from -0.8 °C to 39.7 °C at a fixed injection current 795.5 mA.

5.4.5 Wavelength Referencing

The PAS signals obtained using the oscilloscope or the PXIe are always recorded as a function of time. However, for spectral fitting the absolute wavelength tuning is required, which is not always linearly proportional with the injection current and hence with time-index. For this reason, it is essential to convert time-indexed data to wavelength-indexed signals for the recovery of accurate absorption spectra. This process is typically achieved by measuring the output of the transmission through an etalon, either before, during or after the data signal acquisition.

In this work, a germanium etalon is used for deriving a relative frequency index from the time index. The input to and output from a germanium resonator recorded using a photo-diode is shown in figure 5.14.

The free spectral range (FSR) of the etalon is calculated using the equation:

$$FSR = \frac{c}{n2L} \tag{5.5}$$
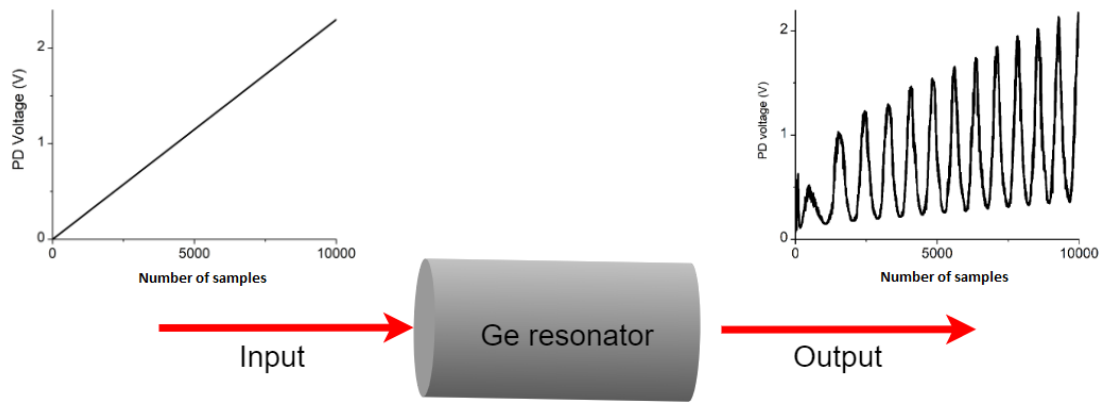
Figure 5.14: Input into and output from a Germanium etalon resonator.

where L is the germanium length (2.5 cm) and n is the refractive index (4.0026) of the germanium at the wavelength of interest. Hence, the FSR of the germanium resonator has been calculated as 1.448 GHz.

The peaks shown in the output section of the figure 5.14 are equally spaced out in the frequency domain with a separation of 1.448 GHz. However, the peaks are not equally spaced in the time domain as laser's optical frequency is not linearly proportional with the injection current.

The wavelength referencing process is carried out as follows: a gas absorption signal is obtained simultaneously with the peaks plot from the etalon as shown in figure 5.14. The resonator output is filtered to remove spurious peaks due to noise, which causes distortion of the wavelength referencing procedure. Next, the nearest etalon peak to the line centre is identified and assigned the line center frequency to this resonator index. The line centre acts as a zero point for the wavelength scaling process as the right and left side of this centre point is extrapolated with a polynomial fit depending on the index values of other peak points. Using the known line centre wavelength obtained from HITRAN database, a wavelength reference for the whole scan range is obtained. The Matlab code, originally developed by Duffin [121], for wavelength referencing during this work is given in appendix B. The technique described above has an inherent $\pm$FSR/2 error in the referencing procedure, corresponding to $\pm$0.15 nm for a laser centred at 8625.5 nm wavelength.
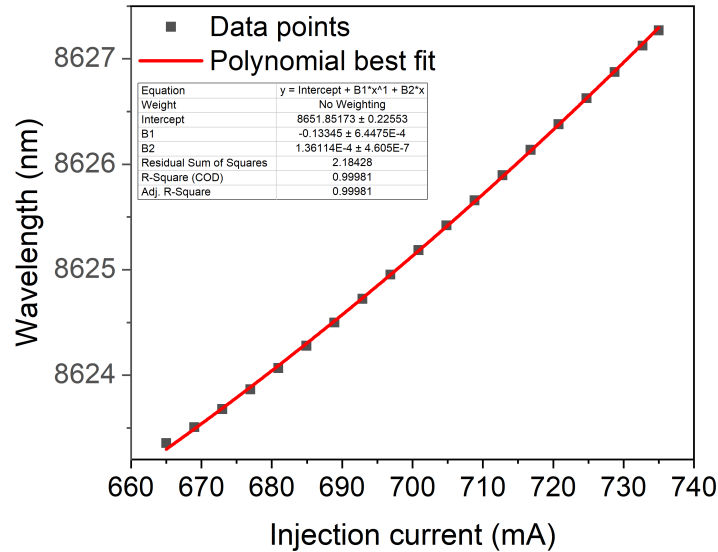
Figure 5.15: Plot showing the nonlinear relationship of the laser's injection current with the wavelength of the optical beam.

The plot in figure 5.15, shows the final relationship of the injection current with the wavelength, along with a fitted second order polynomial, with the etalon peaks identified as the square points in the plot. The adjusted R-square of the best fit is 0.99981. Hence, the aforementioned code has been used throughout this thesis when converting time domain x-axis to frequency domain, whenever required.

5.4.6 Wavelength Modulation Amplitude Determination

As previously discussed, the maximum achievable R_{1f} and R_{2f} signals are obtained at m-values 2.0 and 2.2 respectively, according to previous studies [48]. This was confirmed experimentally using a modified version of the LabVIEW PXIe scanning code. The laser was current modulated for m-values from m = 0.5 up to m = 3.0 and the corresponding R_{1f} peak-to-peak, R_{2f} maximum and R_{2f}/R_{1f} maximum values were obtained and plotted, as shown in figure 5.16. As expected peak-to-peak R_{1f} and peak R_{2f} signals increases up to approximately m = 2.0 and m = 2.2 respectively, but stabilises after these modulation indexes. Although maximal R_{2f}/R_{1f} signal was originally expected when R_{2f} is the

highest, interestingly the optimal m-value for 2f/1f ratio is below m = 2.0, at
m = 0.9, as indicated with a blue line on figure 5.16.
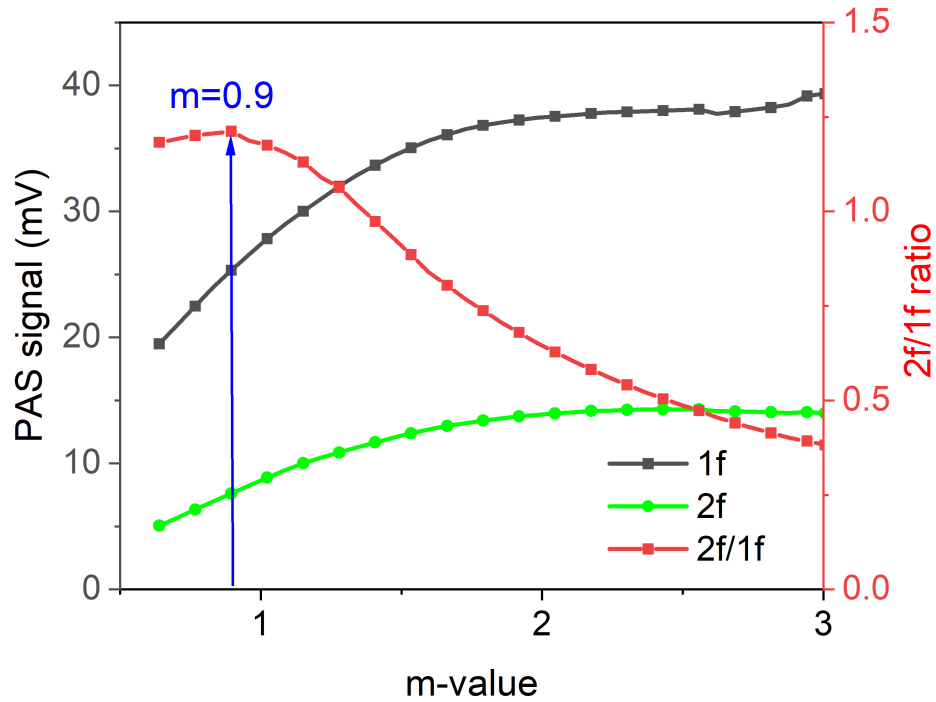
Figure 5.16: 1f, 2f and 2f/1f signal amplitudes at different m-values.

5.5 Comparison of Various Acoustic Transducers

The selection of the acoustic transducer is important for the overall sensitivity,
applicability to a certain use, cost and size of the PAS sensor. As mentioned in
section 4.4 of chapter 4, two different acoustic transducers are used in this study:
MEMS and ECM.

MEMS microphones, as seen in figure 5.17, contain a MEMS sensor with a
mechanical diaphragm as a sensing element and an application specific integrated
circuit (ASIC) which commonly includes a pre-amplifier and an ADC, all mounted
on a PCB encased in a cover. The acoustic waves are guided into the enclosure
through a sound port located on the cover for top-port MEMS microphone and

on the PCB for bottom-port MEMS microphone.

In ECMs, (figure 5.18), the diaphragm is made out of electret material that is separated from a pickup plate by an air gap, forming a capacitor. Any voltage variations across this capacitor due to sound pressure are amplified by a transistor, before electrical output via wire leads.
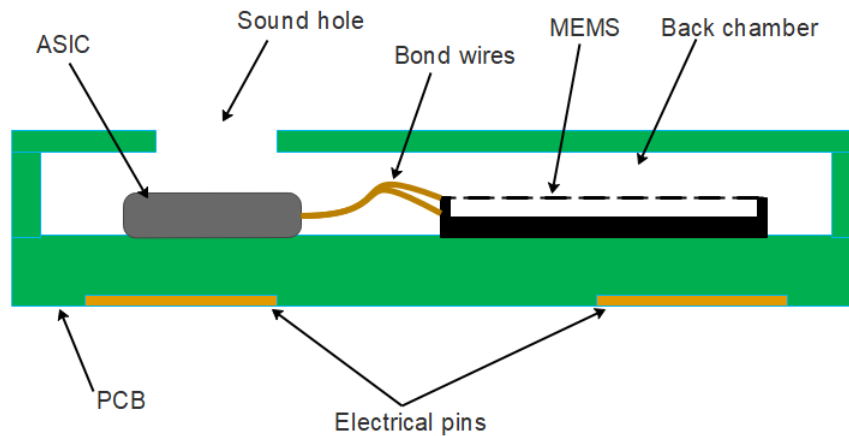
Figure 5.17: Internal construction of a MEMS microphone. The dimensions of the MEMS microphone used in this comparison are 3.35 mm x 2.50 mm x 0.98 mm with 0.6 mm sound hole diameter.

Figure 5.18: Internal construction of an electret condenser microphone. The dimensions of the ECM used in this comparison are 2.54±0.05 mm height and 2.565±0.025 mm diameter and 0.76±0.02 mm sound hole diameter.

In recent years, the use of MEMS microphones for PAS increased rapidly compared to EC microphones due to some of the advantages provided by this new technology. For applications prioritising compactness, MEMS microphones are more attractive over ECM especially for requirements of digital output as an ADC can be readily 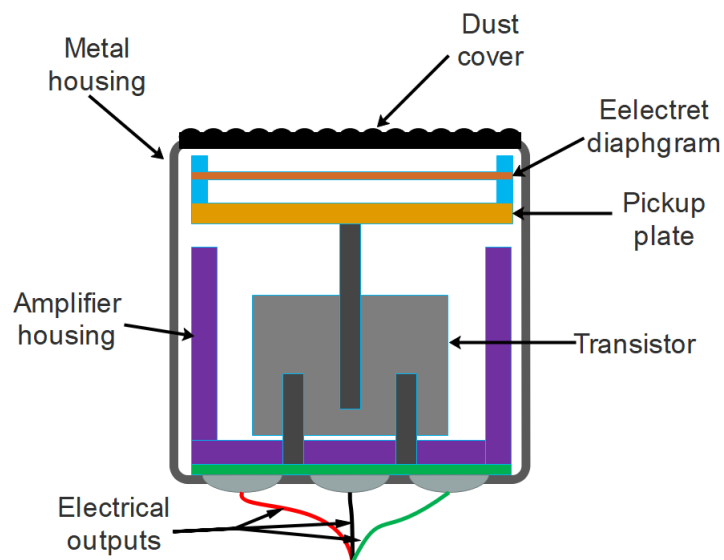integrated into MEMS construction, whereas ECM requires external circuitry for digital output. As MEMS microphones have lower output impedance, electrical noise can be minimised. Also, the use of increasingly advanced semiconductor fabrication methods and the inclusion of pre-amplifiers allows temperature stable operation. As previously discussed in section 3.8.1, MEMS microphones can tolerate higher temperatures as they are commonly soldered using reflow soldering processes using precise pick-and-place machines during assembly of components.

Despite the advantages presented for MEMS microphones, ECMs are still preferred for some applications of PAS. As they have been on the commercial market longer than MEMS microphones, they are available with far greater variants and packaging than MEMS microphones - ultrasonic, noise-cancelling, omnidirectional and unidirectional. In addition, for pin connections ECMs are available with pins, pre-soldered wires, solder pads and springed contacts unlike limited connection options of MEMS. ECM can be operated on a larger voltage range than MEMS microphones, giving flexibility of use particularly with unregulated power supplies. However, EC microphones are often larger in size than MEMS microphones, this larger size allows better performance when the environment has high moisture or dust. For this reason, ECMs often have higher ingress protection ratings than MEMS microphones.

In this section, two PAS cells with identical internal designs but using either an ECM or a MEMS microphone are compared.

5.5.1 COMSOL Comparisons

The characteristics of both cells have been modelled using 3D FEM software COMSOL Multiphysics, using the pressure and acoustics physics modules, to

obtain estimates for eigenfrequencies, frequency dependency and losses within the cell. The internal geometry used in these simulations can be seen in figure 5.19 for MEMS microphone and in figure 5.20 for ECM variant.
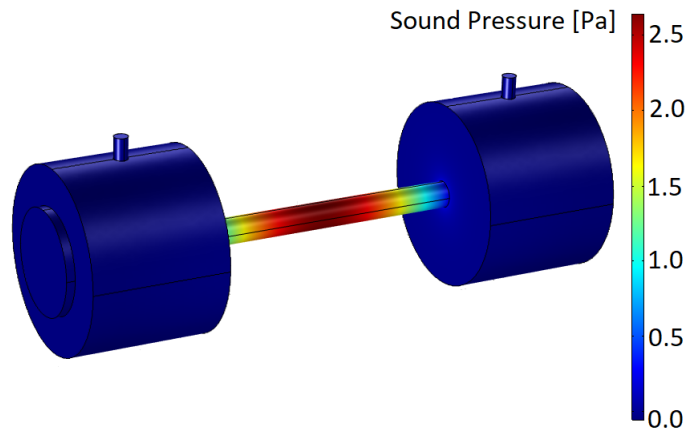
Figure 5.19: FEM simulation of the acoustic pressure distribution at resonance for PAS cell with MEMS microphone.
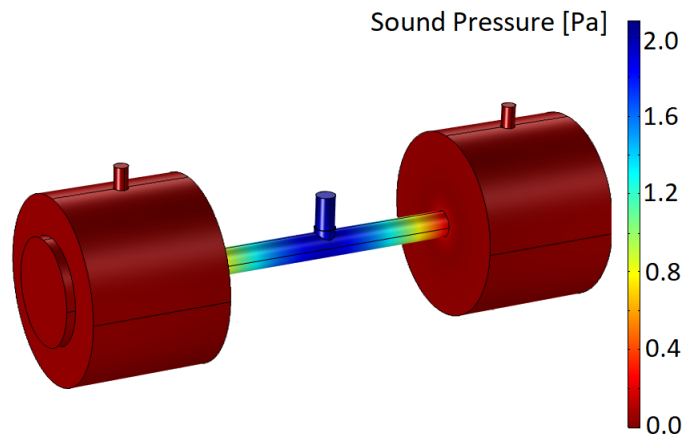
Figure 5.20: FEM simulation of the acoustic pressure distribution at resonance for PAS cell with electret microphone.

As can be seen in figure 5.18, EC microphones contain a much larger air chamber within the microphone than MEMS microphones. This additional chamber of air is comparable to the volume of the resonator and cannot be neglected from simulations. For this reason, an additional small cylinder representing the internal chamber of the ECM is added to the detection point, as seen in figure 5.20. All walls except gas inlet/outlet were defined as hard acoustic boundaries, where acoustic impedance is infinite and the acoustic wave is not dampened. Gas inlet/outlets were defined as soft acoustic boundaries, as gas molecules can move

freely and cannot be assumed fixed in space. The resonator was defined as a monopole acoustic source and a line heat source was added through the centre to simulate the heat transfer via the incident laser beam. The acoustic losses were accounted for by implementation of an electrical equivalent model and inclusion of acoustic impedance into the resonator section, as the resonator's small radius and long length results in high viscothermal damping in the system. During all simulations, the internal volume was filled with 100 % N_2 gas to replicate trace gas measurement with N_2 buffer gas. Hence, the first fundamental longitudinal resonances for both designs, estimated to be at $f_r = 10.139$ kHz for MEMS and $f_r = 9.466$ kHz for the ECM variant, identified using the eigen-frequency study tool, (figures 5.19 and 5.20).

The frequency domain analysis with 10 Hz step size and extra-fine mesh settings for both cells can be seen in figure in figure 5.21. The estimated Q-factors were found to be 20.4 and 24.1 for ECM and MEMS microphone designs respectively. These simulated findings for Q-factor and f_r are compared to the experimental findings in next subsection.
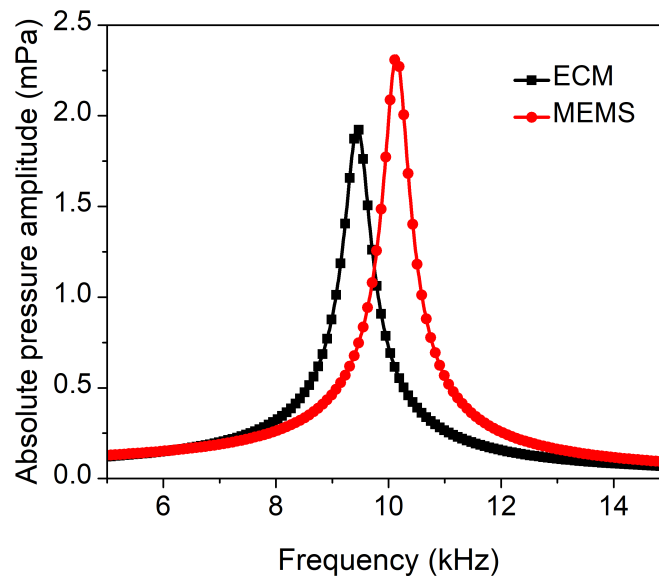
Figure 5.21: FEM simulation sound pressure profile in frequency domain for both cells.

5.5.2 Experimental Conditions for the Comparison of ECM and MEMS Microphones

The WM-PAS setup for cell characterisation was setup as described in section 5.2. The absorption line of CH_4 at 8632.04 nm wavelength was used (absorption coefficient $= 1.75 \times 10^{-6}$ cm^{-1}). The laser bias current was set to 800 mA and the TEC was set to 35.8 °C to target this centre wavelength. A low frequency ramp of 5 Hz, 110 mA$_{pp}$ is applied to the laser, resulting in a wavelength tuning range of $\sim$ 6 nm. Secondary frequency modulation, which is a high-frequency sinusoid, is applied with a current amplitude of 63 mA$_{pp}$, which corresponds to a modulation index of m $=$ 2.0 to maximise the 1f signal.

The R_{1f} signals at the fundamental longitudinal resonance for ECM and MEMS variants of the PAS cell are shown in figure 5.22. The R_{1f} signal magnitude for the ECM variant at its resonant frequency is $\sim$ 3 times larger than the signal from MEMS variant at its resonant frequency. This is an unexpected result as the acoustic sensitivity of the MEMS microphone is $\sim$ 77.5 % higher than the ECM, as previously mentioned in section 4.4. The difference in signal is more prominent if the signal from the ECM is normalised to MEMS sensitivity, as shown with 'ECM normalised' labelled line in figure 5.22. Comparing this normalised ECM signal with the MEMS signal, it was found that ECM has 532.1 % larger signal. The SNR for the non-normalised measurements are 104 for the ECM and 52 for the MEMS microphone variants.
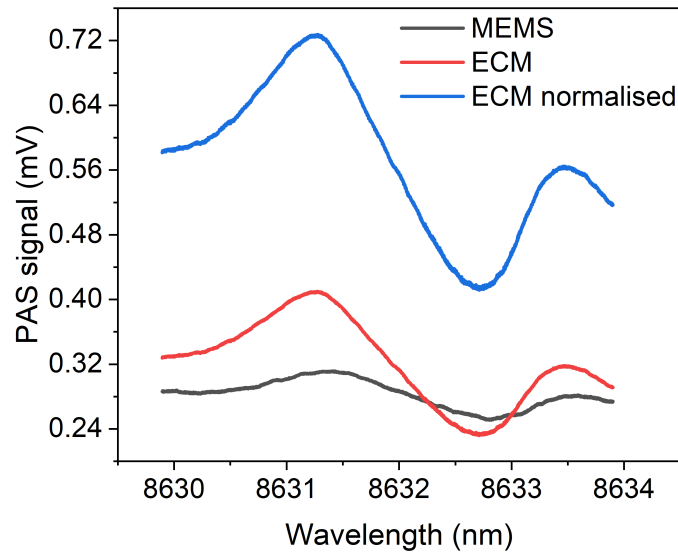
Figure 5.22: R_{1f} plots comparing the use of ECM and MEMS microphones for PAS. Line labelled 'ECM normalised' represents the signal from the ECM, if ECM had equal sensitivity as the MEMS microphone used.

One explanation for this difference is more efficient coupling of the PAS signal generated in the resonator with the ECM diaphragm, at the resonance frequency. This results from ECM acoustic input port (0.79 mm diameter) being significantly larger than the acoustic input port of the MEMS microphone (0.6 mm diameter). Different sizes of microphone ports have been used in order to match the acoustic input port dimensions of the microphones. On the other hand, the difference in signal size could also be formation of a Helmholtz resonance as air in the diaphragm of the ECM is coupled with the resonator, amplifying the signal higher than expected. In addition, epoxy glue used to seal the MEMS cell could lift the MEMS microphone up as it cured, making coupling between the resonator centre and the microphone ineffective, leading to signal reductions previously discussed in figure 4.10 in chapter 4.

The resonance plots for the fundamental longitudinal acoustic resonance of both acoustic transducer types used in the PAS cells are shown in figure 5.23 for 10 % CH_4 flown at a rate of 100 ml/min.
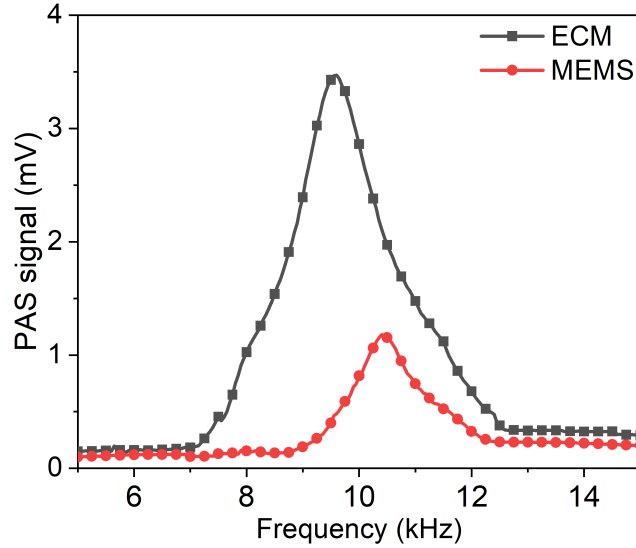
Figure 5.23: Frequency response of the PAS cells with MEMS and ECM.

In figure 5.23, the signal given on y-axis is the peak-to-peak of the R_{1f} signal as a function of laser drive frequency on the x-axis, ranging from 5 kHz to 15 kHz in 50 Hz increments. The resonant frequencies for ECM and MEMS microphone configurations were determined as 9.55 kHz and 10.35 kHz and the Q-factors were measured to be 12.5 and 8.1 respectively. The lower Q-value with the MEMS microphone is another indicator of an inefficient acoustic coupling compared to ECM. The frequency values match well with the modelled values given in figure 5.21, with only a +0.88 % and +2.0 % difference respectively. However, analytical calculations using equation 3.6, suggest that the difference should be about ~ 425 Hz, or 4.5 % and 4.2 % for ECM and MEMS variants respectively. This difference of analytical calculations to COMSOL simulated values can be attributed to the omission of the effect of buffer volumes in the analytical calculations giving a rough estimation and shows the importance of multiphysics simulation tools over analytical calculations for pre-fabrication simulations.

On the other hand, the simulated values for the Q-factors are considerably higher than the experimental values; 60.7 % higher for the ECM and 48.1 % for the MEMS sensor variant. This discrepancy could be attributed to the simplicity of the COMSOL model, where internal surface finish quality, gas flow and potential

air cavities at microphone to cell or window to cell boundaries are ignored. In addition, only the acoustic-pressure module was used in the COMSOL simulation, ignoring the effects of thermal and viscous losses on the Q-factor.

The ultimate detection sensitivity for both variants has been determined by performing an Allan-Werle variance analysis, shown in figure 5.24. For each microphone type, this analysis was performed by recording peak-to-peak R_{1f} amplitude continuously for two hours with 0.2 s measurement interval at 100 ml/min 10 % CH_4 flow rate through the cell. The data was analysed using a Matlab code originally developed by Bauer [61], given in appendix D. Without any averaging (t $\sim$ 0.2 s) the ECM cell can measure up to 635 ppm, whereas the MEMS cell is limited at 2235 ppm.

At optimum integration time, $\sigma = 45$ ppm can be achieved for the ECM with an integration time of 266.4 s and $\sigma = 77$ ppm can be achieved with the MEMS microphone with an integration time of 315.2 s as shown in figure 5.24.

The NNEA coefficients which incorporates all system variables into one coefficient, is used to represent ultimate detection sensitivity [61][66] and it is expressed by the equation 5.6:

$$NNEA = \frac{P_L \alpha_{3\sigma}}{\sqrt{\Delta f_{LIA}}} \tag{5.6}$$

where $\alpha_{3\sigma}$ is the optical absorption at 3σ sensitivity to employ a more representative limit and Δf_{LIA} is the frequency bandwidth of the LIA. Using 3σ values of 135 ppm and 231 ppm for ECM and MEMS microphone variants respectively, and P_L of 46.7 mW from figure 5.12, NNEA values are calculated as follows: 6.31×10^{-9} $Wcm^{-1}Hz^{-1/2}$ for ECM and 1.07×10^{-8} $Wcm^{-1}Hz^{-1/2}$ for MEMS. It must be noted again that sensitivity values presented here are different compared to the values shown in next section of this thesis as a different weaker methane doublet line is used during this microphone comparison experiments.
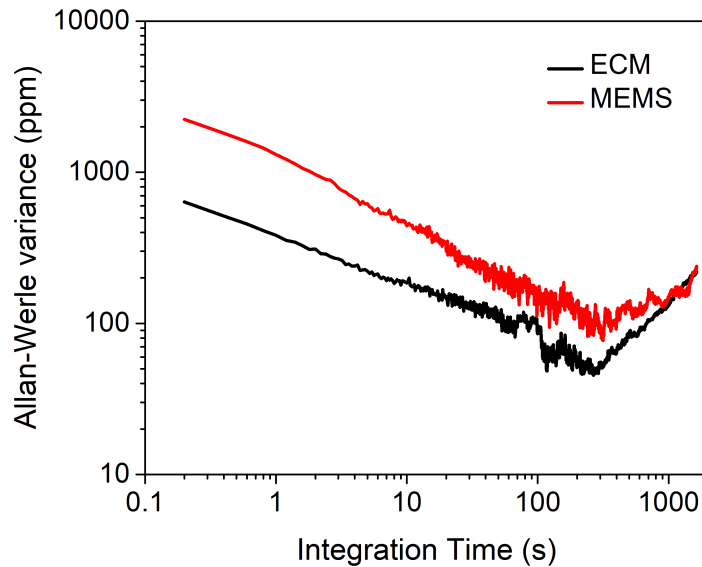
Figure 5.24: Allan-Werle variance for ECM and MEMS microphone variants of PAS cell.

Using the NNEA values given above as a comparison metric, it can be argued that ECM has 70 % superior performance to MEMS microphone in terms of sensitivity within this work. The ECM has higher SNR and better sensitivity for both live measurements and averaged measurements compared to the PAS cells using MEMS. The inferior performance of the MEMS compared to ECM for the case presented here most likely originates from the difficulties in effective coupling of acoustic cell resonator with the diaphragm of the MEMS microphone during the assembly processes of cells. Although larger sizes of ECMs often limit the overall sensor compactness, a more effective acoustic coupling is presented by the larger size of diaphragm air volume.

Overall, the choice of microphone for any PAS cell should depend on the application: operation temperature, ruggedness, size of the cell and target gas and the PAS sensor needs to be designed carefully for optimal effectiveness of the whole assembly.

5.6   Summary

In section 5.2, the complete experimental setup was shown, as well as the details of an automated PXIe based measurement system. Section 5.3, the targeted CH_4 line used throughout this work is presented. Laser characterisation and related parameters was shown in detail in section 5.4 including beam-shape analysis, power and wavelength output characterisation, wavelength referencing process and determination of modulation amplitude. Finally, a detailed comparison on the use of ECM and MEMS microphones for PAS applications was given in section 5.5 including relevant COMSOL simulations.

Chapter 6

Calibration- free MIR PAS

6.1 Introduction

This chapter presents 2f/1f calibration free PAS technique in depth. The source of the CDAS signal and its properties are investigated comprehensively, then the sensor used throughout this calibration-free research work is characterised thoroughly and the results of the calibration-free measurements are presented. Finally, the 2f/1f calibration technique is validated to show accurate signal recovery at varying modulation frequencies, gas concentrations and optical intensities.

6.2 Evidence for CDAS

The evidence for CDAS is shown in figures 6.1 and 6.2 showing the R_{1f} and R_{2f} signals generated at the resonant frequency of a cell, $f_r = 9.6$ kHz and $f_r/2 = 4.8$ kHz respectively, for both 10 % CH_4 target gas and 100 % N_2.

The presence of an offset level is clear in figure 6.1 in the absence of the target gas CH_4. Whereas, non-linear CDAS contribution in second harmonic signal in figure 6.2 is insignificant. Hence, the major R_{2f} contribution is the H_2 component generated by the WM-gas interaction.

Figure 6.1: Magnitudes of the first harmonic components output from the LIA for both at 10% CH_4 mixed with N_2 and also 0 % CH_4. The CDAS signal is clearly present even in the absence of any target gas.
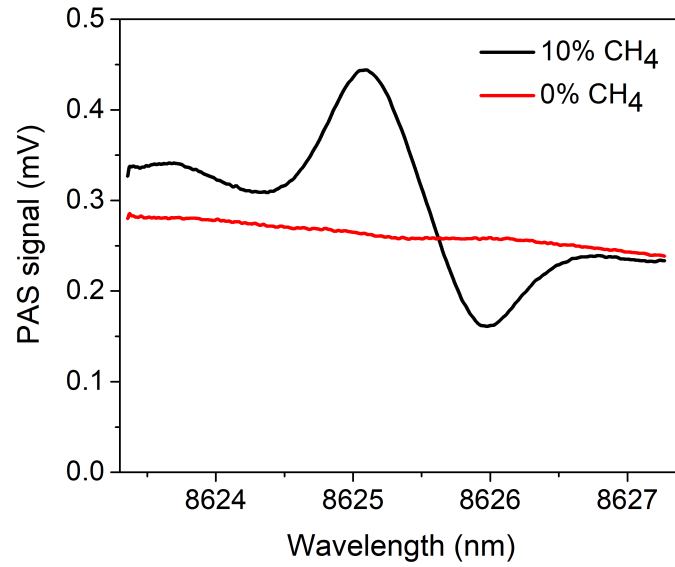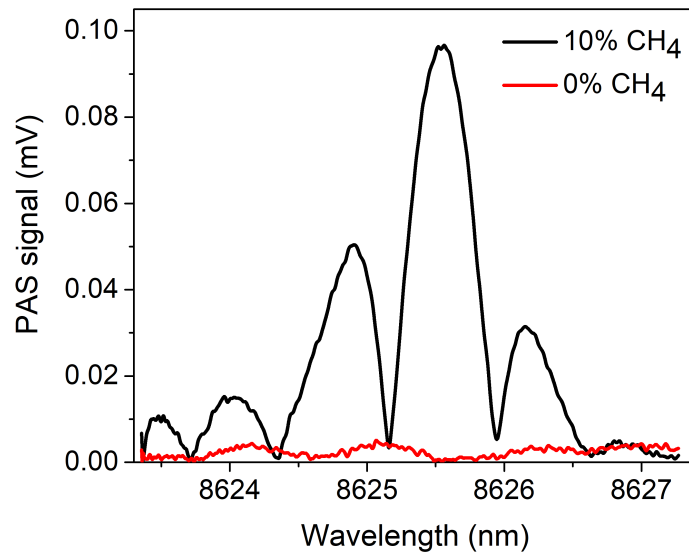

Figure 6.2: Magnitudes of the second harmonic components output from the LIA for both at 10 % CH_4 mixed with N_2 and also 0 % CH_4. There is minimal significant non-linear CDAS present, with the most dominant signal being the second order Fourier component due to laser-gas interaction.

6.3 Identifying the Source of CDAS

As described in section 3.10, a baseline signal in WMS-PAS can be used as a normalisation term, as evidenced in the 2f/1f technique in TDLS-WMS [123]. For this reason, the source of the CDAS signal is investigated in this section, as the identification of the CDAS signal source is highly important for the reliability and repeatably of the calibration-free measurements using different PAS cell designs, fabrication materials and components.

The CDAS signal generated in PAS is not caused by the same mechanism as in TDLS, where the DC level is caused by direct IM of the laser. In PAS, the detection is an indirect measurement of an acoustic signal generated by the lasers IM and WM, and therefore there should be no DC level in the absence of any absorbing materials or gas species. The CDAS signal is not due to the microphone itself, as it is absent when the laser is off but the microphone is on and the signal is demodulated using the LIA with reference frequency at the resonance frequency of a PAS cell. For these reasons, two potential non-selective sources of laser absorption, within the PAS cell being used, were identified: the CaF_2 windows or absorption by the resin. These two potential CDAS sources will be explored in detail in the following subsections.

6.3.1 Effect of the Calcium Fluoride Windows

There has been detailed publications of optical noise being generated by absorption into the coupling windows of a PAS cell [127]. However, the majority of this noise should be theoretically removed by the buffer volumes. To confirm the performance of the buffer volumes, and ensure the source of the CDAS is not due to the vibration caused by the CaF_2 windows as light is absorbed, a specialised cell was designed and manufactured. This cell has the exact internal dimensions as the standard cell but the CaF_2 window at the front of the cell was removed making this cell open to the atmosphere. The posterior window is sealed shut with a resin plug after alignment to allow gas flow through the resonator into the posterior buffer region. 1f signals were then recorded for the cell without

the front window, and then after the attachment of a CaF_2 window to the same cell. In both cases, the gas flowing through the cell was 100 % N_2 at 100 ml/min flow rate.

For both cases the resonant frequency of the cell was initially found using a frequency sweep of the laser, and it was found that there is a slight shift in the resonant frequency of the cell when the window is attached due to changing boundary conditions. Therefore, the comparative study was carried out for data recorded at the respective resonant frequencies. It can be seen in figure 6.3 that the windowless cell has a slightly higher CDAS level at 5.3 % mean difference. This may be simply explained by the increased available optical power in the resonator when the window is not in place, thus increasing the generated acoustic CDAS. This explanation is also supported by the quoted [128] 95 % transmissivity of a 0.5 mm thick CaF_2 window at 8.65µm, which suggests a 5 % reduction in optical power available for PA signal generation when windows are attached. Another explanation for the loss of optical power available is the potential optical divergence caused by the CaF_2 windows. As evidenced from the plot and discussion above, it was decided that further investigation was unnecessary as the CDAS effect is clearly not caused by the CaF_2 windows.
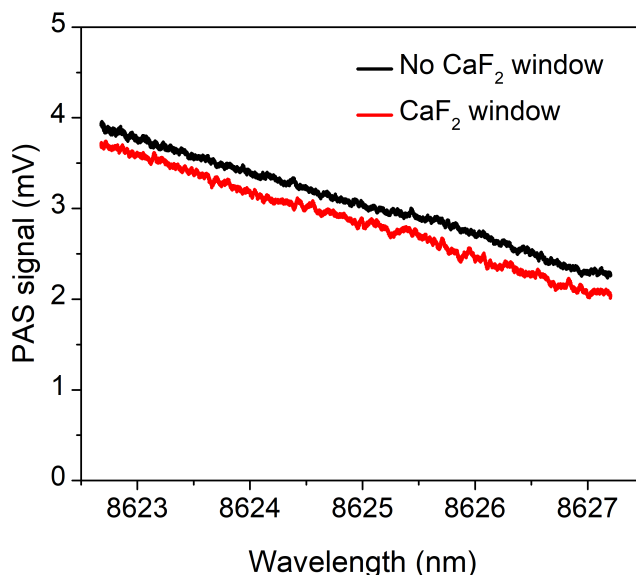
Figure 6.3: Comparison of resonant 1f CDAS signals of the same sensor without any attached windows and after CaF_2 windows have been attached.

6.3.2 Optical Absorption by 3D-Printer Resin

To test the optical transmission-absorption properties of the resin, discs with varying thicknesses were manufactured using the same resin used to manufacture cells.

The schematic and the printed design of the discs are shown in figure 6.4. The annulus part of the design is used for attachment to the standard optical mounts and the central diaphragm is a thinner area of various depths used to measure optical absorption. For these tests, 6 discs at various diaphragm thicknesses under 2,000 µm were designed and printed. However, as 3D-printing thin structures ($<$ 500 µm) can lead to inaccuracies in thickness, the diaphragm of each disc was measured separately using a digital caliper with ± 1 µm accuracy and these values are used in the analysis below.
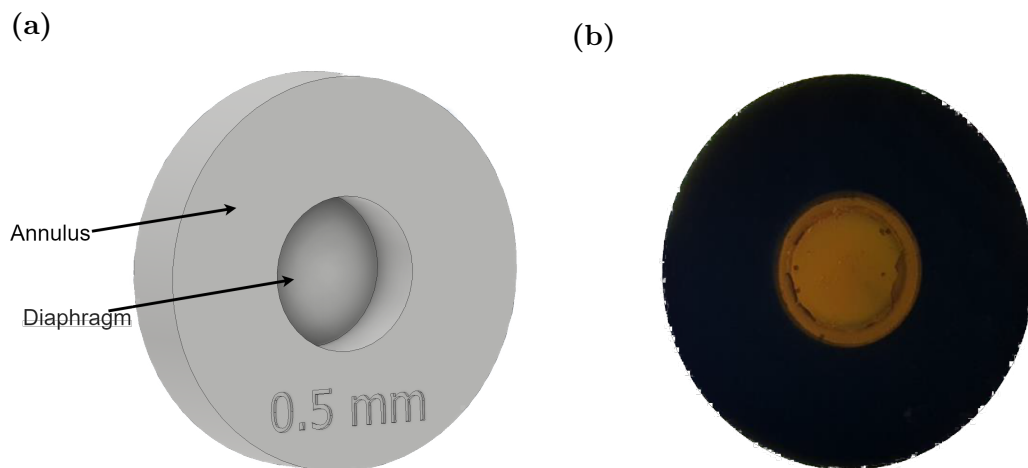
Figure 6.4: (a) Schematic 3D model of disc design, (b) actual 3D-printed design.

The setup for these absorption measurements consisted of light from either 8.65 µm or 5.25 µm QCL laser incident directly onto one of the 3D-printed discs attached to an optical mount. The light passing through the disc is the measured using a Mercury Cadmium Telluride (MCT) detector (Vigo PVI-2TE-8) as shown in figure 6.5. The laser was set at 35.5 °C and the LDC was set at 795.3 mA DC bias current for 8.65 µm QCL and -6 °C at 200 mA for 5.25 µm QCL.
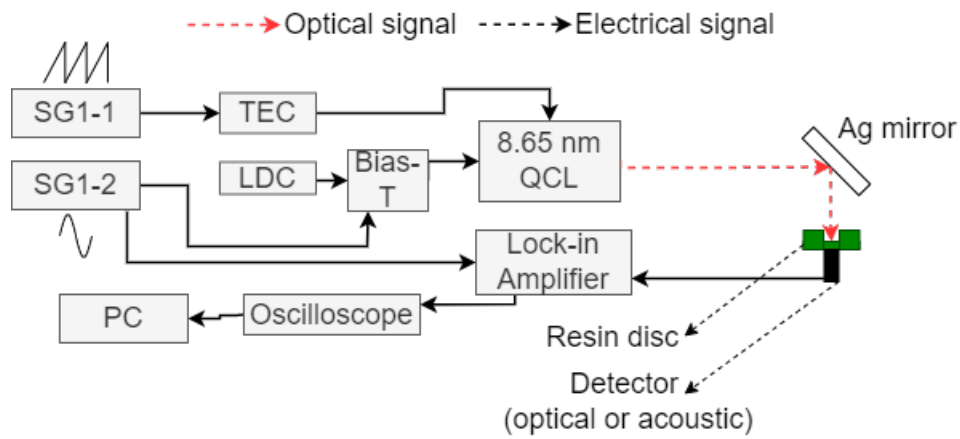
Figure 6.5: A schematic of the experimental setup for optical and acoustic tests on HTM140 resin using 3D-printed discs.
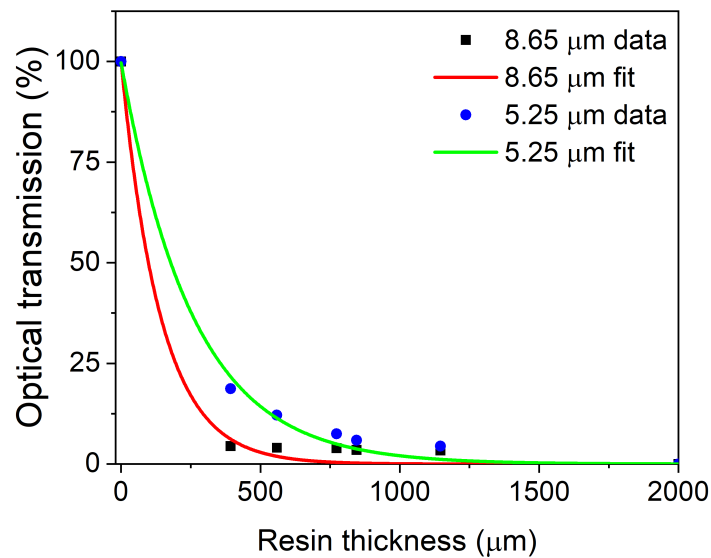
Figure 6.6: The optical transmission versus HTM140 resin thickness with an exponential decay fitting.

The transmission data with a fitted exponential decay for both lasers using the same discs is shown in figure 6.6. As can be seen from these figures, the fit between the exponential and the data points is poor, particularly for the 8.65 µm laser. This is due to the limited number of data points, especially below 400 µm resin thickness, as a result of the inability to control the thickness of thin 3D-printed discs precisely. The exponential equations for the transmission of both lasers through the HTM140 resin are given in equations 6.1 and 6.2 below

for 8.65 µm and 5.25 µm QCL lasers respectively:

8.65 µm :

$$y = 100e^{-0.00707x} \tag{6.1}$$

5.25 µm:

$$y = 100e^{-0.00388x} \tag{6.2}$$

The calculated absorption coefficients for HTM140 resin using this technique are $\alpha_R = 0.00707$ µm^{-1} for 8.65 µm and $\alpha_R = 0.00388$ µmm^{-1} for 5.25 µm. Hence, for HTM140 resin it can be concluded that attenuation of the beam is greater at 8.65 µm as compared to 5.25 µm laser by around 80 %.

The tests on resin were repeated using a different, more optically transparent resin, R11, again supplied by the same company, EnvisionTEC, using the same 3D-printer and disc printing techniques. The resulting transmission data and exponential decay fits for using both lasers are shown in figure 6.7.
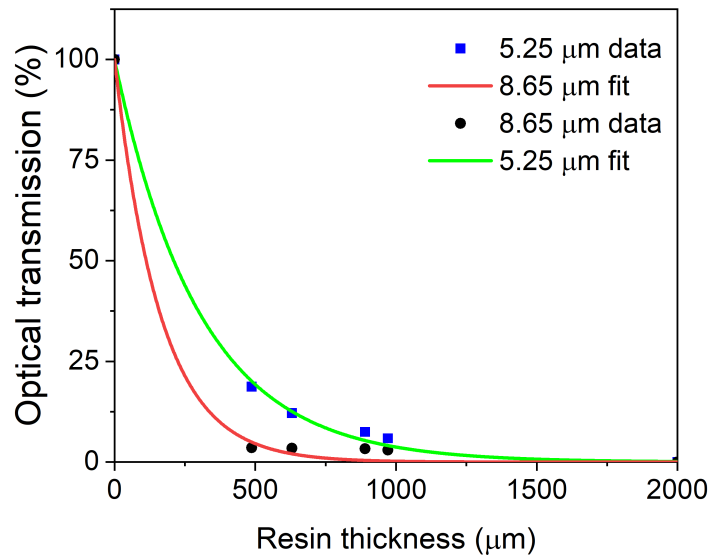
Figure 6.7: The optical transmission versus R11 resin's thickness with an exponential decay fitting.

The exponential equations for the transmission of both lasers through the R11 resin are given in equations 6.3 and 6.4 for 8.65 µm and 5.25 µm light respectively:

8.65 µm:

$$y = 100e^{-0.00617x} \tag{6.3}$$

5.25 µm:

$$y = 100e^{-0.00329x} \tag{6.4}$$

The absorption coefficients for R11 resin are $\alpha_R = 0.00617$ µm^{-1} for 8.65 µm and $\alpha_R = 0.00329$ µm^{-1} for 5.25 µm. Hence, a similar trend to the result in HTM140 resin tests is obtained where attenuation of the beam is greater at 8.65 µm as compared to 5.25 µm by around 87 %.

The figures 6.6 and 6.7 show that the resins used in this study absorb MIR light. In both resin tests, stronger attenuation was observed at 8.65 µm suggesting that these types of 3D-printable polymers may have increasing α_R as the incident wavelength is increased. On the other hand, attenuation decreased when R11 is used for both wavelengths. Hence, different PAS cells made out of more attenuating resins can be used in further studies to potentially increase the CDAS signal.

6.3.3   Acoustic Signal Generation From 3D-printing Resin

The acoustic signal generation from the HTM140 resin was tested using a similar experimental setup to that used in section 6.3.2 with the addition of a microphone (Sennheiser K6) to measure an acoustic signal generated by the polymer discs, instead of an optical detector, as shown in figure 6.5. The microphone was connected to a lock-in amplifier and the subsequent signal is then recorded via an oscilloscope and GPIB.

A modulation frequency of 10 kHz was applied to the QCL using a signal generator, and the TEC and LDC were set to 35.5 °C and 795.3 mA for 8.65 µm QCL and -6 °C at 200 mA for 5.25 µm QCL respectively. Prior to taking any measurements, the background noise was measured and subtracted from the final data. The acoustic signals detected from HTM140 and R11 discs at various diaphragm thicknesses for both lasers are shown in figure 6.8 below.
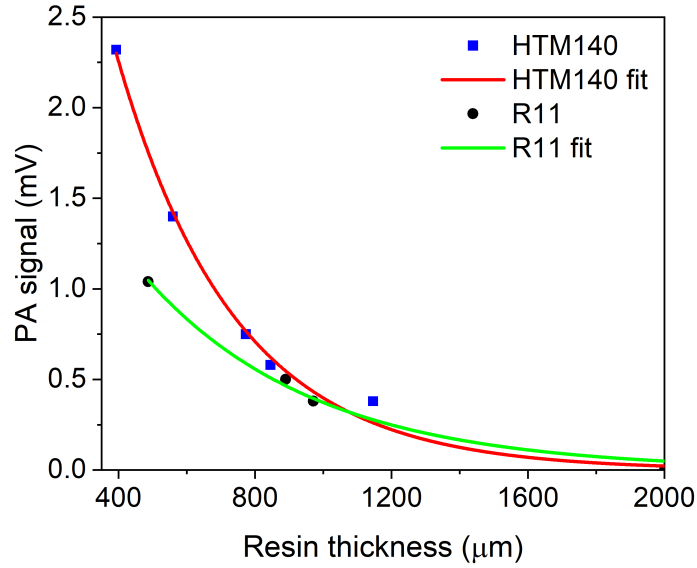
Figure 6.8: PA signal generation from HTM140 and R11 resins at different diaphragm thicknesses. The equations for the exponential best fits are y = $7.17e^{-0.00289x}$ for HTM140 and y = $2.80e^{-0.00202x}$ for R11.

The exponential equations for the PA signal generation using 8.65 µm QCL are given in equations 6.5 and 6.6 for HTM140 and R11 resins respectively:

HTM140:

$$y = 7.17e^{-0.00289x} \tag{6.5}$$

R11:

$$y = 2.80e^{-0.00202x} \tag{6.6}$$

As can be seen from the figure 6.8 an acoustic signal is registered for both resins, and the magnitude of the acoustic signals reduce exponentially as the resin thickness increases. However, as evidenced from the figure 6.8, more PA signal is observed with HTM140 up to ∼ 1100 µm diaphragm thickness when the exponential fitted curves start overlapping. For instance, at 490 µm thickness 67 % more PA signal is obtained when HTM140 is used. The difference in resins could also be explained by their physical properties, as R11 is a more flexible material with modulus of elasticity of 1,245 - 1,510 MPa, whereas this value is 3,350 MPa for HTM140 [125][129].

When the exponential decay constant of HTM140 for PA signal generation and transmission is compared, as shown in equations 6.5 and 6.1, a nearly twofold lower decay constant in PA signal is observed in acoustic tests. One explanation for this difference could be variable deposition of laser power on each side of a diaphragm. As the thickness of the diaphragm is increased, more laser power could be absorbed by one side of the resin in a non-linear manner, leading to a change in acoustic decay constant compared to the optical decay constant. As cell wall thickness is much higher than diaphragm thicknesses, acoustic generation on the other side of the cell walls is not expected. For this reason, it was decided that the use of the optical decay constant is more valid for PAS cells compared to the acoustic decay constant for any future analysis.

It must be noted that, negligible signal was registered when using 5.25 µm QCL for these PA signal generation tests. This could be explained by reduced laser absorption by the both resins at this wavelength, as previously explored in figures 6.6 and 6.7, not being able to generate adequate acoustic signal to be detected in this test.

The results from this section indicate that the source of the CDAS signal is the 3D-printing resin (HTM-140) absorbing incident light and subsequently leading to a photoacoustic CDAS signal.

6.3.4   Origin of CDAS Within the Cell

There are two competing theories about the exact location of the CDAS generation from the resin within a PAS cell. One idea is the localised signal generation on the posterior surface of the first buffer region: front end of the resonator, where the laser beam is larger than the diameter of the resonator ($>$ 1.5 mm) leading to interaction with the resin. The second theory is the acoustic signal generation is due to the expanding laser beam interacting with the sidewalls of the resonator as it passes through.

To attempt to measure the contribution of the CDAS from the posterior face of the buffer volume two new gas cells were built: the first cell had a CaF_2 window

with a diameter of 10 mm, rather than 6 mm of the original, to introduce increased optical signal to the buffer face; the second cell was a hollow cell with a buffer face only 19 % of the original design.

Initially, the larger windowed cell was placed at a distance where the beam waist of the optical beam is larger than the 6 mm opening to the cell. It was assumed that if the CDAS was caused by the posterior wall of the first buffer volume then this setup would cause an increased CDAS amplitude, as more radiation will be absorbed by the targeted location. Both the new cell and the original cell were placed at a position where the tangential beam waist is 5.39 mm and the sagittal beam waist is 10.8 mm. For the original cell this resulted in 56 % of the beam being blocked by the front surface of the original sensor before reaching the inner resonator surface. In this new design 99.07 % of the incident beam hits the buffer end surface.

The hollow core cell had only 19 % of the front surface area of the original cell. The resonator has 1 mm thick walls that are suspended in the hollow core using resin columns and a 10 mm CaF_2 window inlet. This design leads to 81 % lower surface area of the resonator front end which would lead to reduced background RAM according to this theory. A CAD drawing of this cell is shown in figure 6.9.
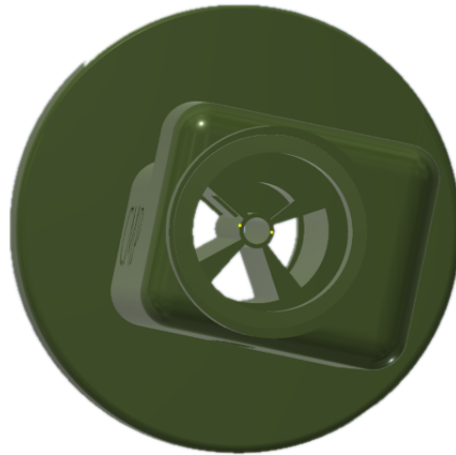
Figure 6.9: CAD schematic of hollow-core cell.

The comparison of the CDAS signals for original (6 mm inlet), larger inlet (10 mm inlet) and hollow core cells is shown in figure 6.10.
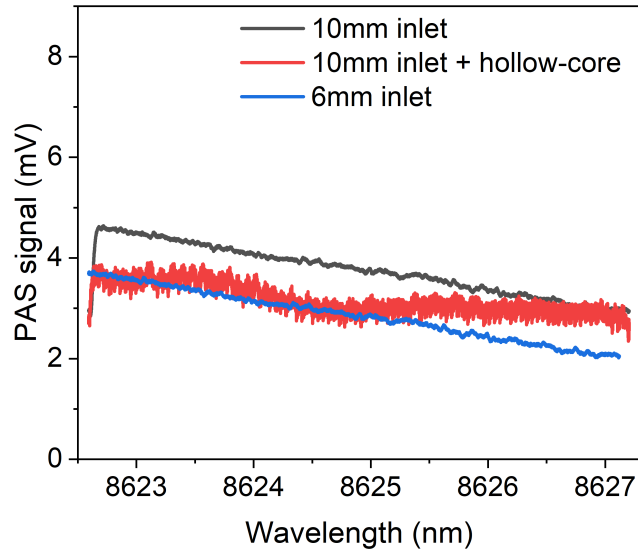
Figure 6.10: Plot comparing CDAS signals at the original (6 mm inlet) cell, larger inlet (10 mm inlet) cell and hollow-core cell.

This data shows that the mean CDAS level is 23.9 % higher when a 10 mm inlet is used, compared to 6 mm inlet cell. As described above, the 10 mm inlet cell receives 43.07 % (99.07 % - 56 %) more beam deposition on the buffer end surface. Despite this increase of light deposited on the buffer end surface, only 23.9 % increase in CDAS signal is observed. Hence, it can be concluded that light absorbed by the buffer end surface might lead to an increased CDAS signal. However, the increased CDAS signal observed during this comparison is not enough to justify the proposed suggestion about the CDAS location and the increase could also be result of alignment issues, which changes the amount of light absorbed by the resonator walls, or fabrication inconsistencies.

As shown by the comparison CDAS signals of the original (6 mm inlet) cell with the hollow core cell in figure 6.10, the mean CDAS level is 9.5 % larger in the hollow core cell compared to the original. This indicates that the CDAS signal increased, even though the surface area of the buffer end was reduced by 89 %, implying that the buffer end area is not the source of the CDAS signal. The increase in the CDAS signal also supports the suggestions above about the increased CDAS signal in the 10 mm input cell, such as alignment issues and

fabrication inconsistencies.

In addition, the SNR reduces significantly in the hollow-core cell, as 32.7 % reduction in R^2 = 0.6623 is observed compared to the original cell with R^2 = 0.9853 using linear fitting for each signal. This most likely originates from the extra external noise picked up by the microphone as the bulk of the resin around the location of the microphone was removed to design the hollow-core cell, reducing noise isolation.

The tests in this chapter indicates that even though a PA signal might be created by the buffer end area, it is not high enough to be picked up by the microphone in the resonator. Hence the main source of CDAS signal is the laser beam absorbed to the walls of the resonator as it passes through.

6.4   Manipulating the CDAS Signal

As suggested by equation 3.4 in chapter 3, the magnitude of the CDAS signal should also be proportional to the light absorbed by the resin. To confirm the suggestion that CDAS is generated by the resonator walls and test the effect of increasing optical power on CDAS, the optical power incident on the walls of the resonator are varied.

An experiment was setup as in figure 5.1. However, in this case the PAS sensor is removed from an optical cage and attached to a two-axis mirror mount to allow its rotation. As the incident angle, θ, between the resonator plane and the laser beam is increased by manipulating the mirror mount, the laser beam interaction with the resonator walls is increased. A schematic for this interaction is shown in figure 6.11.
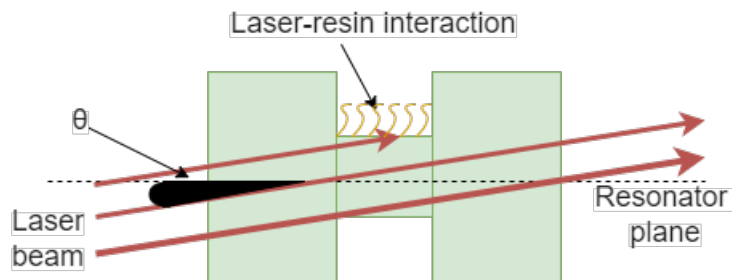
Figure 6.11: A schematic showing the laser beam-resonator interaction as the angle between the laser beam axis and resonator axis is changed.

It was found that the magnitude of the CDAS signal is minimum when the sensor is co-linearly aligned in a cage mount, thus allowing the beam to pass through with minimal interaction with the resin material on resonator walls. As θ is increased, the 1f and 2f PAS signals for the 10 % CH_4 and 100 % N_2 gases were recorded for increasing CDAS levels. At each step, the total laser power absorbed by the resonator walls must also be found. However, due to the comparable size of the resonator radius to the beam diameter, the beam diffracts, consequently the total power exiting a sensor device can not be measured using a simple photo-diode commonly used at other sections of this work with a small pinhole input section (0.25 mm x 0.25 mm). For the purpose of measuring the beam shape and the power deposited, a 3D beam shape characterisation technique, previously described in section 5.4.2, was used. At each θ value, the 3D beamshape is also obtained for a 3D-printed pinhole with a radius equal to the resonator placed at the mirror mount. The use of this pinhole allows quantification and subsequent exclusion of the laser beam deposited on the front end of the resonator and the beam passing without any interaction with the resonator walls, which does not contribute to the generation of CDAS signal. The laser power deposited on the resonator walls, I_r, is found by the following equation:

$$I_r = I_{pinhole} - I_c \tag{6.7}$$

where $I_{pinhole}$ and I_c are two-dimensional integrations of the 3D beam shape at each θ angle, representing the total power. The 3D intensity maps for a cell

output and a corresponding pinhole output are shown in figures 6.12 and 6.13. These figures show the necessity of using a 3D-beam scan technique, as after exiting the pinhole or cell the beam size diffracts to a larger shape than the input size of a common photo-diode.
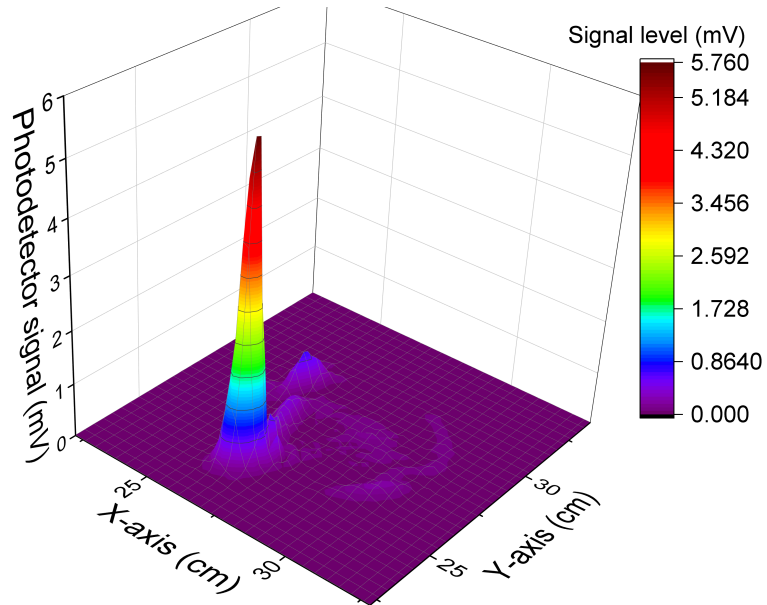
Figure 6.12: 3-dimensional intensity heat map cell output.
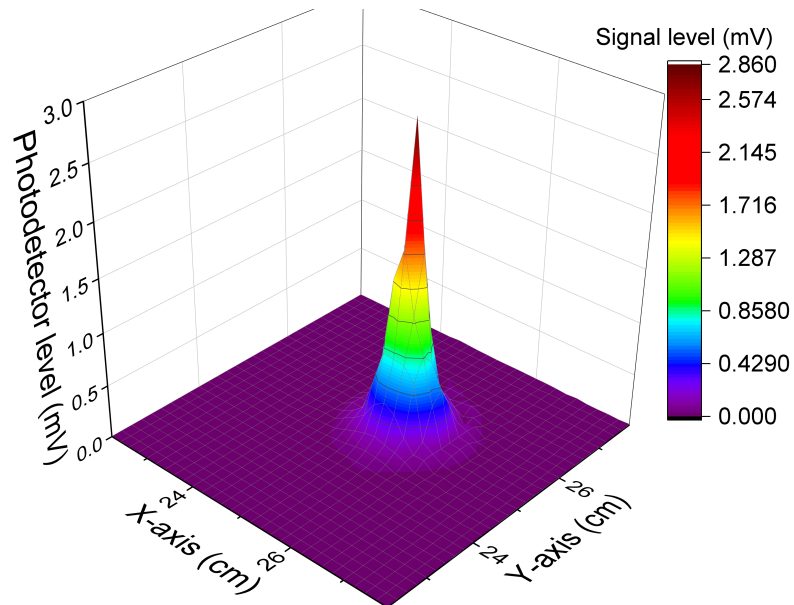
Figure 6.13: 3-dimensional intensity heat map pinhole output.

The relationship of this absorbed power to the CDAS baseline level is shown in figure 6.14.
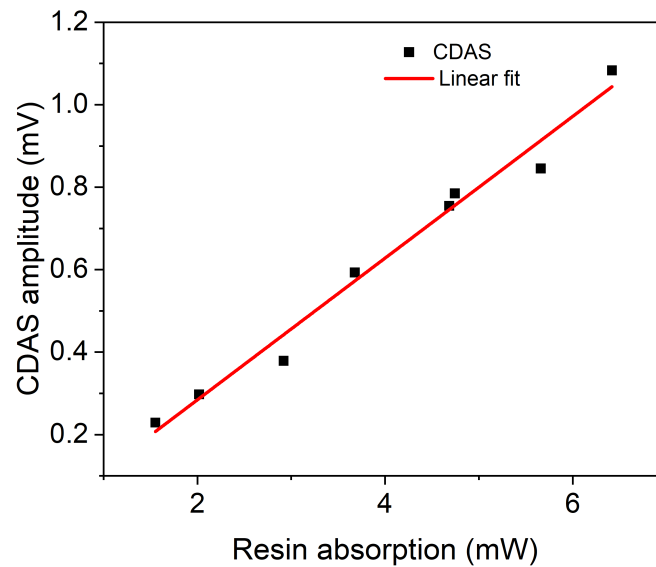
Figure 6.14: CDAS amplitude against absorbed power by the resonator walls.   The equation for the best fit is given by y = 0.6x-0.016.

As can be seen from the figure 6.14, there is a linear relationship between the CDAS amplitude and the absorption of the laser by the resin. However, as the resin absorption is increased further than the limits of this test at increased θ angle, the CDAS signal level falls sharply as most of the laser power is blocked at the front end of the resonator rather then being absorbed by the resonator walls. Using a linear fit, it was estimated that for a 16 mm resonator length the threshold absorption into the resin is 0.027 mW for the observation of a CDAS signal. Assuming a homogeneous absorption throughout the resonator, this value corresponds to 1.7 µW/cm per unit length of a resonator.

6.5   Calibration-Free Measurements

6.5.1   Sensor Frequency Characterisation

Acoustic characterisation tests of the PAS sensor were performed using a customised version of the LabVIEW software previously described in section 5.2.2,

to acquire the R_{1f}, R_{2f} and R_{2f}/R_{1f} signals as a function of modulation frequency with and without the target gas CH_4, to highlight the presence of CDAS in the 1f harmonic and its absence in 2f component.

For this characterisation process, the modulation frequency was varied between 3 kHz and 20 kHz, with 200 Hz increments and the first harmonic components X_{1f} and Y_{1f}, and second harmonic components, X_{2f} and Y_{2f}, were obtained after 128 averages. At each increment, the LIA reference phase was adjusted using custom made LabVIEW code to isolate the FM signal on the Y-axis of the LIA as previously described in equations 3.30 and 3.31, to result in amplitude of the isolated FM signal at both ω_r and $\omega_r/2$ [130]. Subsequently, for each measurement R_{1f}, R_{2f} and R_{2f}/R_{1f} values were obtained. The obtained frequency response of R_{1f} peak-to-peak and R_{2f} amplitude are shown in figure 6.15. This figure also includes median value of R_{1f} signal and amplitude of R_{2f} signal for the background measurements using 100 % N_2 flowing at 100 ml/min flow rate, named $R_{1fB-CDAS}$ and R_{2fB} signals respectively.
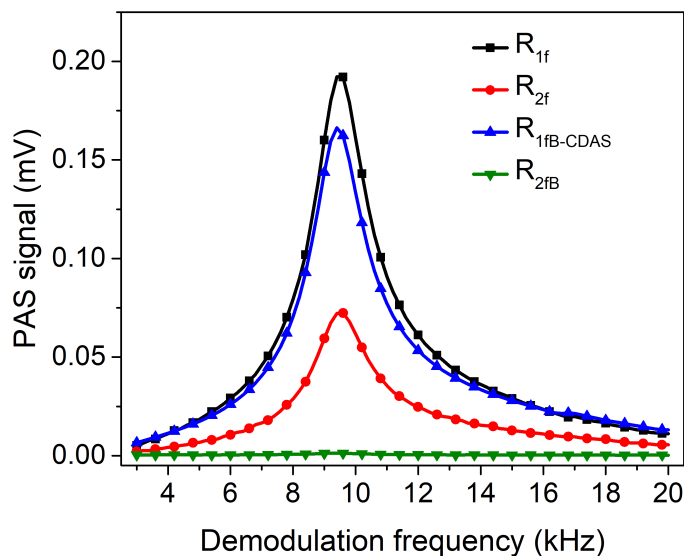
Figure 6.15: Acoustic characterisation profile as a function of modulation frequency of R_{1f} peak-to-peak and R_{2f} amplitude for 10 % CH_4, and $R_{1fB-CDAS}$ amplitude and R_{2fB} amplitude for the background measurements using 100 % N_2. For all data-set in this plot, gases were flown at 100 ml/min flow rate.

As shown in figure 6.15, the amplitude of the R_{1f} signal is approximately $\sim$ 1.16 times larger than the generated CDAS signal at $R_{1fB-CDAS}$ amplitude. However, it must be noted that this ratio is highly dependent on the incident beam direction, beam shape and alignment as these factors affect the optical power deposited on the side walls of the resonator and CDAS amplitude. The amplitude of the R_{2f} frequency response is approximately $\sim$ 2.6 times smaller than the R_{1f} response, displaying the reduced sensitivity of the second harmonic measurement technique. Furthermore, the non-linear CDAS signal, R_{2fB}, is approximately $\sim$ 128 times smaller than the $R_{1fB-CDAS}$ and 56 times smaller than the R_{2f} signal. As R_{2fB} signal is clearly insignificant and has a very small contribution towards the recovered R_{2f}/R_{1f}, it is excluded from any further characterisation tests and normalisation.

In order to ensure the same acoustic mode is being excited in the resonator, the recovered frequency profiles were all normalised to the maximum peak-to-peak value of the R_{1f} acoustic profile, as shown in figure 6.16, along with the percentage residuals compared to the R_{1f} signal.

As shown in the figure 6.16, there is a clear overlap between the normalised signals, solidifying the suggestion that all acoustic profiles are originating from the same acoustic mode of the resonator. However, as evidenced from the residual, the overlap between the signals is significantly better within 4.5 kHz to 18 kHz frequency range. R_{2f} residual is within ± 10 % between 4.4 kHz and 17.6 kHz, whereas $R_{1fB-CDAS}$ residual is within ± 10 % between 5.4 kHz and 18.2 kHz.

From the figure 6.16, it is clear that the SNR of the R_{2f}/R_{1f} reduces when operating further off resonance, as the recovered R_{2f} and R_{1f} signal magnitudes reduce, with a maximum percentage variation of 4.45 %. This implies that the concentration data recovered with the suggested 2f/1f normalisation procedure will divert from its expected value, if there is a variation in the gas matrix parameters, and therefore the speed of sound in the cell. If the methane concentrations with N_2 host gas is changed from 0 % to 100 %, the total speed of sound will reduced from 448 ms^{-1} to 350 ms^{-1}. It was calculated that this
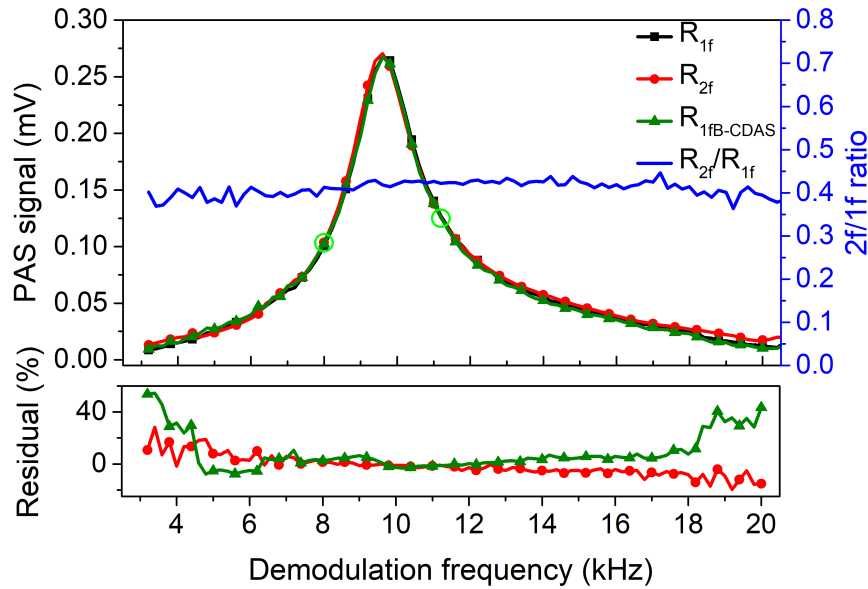
Figure 6.16: Frequency response profile of 1f peak-to-peak and 2f amplitude as a function of modulation frequency for 10 % CH_4 (R_{1f} and R_{2f}) and 0 % CH_4 ($R_{1fB-CDAS}$) concentrations, normalised to R_{1f} peak, along with the percentage residuals. Data was obtained using ram-nulling technique, by isolating the FM signal on Y-axis and eliminating RAM distortions to the X-axis. Green circles mark the f_r ±1600 Hz range, indicating the range of calibration-free tests in section 6.5.2.

change in speed of sound will only shift the resonant frequency of a PAS cell by 3.2 kHz. Thus, considering a range of ±1.6 kHz from the maximum of the resonant curve marked with green circles in figure 6.16, the percentage variation in the R_{2f}/R_{1f} signal corresponding to the full range of methane concentrations of 0 % to 100 % is reduced to 1.45 %. This negligible R_{2f}/R_{1f} within the full target gas range, shows the ability of this normalisation technique to calibrate for gas density variation, and therefore resonant frequency variation, without the requirement for any feedback.

Finally, using the RAM-nulled frequency response profiles in figure 6.16, the overall Q-Factor and resonant frequency for this sensor was calculated to be 6.6 and 9.59 kHz respectively. The f_r for the $R_{1fB-CDAS}$ is 9.49 kHz, which is $\sim$ 100 Hz lower than the f_r of the R_{1f} signal. This difference originates from the increase in the total molar mass due to reduced number of heavier CH_4 molecules, leading to a reduced average speed of sound and hence a lowered resonant frequency for

the $R_{1fB-CDAS}$ signal.

6.5.2 Validation of 2f/1f Calibration Technique with Changing Demodulation Frequency

To validate the 2f/1f PAS calibration technique for varying frequencies off-resonance, the R_{1f}, R_{2f} were recorded and compared to the corresponding R_{2f}/R_{1f} signals. This was carried out for modulation frequencies 1600 Hz on either side of the resonance frequency with 800 Hz increments. Using a modified version of the automated LabVIEW program, previously described in section 5.2.2, all signals are obtained with 128 averaging for 10 % CH_4 flowing at 100 ml/min and the obtained results are shown in figures 6.17, 6.18 and 6.19 for R_{1f}, R_{2f} and R_{2f}/R_{1f} signals respectively. For figure 6.19, residuals compared to R_{2f}/R_{1f} signals at f_r are also included to highlight the signal overlap.
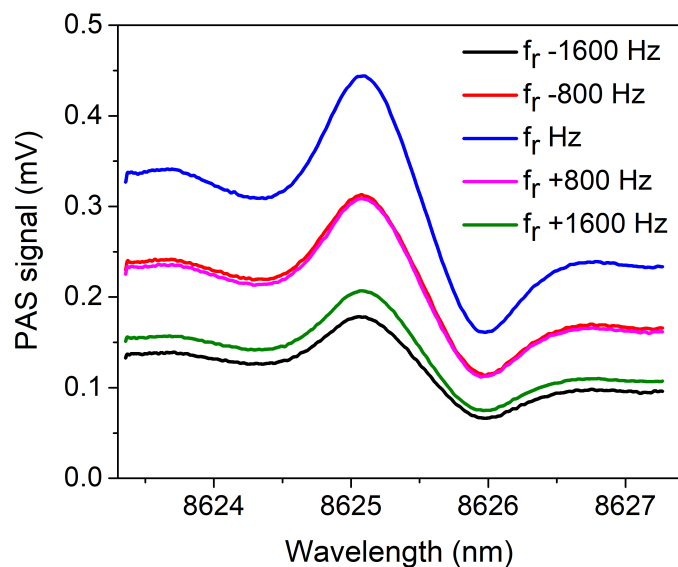
Figure 6.17: PXIe acquired R_{1f} PAS signals of at modulation frequencies ± 1.6 kHz around the f_r frequency with 800 Hz increments. The signals are obtained when the laser modulation frequency is equal to the LIA frequency.
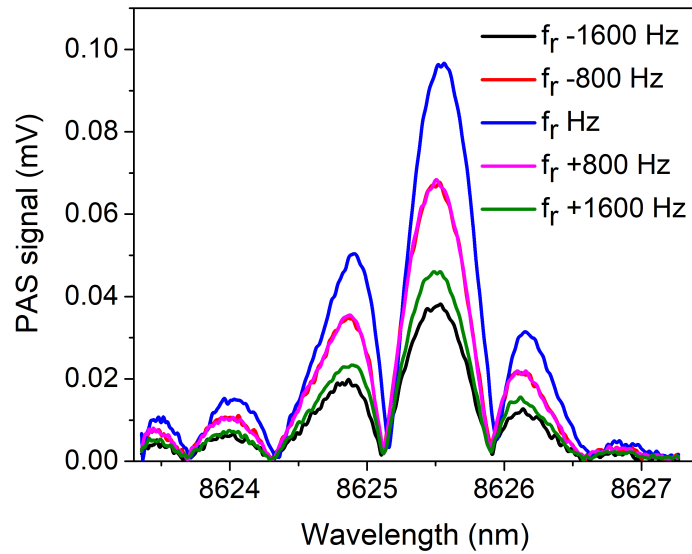
Figure 6.18: PXIe acquired R_{2f} PAS signals of at modulation frequencies ± 1.6 kHz around the f_r frequency with 800 Hz increments. The signals are obtained when the laser modulation frequency is half the LIA reference frequency.
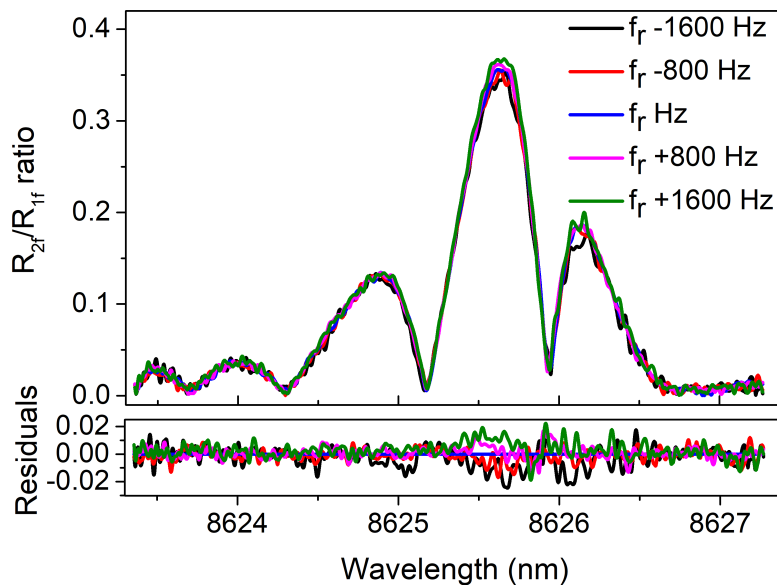
Figure 6.19: PXIe acquired R_{2f}/R_{1f} PAS signals of at modulation frequencies ± 1.6 kHz around the f_r frequency with 800 Hz increments.

As previously discussed in section 6.5.1 and shown in figure 6.16, this demodulation frequency range represents a complete change in target gas CH_4 concentration from 0 % to 100 %. Figures 6.17 and 6.18 show an expected

reduction in signal size off-resonance frequency for both signals, as well as a variation of CDAS as a function of demodulation frequency. However, for the R_{2f}/R_{1f} signals in figure 6.19, there is a clear complete overlap at all demodulation frequencies, showing the validity of the 2f/1f technique for changing demodulation frequency around resonance. However, the increase in residuals at the extremities of demodulation frequency, ± 1.6 kHz, must also be noted, particularly for peak points of R_{2f}/R_{1f} signals, which is due to reduced SNR at extreme off-resonance frequencies.

6.5.3 Validation of 2f/1f Calibration Technique with Changing Gas Concentration

In section 6.5.2, the demodulation frequency was shifted on either side of the fixed resonance frequency using 10 % CH_4 to simulate resonant frequency change from 0 % to 100 % gas concentration, whereas in this section the 2f/1f calibration technique will be tested under changing gas concentration conditions at a fixed demodulation frequency. For this test, 10 % CH_4 with N_2 (BOC - ± 5 % quoted supplier uncertainty) was mixed with 100 % N_2 at varying flow rates using two mass flow controllers (Bronkhorst - quoted error of ± 1 %), to produce concentrations ranging from 1 % to 10 % in 1 % increments. At each gas mixture the total gas flow rate was kept at 100 ml/min and R_{1f}, R_{2f} and R_{2f}/R_{1f} were acquired after 128 averages using the automated LabVIEW code. Figure 6.20 shows R_{1f} signals as a function of CH_4 concentration ranging from 0 % to 10 %, highlighting the independence of the CDAS level from the target gas concentration.
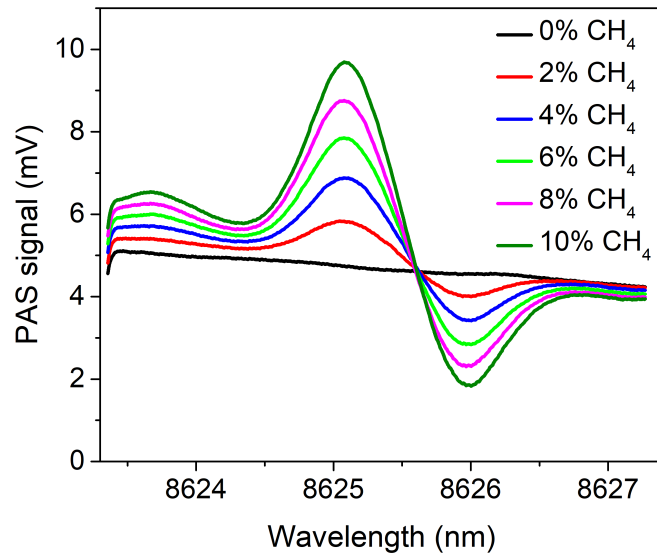
Figure 6.20: R_{1f} signals as a function of CH_4 concentration from 0 % to 10 % with 2 % increments. It is clear that the CDAS is constant for a given target gas concentration and dependent on the laser-resin interaction.

Figure 6.21 shows the plot of the R_{2f}/R_{1f} signal as a function of CH_4 concentration, with a linear best fit displaying a $R^2 = 0.99982$. From the figure 6.16, the percentage variation of R_{2f}/R_{1f} within previously discussed ± 1.6 kHz range was calculated as $\sigma = 1.45$ %, corresponding to an estimated concentration measurement variation of ± 0.12 % for a complete measurement range of 0 % to 100 % CH_4 in figure 6.21. The percentage variation for concentration measurement of SO_2 gas from 0 % to 100 %, was calculated as ± 0.009 %. These results further highlights the effectiveness of the 2f/1f technique to normalise in-situ PAS signals for varying target gas concentration.
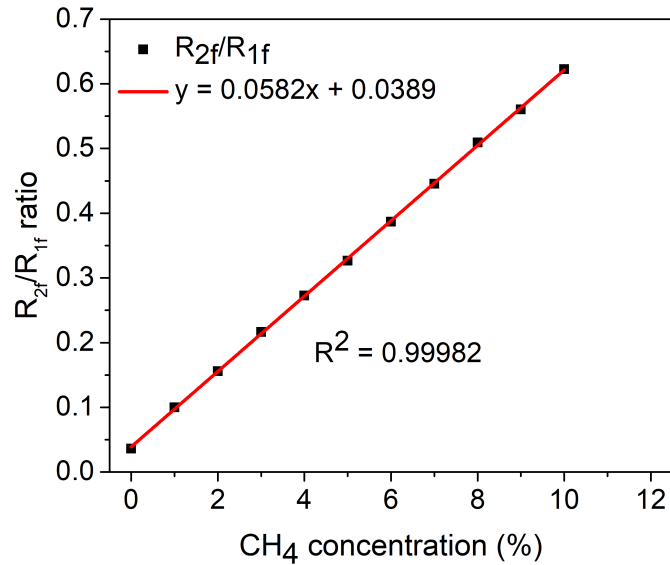
Figure 6.21: R_{2f}/R_{1f} amplitude as a function of CH_4 concentration.

6.5.4 Validation of 2f/1f Calibration Technique with Changing Light Intensity

In order to test the validity of the PAS 2f/1f technique for changing optical powers, the optical beam incident on the cell was attenuated using acetate filters with progressively increasing thickness ranging from a thickness of 40 µm to 240 µm with 40 µm increments. At each thickness the R_{1f}, R_{2f} and R_{2f}/R_{1f} signals were acquired after 128 averages using the automated LabVIEW code and 10 % CH_4 gas flowing through the cell at 100 ml/min. In addition, the laser power was also monitored at each step, using an optical power-meter at a location of 5 cm from the laser output.

An important aspect of this experiment is to keep the beam shape and direction after attenuation constant, as the 2f/1f normalisation technique was found to be ineffective for beam misalignment. This is due to the change in CDAS level via changes in the light-resonator wall interaction. In figures 6.22, 6.23 and 6.24 the R_{1f}, R_{2f} and R_{2f}/R_{1f} signals are shown respectively for optical power attenuation up to 78.3 %.
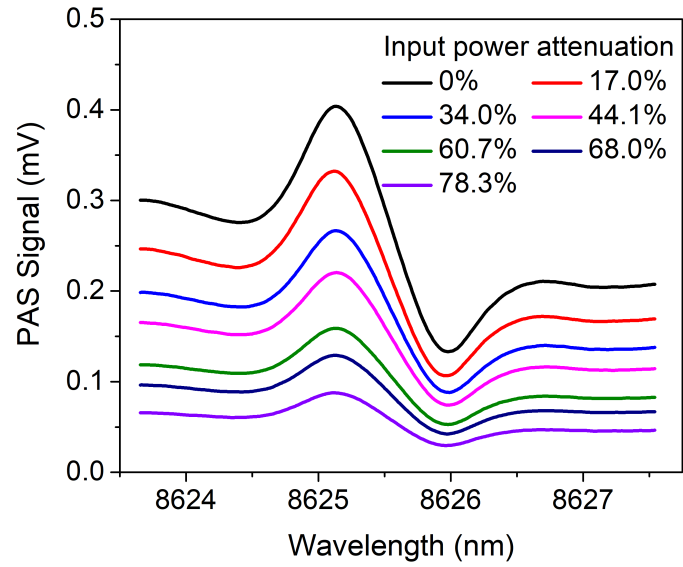
Figure 6.22: R_{1f} signals obtained at varying input optical powers measured at the output of the PAS cell.
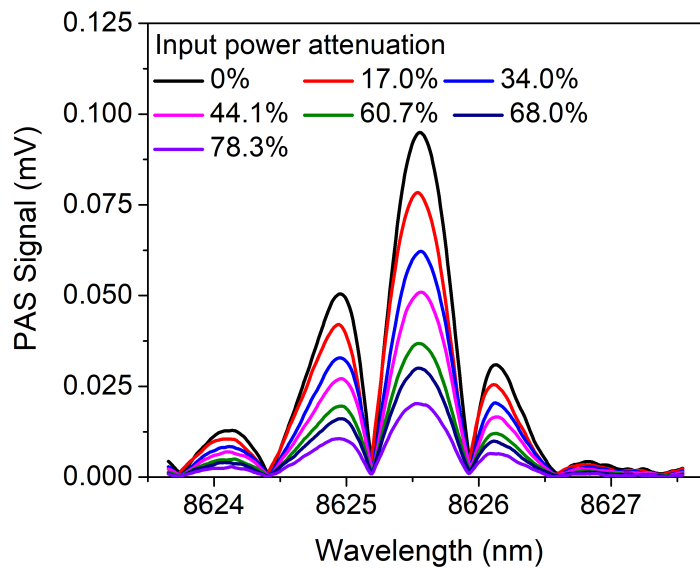
Figure 6.23: R_{2f} signals obtained at varying input optical powers measured at the output of the PAS cell.
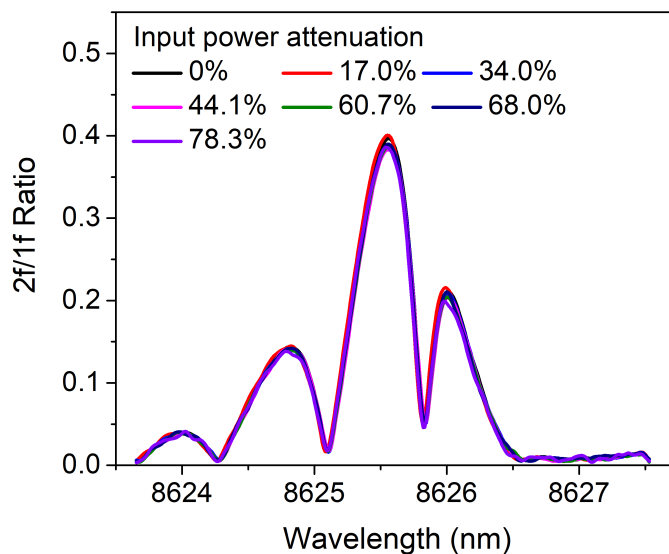
Figure 6.24: R_{2f}/R_{1f} signals obtained at varying input optical powers, showing a complete overlap.

As expected, the R_{1f} signals in figure 6.22 and R_{2f} signals in figure 6.23 reduce in magnitude as a function of reduced optical power. However, the R_{2f}/R_{1f} signal shown in figure 6.24 show a complete overlap, implying the same rate of reduction in the CDAS level with the R_{1f} peak-to-peak signal as the input optical power is attenuated. This highlights the efficacy of the 2f/1f technique for calibration against changes in input power variations.

6.6 The Effect of Changing Flow-Rate on 2f/1f Normalisation

The validity of 2f/1f calibration was tested at increasing 10 % CH_4 gas flow rate through a PAS cell starting from 100 ml/min to 400 ml/min, at increments of 50 ml/min. At each flow rate, R_{1f}, R_{2f} and R_{2f}/R_{1f} signals were acquired after 128 averages using the automated LabVIEW code. During this test, each measurement was taken after 15 mins of waiting time following the change of the flow rate, in order to allow signal stabilisation and to increase accuracy. The figure 6.25, shows peak-to-peak R_{1f}, mean R_{2f}, R_{1fB} and mean R_{2f}/R_{1f} ratio

from this experiment. At high flow rates, the signals are dominated by the noise, hence for these tests mean values were used to represent R_{2f}, R_{1fB} and R_{2f}/R_{1f}, instead of amplitudes.
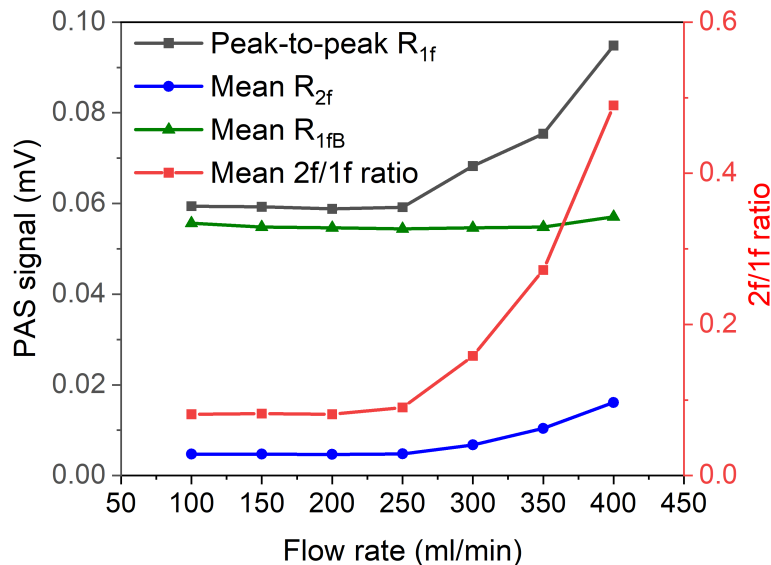
Figure 6.25: Peak-to-peak R_{1f}, mean R_{2f}, mean R_{1fB} and mean R_{2f}/R_{1f} ratio as gas flow rate through the cell was increased from 50 ml/min to 400 ml/min.

As can be seen from the figure 6.25, The peak-to-peak R_{1f}, mean R_{2f}, mean R_{1fB} and R_{2f}/R_{1f} ratio stays relatively stable until 250 ml/min flow rate, which signifies the validity of 2f/1f calibration free PAS technique until this point for increased sample gas flow rates. However, starting from 250 ml/min flow rate, an upward trend in all signals apart from R_{1fB} signal, were observed. For a flow rate increase from 250 ml/min to 400 ml/min, following changes were observed: R_{1f} by 60.2 %, R_{2f} by 236.5 %, R_{1fB} by 4.8 % and R_{2f}/R_{1f} ratio by 444.1 %. This increase R_{1f}, R_{2f} and R_{2f}/R_{1f} signals are due to increased noise which increased the mean value of each signal, however, R_{1fB} signals stayed relatively constant throughout the test. This is due to CDAS signals, as previously shown in figures like 6.10, being given by a DC-offset which results in stable mean levels even when dominated by noise.

The SNR of R_{1f}, R_{2f} and R_{2f}/R_{1f} signals are shown in figure 6.26 below.
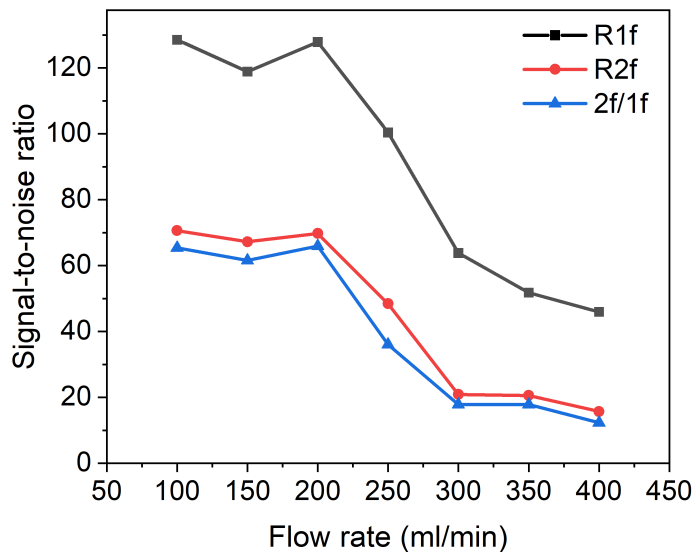
Figure 6.26: Signal-to-noise ratio for R_{1f} , R_{2f} and R_{2f}/R_{1f} ratio as gas flow rate through the cell was increased from 50 ml/min to 400 ml/min.

Figure 6.26 shows a rapid reduction in SNR of R_{1f}, R_{2f} and R_{2f}/R_{1f} signals after flow rate of 200 ml/min, confirming the trend described above for figure 6.25. Prior to 250 ml/min flow rate average SNR of signals are given by: $\sim$ 125.0 for R_{1f}, $\sim$ 69.2 for R_{2f} and $\sim$ 64.3 for R_{2f}/R_{1f} signals. After 250 ml/min a sharp decline in SNR is observed on all signals as the gas flow rate is increased and SNR reductions of 63.26 % in R_{1f} and 77.3 % R_{2f} is observed. This presents another evidence for the turbulence suggestion given above.

Finally, it can also be concluded that, turbulent fluid flow regime likely starts for the cylindrical resonator being used in this study after 250 ml/min flow rate as evidenced from the sharp reduction in SNR and increase in signal noise. Hence, 2f/1f calibration free technique is not applicable at increasing gas flow rates without any compensation procedure.

6.7   Allan-Werle Variance Analysis for 2f/1f

So far, the 2f/1f technique has only been considered with short integration times using up to 128 averages. In order to determine the potential detection sensitivity

and sensor drift for longer integration times, an Allan-Werle variance analysis was performed using a sample gas with 2 % CH_4 in N_2 [131][132]. Using the previously described setup, the sample gas was flowed through the cell at 100 ml/min rate for 4 h. The PXI-DAQ acquisition software was modified to capture 1f, 2f and R_{2f}/R_{1f} signals with a 1.25 Hz sampling rate. The resulting Allan-Werle plots are shown in figure 6.27 showing R_{1f}, R_{2f} and R_{2f}/R_{1f} signals.
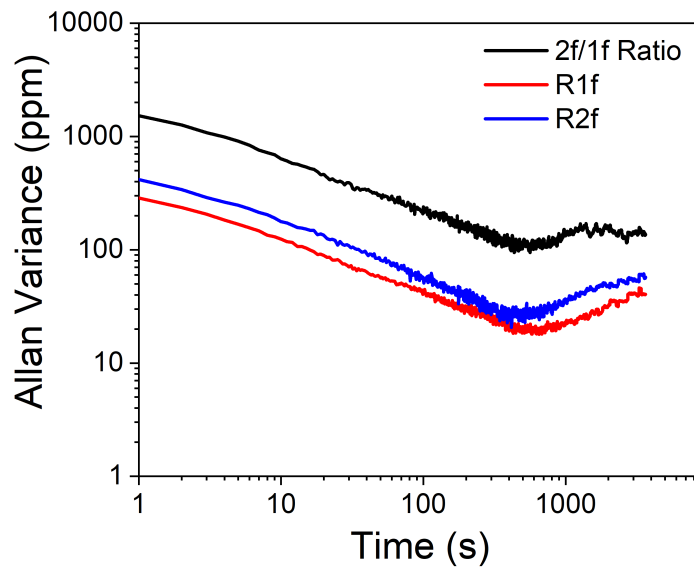
Figure 6.27: Allan-Werle variance plots for R_{1f}, R_{2f} and R_{2f}/R_{1f} measurements. For these plots 2 % CH_4 was flown through a PAS cell at 100 ml/min rate for 4 h, using 1.25 Hz sampling rate.

As shown in figure 6.27, without averaging (t $\sim$ 1), detection limits of 286 ppm for R_{1f}, 416 ppm for R_{2f} and 1523 ppm for R_{2f}/R_{1f} is obtained. For these signals the estimated sensitivities using SO_2 gas are 680 ppb for R_{1f}, 989 ppb for R_{2f} and 3.62 ppm for R_{2f}/R_{1f}. SNR values for these signals were calculated as 443 for R_{1f}, 289 for R_{2f} and 241 for R_{2f}/R_{1f}.

Using averaging, the sensitivity of the measurements can be improved to $\sigma = 18$ ppm at an integration time of $\tau \sim 654$ s for R_{1f}, $\sigma = 25$ ppm at an integration time of $\tau \sim 498$ s for R_{2f} and $\sigma = 98$ ppm at an integration time of $\tau \sim 465$ s for R_{2f}/R_{1f}. Referring back to section 5.3, the estimated sensitivity for SO_2 could be calculated as $\sigma = 43$ ppb for R_{1f}, $\sigma = 59$ ppb for R_{2f} and $\sigma = 232$ ppb for R_{2f}/R_{1f}.

Using 3σ values of 54 ppm for R_{1f}, 75 ppm for R_{2f} and 294 ppm for R_{2f}/R_{1f}, and using P_L of 48.93 mW from figure 5.12 and 260 Hz detection bandwidth at LIA the NNEA values are calculated as follows: 2.51×10^{-9} Wcm^{-1}Hz$^{-1/2}$ for R_{1f}, 3.49×10^{-9} Wcm^{-1}Hz$^{-1/2}$ for R_{2f} and 1.37×10^{-8} Wcm^{-1}Hz$^{-1/2}$ for R_{2f}/R_{1f}.

The NNEA values for R_{1f} and R_{2f} are are both superior compared to NNEA value for the R_{2f}/R_{1f} technique due to combination of noise from both signals. However, this is traded off against the ability to fully calibrate the PAS signals against optical variations and cell performance. The NNEA for the R_{2f}/R_{1f} calibration method represents a value of ~ 5 % superior that for a similar calibration technique using ICLs [78]. The NNEA for R_{2f}/R_{1f} is also a comparable value to NNEA value for fibre-based 3D-printed miniaturised PAS cells with 4.5×10^{-9} Wcm^{-1}Hz$^{-1/2}$ [61].

These results show that R_{1f} is the most sensitive measurement technique compared to R_{1f} and 2f/1f techniques at any averaging time. In addition the results highlights that although 2f/1f measurement is highly useful for calibration in harsh environments, its sensitivity is inferior compared to R_{1f} and R_{2f} detection techniques, as the noise in both harmonics are multiplied together.

6.8   Summary

This chapter is the main experimental results chapter of this thesis, describing the results of 2f/1f calibration free PAS technique. In first part of this chapter, section 6.3, the source of CDAS has been investigated thoroughly. Various competing theories about the origin of this signal in a PAS cell was tested and conclusions were drawn. In section 6.4, the effect of externally changing the CDAS signal on the validity of 2f/1f calibration free technique was investigated. In section 6.5, the PAS sensor being used was characterised with a frequency analysis and in section 6.5.2 the results of the 2f/1f normalisation at different modulation frequencies has been reported. Finally in sections 6.5.3 and 6.5.4, the 2f/1f technique was validated for changing gas concentrations and input light intensities respectively. Finally, the limit of detection of a 2f/1f calibrating sensor was explored using

Allan-Werle variance analysis in section 6.7.

Chapter 7

3D-printed Multigas Measurement Sensor

7.1 Introduction

This chapter presents the fabrication and complete characterisation of single and dual resonator cells at telecommunications wavelength range using fiber optics, designed for single and multi-gas measurements in a compact form for industrial process control. Unlike the gas sensor described in chapters 5 and 6, the dual-resonator cell can be designed with two different resonant frequencies, allowing the measurement of two gas species simultaneously. Further use, in combination with TDLS-WMS and wave division multiplexing using optical fibre components may provide a valuable alternative for gas chromatography. Initially, a single resonator fiber based cell was constructed and characterised to provide a baseline performance for comparison with the dual-resonator cell.

7.2 Fabrication

The design of the single-resonator and double resonator fibre coupled cells are shown in figures 7.1 and 7.2 respectively. The designs presented here are adaptations and optimisations of the design criteria given in chapter 4, for optical

fiber-based laser systems operating in telecommunications range.

As shown in figure 7.1, the single-resonator cell is made up of a 10 mm long cylindrical resonator with 1.8 mm diameter. The dual-resonator cell is made up of two separate cylindrical cells with path lengths of 12 mm and 9 mm, each of 1.8 mm diameter. All other design parameters of these two cells are exactly the same, including the microphone port size (0.74 mm) and wall thickness above microphone (0.25 mm).
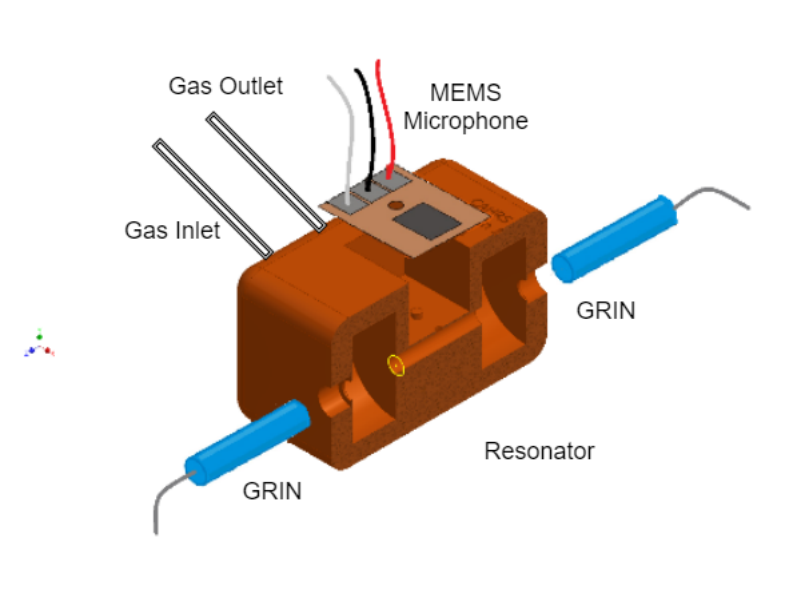
Figure 7.1: Cross-section of the single-resonator sensor.

For dual-resonator cells, there are other designs available in literature such as the designs where both resonators placed at the same location but at different heights sharing two buffer regions on both ends [67]. However, these designs do not allow the use of resonators at different lengths and due to the vicinity of microphones on top and bottom side of the sensor, cross-talk is an issue. For this reason a sequential resonator approach has been selected in this design, where two resonators are placed back-to-back illuminated by the beam sequentially. In this design, due to the large distance between the two resonators and microphones, cross-talk is minimised. However, the overall compactness is sacrificed.
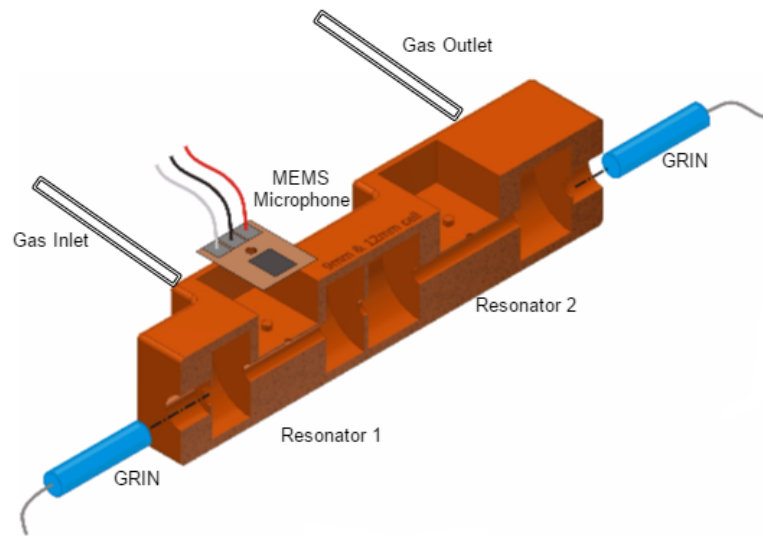
Figure 7.2: Cross-section of the double-resonator sensor.

For the suppression of flow noise and reflected beam noise, $\lambda/4$ buffer volumes were used in both cells on each end of the resonators. In dual-resonator cell two buffer regions in the middle are connected through an inlet to allow laser beam to pass through, for this reason $\lambda/4$ buffer regions must be used on either side for acoustic node formation at the inlet point. The buffer region sizes were calculated using the design criteria in chapter 4. Hence, the single-resonator buffers are given as cylinders with 10.8 mm diameter and 5 mm length, whereas for the dual-resonator the buffer sizes are 10.8 mm diameter and 6 mm or 4.5 mm depending on the resonator in contact with the buffer. Although one buffer region might also be used instead of two between the resonators, the use of two buffer regions maintains the acoustic boundary conditions mentioned in chapter 4, and reduces the overall external and pipe noise at the expense of overall sensor dimensions.

The microphones used in these cells are top-port MEMS invensense/ICS-40181, with high SNR and extended flat frequency response up to 20 kHz. The 3D-printed microphone holders are the same as previously shown in figure 4.9, with an increased thickness for extra strength during the manual soldering process.

The cells were also fabricated using the stereolithography 3D-printer (EnvisionTec/Perfactory-Desktop-Aureus) and R5 acrylic resin [129] using the methodology described in chapter 4. This resin can withstand temperatures up to 150 °C, therefore, the cell could easily be adapted for commercial vehicle exhaust systems.

Unlike the PAS sensors studied in previous chapter, the cells studied in this chapter are fiber optics based. The cells contained two optical input holes with radius 3.55 mm for the insertion of the input and output fiber-coupled single-mode 3.30 mm GRIN lenses (Thorlabs 50-1550A) with 0.25 mm beam radius. The use of fiber optics also allows the use of small diameter resonators due to the reduced beam divergence and by considering the equation 3.13, the reduced cross section leads to an increased PAS signal. However, the 3D-printing constraints make the smaller resonator diameters perform poorly, and the final design does not include reduced diameter resonators.

The GRIN collimators were aligned using kinematic (XYZ) mounts and a total of 6.01 dB loss (including splicing and connectors) was obtained after gluing for the dual-resonator cell. The gluing process of the collimator required cyanoacrylate (Loctite - Black-Tak4105) for fixing and epoxy for gas sealing (Araldite - fusion). Steel piping with 1.6 mm diameter was also fixed with epoxy glue to enable the gas flow. The microphone adapters were secured onto a small cylindrical support extrusion on the cells, held in place with an external support and glued with epoxy.

7.2.1 COMSOL Simulations

Finite element modelling using COMSOL multi-physics was again used to determine the Q-factor and eigenfrequencies of the resonant modes, and the expected amplitude of pressure waves.

The two gas samples available for this study were 100 % CO_2 and 500 ppm CO_2 mixed with N_2. Hence, COMSOL modelling was carried out twice using 100 % N_2 and 100 % CO_2, in order to simulate the effect of different gases on the acoustic

distribution within the resonator. It was assumed that the 500 ppm CO_2 gas mixture would generate the same resonant frequency as 100 % N_2.

The surfaces were modelled as hard boundaries ($\frac{\partial P}{\partial t} = 0$), and the gas inlets were assigned as soft boundaries with zero acoustic pressure ($P = 0$). The fundamental longitudinal resonances are shown in figures 7.3, 7.4, 7.5 and 7.6 below for CO_2 and N_2 gases and for both resonators. In these figures resonator 1 and 2 are defined as the resonators with 12 mm and 9 mm length respectively.
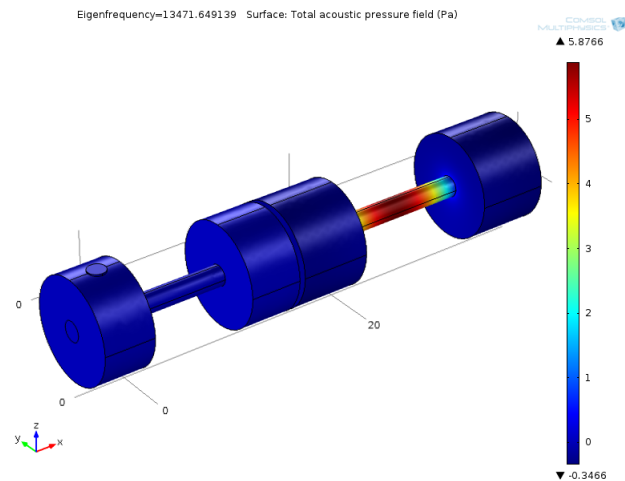
Figure 7.3: Resonator 1 at 13,471 Hz using N_2 at fundamental longitudinal eigenmode.
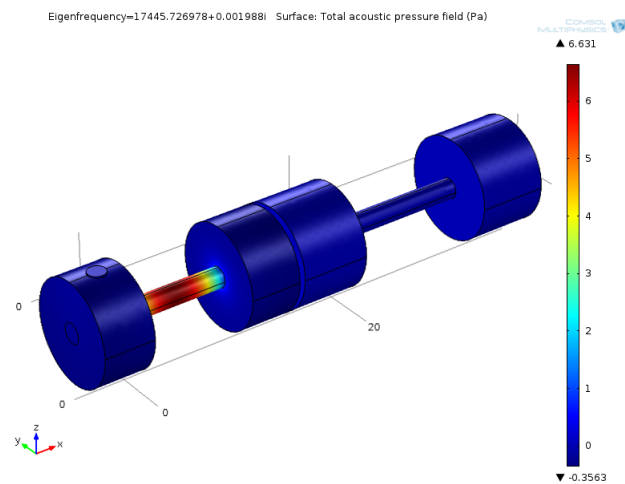
Figure 7.4: Resonator 2 at 17,445 Hz using N_2 at fundamental longitudinal eigenmode.
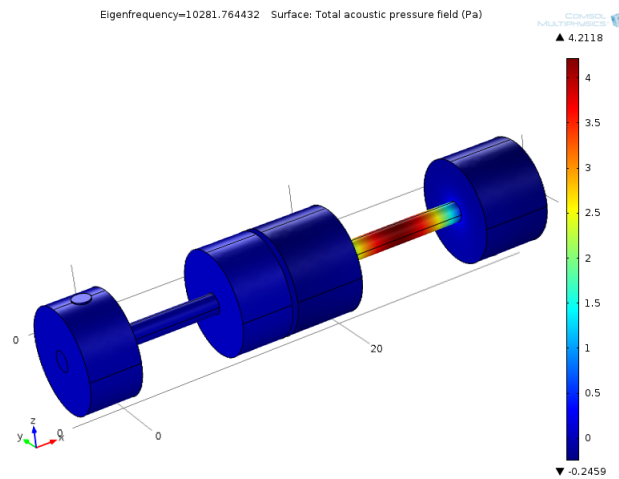
Figure 7.5: Resonator 1 at 10,281 Hz using CO_2 at fundamental longitudinal eigenmode.
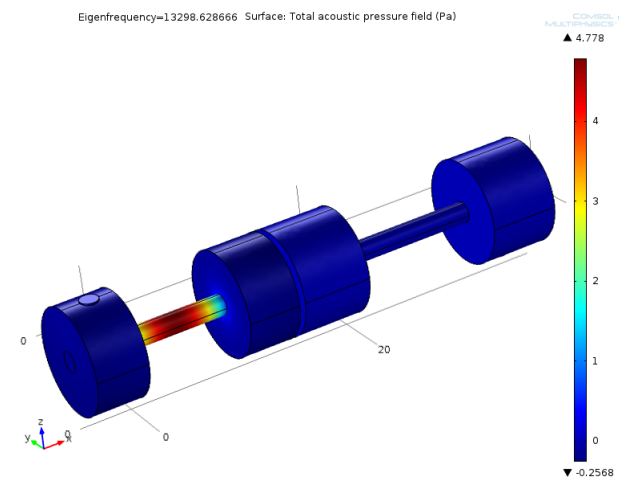
Figure 7.6: Resonator 2 at 13,298 Hz using CO_2 at fundamental longitudinal eigenmode.

Using N_2 gas, the resonances were found to be at 13,471 Hz and 17,445 Hz as shown in figures 7.3 and 7.4. When 100 % CO_2 gas is used, the resonances were found to drop to 10.281 kHz and 13.298 kHz as shown in figures 7.5 and 7.6, which demonstrates the effect of changing overall gas density on resonance frequencies as previously explored in section 3.8.1.

For both gases, parametric frequency analysis was performed with a linear step of 1 Hz from 0 to 20 kHz. The results of these analyses, including the calculated Q-factors for both simulations are shown in figures 7.7 and 7.8 below.
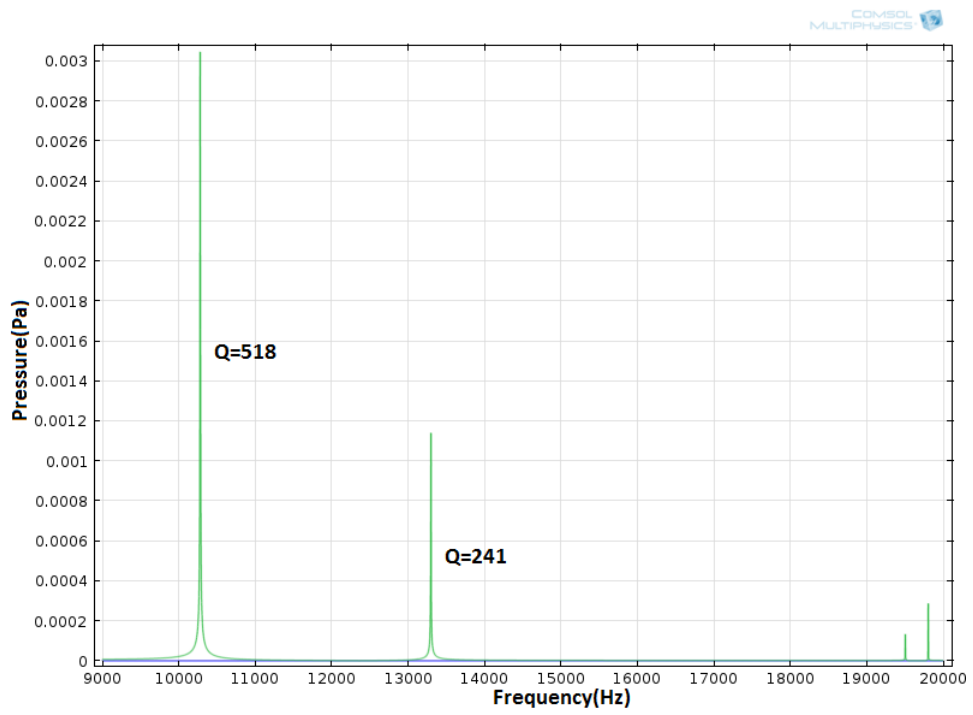
Figure 7.7: Simulated eigenfrequencies for CO_2. Note the appearance of additional peaks between 19,500 Hz and 20,000 Hz, these are due to secondary longitudinal modes in each resonator (002).
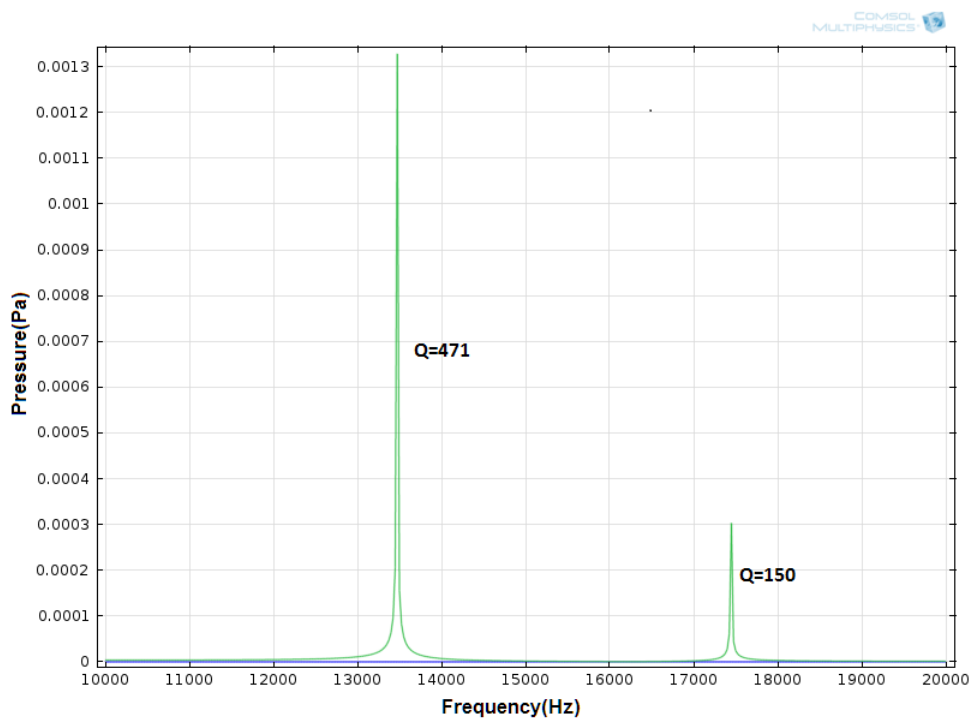
Figure 7.8: Simulated eigenfrequencies for N_2.

As can be seen from the figures 7.7 and 7.8, the resonance frequencies when 100 % CO_2 gas is lower compared to 100 % N_2 gas, due to increased molar mass of the CO_2 molecule. For this reason the appearance of secondary peaks of successive longitudinal modes (002) at higher frequencies can also be seen in figure 7.7.

The Q-factors for 100 % N_2 gas is found as 471 and 150 for resonator 1 and 2 respectively. Similarly for using 100 % CO_2 gas the Q-factors were found as 518 and 241 for resonator 1 and 2 respectively. The Q-factors found above are higher than experimentally expected, as COMSOL surface dampening factors has been excluded due to the complexity of the dual resonator design being considered. Hence in this COMSOL model only Q_v terms are calculated. However, the simulated Q-factors here gives an indication that resonator 1 Q-factor might be $\sim$ 3 times larger than resonator 2 Q-factor. The actual Q-factor values are measured in section 7.5.1. Approximations to the Q-factors can also be obtained by analytical calculations using equations 3.10, 3.11, 3.12 for the total Q-factor, surface Q-factor and volumetric Q-factor respectively. The results of this calculation are shown below in table 7.1.

Table 7.1: Analytical Q-factor calculations. Q_{1T} and Q_{2T} represents resonator 1 and 2 Q-factors respectively.

-	Q_j	CO_2	N_2
	Q_{1s}	33.7	24.4
Resonator 1 (12mm)	Q_{1v}	1,152,477.8	59,686.8
	Q_{1T}	33.7	24.4
	Q_{2s}	37.5	26.9
Resonator 2 (9mm)	Q_{2v}	859,916.2	44,642.9
	Q_{2T}	37.5	29.9

The total Q-factors in table 7.1 are more realistic than COMSOL calculations. As expected from miniaturised cells, surface Q_s terms are dominant over Q_v terms at ambient pressure levels. Similar to the model, the Q_v factor is smaller for resonator 2 than 1. However, the Q_v terms are 4 orders of magnitude larger

than the COMSOL Q-factors, this discrepancy could be due to the definition of the analytical equations for a perfect cylindrical resonator, whereas the real shape also includes the inlets and buffer regions. One of the unmanageable losses, that is ignored from this calculation is the surface roughness due to the layered fabrication procedure which disturbs the signal. The addition of this loss could reduce Q_T as much as a factor of 2 as the roughness exponent is halved [133].

7.3   DFB Laser Characterisation

In this study two DFB lasers (NEL NLK1556STG) have been used with emission centres at 1573 nm and 1569 nm, as the optical source. In this section a complete characterisation of the lasers used in this chapter is presented. The power and wavelength response profiles of the DFB lasers centred at 1569 nm and 1573 nm are shown. Finally, laser tuning coefficients are investigated.

7.3.1   Wavelength - Power Output Characterisation

For wavelength and power characterisation both lasers were analysed using an optical spectrum analyzer (OSA) (Yokogawa AQ6370D). The lasers were operated by both temperature (TEC) (Thorlabs-TED200C) and drive current (LDC) (Thorlabs-LDC205C). Figures 7.10, 7.9, 7.12 and 7.11 show the 1569 nm wavelength and power output, and the 1573 nm wavelength and power output characterisations respectively.

These results were obtained by increasing the resistance on the TEC from 6 kΩ to 20 kΩ with 2 kΩ increments to change temperature of the laser. The resistance R of the TEC, was converted into temperature T using the equation 7.1 given in the data-sheet of the TEC:

$$T = \frac{3970}{ln(\frac{R}{2.124\times10^{-5}})} - 273.15 \tag{7.1}$$

At each temperature setting the injection current to the laser was scanned from

0 mA to 150 mA with 10 mA increments. In addition, more frequent increments (2 mA/step) were used around the laser threshold (15-20 mA) for the accurate determination of the laser's threshold point.

As displayed in figures 7.10 and 7.12 the thermal tuning provides a larger range of wavelength tuning compared to current tuning but with considerably reduced precision. For instance, At 30.9 °C for both lasers a tuning range of 0.8114 nm and 0.4878 nm is obtained for the 1569 nm and 1573 nm lasers respectively, between the threshold and the maximum injection current at 150 mA. On the other hand, at 95 mA injection current for both lasers, a tuning range of 2.98 nm and 3.55 nm are obtained for 1569 nm and 1573 nm lasers respectively, by changing the TEC temperature from 15.6 °C to 43.4 °C. Hence, wavelength-temperature tuning provides 3.67 and 6.1 times higher tuning range than wavelength-injection current tuning for 1569 nm and 1573 nm lasers respectively.
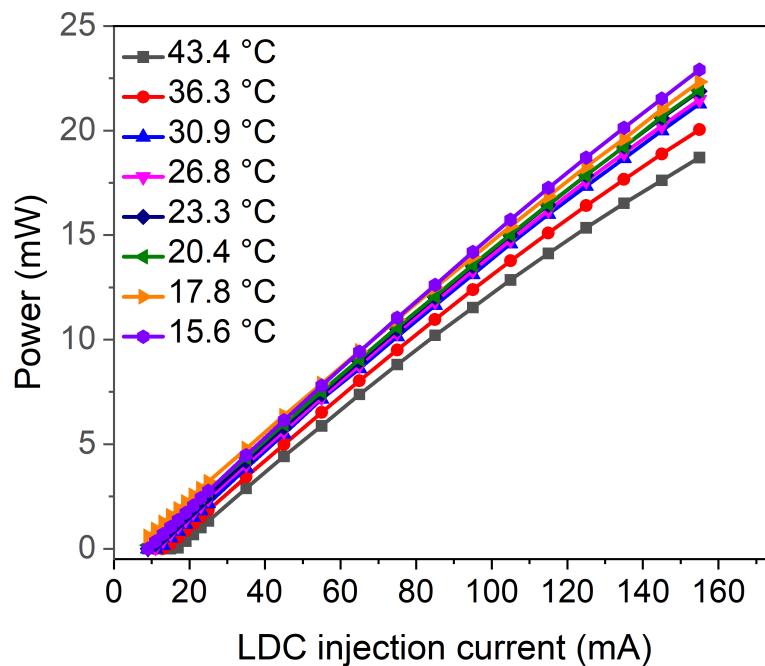
Figure 7.9: Plot showing current versus peak power output for 1569 nm DFB laser. The average slope efficiency is 0.16056 mW/mA.
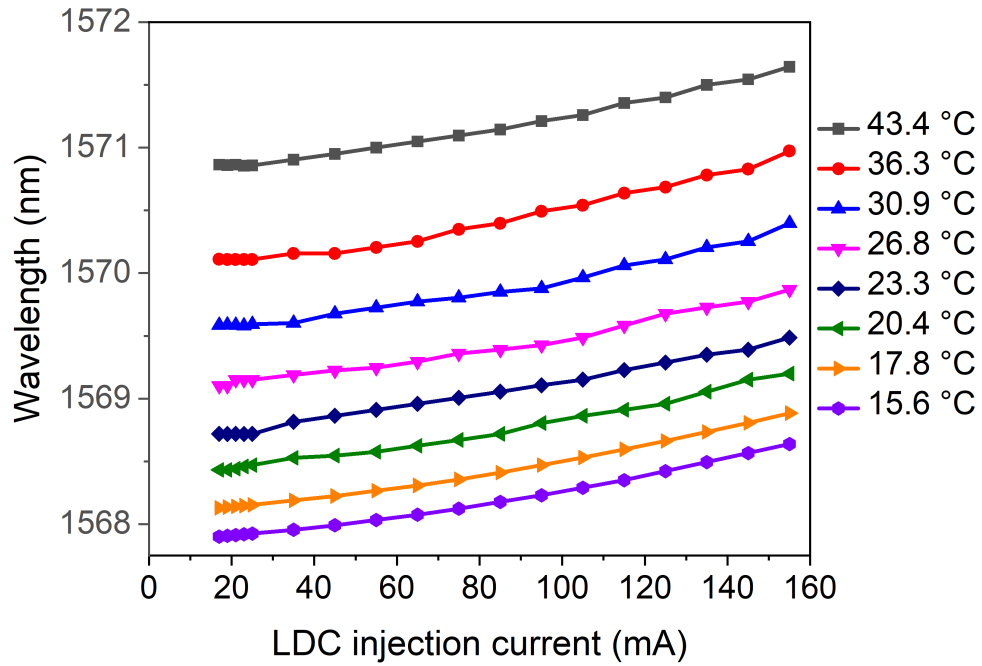
Figure 7.10: Plot showing current versus wavelength output for 1569 nm DFB laser. The average tuning constant is 0.00506 nm/mA.
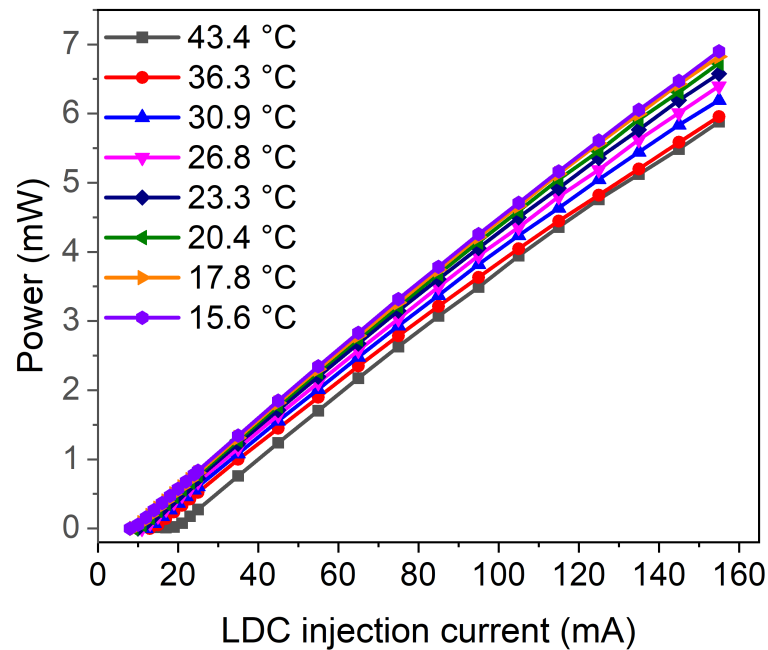
Figure 7.11: Plot showing current versus peak power output for 1573 nm DFB laser. The average slope efficiency is 0.04412 mW/mA.
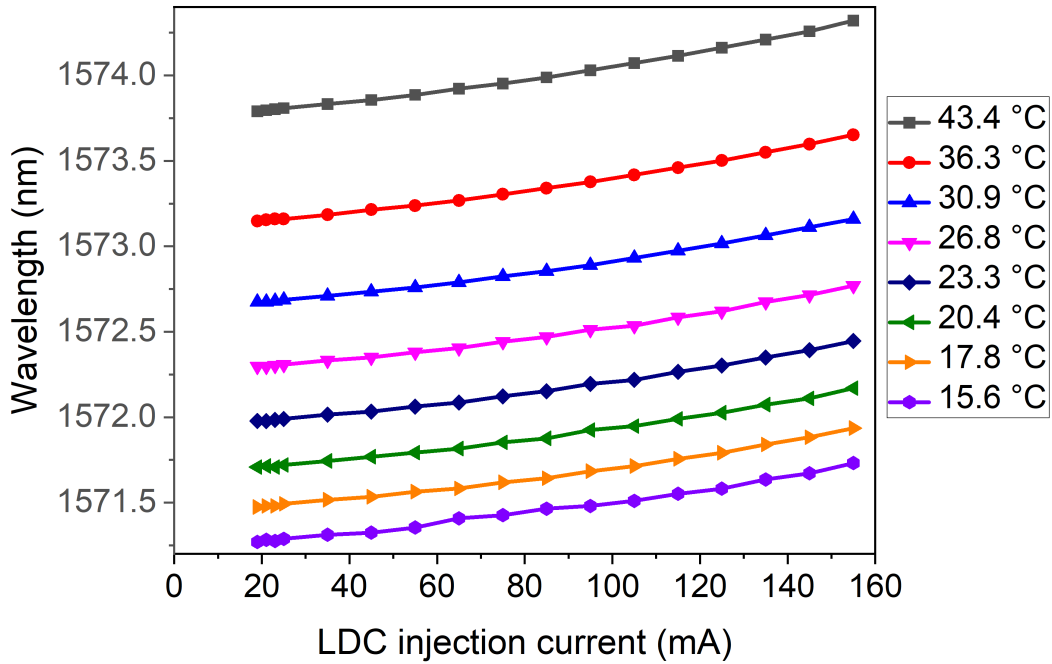
Figure 7.12: Plot showing current versus wavelength output for 1573 nm DFB laser. The average tuning constant is 0.00291 nm/mA.

For power characterisation, as shown in figures 7.9 and 7.11, on average 1569 nm laser provides around ~ 3.4 times more power output than the 1573 nm laser. Unlike the trend in wavelength characterisation above, current tuning provides a larger range of power tuning compared to temperature tuning. The average tuning constants are 0.16056 mW/mA and 0.04412 mW/mA for the 1569 nm and 1573 nm DFB lasers respectively. Due to the higher power output of the 1569 nm laser, it is used for the single-resonator characterisation in the next section of this chapter, as higher power lasers leads to stronger PA signal.

7.3.2 Measuring Tuning Coefficient and Optimum Modulation Voltage for Maximum 1f signal

The lasers tuning coefficient was found using the setup in figure 7.23 and a similar approach previously described in section 5.4.5.

In this setup, the laser was modulated using a high-frequency signal generator (f_r

= 12 kHz around the expected resonances of the cell from analytical calculations) with a bias-tee and it was directly connected to a well-characterised fiber-ring resonator with a 0.4275 GHz FSR. Then by using a photo-diode, the signal was recorded with a oscilloscope. This configuration results in equally spaced N_p number of peaks on the scope screen in one cycle of sinusoidal modulation with V_{pp} amplitude.
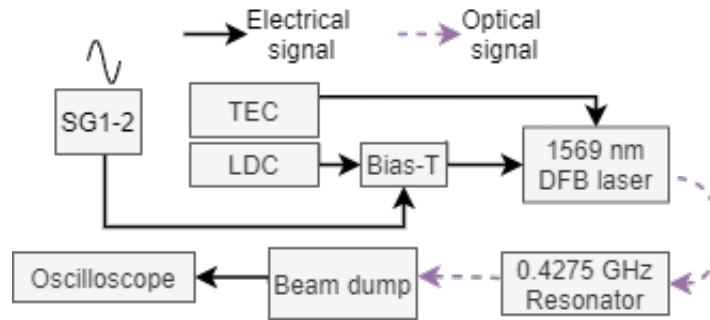
Figure 7.13: Setup for finding the laser tuning coefficient.

The total frequency tuning of a laser for a given drive current is given by $N_p \times FSR = \partial\nu$. By changing the V_{pp} from 0.5 V to 4 V with 0.1 V increments, N_p was recorded and converted into the total frequency tuning, $\partial\nu$ by the relationship above. This results in the plot in figure 7.14.
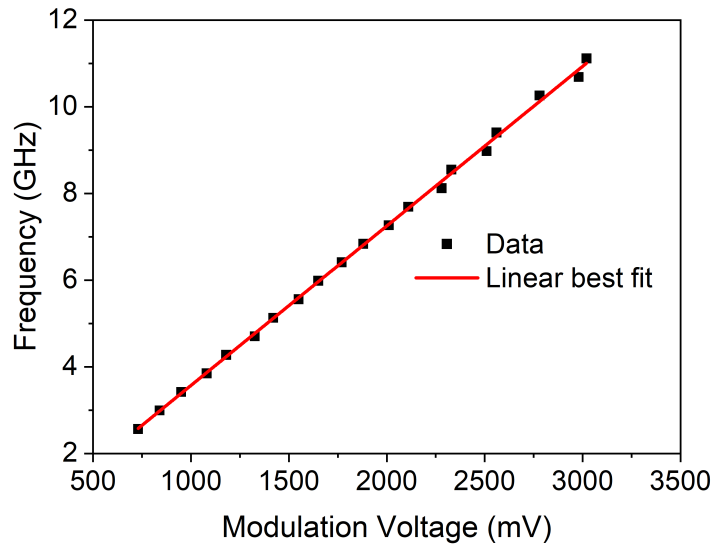
Figure 7.14: Plot showing modulation frequency against peak-to-peak modulation voltage for 1569 nm DFB. The best fit line is given by y = (0.00368)x - 0.11126.

The total tuning rate of a laser, $\frac{d\nu}{dV}$, is found by the equation 7.2:

$$\frac{d\nu}{dV} = \frac{\partial N_p \times FSR}{\partial V_{pp}} \tag{7.2}$$

which represents the slope of the plot in figure 7.14 and it was calculated as 3.680 MHz/mV for the 1569 nm laser.

The modulation voltage at optimum R_{1f} signal, V_{PPmax}, when modulation index m = 2.0 is found by using the equation 7.3 below:

$$V_{PPmax} = \frac{m\gamma}{d\nu/dV_{pp}} \tag{7.3}$$

where m = 2.0, γ is calculated as 6.07 GHz from HITRAN data [94] for the line of interest in figure 7.17 and $\frac{d\nu}{dV}$ is 3.680 MHz/mV from the analysis above. This calculation results in a V_{PPmax} = 3303.1 mV.

The calculated V_{PPmax} was tested by obtaining 1f signals at different V_{pp} amplitudes between 1 V to 4 V with 50 mV increments using LabVIEW - Scopegrab and the data is shown in figure 3.28. During the test 500 ppm of CO_2 was flown through a PA cell at 100ml/min flow rate, targeting line of interest in figure 7.17.
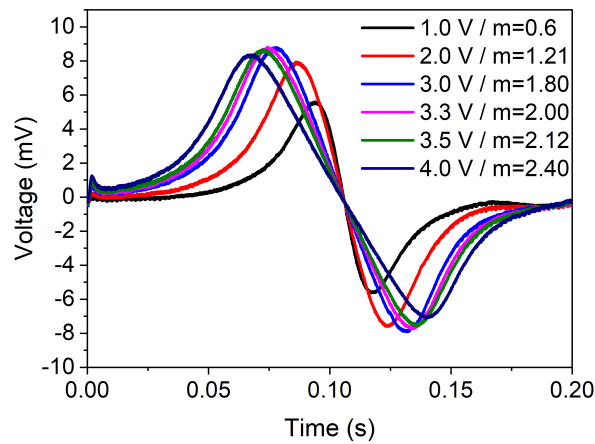
Figure 7.15: The effect of different modulation voltage amplitudes on the R_{1f} signal. As can be seen signal peak and trough drifts apart with increasing voltage, however, the signal they correspond to peaks around 3150 mV.

As shown in the figure 7.15, the signal peak-to-peak is a function of the modulation amplitude and is a maximum between 3 V and 3.3 V. It was found from the measurements that the highest R_{1f} peak-to-peak signal is obtained at a voltage of 3,150 mV, only 4 % higher than the calculated value, confirming the validity of the calculation above.

It is important to note the lack of DC level or CDAS signal in the R_{1f} signals presented in the figure 7.15, compared to R_{1f} in chapters 5 and 6. The difference is due to the use of lasers at NIR-IR wavelengths which are not absorbed as efficiently as MIR lasers and do not generate a solid-PAS signal.

7.4   Single Resonator PAS Cell Characterisation

This section presents the complete characterisation of the single-resonator PAS sensor. The essential system characteristics obtained are the cell's resonant frequency and Q-factor. The operation with a high power L-Band erbium doped fibre amplifier is then discussed and a normalised noise equivalent absorption and the minimum absorbance of the system are calculated. Finally, temporal sensor response as a function of flow was investigated and a response time was found. The figure in 7.16 shows the main experimental setup used for sensor characterisation throughout this section.
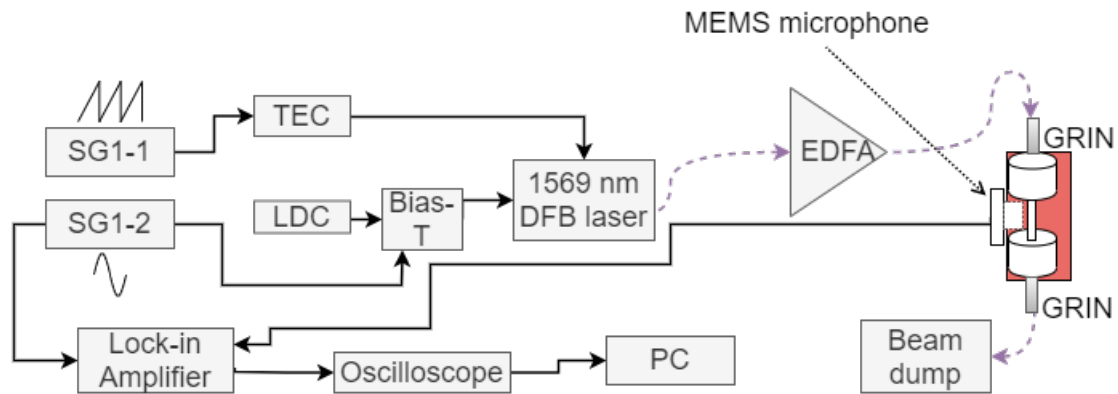
Figure 7.16: Experimental setup for the gas sensing with the single-resonator PAS cell.

The CO_2 line at 1571.105 nm (6364.95 cm^{-1}) was selected as the target gas line for the characterisation process with HWHM $\gamma = 3.035$ GHz. The spectrum

displaying this feature is shown in figure 7.17.
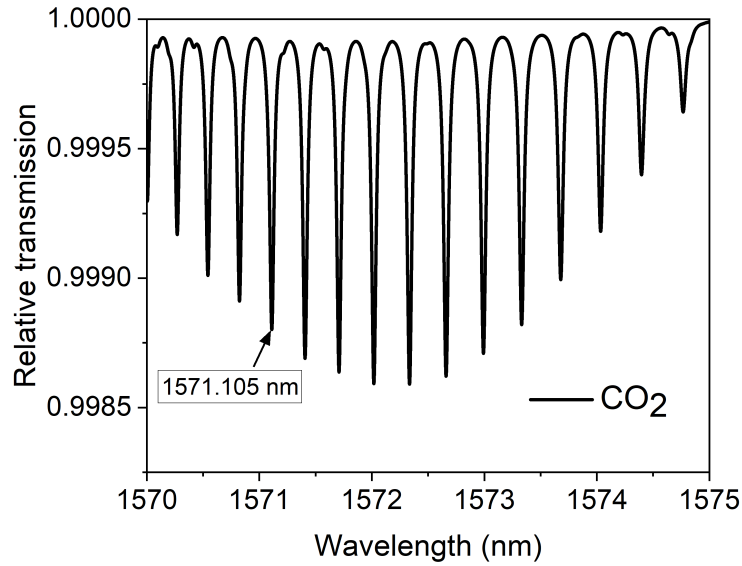
Figure 7.17: 1570-1575 nm spectrum for CO_2 from the simulation of HITRAN 2008. The line of interest at 1571.105 nm (6364.95 cm^{-1}) is marked.

The 1569 nm DFB laser is set to 106.58 mA and 43.4 °C and the wavelength modulation was achieved by using a double modulation scheme by summing a low-frequency ramp (SG1-1) (5 Hz) to sweep the frequency through the absorption feature and high-frequency sinusoidal (SG1-2) (>8 kHz) using a bias-tee as shown in figure 7.16.

7.4.1   Frequency Response Characterisation

The single-resonator sensor's resonant behaviour was investigated using the setup in figure 7.16, using 500 ppm CO_2 mixed with N_2 flown at 100 ml/min flow rate. The modulation frequency was scanned from 8 kHz to 16 kHz with 100 Hz increments and the microphone output was passed to a LIA (time constant = 300 µs) and the 1st harmonic resultant was recorded using LabVIEW via Tektronix scope. Figure 7.18 shows the R_{1f} amplitude as a function of frequency.
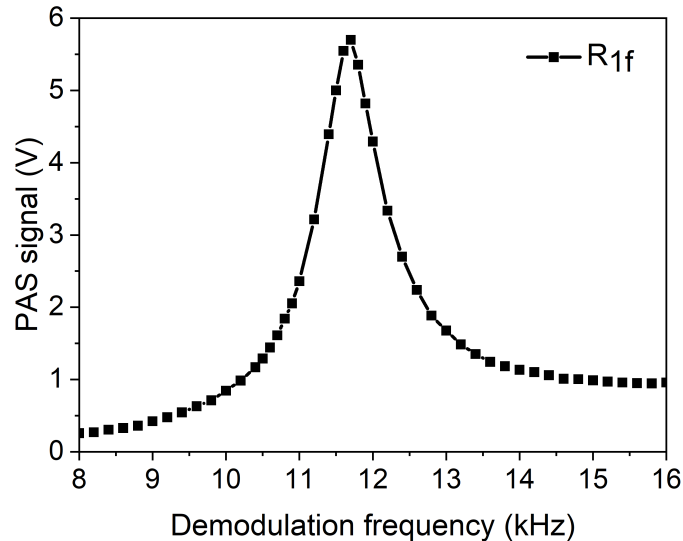
Figure 7.18: Single resonator acoustic response with 500 ppm CO_2 at 100 ml/min flow rate.

From the figure 7.18, the resonance frequency was calculated to be 11.7 kHz and the Q-factor is 10.0. The internal design of the cell being used in this study is a reproduction of a design previously used in other studies [61][66]. The Q-factor calculated in the original work was 15 using 1 % Acetylene (C_2H_2) at 50 ml/min flow rate. The differences in Q-factor can be attributed to use of different sample gas during characterisation as $Q_s \propto \sqrt{f_r}$ as previously provided in chapter 3 and use of different assembly techniques resulting in poorer Q-factor.

7.4.2 Signal Amplification Using Erbium Doped Amplifier

The PA signal dependence on optical power was investigated using the same set-up as previously given in equation 3.1.

For this test, the output power of an L-Band erbium doped fiber amplifier (EDFA) was increased from 15 dBm (31 mW) to its maximum 32 dBm (1.584 W) with 1 dBm steps and the 1f signals were recorded. The peak-to-peak signal magnitudes were obtained and plotted in figure 7.19 as a function of EDFA power in mWs.
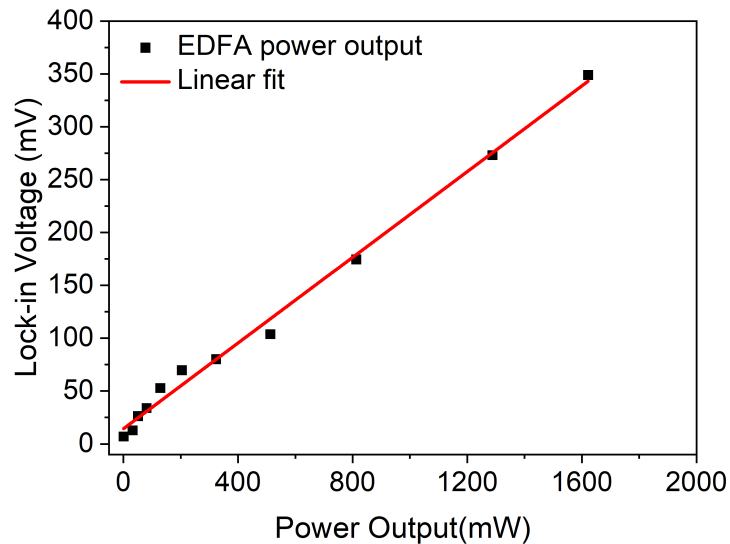
Figure 7.19: The effect of increasing EDFA output on R_{1f} signal amplitude.

As expected from the equation 3.1 and previous studies the increasing power does imply an increase in output acoustic signal [58]. However, the expected linearity is not present and there is a clear variance in the linearity prior to and post 200 mW power output of EDFA.

The shift in linearity is further investigated by calculating the SNR of R_{1f} signals, by calculating the noise using 50 data points between at the beginning of the scan. The plot of SNR versus power is shown in figure 7.20 where the error bars represent the variation of noise in different 50-point sections of the signal.
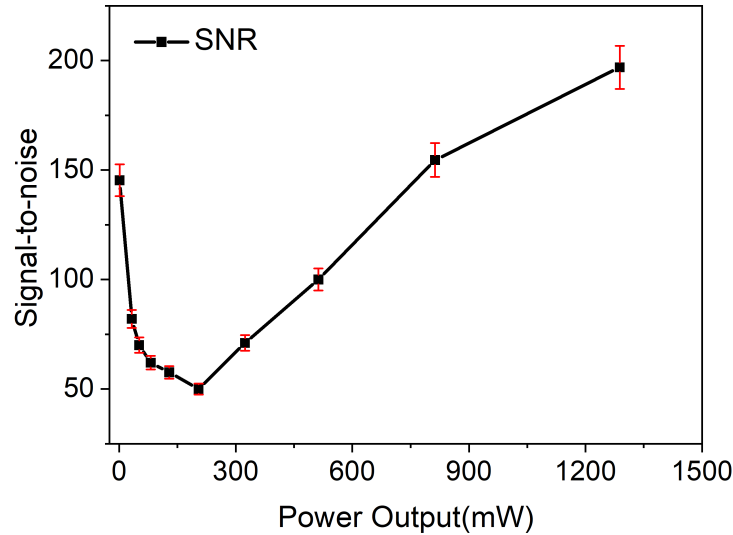
Figure 7.20: The effect of EDFA on the SNR.

As shown in figure 7.20, the use of amplification deteriorates the SNR up to 200 mW, which also coincides with the changing gradient trend observed in figure 7.19. These results could be attributed to several factors such as increased amplified spontaneous emission (ASE) noise, saturation and lowered beam quality up to 200 mW output as suggested by Lindley [134]. In addition, the power of the pump laser could have been lowered for low power output settings, leading to the variable SNR. Hence, when the EDFA is used in this setup, the power output should be set to at least $\sim$ 800 mW, so that the PAS signal SNR is at the level of no amplification.

7.4.3 Allan-Werle Variance Analysis

The detection sensitivity for the single-resonator cell has been determined by performing an Allan-Werle variance analysis using the laser without the EDFA in place. During this analysis the peak-to-peak R_{1f} signal was recorded continuously for an hour with 100 % CO_2 flowing at 100 ml/min for 1 h and the modulation index set to m = 2.0. The resulting plot is shown in figure 7.21, analysed using Matlab code given in appendix D.
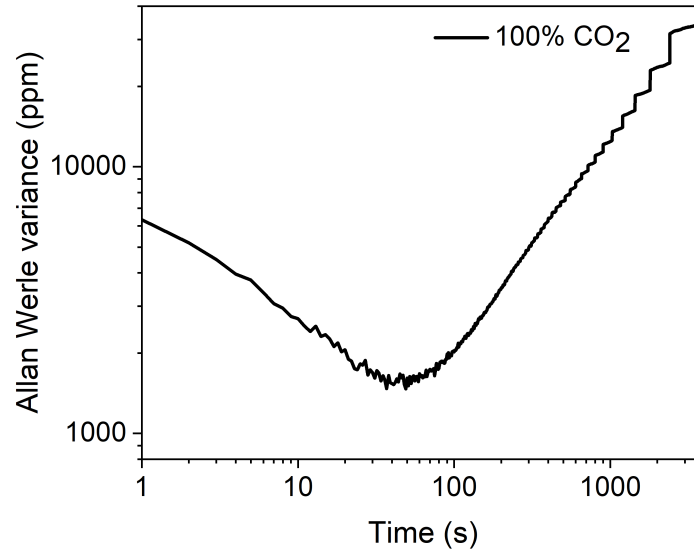
Figure 7.21: Allan-Werle varience plot for the 100 % CO_2 flowing at 100ml/min.

Without any averaging (t $\sim$ 1 s) the single resonator can measure up to 6,663 ppm. Without amplification by EDFA, SNR of the single resonator is calculated as 145. At the optimum integration time of 50 s, $\sigma = 1,533$ ppm can be achieved for the cell, as shown in figure 7.21. Using 3σ value as a more realistic approximation with $\Delta f_{LIA} = 260$ Hz LIA noise bandwidth and 12.85 mW P_L from figure 7.9 according to laser settings given in section 7.4, the NNEA for the single-resonator cell is found, using equation 5.6, as 6.09×10^{-9} $Wcm^{-1}Hz^{-1/2}$. The NNEA and sensitivity calculated here for single-resonator cell will be compared to dual-resonator cell in section 7.5.2.

7.4.4 Step-Wise Flow Rate Response Analysis

As previously discussed in section 3.8.2, at higher flow rate turbulence begins to increase the noise detected at the acoustic element.

To test the immediate effects of increasing gas flow rate on the PAS signals, the response profile of the sensor was determined for a step-wise function of flow rate. This was achieved by turning on the gas flow (100 % CO_2) at a rate of 100 ml/min at 1000th s of the data acquisition for a period of 1000 s. Then turning off the

flow through the main valve for the rest of the 3400 s data acquisition time. The plots for flow rate and PAS signal are shown in figure 7.22 below.
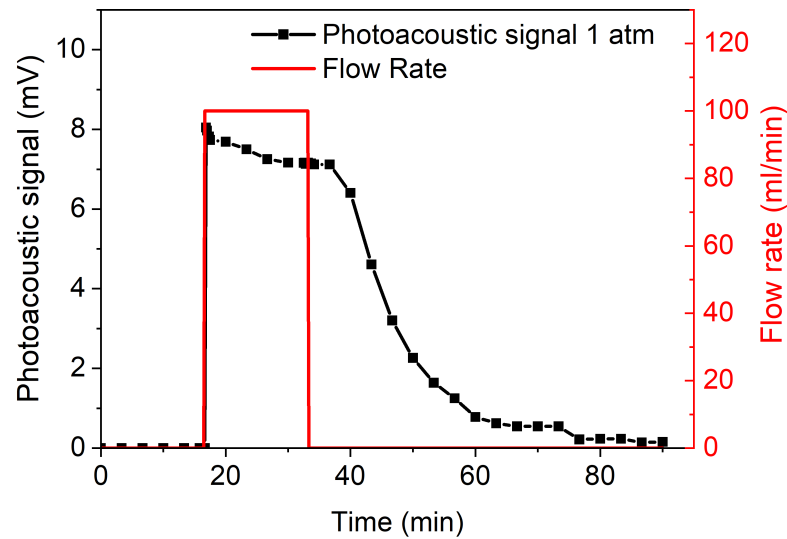
Figure 7.22: Sensor response to a step increase in flow.

As can be seen in figure 7.22, the decay in the signal once flow rate is switched off is the CO_2 diffusing out of the cell to the atmospheric levels. By fitting an exponential decay ($\propto e^{-t/T}$) the time constant for the diffusion was found to be T = 16.8 min. Another interesting feature in the data is the peak in the signal when the flow was initially turned on at t = 16 min, which then decays to a stable level before the gas flow was turned off. The decay constant during the flow period, between t = 16 mins and t = 34 mins, is calculated as T = 9 mins.

To determine the source of this peak and signal decay a number of investigations were carried out. Firstly, the microphone response was measured when using an external loudspeaker set to the 11.7 kHz resonance of the cell. Secondly, the output power of the laser was monitored for 2 h using a photo-diode. Finally, the response of the microphone to a non-resonantly laser modulated signal at a different wavelength was also monitored for potential drift due to heat accumulation within the cell.

It was found that none of these ideas predicted reasons causing the signal drift.

A possible further explanation for the noise could be the high gas flow rate leading to a pressure spike as the valve is turned on. This would be due to the small diameter of the valve inlet radius as compared to the diameter of the flow controller pipework. This could lead to a variable performance of the microphone until it reaches back to a steady case as gas flow rate returns to normal levels. This can be avoided by using a three way valve to ensure the valve opening leads to the pressure spike not interfering with the cell.

Another interesting feature is the signal level being maintained for nearly 2 mins before the onset of decay due to gas leaking. These results are important to shown on why operating PAS sensors on a steady gas state is crucial for a reliable signal.

7.5   Dual-Resonator PAS Cell Characterisation

In this section the dual-resonator cell is characterised in detail in terms of its acoustic properties including its resonant frequency and Q-factor. The cross-talk between the resonators is also investigated, as well as the long term behaviour of the sensor using Allan-Werle variance analysis.

The figure in 7.23 shows the main experimental setup used for the sensor characterisation throughout this section. This experimental design is similar to the experimental setup previously presented for the characterisation of single-resonator cell in figure 7.16, with the addition of the second laser and drive electronics and a 3 dB coupler to combine the outputs.
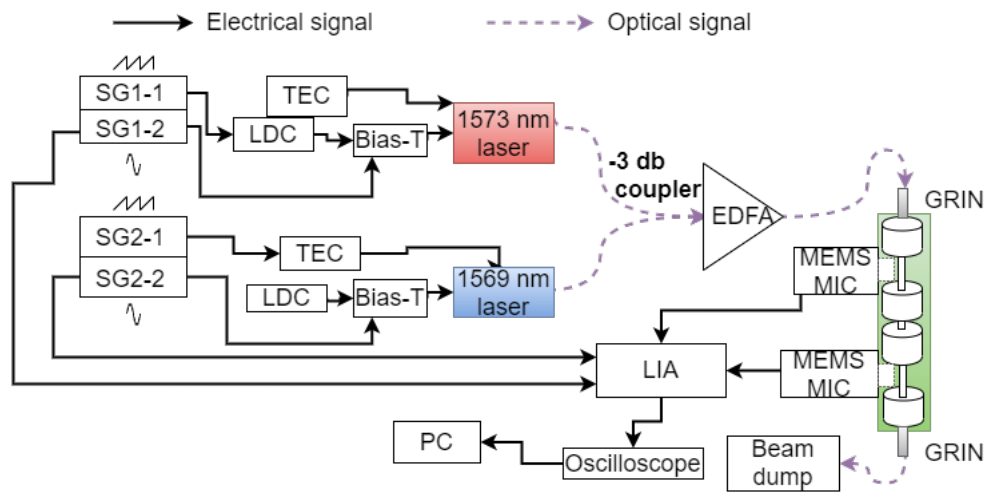
Figure 7.23: Experimental setup for dual-resonator sensor.

Since it is extremely dangerous to use CO even at low concentrations, the spectral line of CO_2 (1571.105 nm) which is closely coinciding with a CO line (1571.605 nm) is excited with the 1569 nm laser, which was also used previously in characterisation of the single-resonator cell in section 7.4. CO_2 was also measured with the isolated spectral line (1573.32 nm) with a HWHM of $\gamma = 3.21$ GHz using the 1573 nm laser as shown in figure 7.24.
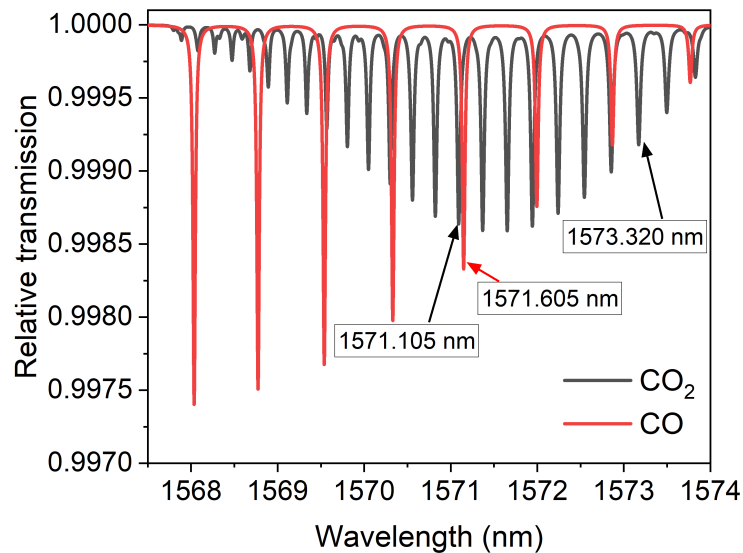
Figure 7.24: Spectrum of CO and CO_2 together. The lines of interest at 1571.105 nm (6364.95 cm^{-1}) and 1573.32 nm (6355.99 cm^{-1}) are marked, as well as CO line at 1571.605 nm aimed to be measured in future tests.

7.5.1   Frequency Response Characterisation

The dual-resonator's resonant behaviour was investigated using the setup in figure 7.16, initially using only 1390 nm DFB laser, targeting ambient water vapour. Both resonators were used to target same H_2O line at 1392.53 nm in a sequential measurement approach, as the modulation frequency is scanned from 8 kHz to 20 kHz with 100 Hz increments. The resulting plots are shown in figure 7.25.
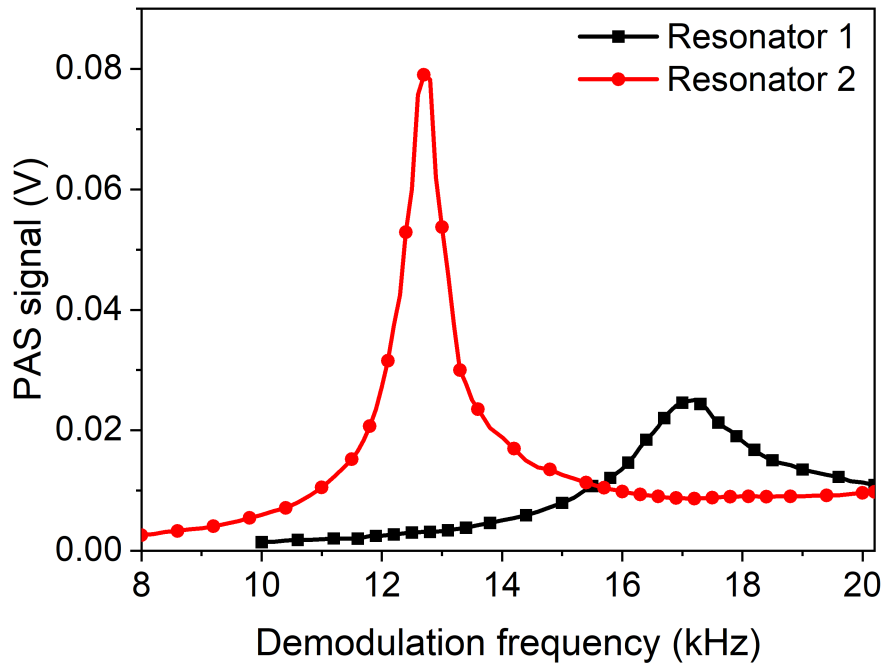
Figure 7.25: Dual-resonator resonance profile for water vapour.

Using ambient water vapour the resonant frequencies were measured as 12.7 kHz and 17.2 kHz for resonators 1 and 2 respectively. The Q-factors for resonators 1 and 2 were found as 15 and 6 respectively.

The resonances of the cell were also found for 100 % CO_2 gas flown at 100 ml/min in a sequential measurement approach, as the modulation frequency is scanned from 8 kHz to 20 kHz with 100 Hz increments. In this arrangement, the 1569 nm laser targeted resonator 1, while the 1573 nm laser targeted resonator 2 with the EDFA output set to 30 dBm. The obtained microphone output was passed to a LIA (time constant = 300 µs) and the R_{1f} signal was recorded using LabVIEW

with a Tektronix scope and recorded. The resulting plots are shown in figure 7.26.
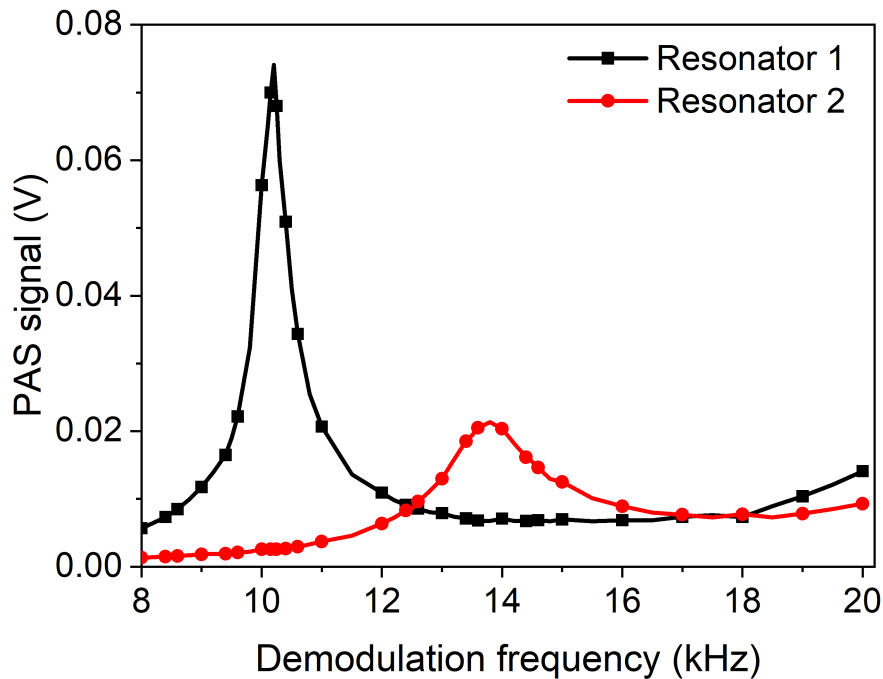
Figure 7.26: Dual-resonator resonance profile for pure CO_2.

As shown in figure 7.26, the resonant frequencies were measured as 10.25 kHz and 13.8 kHz for resonators 1 and 2 respectively. As expected, the Q-factors are the same as the Q-factors found for water vapour as 15 and 6 for resonator 1 and 2 respectively.

Comparing the experimental and COMSOL resonant frequencies for 100 % CO_2, a good quantitative agreement was found. For resonator 1, the modelled values are 0.3 % larger than the experimental values, whereas this percentage is 3.68 % for the resonator 2. However, as expected, the actual Q-factors were found to be significantly lower than expected from figures 7.7 and 7.8. Considering the analytical Q-factor calculations previously given in table 7.1, Q_{2T} was expected 11.3 % higher than Q_{1T}, however, the experimental tests resulted in 60 % Q_{2T} compared to Q_{1T}. In addition, the peak signal in resonator 2 was found as ~ 3.4 times smaller than the peak signal of resonator 1. On the other hand, compared

to the Q-factor of single-resonator cell in section 7.4.1, resonator 1 has exactly the same Q-factor. Hence, the poorer Q-factor and peak signal of resonator 2 compared to analytical calculations, COMSOL simulations, resonator 1 and single-resonator cell indicates an inferior assembly of resonator 2 microphone compared to resonator 1. It is estimated that the microphone in the second resonator was not fitted in as tight as the first, creating a small air gap, which causes an additional Helmholtz loss in the signal. Another reason could be additional surface resin left on the resonator 2 which was not removed properly during the IPA bath.

7.5.1.1   Cross-talk Between Resonators

For simultaneous dual measurement the cross-talk between the resonator microphones must be minimal, if not zero. The measurement of this was conducted by scanning the modulation frequency of the laser through only the resonance peak of each resonator with 100 Hz increments and measuring the signal amplitude on both microphones at m = 2.0 for both lasers. Using the setup given in figure 7.23, the gas used was 100 % CO_2 at 100 ml/min flow rate. Since 1569 nm laser has a larger power output, it was assigned to the resonator 2 for a larger signal output. The plots given in figures 7.27 and 7.28 show the cross-talk of both resonance frequencies.
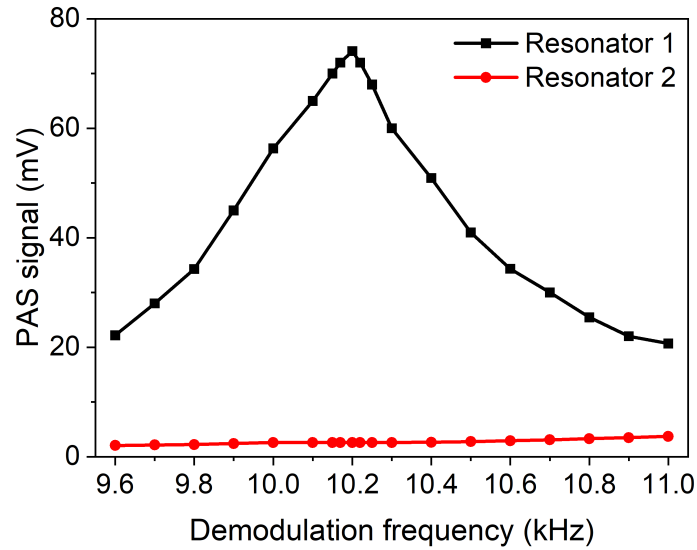
Figure 7.27: Cross-talk between the resonators for 100 % CO_2 flowing at 100 ml/min around the resonance frequency of resonator 1.
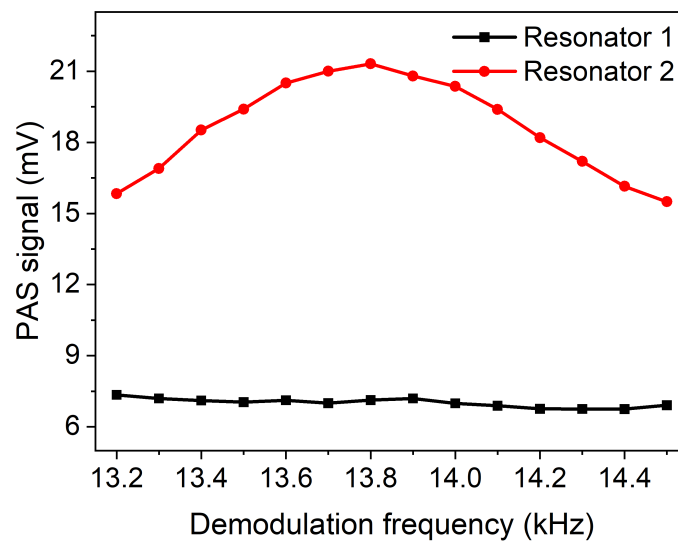
Figure 7.28: Cross-talk between the resonators for 100 % CO_2 flowing at 100 ml/min around the resonance frequency of resonator 2.

In figure 7.27 the cross-talk (the ratio of the signal in the resonator 1 to resonator 2 at resonance) is only 3.5 %. However, as shown in figure 7.28, the cross-talk for resonator 2 is more prominent with 30 %. This is due to the reduced peak signal of resonator 2 compared to resonator 1, previously discussed in section

7.5.1. These results suggests that simultaneous measurement is possible, and longer integration times or changes in the cell design such as attachment of one microphone on the opposite face of the sensor might reduce the cross talk even further [58].

7.5.2 Allan-Werle Variance Analysis for Dual-Resonator Cell

The detection sensitivity for both resonators have been determined by performing an Allan-Werle variance analysis. During this analysis the peak-to-peak R_{1f} signal was recorded continuously at 1 bar 100 % CO_2 flowing at 100 ml/min for 2 h and modulation index is set to m = 2.0.

The setup in figure 7.23 shows that the lasers are amplified to 30 dBm output after passing through a -3 dB coupler. Hence, if one of the lasers is turned off, the power available for the remaining laser is significantly increased. For this reason Allan-Werle variance analysis was performed four times for each resonator: once when both lasers are on, and when the laser targeting the other resonator is turned off. Figure 7.29 shows the Allan-Werle plots for both resonators when the other laser is turned off, called single species measurement mode, analysed using the Matlab code given in appendix D.

Figure 7.30 shows the Allan-Werle plots for both resonators when both lasers are on, called dual species measurement mode, analysed using the Matlab code given in appendix D.
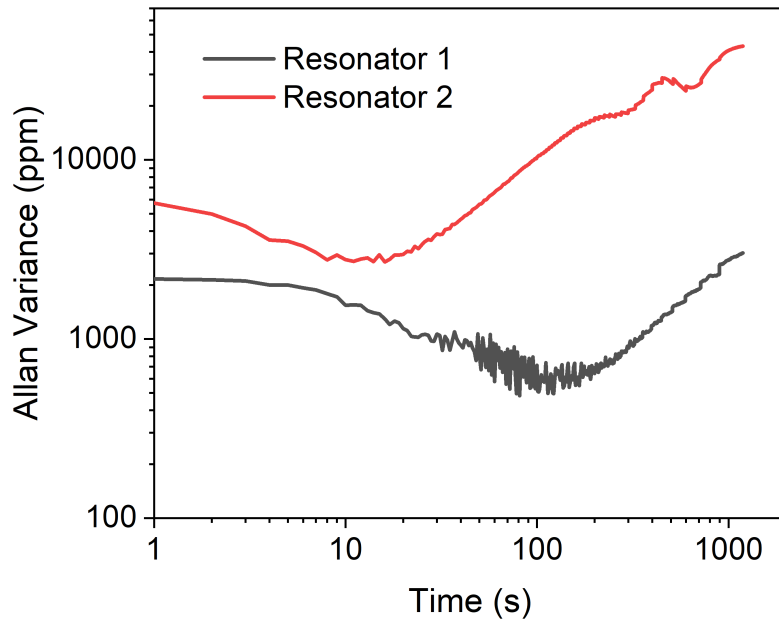
Figure 7.29: Allan-Werle variance plot for the 100 % CO_2 flowing at 100ml/min for single species measurement.
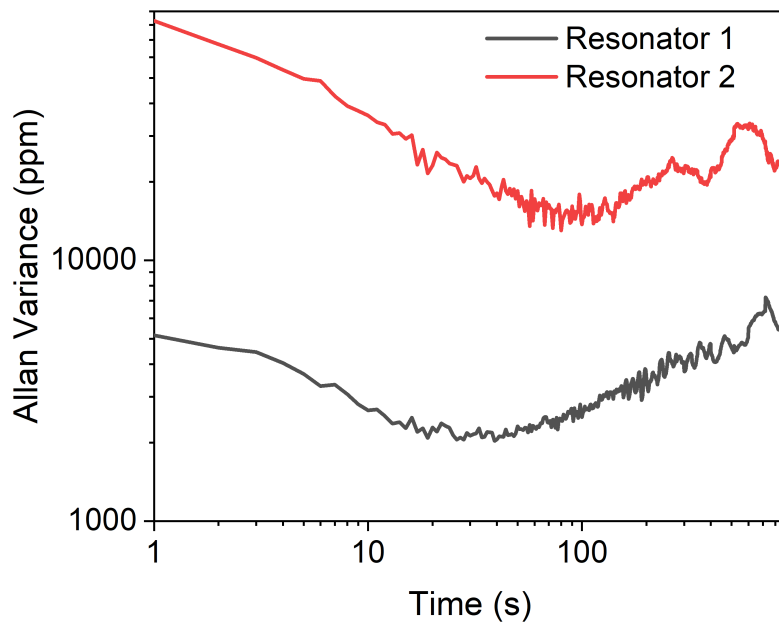
Figure 7.30: Allan-Werle variance plot for the 100 % CO_2 flowing at 100ml/min for multi specie measurement.

The zero averaging and 1σ sensitivities shown in figures 7.29 and 7.30, along with optimum integration times are presented in table 7.2

Table 7.2: Sensitivity for the dual-resonator.

Specie(s)	Resonator#	Sensitivity at $\tau = 1$ s [ppm]	1σ sensitivity [ppm]
Single	1	2,159	482 at 81 s
	2	5,739	2,692 at 10 s
Dual	1	5,156	2,032 at 26 s
	2	82,839	13,008 at 81 s

As shown in table 7.2, for both the dual and single measurement modes resonator 1 has significantly better sensitivity compared to resonator 2. When 1σ values are compared there is 458.5 % and 540.2 % better performance for single and dual measurements respectively at resonator 1 compared to resonator 2. The estimated 1σ sensitivity for CO is calculated as 482.2 ppm and 2,033 ppm for single and dual measurement respectively, using the same measurement settings and resonator 1.

More accurate descriptions of the sensor performance including other system parameters is given by the NNEA, calculated using equation 5.6 with Δf_{LIA}=260 Hz LIA noise bandwidth and presented in table 7.3 along with the input power, P_L.

Table 7.3: NNEA values for the dual-resonator.

Specie(s)	Resonator #	P_L [W]	NNEA [Wcm^{-1}Hz$^{-1/2}$]
Single	1	1	1.45×10^{-7}
	2	1	8.06×10^{-7}
Dual	1	0.249	1.52×10^{-7}
	2	0.751	2.89×10^{-6}

As shown in table 7.3, resonator 1 has a similar performance in both modes of operation with only 4.8 % better performance for single mode operation. However,

258.6 % worsening in resonator 2 performance is observed in dual measurement mode compared to single measurement. This difference could be explained by the detrimental effects of acoustic cross-talk from resonator 1. In addition, the EDFA was assumed to amplify both lasers at the same factor to a total output of 30 dBm. However, in reality the gain often varies as a function of wavelength for EDFAs. Hence, the reduced NNEA of the resonator 2 could be due to the use of a higher P_L used in NNEA calculation, resulting from reduced EDFA output or unaccounted losses for 1569 nm laser connections to -3 dB coupler.

On the other hand, 455.9 % and 1,801.3 % better resonator 1 performance compared to resonator 2 is found for single and dual measurement modes respectively. These results are in line with the expectations, confirming the poorer resonator 2 performance found in sections 7.5.1 and 7.5.1.1.

The NNEA measurements in single measurement mode are 23.9 and 132.3 times lower for resonator 1 and 2 respectively, when compared to single resonator cell in section 7.4.3. The sensitivities presented by the dual resonator could find multiple uses in industry for rough measurements. However, these sensitivities are poorer compared to calibration-free sensor in chapter 6, single-resonator cell and other reported multi-gas techniques reaching 2.4 ppb NH_3 sensitivities using EDFA at 30dBm output [56]. The main reasons for the poorer performance can be listed as: power losses at fiber connections, difficulties in removing internal 3D-printing debris due to intricate design reducing Q-factor, loss of laser power due to divergence particularity for resonator 2 and poor acoustic coupling of microphones with the resonators during the assembly of the dual-resonator cell.

Summary

This chapter presented characterisation of single and dual resonator cells using fiber optics, which enable multi-gas detection in miniaturised PAS cells. The dual-resonator cell can measure two gas species simultaneously presenting a valuable alternative for gas chromatography as a PAS based technique.

ın section 7.2, the fabrication and assembly of single-resonator and double resonator cells are discussed in detail, with particular emphasis on the differences to the cells presented in previous chapter of this thesis. The COMSOL simulations of the dual-resonator cell is given in section 7.2.1, in addition to analytical calculations of the Q-factors using the equations given in chapter 3. In section 7.3, 1569 nm and 1573 nm DFB lasers used in this chapter were characterised in terms of their power and wavelength output characteristics, as well as the tuning coefficients. Single-resonator cell was characterised in section 7.4 including frequency response, amplification of the signal using EDFA, Allan-Werle variance analysis and step-wise flow-rate analysis. Finally in section 7.5, the frequency response, cross-talk between the resonators and Allan-Werle variance analysis for the dual-resonator cell were found.

Chapter 8

Conclusions and Further Work

8.1 Overall conclusions

8.1.1 Project Aims and Objectives

The aim of this project is to develop 3D-printed, miniaturised photoacoustic sensors to measure trace gases for industrial process control and to advance the state art of photoacoustic spectroscopy for gas measurement for real world applications with variable environmental conditions and requirements. The target gas measurements for industrial process control investigated in this work is the measurement of SO_2 gas in desulphurisation process and measurement of CO_2 and CO gases as an alternative to gas chromatography technique.

The initial objectives of this thesis was given in chapter 1, however, these objectives were revised during the work in order to realise the overall aim of the project, which are given as:

- To compare the differences of PAS cells using different types of acoustic sensors: electret-condenser and MEMS microphones.

- To develop a calibration-free CDAS based PAS-WMS technique for various changing gas parameters such as gas concentration, light intensity and flow rate for the detection of SO_2 gas.

- To identify and investigate the source of CDAS signal in first harmonic PA signals which enables 2f/1f calibration in PAS.

- To develop and investigate a fiber optic based dual-resonator PAS cell for measuring two gases simultaneously for detection of CO_2 and CO.

8.1.2 Comparison of Electret-Condenser and MEMS Microphones for PAS

An important challenge during the design and construction phase of new PAS cells is the selection of an acoustic sensor. Due to the availability of large variety of commercial acoustic sensors on the market, the choice of the acoustic sensor is not always trivial. For this reason, in section 5.5 of chapter 5, a through comparison of two microphones often used in PAS: ECM and MEMS microphones were described in detail.

During this comparison, two identical, miniaturised, 3D-printed PAS cells with different microphones were built with minor structural differences to allow attachment of microphones and efficient acoustic coupling. The COMSOL based comparisons of these cells were made prior to construction, by inclusion of the minor structural differences and addition of the larger diaphragm volume of the ECM to the simulation models. The results of the simulation indicated 20.83 % larger signal when MEMS is used with resonant frequencies at $f_r = 10.139$ kHz for MEMS and $f_r = 9.466$ kHz for ECM variant. The Q-factors were found as 20.4 and 24.1 for ECM and MEMS microphone designs respectively.

Despite COMSOL characterisations, experimental results indicates a superior performance from the cell with ECM compared to MEMS. ECM R_{1f} signal was found to be ~ 3 times higher than MEMS, this difference increases to 532.1 % when ECM signals are normalised to the supplier quoted microphone sensitivity of MEMS. The frequency response analysis of both sensors revealed resonant frequencies for ECM and MEMS microphone as 9.55 kHz and 10.35 kHz and the Q-factors were measured to be 12.5 and 8.1 respectively. Finally, the ultimate detection sensitivity of both sensors was compared with Allan-Werle

variance analysis, resulting in $\sigma = 45$ ppm in $\tau \sim 266.4$ s for ECM and $\sigma = 77$ ppm in $\tau \sim 315.2$ s for MEMS. Finally, using 3σ values, Normalized Noise Equivalent Absorption (NNEA) were found as 6.31×10^{-9} Wcm^{-1}Hz$^{-1/2}$ for ECM and 1.07×10^{-8} Wcm^{-1}Hz$^{-1/2}$ for MEMS. Considering the NNEA values given, it was argued that ECM has 70 % superior performance to MEMS microphone in terms of sensitivity within this work, despite ~ 77.5 % higher MEMS microphone sensitivity compared to ECM as quoted by suppliers. The overall inferior performance of the MEMS compared to ECM originates from the difficulties in effective acoustic coupling of the resonator with the diaphragm of the MEMS microphone during the assembly processes. Although larger sizes of ECMs often limit the overall sensor compactness, superior acoustic coupling and better sensor performance can be obtained.

8.1.3 Development of a Calibration-free CDAS Based PAS-WMS Technique

In chapters 3 and 6, theoretical basis and experimental results for the novel calibration-free CDAS based PAS-WMS technique has been presented respectively. In section 3.10, a mathematical CF-PAS-WMS model has been presented by the introduction of a new parameter to PAS-WMS model to account for a newly discovered cell dependent absorption signal generated by the cell fabrication material. The CDAS signal is shown to be similar to residual amplitude modulation in TDLS and can be used as a normalisation term, as evidenced in the 2f/1f technique. Hence, the same normalisation technique can be applied to compensate for optical power drift, system gain and changing environmental parameters.

Firstly, frequency characterisation and normalisation has been presented in section 6.5. It was found that R_{1f}, R_{1fB}, R_{2f} R_{2f}/R_{1f} are all sourced from the same resonant mode of the resonator with Q-Factor and resonant frequency of 6.6 and 9.59 kHz respectively. Then 2f/1f technique was validated by complete overlap of R_{2f}/R_{1f} signals for changing demodulation frequency ± 1600 Hz near

resonance, to represent a change in CH_4 concentration from 0 % to 100 %. In section 6.5.3, 2f/1f technique was tested and confirmed for changing CH_4 concentration from 1 % to 10 % and a linear relationship was found with R^2 = 0.99982, corresponding to a percentage variation of 0.009 % for concentration measurement of SO_2 gas from 0 % to 100 %. Finally, the normalisation technique was tested and confirmed for changing input light intensity, by increasing attenuation of the beam, where a complete overlap and normalisation of R_{2f}/R_{1f} signals were found. Hence, it can be concluded that 2f/1f technique can normalised PAS signals for changing concentration, shift in modulation frequency and variations in input light intensity.

In section 3.8.2, the effect of increasing flow rate on signals was investigated. A stable system operation was observed for flow rates less than 250 ml/min, above this threshold the start of turbulent fluid flow leads to a sharp decline in signal SNR.

Finally, the ultimate detection sensitivity of R_{1f}, R_{2f} and R_{2f}/R_{1f} signals were compared with Allan-Werle variance analysis, resulting in σ = 18 ppm in $\tau \sim$ 654 s for R_{1f}, σ = 25 ppm in $\tau \sim$ 498 s for R_{2f} and σ = 98 ppm in $\tau \sim$ 465 s for R_{2f}/R_{1f} for CH_4 gas. These sensitivities correspond to SO_2 sensitivities of σ = 43 ppb for R_{1f}, σ = 59 ppb for R_{2f} and σ = 232 ppb for R_{2f}/R_{1f}.

Finally, using 3σ values, NNEA values were found as 2.51×10^{-9} $Wcm^{-1}Hz^{-1/2}$ for R_{1f}, 3.49×10^{-9} $Wcm^{-1}Hz^{-1/2}$ for R_{2f} and 1.37×10^{-8} $Wcm^{-1}Hz^{-1/2}$ for R_{2f}/R_{1f}. Although superior NNEA values are obtained for R_{1f} and R_{2f}, R_{2f}/R_{1f} technique is a highly useful method for calibrating signals in harsh environments with a sensitivity 5 % superior to another calibration free technique using QTF's.

8.1.4 Identification of the Source and Properties of CDAS Signals

The calibration-free PAS-WMS technique developed in this work is dependent on the presence of DC offset in R_{1f} called CDAS similar to RAM in TDLS. The source of this signal is investigated using various tests in chapter 6.

The CDAS signal is absent when laser or modulation is turned off, which means it originates from the interaction of the laser beam with sensor components. Firstly, calcium fluoride cell windows were investigated by obtaining PAS signals before and after attachment of windows, which causes a reduction of 5.3 % for R_{1fB} signals. This reduction is caused by absorption of the optical power by the window itself, quoted by the supplier data-sheet as ~ 5 % for the laser wavelength and window thickness, hence windows were eliminated as a potential CDAS source.

Optical absorption by the 3D-printing resin has been investigated by 3D-printing a number of thin discs using two different types of resin and measuring their optical absorption and subsequent acoustic signal generation using 8.65 nm and 5.25 nm QCLs. It was found that resins absorb optical beam exponentially as the disc thickness is increased. For both resins, increased absorption is observed when 8.65 nm QCL was used indicating a possibility that the absorption of 3D-printing polymers increases with increased optical wavelength. In addition during acoustic tests, no acoustic signals were registered from both resins when 5.25 nm QCL was used, supporting this suggestion. On the other hand, attenuation decreased when R11 resin is used with both lasers compared to HTM140 resin indicating that CDAS signal is dependent on the chemical composition of the fabrication material. This was also evidenced in subsequent acoustic tests on same discs, where ~ 67 % lower acoustic signal was registered by the microphone when R11 resin was used. Hence, the origin of the CDAS was established as resin-laser interaction within the cell either by the resonator walls or resonator front end.

The origin of CDAS signal within a PAS cell was investigated by building two PAS sensors: hollow-core cell and 10 mm inlet cell. When laser beam is incident on 10 mm inlet cell, resonator front end receives 43.07 % increased area of laser-resin interaction, which should theoretically lead to an increased CDAS signal, conversely, in hollow-core cell 81 % on the resonator front end area is removed, conversely leading to a reduction of CDAS signal if resonator front end is the source of CDAS. The tests showed 23.9 % CDAS increase for 10 mm inlet cell and 9.5 % CDAS increase for hollow-core cell. The conflicting values

obtained by these tests suggests the variations in signal size likely originates from factors such as: alignment issues, which changes the amount of light absorbed by the resonator walls, or fabrication inconsistencies. Hence, it is concluded that, although a CDAS signal might be created by the resonator front end, it is not detected by the microphone at centre point of the resonator.

Finally, a test was conducted in section 6.4, where the angle, θ, between the resonator plane and the laser beam is increased by the using a mirror mount leading to an increased laser beam interaction with the resonator walls. As a result of this test, a linear relationship between the resin absorption by the resonator walls and CDAS level is obtained with an absorption constant of 1.7 µW/cm, confirming the suggestion that resonator walls are the source of CDAS.

8.1.5 Development of a Fiber Optic Based Dual-Resonator PAS Cell

In chapter 7, a fiber optic based dual-resonator PAS cell is developed and characterised, capable of measuring two gases simultaneously with two resonators, as an alternative to gas chromatography technique for detection of CO and CO_2. Unlike previous chapters, DFB lasers in telecommunications wavelength range were used in this work instead of MIR QCLs.

In section 7.4, a single resonator cell with similar fabrication and assembly procedure to dual-resonator is characterised as a comparative tool to dual-resonator. The resonant frequency and Q-factor of this cell was found as 11.7 kHz and 10 respectively. Subsequently, a linear relationship between the PA signal and power input was found by increasing the power output an EDFA. However, the use of EDFA deteriorates the signal up to 200 mW input, hence it was concluded to only incorporate the EDFA into an experimental setup for power outputs above 800 mW, when SNR is at the same level as no EDFA amplification. The detection sensitivity of the sensor was investigated using Allan-Werle variance analysis leading to a calculation of $\sigma = 1{,}533$ ppm in $\tau \sim 50$ s. Using corresponding 3σ value, NNEA was found as 6.09×10^{-9} $Wcm^{-1}Hz^{-1/2}$.

Finally, the response of the cell to step-wise increase and decrease in target gas flow was investigated, to identify a decay exponential coefficient of 9 mins which is used to find ideal time for gas signal to settle after changing the concentration for future measurements.

In section 7.5, both resonators of the dual-resonator cell were characterised to identify resonant frequency and Q-factors as 10.25 kHz and 15 for resonator 1, and 13.8 kHz and 6 for resonator 2 respectively using 100 % CO_2 gas. The cross-talk between the resonators was measured to confirm the potential for simultaneous measurement of gases, resulting in 3.5 % cross talk in resonator 1 and 30 % cross talk in resonator 2. Finally, the ultimate detection sensitivity of dual resonator was found by performing Allan-Werle variance analysis twice for each resonator once when both lasers are on called dual measurement mode, and again when the laser targeting the other resonator is turned off called single measurement mode. The analysis resulted in 1σ sensitivities of 2,032 ppm at 26s for resonator 1 and 13,008 ppm at 81s for resonator 2 in dual measurement mode. The corresponding NNEA values in dual measurement mode are 1.52×10^{-7} $Wcm^{-1}Hz^{-1/2}$ for resonator 1 and 2.89×10^{-6} $Wcm^{-1}Hz^{-1/2}$ for resonator 2. In single measurement mode, the sensitivity from each resonator improved by 455.9 % and 1801.3 % for resonators 1 and 2 respectively due to more optical power available for each resonator and reduced detrimental effects from cross-talk.

The sensitivities presented by the dual resonator are poorer compared to calibration-free sensor, single-resonator cell and other reported multi-gas techniques, due to power losses at fiber connections, difficulties in cleaning internal structures with 3D-printing, loss of laser power due to divergence and poor acoustic coupling of microphones.

8.1.6   Summary of conclusions

The aims of this thesis were previously identified in section 1.5 of chapter 1, and restated in section 8.1.1 in this chapter. The outcomes related to the aims are summarised in following points below:

- A complete comparison of PAS cells using electret-condenser and MEMS microphones were presented.

- A calibration free 2f/1f based technique was developed for PAS for normalising PAS signal against changes in gas parameters such as gas concentration, light intensity and flow rate.

- The source of CDAS enabling 2f/1f technique in PAS was investigated and determined after through analysis.

- A fiber optic based dual-resonator PAS cell for measuring two gases simultaneously is developed and characterised.

8.2 Further Work

8.2.1 Improving Microphone-resonator Coupling

In chapter 5 comparison of ECM and MEMS microphones for PAS applications were presented. Despite the COMSOL simulated results and supplier quoted sensitivity, ECM was found to have a superior performance compared to MEMS, owing mainly to the more effective acoustic coupling between the resonator and microphone diaphragm.

A method to improve this acoustic coupling could be optimisation of the resonator diameter and length depending on the diaphragm volume and type of microphones, using extensive COMSOL simulations which also incorporates gas flow. This could be achieved by using parametric analysis toolkit of COMSOL, to scan through range of resonator radius and lengths to find optimal resonator length for the microphone being used.

An improvement to the methodology of this comparison test is the development of new assembly techniques to improve the attachment process of the acoustic sensors to the PAS cells such as ability to attach microphones without gluing for potential reusing or external testing. This will allow the use of same PAS cell for comparing different acoustic transducers, in order to the exclude the

effects of fabrication inaccuracies. For further future work, the acoustic sensor comparison could be extended to a comparison of MEMS, ECM, QTFs and optical cantilever based microphones for a more comprehensive comparison of acoustic transducers for PAS. As QTFs and optical cantilever microphones lack conventional diaphragms, a novel PAS sensor ought to be designed for an accurate comparison.

8.2.2 Exploring Different Resonances and Fabrication Materials for 2f/1f Calibration

In section 5 and 6 2f/1f technique was only shown for longitudinal type resonators built by using HTM140 resin. For future work, CDAS generation from wider variety of polymers using Helmholtz or azimuthal resonators could be investigated.

3D-printing companies often supply wide variety of resins for different uses such as: hard plastics, temperature resistant and elastic materials. The CDAS generation from cells built using these different resins could be tested in future for adapting cells for the requirements of certain applications.

As mentioned in chapter 3, both azimuthal and Helmholtz resonators can be used for noise cancelling by placing microphones on the anti-nodes of resonators. As off-centre optical input is required for azimuthal excitation, beam can potentially interact with the resin material in vicinity and lead to generation of a CDAS signal. Similar to longitudinal cells, the thin cylindrical vessels of the Helmholtz resonators allow interaction of resin and optical beam for generation of a CDAS signal. Hence both of these resonators can be tested in future studies to test 2f/1f calibration in conjunction with noise cancelling to improve the sensitivity of R_{2f}/R_{1f} measurements.

8.2.3 Extended Verification for 2f/1f Calibration Technique

In chapter 6, 2f/1f calibration method was tested against changing changing demodulation frequency, gas concentration, light intensity and gas flow-rate. However, in chapter 3, in addition to these factors temperature and pressure were also mentioned as environmental factors effecting resonant frequency of PAS cells, hence changes in these parameters can be tested in future studies to verify 2f/1f calibration technique. As both of these tests might potentially damage the structural integrity of 3D-printed cells and assembly parts, the design must be changed to ensure stability in extreme conditions. The use of thin resin structures could be minimised to avoid melting at high temperatures and CaF_2 window thickness could be increased from 0.5 mm to withstand higher pressures.

A method to test the effect of increased temperature can be encompassing a sensor in insulation material and heating the whole assembly using a heating wire to ensure homogeneous increase in temperature. It is important to include one miniaturised temperature sensor in each buffer region of the cell to monitor temperature real time and ensure maximum temperature does not exceed the quoted maximum operating temperature of the microphone being used. As temperature is increased, gas pressure must be kept fixed at 1 bar by using pressure sensors and gas regulators, to ensure increase in temperature does not lead to increased gas pressure.

For verifying calibration for increased pressure two methods are proposed. One is raising the gas pressure through gas inlets of a sensor while valves on the output from the cell are turned off. However, the increase in pressure will be limited regardless of any design changes to the cell, as higher pressure will lead to structural deformations due to low strength of polymer resin materials. The second option is to place the PAS cell into a stainless steel case with inputs and outputs windows for optical beam and piping for the gas, so that the pressure can be raised to higher levels safely.

8.2.4   Concluding Dual-resonator Cells

In chapter 7, dual-resonator fiber optic cells were developed as an alternative to GC. However, due to the onset of the global pandemic in 2020, the complete characterisation of these sensors could not be finished. In addition, some work presented in this thesis was required to be repeated to ensure validity and improve quality of the results. For future work, the dual gas sensing could be tested for the detection of two different gases in each resonator rather than use of different CO_2 lines and Allan-Werle variance results could be repeated to ensure reliability. The microphone used in this work could be changed to ECM, to improve acoustic coupling at resonators, as outlined in chapter 5 and a design where one buffer region is used between two resonators with exact same length could be tested to further miniaturise the sensor.

8.2.5   On-site   Tests   for   2f/1f   Technique   and Dual-resonator cells

In chapters 5, 6 and 7 the development two sensors: calibration-free and dual-resonator PAS sensors have been presented and characterised in laboratory settings. However, due to challenges presented by the Covid-19 pandemic in 2020, the on-site tests of these sensors had to be cancelled. For future work, these sensors could be tested for the originally aimed on-site applications.

The calibration-free sensor, could be used for the detection of SO_2 gas in desulphurisation process of industrial applications, such as fuel cell plants. For this purpose, more work is required to make the whole setup more compact, all fitted inside a steel-box.

The dual-resonator sensor, could be used for simultaneous detection of CO and CO_2 for applications in fuel cells. The whole setup is required to be miniaturised in an enclosure for any on-site application. However, another type of application could be placing of the PAS sensor in the detection point without any enclosure while optical input and output are delivered using fiber optics to laser and detector located at a remote location.

References

[1] J. Hodkingson and R. P. Tatam, "Optical gas sensing: a review," *Measurement Science and Technology*, vol. 24, no. 1, 2012.

[2] D. Hartley, "The impact of spectroscopy and diagnostics on combustion research," *Journal of Quantitative Spectroscopy and Radiative Transfer*, vol. 40, no. 3, pp. 291–308, 1988.

[3] G. Wysocki, A. A. Kosterev, and F. K. Tittel, "Spectroscopic trace-gas sensor with rapidly scanned wavelengths of a pulsed quantum cascade laser for in situ no monitoring of industrial exhaust systems," *Applied Physics B*, vol. 80, p. 617–625, 2005.

[4] C. Massie, G. Stewart, G. McGregor, and J. R. Gilchrist, "Design of a portable optical sensor for methane gas detection," *Sensors and Actuators B: Chemical*, vol. 113, no. 2, p. 830–836, 2006.

[5] W. Cao and Y. Duan, "Breath analysis: Potential for clinical diagnosis and exposure assessment," *Clinical Chemistry*, vol. 52, no. 5, p. 800–811, 2006.

[6] H. S. Lee, K. Gwee, L. Y. Teng, J. Y. Kang, K. G. Yeoh, A. Wee, and B. C. Chua, "Validation of [13c] urea breath test for helicobacter pylori using a simple gas chromatograph-mass selective detector," *Eur J Gastroenterol Hepatol*, vol. 10, no. 7, pp. 569–572, 1998.

[7] J. Hodgkinson, J. Saffell, J. Luff, J. Shaw, J. Ramsden, C. Huggins, R. Bogue, and C. R., "Gas sensors 1. the basic technologies and applications," *Nanotechnology Perceptions*, vol. 5, pp. 71–82, 2009.

References

[8] L. Menzel, A. A. Kosterev, R. F. Curl, F. K. Tittel, C. Gmachl, F. Capasso, D. L. Sivco, J. N. Baillargeon, A. L. Hutchinson, A. Y. Cho, and W. Urban, "Spectroscopic detection of biological NO with a quantum cascade laser," *Applied Physics B*, vol. 72, no. 7, pp. 859–863, 2001.

[9] R. Capuano, C. A., R. Paolesse, and C. Di Natale, "Sensors for lung cancer diagnosis," *Journal of Clinical Medicine*, vol. 8, no. 2, p. 235, 2019.

[10] G. F. Fine, L. M. Cavanagh, A. Afonja, and R. Binions, "Metal oxide semi-conductor gas sensors in environmental monitoring," *Sensors(Basel)*, vol. 10, no. 6, p. 5469–5502, 2010.

[11] S. M. Kanan, O. M. El-Kadri, I. A. Abu-Yousef, and M. C. Kanan, "Semiconducting metal oxide based sensors for selective gas pollutant detection," *Sensors (Basel)*, vol. 9, no. 10, p. 8158–8196, 2009.

[12] D. Marinov and M. W. Sigrist, "Monitoring of road-traffic emissions with a mobile photoacoustic system," *Photochemical and Photobiological Sciences*, vol. 2, no. 7, p. 774– 778, 2003.

[13] M. Ioannis, S. Elisavet, S. Agathangelos, and B. Eugenia, "Environmental and health impacts of air pollution: A review," *Frontiers in Public Health*, vol. 8, 2020.

[14] I. M. Storm, A. L. Hellwing, N. I. Nielsen, and J. Madsen, "Methods for measuring and estimating methane emission from ruminants," *Animals*, vol. 2, no. 2, pp. 160–183, 2012.

[15] X. Liu, S. Cheng, H. Liu, S. Hu, D. Zhang, and H. Ning, "A survey on gas sensing technology," *Sensors (Basel)*, vol. 12, no. 7, pp. 9635–9665, 2012.

[16] J. Davalle, "Gas detection through the ages." `https://www.ehstoday.com/industrial-hygiene/article/21913604/gas-detection-through-the-ages`, May (Online; Accessed: 26-01-2022).

[17] P. Makoś, P. Andrzej, and B. Grzegorz, "Methods of assaying volatile oxygenated organic compounds in effluent samples by gas

chromatography—a review," *Journal of Chromatography*, vol. 689, no. 1, pp. 143–160, 2019.

[18] E. Jones, "The pellistor catalytic gas detector," in *Solid State Gas Sensors* (P. T. Moseley and B. C. Tofield, eds.), Bristol: Adam Hilger, 1 ed., 1987.

[19] E. Bakker and M. Telting-Diaz, "Electrochemical sensors," *Analytical Chemistry*, vol. 74, no. 12, p. 2781–2800, 2002.

[20] D. E. Williams, "Conduction and gas response of semiconductor gas sensors," in *Solid State Gas Sensors* (P. T. Moseley and B. C. Tofield, eds.), Bristol: Adam Hilger, 1 ed., 1987.

[21] C. Liaud, N. T. Nguyen, R. Nasreddine, and S. Le Calvé, "Experimental performances study of a transportable gc-pid and two thermo-desorption based methods coupled to fid and ms detection to assess btex exposure at sub-ppb level in air," *Talanta*, vol. 127, p. 33–42, 2014.

[22] R. K. Jha, "Non-Dispersive Infrared Gas Sensing Technology: A Review," *IEEE Sensors Journal*, vol. 22, no. 1, pp. 6–15, 2022.

[23] S. Lin, J. Chang, J. Sun, and P. Xu, "Improvement of the detection sensitivity for tunable diode laser absorption spectroscopy: A review," in *State-of-the-Art Laser Spectroscopy and its Applications : Volume II* (Y. Ma, ed.), Frontiers in Physics, 2022.

[24] A. Maity, S. Maithani, and M. Pradhan, "Cavity Ring-Down Spectroscopy: Recent Technological Advancements, Techniques, and Applications," *Analytical Chemistry*, vol. 93, no. 1, pp. 388–416, 2021.

[25] S. Palzer, "Photoacoustic-based gas sensing: A review. sensors," *Sensors (Basel)*, vol. 20, no. 9, p. 2745, 2020.

[26] J. R. P. Bain, *Near Infrared Tunable Diode Laser Spectroscopy for Aero Engine Related Applications*. PhD thesis, University of Strathclyde, 2012.

[27] I. Galli, S. Bartalini, R. Ballerini, M. Barucci, P. Cancio, M. Pas, G. Giusfredi, D. Mazzotti, N. Akikusa, and P. Natale, "Spectroscopic

detection of radiocarbon dioxide at parts-per-quadrillion sensitivity," *Optica*, vol. 3, pp. 385–388, 2016.

[28] M. Mattiello, *Gas Traces Measurement by Photoacoustic Spectroscopy using Helmholtz resonator-based sensors*. PhD thesis, Ecole Polytechnique Federale De Lausanne, 2008.

[29] A. Miklós, S. Schäfer, and P. Hess, "Photoacoustic spectroscopy, theory," in *Encyclopedia of Spectroscopy and Spectrometry* (J. C. Lindon, ed.), pp. 1815–1822, University of Heidelberg Academic Press, 1999.

[30] P. M. Hundt, B. Tuzson, O. Aseev, C. Liu, P. Scheidegger, H. Looser, F. Kapsalidis, M. Shahmohammadi, J. Faist, and L. Emmenegger, "Multi-species trace gas sensing with dual-wavelength QCLs," *Applied Physics B*, vol. 124, no. 108, pp. 1–9, 2018.

[31] R. Cui, L. Dong, H. Wu, W. Ma, L. Xiao, W. Jia, S. Chen, and F. K. Tittel, "Three-dimensional printed miniature fiber-coupled multipass cells with dense spot patterns for PPB-level methane detection using a near-IR Diode Laser," *Analytical Chemistry*, vol. 19, p. 13034–13041, 2020.

[32] T. Tomberg, M. Vainio, T. Hietai, and L. Halonen, "Sub-parts-per-trillion level sensitivity in trace gas detection by cantilever-enhanced photo-acoustic spectroscopy," *Scientific Reports*, vol. 8, no. 1848, 2018.

[33] A. G. Bell, "The Production of Sound by Radiant Energy," *Science*, vol. 2, no. 49, pp. 242–253, 1881.

[34] J. G. Tyndall, "Action of an intermittent beam of radiant heat upon gaseous matter," *Proceedings of the Royal Society of London*, pp. 307–317, 1881.

[35] E. Mercadier, "Sur la radiophonie," *Journal of Physics: Theories and Applications*, vol. 10, pp. 53–68, 1881.

[36] W. H. Preece, "Radiophony," *Journal of the Society of Telegraph Engineers and of Electricians*, vol. 10, pp. 212–231, 1881.

References

[37] W. C. Röntgen, "Ueber töne, welche durch intermittirende bestrahlung eines gases entstehen," *Annals of Physics*, vol. 248, p. 155–159, 1881.

[38] J. W. Strutt (Rayleigh), "The photophone," *Nature*, vol. 23, p. 274–275, 1881.

[39] S. Manohar and D. Razansky, "Photoacoustics: a historical review," *Advances in Optics and Photonics*, vol. 8, pp. 586–617, 2016.

[40] M. L. Veingerov, "A method of gas analysis based on the tyndall-röntgen optico-acoustic effect," *Proceedings of the USSR Academy of Sciences*, vol. 19, pp. 687–688, 1938.

[41] M. L. Veingerov, "Spectrophone - an instrument for investigation of infrared absorption spectra of gases and for quantitative and qualitative spectrum analysis of multi-component gas mixtures [in russian]," *Proceedings of the USSR Academy of Sciences*, vol. 46, no. 182, 1945.

[42] G. Gorelik, "On a possible method of studying the energy exchange time between the different degrees of freedom of molecules in a gas," *Proceedings of the USSR Academy of Sciences*, vol. 54, p. 779, 1946.

[43] P. V. Slobodskaya, "Determination of the energy transfer rate from vibrational to translational molecular motion by means of a spectrophone [in russian]," *Proceedings of the Academy of Sciences of the USSR*, vol. 12, pp. 656–662, 1948.

[44] E. L. Kerr and J. G. Atwood, "The laser illuminated absorptivity spectrophone: A method for measurement of weak absorptivity in gases at laser wavelengths," *Applied Optics*, vol. 7, pp. 915–921, 1968.

[45] L. B. Kreuzer, "Ultralow gas concentration infrared absorption spectroscopy," *Journal of Applied Physics*, vol. 42, p. 2934–2943, 1971.

[46] E. Max and L. G. Rosengren, "Characteristics of a resonant opto-acoustic gas concentration detector," *Optics Communications*, vol. 11, pp. 422–426, 1974.

References

[47] F. G. C. Bijnen, F. J. M. Harren, J. H. P. Hackstein, and J. Reuss, "Intracavity CO laser photoacoustic trace gas detection: cyclic CH4, H2O and CO2 emission by cockroaches and scarab beetles," *Applied Optics*, vol. 35, no. 27, p. 5357–5368, 1996.

[48] S. Schilt, J. P. Besson, L. Thevenaz, and M. Gyger, "Continuous and simultaneous multigas monitoring using a highly sensitive and selective photoacoustic sensor," in *in Conference on Lasers and Electro-Optics*, vol. 2, pp. 1215–1217, 2005.

[49] S. Schilt, L. Thevenaz, M. Nikles, L. Emmenegger, , and C. Huglin, "Ammonia monitoring at trace level using photoacoustic spectroscopy in industrial and environmental applications," *Spectrochimica Acta Part A: Molecular and Biomolecular Spectroscopy*, vol. 60, no. 14, pp. 3259–3268, 2004.

[50] P. L. Meyer and M. W. Sigrist, "Atmospheric pollution monitoring using CO2-laser photoacoustic spectroscopy and other techniques," *Review of Scientific Instruments*, vol. 61, no. 7, pp. 1779–1807, 1990.

[51] M. Szakall, Z. Bozoki, A. Mohacsi, A. Varga, and G. Szabo, "Diode laser based photoacoustic water vapor detection system for atmospheric research," *Applied Spectroscopy*, vol. 58, no. 7, p. 792–798, 2004.

[52] M. D. Silva, A. Miklos, A. Falkenroth, , and P. Hess, "Photoacoustic measurement of N2O concentrations in ambient air with a pulsed optical parametric oscillator," *Applied Physics B-lasers and Optics*, vol. 82, no. 2, p. 329–336, 2006.

[53] Y. A. Bakhirkin, A. A. Kosterev, R. F. Curl, F. K. Tittel, D. A. Yarekha, L. Hvozdara, M. Giovannini, , and J. Faist, "Sub-ppbv nitric oxide concentration measurements using cw thermoelectrically cooled quantum cascade laser-based integrated cavity output spectroscopy," *Applied Physics B*, vol. 82, p. 149–154, 2006.

References

[54] L. R. Narasimhan, W. Goodman, , and C. K. Patel, "Correlation of breath ammonia with blood urea nitrogen and creatinine during hemodialysis," *Proceedings of the National Academy of Sciences of the United States of America*, vol. 98, no. 8, p. 4617–4621, 2001.

[55] S. Gluck, C. Glenn, T. Logan, B. Vu, M. Walsh, and P. Williams, "Evaluation of nox flue gas analyzers for accuracy and their applicability for low-concentration measurements," *Journal of the Air & Waste Management Association*, vol. 53, no. 6, pp. 749–758, 2003.

[56] J. P. Besson, S. Schilt, F. Sauser, E. Rochat, P. Hamel, F. Sandoz, M. Nikles, , and L. Thevenaz, "Multi-hydrogenated compounds monitoring in optical fibre manufacturing process by photoacoustic spectroscopy," *Applied Physics B*, vol. 85, no. 2, p. 343–348, 2006.

[57] I. G. Calasso and M. W. Sigrist, "Selection criteria for microphones used in pulsed nonresonant gas-phase photoacoustics," *Review of Scientific Instruments*, vol. 70, no. 12, pp. 4569–4578, 1999.

[58] J. P. Besson, *Photoacoustic Spectroscopy for Multi-gas Sensing Using Near Infrared Lasers*. PhD thesis, Ecole Polytechnique Federale De Lausanne, 2006.

[59] E. Kluska, P. Gruda, and N. Majca-Nowak, "The Accuracy and the Printing Resolution Comparison of Different 3D Printing Technologies," *Transactions on Aerospace Research*, vol. 2018, no. 2, pp. 75–92, 2018.

[60] A. A. Kosterev, Y. A. Bakhirkin, R. F. Curl, and F. K. Tittel, "Quartz-enhanced photoacoustic spectroscopy," *Optics Letters*, vol. 27, no. 21, pp. 1902–1904, 2002.

[61] R. Bauer, G. Stewart, W. Johnstone, E. Boyd, and M. Lengden, "3d-printed miniature gas cell for photoacoustic spectroscopy of trace gases," *Optics Letters*, vol. 39, no. 16, p. 4796–4799, 2014.

[62] V. Koskinen, J. Fonsen, K. Roth, , and J. Kauppinen, "Progress in

cantilever enhanced photoacoustic spectroscopy," *Vibrational Spectroscopy*, vol. 48, no. 1, pp. 16–21, 2008.

[63] J. P. Waclawek, R. Lewicki, H. Moser, M. Brandstetter, F. K. Tittel, and B. Lendl, "Quartz-enhanced photoacoustic spectroscopy-based sensor system for sulfur dioxide detection using a cw dfb-qcl," *Applied Physics B*, vol. 117, no. 1, 2014.

[64] L. Xiong, W. Bai, F. Chen, X. Zhao, F. Yu, and G. J. Diebold, "Photoacoustic trace detection of gases at the parts-per-quadrillion level with a moving optical grating," *Proceedings of the National Academy of Sciences of United States of America*, vol. 114, no. 28, pp. 7246–7249, 2017.

[65] T. Tomberg, M. Vainio, T. Hieta, and L. Halonen, "Sub-part-per-trillion level detection of hydrogen fluoride by cantilever-enhanced photo-acoustic spectroscopy," *Instrumentation and Detectors*, 2017.

[66] R. Bauer, T. Legg, D. Mitchell, G. M. H. Flockhart, G. Stewart, W. Johnstone, and M. Lengden, "Miniaturized photoacoustic trace gas sensing using a Raman fiber amplifier," *Journal of Lightwave Technology*, vol. 33, no. 18, pp. 3773–3780, 2015.

[67] A. Elia, P. Lugarà, C. Di Franco, and V. Spagnolo, "Photoacoustic Techniques for Trace Gas Sensing Based on Semiconductor Laser Sources," *Sensors (Basel, Switzerland)*, vol. 9, no. 28, pp. 9616–28, 2009.

[68] A. Bismuto, Y. Bidaux, S. Blaser, R. Terazzi, T. Gresch, M. Rochat, A. Muller, C. Bonzon, and J. Faist, "High power and single mode quantum cascade lasers," *Optics Express*, vol. 24, no. 10, pp. 10694–10699, 2016.

[69] J. S. Yu, S. Slivken, A. Evans, S. R. Darvish, J. Nguyen, and M. Razeghi, "High-power $\lambda \sim 9.5$ micron quantum-cascade lasers operating above room temperature in continuous-wave mode," *Applied Physics Letters*, vol. 88, no. 9, 2006.

[70] H. A. Beck, R. Niessner, and C. Haisch, "Development and characterization

of a mobile photoacoustic sensor for on-line soot emission monitoring in diesel exhaust gas," *Analytical and Bioanalytical Chemistry*, vol. 375, no. 8, p. 1136–1143, 2003.

[71] P. L. Meyer and M. W. Sigrist, "Atmospheric pollution monitoring using CO2-laser photoacoustic spectroscopy and other techniques," *Review of Scientific Instruments*, vol. 61, pp. 1779–1807, 1990.

[72] R. Bartlome, M. Kaucikas, and M. W. Sigrist, "Modulated resonant versus pulsed resonant photoacoustics in trace gas detection," *Applied Physics B*, vol. 96, no. 2, pp. 561–566, 2009.

[73] M. Suchenek and T. Starecki, "Pulse measurements of the frequency response of a photoacoustic cell," *International Journal of Thermophysics*, vol. 32, no. 4, 2011.

[74] M. Szakall, A. Varga, A. Pogany, Z. Bozoki, and G. Szabo, "Novel resonance profiling and tracking method for photoacoustic measurements," *Applied Physics B: Lasers and Optics*, vol. 94, no. 4, pp. 691–698, 2009.

[75] J. Saarela, *Gas-Phase Photoacoustic Spectroscopy Advanced Methods for Photoacoustic Detection and Signal Processing*. PhD thesis, Tampere University of Technology, 2011.

[76] A. Kosterev, Y. Bakhirkin, F. Tittel, S. Blaser, Y. Bonetti, and L. Hvozdara, "Photoacoustic phase shift as a chemically selective spectroscopic parameter," *Applied Physics B: Lasers and Optics*, vol. 78, no. 6, pp. 673–676, 2004.

[77] J. Huber, A. Ambs, and J. Wöllenstein, "Miniaturized photoacoustic carbon dioxide sensor with integrated temperature compensation for room climate monitoring," *Procedia Engineering*, vol. 120, pp. 283–288, 2015.

[78] H. Wu, L. Dong, H. Zheng, Y. Yu, W. Ma, L. Zhang, W. Yin, L. Xiao, S. Jia, and F. K. Tittel, "Beat frequency quartz-enhanced photoacoustic

spectroscopy for fast and calibration-free continuous trace-gas monitoring," *Nature Communications*, vol. 8, no. 1, 2017.

[79] Y. Zheng, T. D. Manh, N. D. Nam, M. B. Gerdroodbary, R. Moradi, and I. Tlili, "Optimization of micro knudsen gas sensor for high precision detection of so2 in natural gas," *Results in Physics*, vol. 16, no. 102933, 2020.

[80] Z. Darmastuti, C. Bur, P. Möller, R. Rahlin, N. Lindqvist, M. Andersson, A. Schuetze, and A. L. Spetz, "Sic-fet based so2 sensor for power plant emission applications," *Sensors and actuators B, Chemical*, vol. 194, pp. 511–520, 2014.

[81] C. H. Wu, D. Kang, P. H. Chen, and T. Y. C., "Mems thermal flow actuators," *Sensors and Actuators A: Physics*, vol. 15, no. 241, pp. 135–144, 2016.

[82] T. Zhu, W. Ye, and J. Zhang, "Negative knudsen force on heated microbeams," *Physical Review E*, vol. 84, no. 5, 2011.

[83] J. Nabeth, S. Chigullapalli, and A. A. Alexeenko, "Quantifying the knudsen force on heated microbeams: a compact model and direct comparison with measurements," *Physical Review E*, vol. 83, no. 6, 2011.

[84] M. Sheikholeslami, S. A. Shehzad, Z. Li, and A. Shafee, "Numerical modeling for alumina nanofluid magnetohydrodynamic convective heat transfer in a permeable medium using darcy law," *International Journal of Heat and Mass Transfer*, vol. 127, pp. 614–622, 2018.

[85] M. Sheikholeslami, R. Haq, A. Shafee, Z. Li, Y. G. Elaraki, and T. I., "Heat transfer simulation of heat storage unit with nanoparticles and fins through a heat exchanger," *International Journal of Heat and Mass Transfer*, vol. 135, pp. 470–478, 2019.

[86] C. N. Banwell and E. M. McCash, *Fundamentals of Molecular Spectroscopy*. McGraw–Hill, 4th ed., 1994.

References

[87] W. Demtroeder, *Laser Spectroscopy Vol 1 – Basic Principles.* Springer, 4th ed., 2008.

[88] A. Beiser, *Concepts in Modern Physics.* McGraw-Hill, 6th ed., 2002.

[89] L. S. Rothman, B. A. Jacquemart, D. and, B. D. C., B. M., L. R. Brown, M. R. Carleer, C. Chackerian, K. Chance, L. H. Coudert, V. Dana, V. M. Devi, J. M. Flaud, R. R. Gamache, A. Goldman, J. M. Hartmann, K. W. Jucks, A. G. Maki, J. Y. Mandin, S. T. Massie, J. Orphal, A. Perrin, C. P. Rinsland, M. A. H. Smith, J. Tennyson, R. N. Tolchenov, R. A. Toth, J. V. Auwera, P. Varanasi, , and G. Wagner, "The hitran 2004 molecular spectroscopic database," *Journal of Quantitative Spectroscopy and Radiative Transfer*, vol. 96, no. 2, pp. 139–204, 2005.

[90] N. V. Vitanov, B. W. Shore, L. Yatsenko, K. Böhmer, T. Halfmann, T. Rickes, and K. Bergmann, "Power broadening revisited: theory and experiment," *Optics Communications*, vol. 199, no. 1-4, pp. 117–126, 2001.

[91] S. N. Eberle, "Photoionization of the beryllium atom," Master's thesis, University of Heidelberg, 2013.

[92] J. Binney, *The Physics of Quantum Mechanics.* Oxford University Press, 1st ed., 2013.

[93] A. B. McLean, C. E. J. Mitchell, , and D. M. Swanston, "Implementation of an efficient analytical approximation to the voigt function for photoemission lineshape analysis," *J. Electron Spectroscopy & Related Phenomena*, vol. 69, no. 2, pp. 125–132, 1994.

[94] I. E. Gordon, L. S. Rothman, C. Hill, R. V. Kochanov, Y. Tan, B. P. F., M. Birk, V. Boudon, A. Campargue, K. V. Chance, B. J. Drouin, J. M. Flaud, R. R. Gamache, J. T. Hodges, D. Jacquemart, V. I. Perevalov, A. Perrin, K. P. Shine, M. A. H. Smith, J. Tennyson, G. C. Toon, H. Tran, V. G. Tyuterev, A. Barbe, A. G. Császár, V. M. Devi, T. Furtenbacher, J. J. Harrison, J. M. Hartmann, A. Jolly, T. J. Johnson, T. Karman, I. Kleiner, A. A. Kyuberis, J. Loos, O. M. Lyulin, S. T. Massie, S. N. Mikhailenko,

N. Moazzen-Ahmadi, H. S. P. Müller, O. V. Naumenko, A. V. Nikitin, O. L. Polyansky, M. Rey, M. Rotger, S. W. Sharpe, S. K., E. Starikova, S. A. Tashkun, J. Vander-Auwera, G. Wagner, J. Wilzewski, P. Wcisło, S. Yu, and E. J. Zak, "The hitran2016 molecular spectroscopic database," *Journal of Quantitative Spectroscopy and Radiative Transfer*, vol. 203, pp. 3–69, 2017.

[95] P. Hess, "Resonant photoacoustic spectroscopy," *Physical and Inorganic Chemistry. Topics in Current Chemistry*, vol. 111, 1983.

[96] A. Rosencwaig and A. Gersho, "Theory of the photoacoustic effect with solids," *Journal of Applied Physics*, vol. 47, no. 1, pp. 64–69, 1976.

[97] A. Rosencwaig, "Photoacoustic spectroscopy of solids," *Physics Today*, vol. 28, pp. 23–30, 1975.

[98] S. N. Thakur, "Photoacoustic spectroscopy of gaseous and condensed matter," in *Photoacoustic Imaging - Principles, Advances and Applications* (R. Gharieb, ed.), pp. 1815–1822, IntechOpen, 1 ed., 2019.

[99] S. Barbieri, J. P. Pellaux, E. Studemann, and D. Rosset, "Gas detection with quantum cascade lasers: An adapted photoacoustic sensor based on helmholtz resonance," *Review of Scientific Instruments*, vol. 73, no. 6, p. 2458–2461, 2002.

[100] R. Kastle and M. W. Sigrist, "Temperature-dependent photoacoustic spectroscopy with a helmholtz resonator," *Applied Physics B*, vol. 63, p. 389–397, 1996.

[101] A. Miklos, P. Hess, and Z. Bozoki, "Application of acoustic resonators in photoacoustic trace gas analysis and metrology," *Review of Scientific Instruments*, vol. 72, no. 4, pp. 1937–1955, 2001.

[102] R. D. Kamm, "Detection of weakly absorbing gases using a resonant optoacoustic method," *Journal of Applied Physics*, vol. 47, no. 8, pp. 3550–3558, 1976.

References

[103] B. Baumann, B. Kost, W. M., and H. Groninga, "Modeling and numerical investigation of photoacoustic resonators," in *Modelling and Simulation* (G. Petrone and G. Cammarata, eds.), ch. 2, pp. 17–38, IntechOpen, 2008.

[104] A. Miklos and A. L'orincz, "Windowless resonant acoustic chamber for laser photoacoustic applications," *Applied Physics B*, vol. 48, p. 213–218, 1989.

[105] A. K. Y. Ngai, S. T. Persijn, I. D. Linsday, A. A. Kosterev, P. Grob, C. J. Lee, S. M. Cristescu, F. K. Tittel, K. J. Boller, and F. J. M. Harren, "Continuous wave optical parametric oscillator for quartz-enhanced photoacoustic trace gas sensing.," *Applied Physics B*, vol. 89, p. 123–128, 2007.

[106] V. Spagnolo, A. A. Kosterev, L. Dong, R. Lewicki, and F. K. Tittel, "No trace gas sensor based on quartz-enhanced photoacoustic spectroscopy and external cavity quantum cascade laser," *Applied Physics B*, vol. 100, p. 125–130, 2010.

[107] C. B. Hirschmann, J. Lehtinen, J. Uotila, S. Ojala, and R. L. Keiski, "Sub-ppb detection of formaldehyde with cantilever enhanced photoacoustic spectroscopy using quantum cascade laser source," *Applied Physics B*, vol. 111, no. 4, p. 603–610, 2013.

[108] F. J. M. Harren and S. Cristescu, "Photoacoustic spectroscopy in trace gas monitoring," in *Encyclopedia of Analytical Chemistry* (R. Meyers, ed.), John Wiley & Sons, 2019.

[109] M. M. J. W. van Herpen, A. K. Y. Ngai, S. E. Bisson, J. H. P. Hackstein, E. J. Woltering, and F. J. M. Harren, "Optical parametric oscillator-based photoacoustic detection of co2 at 4.23 μm allows real-time monitoring of the respiration of small insects," *Applied Physics B*, vol. 82, p. 665–669, 2006.

[110] P. Patimisco, G. Scamarcio, F. K. Tittel, and V. Spagnolo, "Quartz-enhanced photoacoustic spectroscopy: A review," *Sensors (Basel)*, vol. 14, no. 4, pp. 6165–6206, 2014.

References

[111] S. Schilt, A. A. Kosterev, and F. K. Tittel, "Performance evaluation of a near infrared qepas based ethylene sensor," *Applied Physics B*, vol. 95, no. 4, p. 813–824, 2008.

[112] J. Mulqueen, "Electret Condenser (ECM) vs MEMS Microphone." `https://forum.digikey.com/t/electret-condenser-ecm-vs-mems-microphone/447/`, 2017. Online; accessed 07.11.2019.

[113] M. Tavakoli, M. Taheri, A. Tavakoli, and H. Saghafifar, "Design, simulation and structural optimization of a longitudinal acoustic resonator for trace gas detection using laser photoacoustic spectroscopy (lpas)," *Optics & Laser Technology*, vol. 42, no. 5, pp. 828–838, 2010.

[114] M. E. Webber, M. B. Pushkarsky, and C. Patel, "Ultra-sensitive gas detection using diode lasers and resonant photoacoustic spectroscopy," *Proceedings of SPIE - The International Society for Optical Engineering*, vol. 4817, no. 11, pp. 4811–17, 2002.

[115] L. C. Philippe and R. K. Hanson, "Laser diode wavelength- modulation spectroscopy for simultaneous measurement of temperature, pressure, and velocity in shock-heated oxygen flows," *Applied Optics*, vol. 32, no. 30, p. 6090–6103, 1993.

[116] S. Schilt, L. Thevenaz, and P. Robert, "Wavelength modulation spectroscopy: combined frequency and intensity laser modulation," *Applied Optics*, vol. 42, no. 33, p. 6728–6738, 2003.

[117] J. A. Silver, "Frequency-modulation spectroscopy for trace species detection: theory and comparison among experimental methods," *Applied Optics*, vol. 31, no. 6, p. 707–717, 1992.

[118] P. Kluczynski and O. Axner, "Theoretical description based on fourier analysis of wavelength-modulation spectrometry in terms of analytical and background signals," *Applied Optics*, vol. 38, no. 27, pp. 5803–5815, 1999.

References

[119] J. Reid and D. Labrie, "Second-harmonic detection with tunable diode lasers - comparison of experiment and theory," *Applied Physics B*, vol. 26, no. 3, pp. 203–210, 1981.

[120] J. Liu, J. Jeffries, and R. Hanson, "Large- modulation-depth 2f spectroscopy with diode lasers for rapid temperature and species measurements in gases with blended and broadened spectra," *Applied Optics*, vol. 43, no. 45, p. 6500–6509, 2005.

[121] K. Duffin, *Development of Robust Calibration Algorithms for Gas Detection in Harsh Industrial Environments*. PhD thesis, University of Strathclyde, 2007.

[122] J. R. P. Bain, W. Johnstone, K. Ruxton, G. Stewart, and M. Lengden, "Recovery of absolute gas absorption line shapes using tunable diode laser spectroscopy with wavelength modulation—part i: Theoretical analysis," *Lightwave Technology, Journal of*, vol. 29, no. 6, pp. 811–821, 2011.

[123] G. B. Rieker, J. B. Jeffries, and R. K. Hanson, "Calibration-free wavelength-modulation spectroscopy for measurements of gas temperature and concentration in harsh environments," *Applied Optics*, vol. 48, no. 29, pp. 5546–5560, 2009.

[124] E. Nodov, "Optimization of resonant cell design for optoacoustic gas spectroscopy (h-type)," *Applied Optics*, vol. 17, pp. 1110–1119, 1978.

[125] EnvisionTEC, "Htm 140 v2 datasheet." `https://envisiontec.com/3d-printing-materials/prototyping/htm140/`. [Online; accessed 01.01.2022].

[126] J. Trägårdh, K. Macrae, C. Travis, R. Amor, G. Norris, S. H. Wilson, G. L. Oppo, and G. McConnell, "A simple but precise method for quantitative measurement of the quality of the laser focus in a scanning optical microscope," *Journal of Microscopy*, vol. 259, no. 1, pp. 66–73, 2015.

[127] L. Liu, H. Huan, X. Zhang, L. Zhang, X. Shao, A. Mandelis, and

References

L. Dong, "Laser induced thermoelastic contributions from windows to signal background in a photoacoustic cell," *Photoacoustics*, vol. 22, no. 100257, 2021.

[128] Crystran, "Calcium flouride window datesheet." `https://www.crystran.co.uk/optical-materials/calcium-fluoride-caf2`. [Online; accessed 01.01.2022].

[129] Envisiontec, "R5/r11 resin datasheet." `http://envisiontec.com/envisiontec/wp-content/uploads/MK-MTS-R5R11-V01-FN-EN.pdf`. [Online; accessed 01.01.2022].

[130] A. J. McGettrick, K. Duffin, W. Johnstone, G. Stewart, and D. G. Moodie, "Tunable Diode Laser Spectroscopy With Wavelength Modulation: A Phasor Decomposition Method for Calibration-Free Measurements of Gas Concentration and Pressure," *J. Lightwave Technol.*, vol. 26, no. 4, pp. 432–440, 2008.

[131] D. Allan, "Statistics of atomic frequency standards," *Proceedings of the IEEE*, vol. 54, no. 2, pp. 221 – 230, 1966.

[132] P. Werle, R. Mücke, and F. Slemr, "The limits of signal averaging in atmospheric trace-gas monitoring by tunable diode-laser absorption spectroscopy (TDLAS)," *Applied Physics B*, vol. 57, no. 2, p. 131–139, 1993.

[133] G. Palasantzas, "Surface roughness influence on the quality factor of high frequency nanoresonators," *Journal of Applied Physics*, vol. 4, no. 103, p. 046106, 2008.

[134] R. E. Lindley, A. M. Parkes, K. A. Keen, E. D. Mcnaghten, and A. J. Orrewing, "A sensitivity comparison of three photoacoustic cells containing a single microphone, a differential dual microphone or a cantilever pressure sensor," *Applied Physics B.*, vol. 86, no. 4, p. 707–713, 2007.

Publications

Journal publications

Accepted

-M. Ilke, R. Bauer, M.Lengden, "*A calibration-free methodology for resonantly enhanced photoacoustic spectroscopy using quantum cascade lasers*, IEEE Sensors Journal, vol. 20, no. 6, pp. 10530-10538, 2020

In preparation

-U. Dwivedi, M. Ilke, M.Lengden, R. Bauer, G. Humphries, "*Performance of 3D Printed Photoacoustic Gas Sensors, and a Comparison with Quartz Enhanced Photoacoustic Spectroscopy*, IEEE Sensors Journal, 2022

-U. Dwivedi, M. Ilke, M.Lengden, R. Bauer, "**A novel 3D Printed Dual-Photoacoustic resonator for multi gas detection in NIR*, IEEE Sensors Journal, 2023

Conference publications

Accepted

-M. Ilke, R. Bauer, M. Lengden, "*Performance of a 3D Printed Photoacoustic Sensor for Gas Detection in Mid-Infrared*, IEEE SENSORS 2017 Conference Proceedings, 2017 ed. Glasgow, pp. 1482 1484, 2017

References

-M. Ilke, R. Bauer, M. Lengden, *"Performance analysis of 3D-printed photoacoustic resonators*, International Conference on Field Laser Applications in Industry and Research, 2018 ed. Assisi, Italy, 2018

-M. Ilke, R. Bauer, M. Lengden, *"Performance of a 3D Printed Photoacoustic Sensor for Gas Detection in Mid Infrared*, IEEE Sensors Summer School on Optical Fibre Sensors, University of Limerick, Ireland, 2018

Appendix A

APPENDIX: Fourier Model for PAS-WMS

```matlab
1   clc;
2   clear all;
3   close all;
4   format long
5
6   methanelines = csvread('CH4_full_hit12.csv');
7   partition = csvread('CH4partitionfunctions.csv'); %Hitran data
8   methanelines = methanelines(82434,:);
9   length = 1000;
10  v = linspace(1156,1163,length);
11
12  dn = 0.2; % GHz of modulation used
13
14  % Test Conditions
15  pressure = 1; %gas pressure
16  L = 18; %length of resonator
17  methane_concentration = 0.1;
18  nitrogen_concentration = 1-methane_concentration;
19
20  total_pressure = pressure*0.986926; %atm
21
22  k = 1.3806503e-23; %Boltzmann
23  M = 16;
24  c = 299792458e2; %speed of light
25  h = 6.626e-34; %Planck constant
26
27  % Defining temperature
28  degreeT = 236;
29  T_0 = 296; % Reference Temperature in Kelvin
30  T_K = 273.15; %0 degrees Celsius in Kelvin
31  T = degreeT+T_K; %Converting to Kelvin
32
33  index1 = find(partition(:,1) == T_0);
34  Q_T0 = partition(index1,2);
35
36  deltaT = abs(partition(:,1)-T);
37  minT = min(deltaT);
38  index2 = find(deltaT == minT);
```

Appendix A. *APPENDIX: Fourier Model for PAS-WMS*

```
39   Q_T = partition(index2,2);
40
41   S1 = 1-exp(-(h*c.*methanelines(1,1))/(k*T));
42   S2 = (1-exp(-(h*c.*methanelines(1,1))/(k*T_0))).^(-1);
43   S3 = S1./S2;
44   S4 = Q_T0./Q_T;
45   S5 = T_0/T;
46   S6 = exp((-h*c*methanelines(1,5)/k)*((1/T)-(1/T_0)));
47
48   S7 = S3.*S4.*S5.*S6;
49   S_T = S7.*methanelines(1,2); %Total linestrength
50   S_T = (7.339e21/T_0).*S_T;
51
52   %**********************************************************************
53    %4.6.1  Gaussian Broadening
54   gammag = 7.1625e-7.*methanelines(:,1).*(T/M)^0.5;
55   air_broadening_parameter = methanelines(:,3).*(T_0/T).^methanelines(:,6);
56   self_broadening_parameter = methanelines(:,4).*(T_0/T).^methanelines(:,6);
57
58   % 4.6.4 Lorentzian Broadening
59   gammal = 2*total_pressure.*((air_broadening_parameter*nitrogen_concentration)
60   +(self_broadening_parameter*methane_concentration));
61   gammal = gammal';
62
63   %%%%%%%%%%%%%%%%%%%WMS Fourier Transform Model%%%%%%%%%%%%%%%%%%%%%%%%%%%%%%%%%%%
64   theta_j = ones(20,length);
65   Vfinal_0 = zeros(20,length); %Initialising arrays for the 0th, 1st, 2nd and
66   %3rd order Fourier coefficients
67   Vfinal_1 = zeros(20,length);
68   Vfinal_2 = zeros(20,length);
69   Vfinal_3 = zeros(20,length);
70   Vfinal_4 = zeros(20,length);
71
72   Absorbance = S_T.*total_pressure .*methane_concentration .*L;  %Pressure in bar, gas conc on mole fractio length in cm
73
74   multiplier_1 = linspace(1,1,length);
75   multiplier_1 = ones([1, length]);
76   multiplier_2 = linspace(1,1,20);
77   theta = linspace(0,pi,20);
78   delta = (v- methanelines(1)-(methanelines(6).*total_pressure));
79   theta_j = theta';
80   theta_j = theta_j*multiplier_1;
81
82   delta_j = delta'*multiplier_2;
83   delta_j = delta_j';
84
85   %%%%%%%%%%%%%%%%%%%%%%%%%%%%%%%%%%%%%%%%%%%%%%%%%%%%%%%%%%%%%%%%%%%%%%%%%%%%%
86   delta_nu = linspace(dn,dn,length);
87   delta_nu = delta_nu'*multiplier_2;
88   %%%%%%%%%%%%%%%%%%%%%%%%%%%%%%%%%%%%%%%%%%%%%%%%%%%%%%%%%%%%%%%%%%%%%%%%%%%%%
89   delta_nu = delta_nu';
90
91   i0 = 0.2;%deltaibyi
92   psi_1 = 45/360*pi;
93   %i2 = 0.9;
94   %psi_2 = 150/360*pi;
95   % Defing X parameters
96   XX = zeros(20,length);
97   XX = 2*sqrt(log(2))*(delta_j+delta_nu.*cos(theta_j))./gammag;
98
99   for kk=1:20
100  X=XX(kk,:);
101  Y = (gammal./gammag)*sqrt(log(2));
102  % mcleans  implementation
```

Appendix A. *APPENDIX: Fourier Model for PAS-WMS*

```matlab
103    A = [-1.2150 -1.3509 -1.2150 -1.3509];
104    B = [1.2359 0.3786 -1.2359 -0.3786];
105    C = [-0.3085 0.5906 -0.3085 0.5906];
106    D = [0.0210 -1.1858 -0.0210 1.1858];
107
108    for i = 1:4
109    V_top(i,:)= (C(i)*(Y-A(i)))+(D(i)*(X(:)-B(i)));
110    V_bottom(i,:) = (Y-A(i))^2+(X(:)-B(i)).^2;
111    end
112
113    V = V_top./V_bottom;
114
115    Vfinal_0_exp(kk,:) = exp(-Absorbance.*(2/gammag)*(log(2)/pi)^0.5*sum(V));
116    Vfinal_1_exp(kk,:) = exp(-Absorbance.*(2/gammag)*(log(2)/pi)^0.5*sum(V)).*cos(theta(kk));
117    Vfinal_2_exp(kk,:) = exp(-Absorbance.*(2/gammag)*(log(2)/pi)^0.5*sum(V)).*cos(2*theta(kk));
118    Vfinal_3_exp(kk,:) = exp(-Absorbance.*(2/gammag)*(log(2)/pi)^0.5*sum(V)).*cos(3*theta(kk));
119    Vfinal_4_exp(kk,:) = exp(-Absorbance.*(2/gammag)*(log(2)/pi)^0.5*sum(V)).*cos(4*theta(kk));
120    % v_trap(kk) =  trapz(v,Vfinal_1(kk,:));  % to see if normalised to 1.
121     end
122
123    H0_exp = (1./(pi)).*trapz(theta,(Vfinal_0_exp));
124    H1_exp = (2./(pi)).*trapz(theta,(Vfinal_1_exp));
125    H2_exp  = (2./(pi)).*trapz(theta,(Vfinal_2_exp));
126    H3_exp = (2./(pi)).*trapz(theta,(Vfinal_3_exp));
127    H4_exp = (2./(pi)).*trapz(theta,(Vfinal_4_exp));
128
129    X_2f_v_exp = H2_exp + .5*i0.*(H1_exp+H3_exp).*cosd(psi_1);
130    Y_2f_v_exp = -1*(0.5.*i0.*(H1_exp-H3_exp).*sind(psi_1));
131
132    R_1f_v_exp = sqrt((H1_exp + i0.*(H0_exp+.5*H2_exp).* cosd(psi_1)).^2 + (i0.*(H0_exp-.5*H2_exp).*sind(psi_1)).^2);
133    R_2f_v_exp = sqrt((X_2f_v_exp).^2 + (Y_2f_v_exp).^2);
134
135    f2_1f_v_exp = sqrt((X_2f_v_exp./R_1f_v_exp).^2 +(Y_2f_v_exp./R_1f_v_exp).^2);
```

206

Appendix B

APPENDIX: Wavelength Referencing MATLAB Code

```
1   format long
2   clear all
3   close all
4
5   signals = xlsread('Book1.xlsx');
6   i1f = signals(:,1);
7   i2f = signals(:,2);
8   i2f1f = signals(:,3);
9
10  %% wav scale
11  % 1.4 Filter resonantor to remove spurious peaks
12  fsr = 1.448; %in ghz
13  Resonator1 = csvread(strcat('wavelengthreference.csv'));
14  [b1 a1] = ellip(2,0.01,90,0.002);
15
16  theory_data = xlsread('THEORY.xlsx');
17
18  ind1 = find(theory_data(:,2) == min(theory_data(:,2)));
19  line_center_exp = theory_data(ind1,1);
20  line_center_exp = 1./line_center_exp*1e7;
21
22  Resonator = Resonator1(:,1)
23  Resonator = filtfilt(b1,a1,Resonator1);
24  Resonator = transpose(Resonator);
25
26  res_length = linspace(1,length(signals(:,3)),length(Resonator1));
27  signal_length = linspace(1,length(signals(:,3)),length(signals(:,3)));
28
29  Normalized_Line_Direct = 1- interp1(signal_length,signals(:,3),res_length);
30
31  start = 101;
32  stop = 10000
33
34  Resonator           = Resonator(start:stop);
35  Normalized_Line_Direct = Normalized_Line_Direct(start:stop);
36
37  [pks,locs_initial] = findpeaks(Resonator,'minpeakdistance',700);
38  figure;hold on;
```

```matlab
39  plot(Resonator,'r');
40  plot(locs_initial,pks,'*')
41  plot(Normalized_Line_Direct,'g')
42
43  delta = locs_initial(end) - locs_initial(1);
44  %% Wavelength Referencing
45  %%
46
47  no_of_peaks = length(locs_initial);% No of resonator peaks
48  res_index = zeros(1,no_of_peaks);% Resonator index points equal to the no of peaks
49  freq_index = 1:(no_of_peaks-1)/delta:no_of_peaks;% Frequency index points equal to the number of resonator peaks are generated
50  temp = locs_initial(1)-1;% Number of points before location(1)
51  locs = locs_initial-temp;% All peak locations are shifted by "temp" towards left
52  % [Max,loc_line_center]=max(Mag_2f_experimental./Mag_1f_experimental);% Find the minima of Normalized and truncated line
53  [Min,loc_line_center] = min(Normalized_Line_Direct);% Find the minima of Normalized and truncated line
54
55  k = dsearchn(locs',loc_line_center);% Find which peak( or the location of peak) is closest to the linecenter
56  c_light = 3E10;% Speed of Light(cm/s)
57
58  res_index(k) = (c_light*line_center_exp)/1e9;% Assign the line center frequency to resonator index
59  line_center = (c_light*line_center_exp)/1e9;% Line center in GHz
60
61  % Obtaining Index value for each peak in GHz
62
63  for i=1:(length(locs)-k)
64  res_index(k+i) = res_index(k+i-1)-fsr;
65  end
66
67  for i=1:k-1
68  res_index(k-i) = res_index(k-i+1)+fsr;
69  end
70  x_range_freq = 1:no_of_peaks; % Xaxis of points equal to number of peaks
71  y_range_freq = res_index;% Yaxis of corresponding frequency values at these peaks
72  % Generate a freq axis of equal number of points as between first and last peak on the time axis
73  freq_scale_index = 1:locs(end);% Index equal to the number of points between the first and last location
74  freq_scale_interpolated = interp1(locs',y_range_freq,freq_scale_index);
75  % Interpolate between the freq values obtained at the locations of the peaks of the resonator
76  m = dsearchn(freq_scale_index',loc_line_center);
77  % Find the index of the line center where index equal to the number of points between the first and last location
78  delta_line_center_loc=m-locs(k);
79  % Find the difference in location of the line center obtained from the resonator peak and the interpolated freq axis
80
81  freq_scale_index_new = freq_scale_index-(delta_line_center_loc);% Find the new index using the line center shift.
82  poly_full_scale = polyfit(freq_scale_index,freq_scale_interpolated,6);% Fit a polynomial to interpolated
83  %frequency values obtained
84  freq_scale_new = polyval(poly_full_scale,freq_scale_index_new);% Fit the polynomial to the new freq scale index
85  wave_scale = c_light./(freq_scale_new.*1e11).*1e9;% Convert freq scale to wavelength scale
86  wave_scale = transpose (wave_scale)
87
88
89  output(:,1) = linspace(locs_initial(1),locs_initial(end),length(wave_scale));
90  output(:,2) = wave_scale;
91
92  figure;hold on;
93  plot(output(:,2),Resonator(output(:,1)),'r');
```

208

Appendix C

APPENDIX: Multigas HITRAN 2008 MATLAB Code

```matlab
clear all
close all
format long
tic
disp(' ')

gases={'CH4'}; % max of 7 gases
pressure=1;
methane_concentrations=[2.31*10^(-4)]; % concentration in %
degreeT=[ 20 ]; %temperatures in degC
L=[1]; %[path length in cm]
wavelength_range=[8600 8640]; % spectral region to plot [nm]
% wavelength_range=[8000 9000]; % spectral region to plot [nm]
individual_plots=0; % option to output a plot for each set of conditions (0=no,1=yes)


leg_end=cell(length(gases),1); % declare leg_end before loop to pre-allocate memory + speed up execution
for ii=1:length(gases)+1
if ii<=length(gases)
leg_end{ii}=[gases{ii} ' (' num2str(methane_concentrations(ii)) '%, ' num2str(pressure) 'bar, ' num2str(degreeT(ii)) -
'C over ' num2str(L(ii)) 'cm)'];
elseif ii==length(gases)+1
leg_end{ii}='Total of Spectra';
end
end

% Trace length
trace_length=133333;
disp(' ')
traces=zeros(trace_length,2,length(gases)+1);
for ii=1:length(gases)

% Concentration unit conversion
%%%finalconc=finalconc*0.01; %conversion to fraction from %
methane_concentration = methane_concentrations(ii)./100;
nitrogen_concentration = 1-methane_concentration;


```

209

```
39   % Reading in pressure and converting from bar to atm
40   % pressure = 1.0; % pressure [bar]
41   total_pressure = pressure*0.986926; %[bar] to [atm] conversion
42   finalairpressure=pressure;
43   finalpress=pressure;
44
45   wavenumber_range=1e7./wavelength_range;
46   % Defining temperature
47   %degreeT=20;
48   % T = input('\n Temperature in Kelvin: ');
49   T_0=296; % Reference Temperature in Kelvin (integer to allow lookup from file)
50   T_K=273.15; %0 degrees celcius in Kelvin
51   T=degreeT(ii)+T_K; %Converting to Kelvin
52
53   gas=gases{ii};
54   texty=[' Processing ' gas ' data...' ' (' num2str(methane_concentrations(ii)) '%, ' num2str(pressure) -
55   'bar, ' num2str(degreeT(ii)) 'C over ' num2str(L(ii)) 'cm)'];
56   disp(texty)
57   theory_path='C:\Users\Sc\Desktop\phd\New folder\plots of gas\NEWPLOTSOFGAS\Multigas data\';
58   partition = csvread([theory_path '\' gas 'partitionfunctions.csv']); %Hitran data
59   methanelines = csvread([theory_path '\' gas '_full_hit12.csv']);
60   truncate=find(wavenumber_range(1)>methanelines(:,1) & methanelines(:,1)>wavenumber_range(2));
61   if isempty(truncate)
62   texty=[' NO ' gas ' ABSORPTIONS IN THE SUPPLIED FILE FOR THE ' num2str(wavelength_range(1)) '-' num2str(wavelength_range(2)) -
63   'nm RANGE!'];
64   disp(texty)
65   texty=[' ' gas ' processing aborted'];
66   disp(texty)
67   else
68   methanelines=methanelines(truncate,:);
69   z = length(methanelines);
70   k = 1.3806503e-23; %Boltzmann [m^2 kg s^-2 K^-1]
71   switch gas   % selects mass of molecule [amu]
72   case 'SO2'
73   M = 64;
74   tweak = 0.97;
75   case 'CH4'
76   M = 16;
77   tweak=0.97;
78   case 'CO2'
79   M = 44;
80   tweak=0.97;
81   case 'C2H2'
82   M = 26;
83   tweak=0.97;
84   case 'NO'
85   M=30;
86   tweak=0.97;
87   case 'H2O'
88   M = 18;
89   tweak=0.97;
90   case 'CO'
91   M = 28;
92   tweak=0.97;
93   case 'N2O'
94   M = 44;
95   tweak = 0.97;
96   case 'N2'
97   M = 14;
98   tweak = 0.97;
99   end
100  c = 299792458e2; %speed of light [m/s]
101  h = 6.626e-34; %Planck [J s]
102  v_min=min(methanelines(:,1))-10; %minimum wavenumber
```

```
103   v_max=max(methanelines(:,1))+10; %maximum wavenumber
104
105   tic % start timer after user variable input
106
107   % Calculation of individual line-strengths
108   index1 = find(partition(:,1) == T_0);
109   Q_T0 = partition(index1,2);
110   deltaT = abs(partition(:,1)-T);
111   minT = min(deltaT);
112   index2 = find(deltaT == minT);
113   Q_T = partition(index2,2);
114   S1 = 1-exp(-(h*c.*methanelines(:,1))/(k*T)); % build Xin Zhou Equn 2.23
115   S2 = 1-exp(-(h*c.*methanelines(:,1))/(k*T_0));
116   S3 = S1./S2;
117   S4 = Q_T0./Q_T;
118   S5 = T_0/T;
119   S6 = exp((-h*c*methanelines(:,5)/k)*((1/T)-(1/T_0)));
120   S7 = S3.*S4.*S5.*S6;
121   S_T=S7.*methanelines(:,2); %Total linestrength
122
123   % Defining Frequency Steps
124   vsteps = trace_length;
125   v=linspace(v_min,v_max,vsteps); %theory frequency range
126   lambda = 1./v.*1e7;
127
128   % Calculation of Broadening Parameters
129   % Gaussian Broadening
130   gammag = 7.1625e-7.*methanelines(:,1).*(T/M)^0.5; % Xin Zhou Equn 2.5
131   gammag = gammag';
132
133   % 4.6.2  Air broadening parameter
134   air_broadening_parameter = tweak.*methanelines(:,3)*(T_0/T).^0.75; % calculated as average of transition 10-16
135   %in 2008 Database
136
137   % Self Broadening parameter
138   self_broadening_parameter = methanelines(:,4).*(T_0/T).^methanelines(:,6);
139
140   X=zeros(length(v),z); % initialise array for loop
141   for j = 1:z
142   %X(:,j) = 2*sqrt(log(2))*(v-methanelines(j,1)-methanelines(j,7).*total_pressure)./gammag(j); % calc line positions
143   %(equn 2.15 Xin Zhou)
144   X(:,j) = 2*sqrt(log(2))*(v-methanelines(j,1))./gammag(j);% no pressure shift
145   end
146   % Voigt parameters
147   A = [-1.2150 -1.3509 -1.2150 -1.3509];
148   B = [1.2359 0.3786 -1.2359 -0.3786];
149   C = [-0.3085 0.5906 -0.3085 0.5906];
150   D = [0.0210 -1.1858 -0.0210 1.1858];
151
152   % Lorentzian Broadening
153   gammal = 2*total_pressure.*((air_broadening_parameter*nitrogen_concentration)
154   +(self_broadening_parameter*methane_concentration));
155   gammal = gammal';
156
157   Y = (gammal./gammag)*sqrt(log(2));
158   V_top=zeros(4,length(v)); % initialise final Voigt-related arrays
159   V_bottom=zeros(4,length(v));
160   Vfinal=zeros(length(v),z);
161
162   for j = 1:z
163   for i = 1:4
164   V_top(i,:)= (C(i)*(Y(j)-A(i)))+(D(i)*(X(:,j)-B(i)));
165   V_bottom(i,:) = (Y(j)-A(i))^2+(X(:,j)-B(i)).^2;
166   end
```

```
167   V = V_top./V_bottom;
168   Vfinal(:,j) = (2/gammag(j))*(log(2)/pi)^0.5*methane_concentration*(7.339e21/T_0)*S_T(j)*sum(V);
169   end
170
171   voigt = pressure*sum(Vfinal,2);
172   voigt = exp(-voigt'.*L(ii));
173   if individual_plots==1
174   % plot stuff
175   set(figure,'WindowStyle','docked')
176   set(gcf, 'color', 'white');
177   [AX,H1,H2] = plotyy(lambda,voigt,(1e9./(methanelines(:,1).*100)),methanelines(:,2),'plot');
178   set(AX,{'ycolor'},{'b';'r'})
179   set(H1,'LineStyle','-')
180   set(H1,'color','b')
181   set(H2,'LineStyle','none')
182   set(H2,'Marker','o')
183   set(H2,'MarkerEdgeColor','r')
184   xlabel('Wavelength [nm]')
185   set(get(AX(1),'Ylabel'),'String','Transmission')
186   set(get(AX(2),'Ylabel'),'String','Line strength [cm/mol]')
187   title({[gas ' spectral data in the FLITES region of interest'] ['(' num2str(methane_concentration*100) '% at '
188   num2str(pressure) 'bar, ' num2str(degreeT(ii)) 'C over ' num2str(L(ii)) 'cm)']})
189   else
190   end
191   traces(:,1,ii)=lambda';
192   traces(:,2,ii)=voigt';
193   end
194   disp(' Done.')
195   end
196
197   % additional figure preparation
198   if length(gases)>1
199   for counter=1:length(gases)
200   traces(:,2,counter)=interp1(traces(:,1,counter),traces(:,2,counter),traces(:,1,1));
201   traces(:,1,counter)=traces(:,1,1);
202   if counter==1
203   traces(:,1,length(gases)+1)=traces(:,1,counter);
204   traces(:,2,length(gases)+1)=1-traces(:,2,counter);
205   else
206   traces(:,2,length(gases)+1)=traces(:,2,length(gases)+1)+(1-traces(:,2,counter));
207   end
208   end
209
210   %Truncate everything to focus on the line of interest
211   low_cutoff=max(find(traces(:,1,1)>wavelength_range(1)+0.3));
212   high_cutoff=max(find(traces(:,1,1)>wavelength_range(2)-0.2));
213   traces=traces(high_cutoff:low_cutoff,:,:);
214
215   traces(:,2,length(gases)+1)=1-traces(:,2,length(gases)+1);% change absorption to transmission
216
217   % plot results
218   figure
219   set(gcf,'color','white','windowstyle','docked')
220   plot(traces(:,1,1),traces(:,2,1),'b')
221   hold on
222   plot(traces(:,1,2),traces(:,2,2),'r')
223   if length(gases)>2
224   plot(traces(:,1,3),traces(:,2,3),'c')
225   if length(gases)>3
226   plot(traces(:,1,4),traces(:,2,4),'m')
227   if length(gases)>4
228   plot(traces(:,1,5),traces(:,2,5),'y')
229   if length(gases)>5
230   plot(traces(:,1,6),traces(:,2,6),'g')
```

```matlab
231   if length(gases)>6
232   plot(traces(:,1,7),traces(:,2,7),'k')
233   if length(gases)>7
234   plot(traces(:,1,8),traces(:,2,8),'k--')
235   end
236   end
237   end
238   end
239   end
240   end
241   % plot(traces(:,1,length(gases)+1),traces(:,2,length(gases)+1),'k','linewidth',2)
242   else
243
244   figure
245   set(gcf,'color','white')
246   set(gcf,'windowstyle','docked')
247   plot(traces(:,1,1),traces(:,2,1),'b')
248   end
249   axis([wavelength_range(1)+0.3 wavelength_range(2)-0.2 0.99*min(min(traces(:,2,:))) 1])
250   for ii=1:length(gases)
251   leg_end(ii)={[char(gases(ii)) ' at ' num2str(methane_concentrations(ii)) '%, ' num2str(pressure) 'bar, &
252   ' num2str(degreeT(ii)) 'C over ' num2str(L(ii)) 'cm.']};
253   end
254   legend(leg_end,'location','best')
255   xlabel('Wavelength [nm]')
256   ylabel('Transmission')
257   stringy=['Species transmission between ' num2str(wavelength_range(1)) 'nm (' num2str(wavenumber_range(1)) 'cm^{-1})
258   and ' num2str(wavelength_range(2)) 'nm (' num2str(wavenumber_range(2)) 'cm^{-1}).'];
259   title(stringy)
260   toc
```

Appendix D

APPENDIX: Allan-Werle Varience MATLAB Code

```matlab
1   clear all
2
3   tic
4   DataFiles = 16406;
5
6   for i=1:1:DataFiles;
7   x = strcat('gas\',(num2str(i)),'.csv');
8   awfile = csvread(x);
9   aw2f1f = awfile(:,1);
10  aw2fand1f = awfile(:,2);
11  signal2f1f(:,i) = peak2peak(aw2f1f(20:950));
12  signal2f(:,i) = peak2peak(aw2fand1f(1050:1950));
13  signal1f(:,i) = peak2peak(aw2fand1f(50:950));
14  %    signal2f1f(:,i) = peak2peak(sgolayfilt(aw2f1f(1:1000),1,21));
15  %    signal1f(:,i) = peak2peak(sgolayfilt(aw2fand1f(1:1000),1,21));
16  %    signal2f(:,i) = peak2peak(sgolayfilt(aw2fand1f(1001:2000),1,21));
17     x=i
18  end
19
20  %% 1
21  %--------- calculation of Allan variance from p-p voltage values of LIA signal ----------
22  for stepsize=1:(floor(DataFiles/2)-1)
23  Difference = 0;
24  Average=0;
25  currentPos = 1;
26  Steps = floor(DataFiles/(stepsize+1));
27  for l=1:Steps
28  Average(l)=mean(signal2f1f(currentPos:currentPos+stepsize));
29  currentPos=currentPos+stepsize+1;
30  end
31
32  for j=1:Steps-1
33  Difference(j)=(Average(j+1)-Average(j))^2;
34  end
35
36  AllanVar2f1f(stepsize)=0.5/(Steps-1)*sum(Difference);
37  end
38
```

214

```matlab
39   for stepsize=1:(floor(DataFiles/2)-1)
40   Difference = 0;
41   Average=0;
42   currentPos = 1;
43   Steps = floor(DataFiles/(stepsize+1));
44   for l=1:Steps
45   Average(l)=mean(signal1f(currentPos:currentPos+stepsize));
46   currentPos=currentPos+stepsize+1;
47   end
48
49   for j=1:Steps-1
50   Difference(j)=(Average(j+1)-Average(j))^2;
51   end
52
53   AllanVar1f(stepsize)=0.5/(Steps-1)*sum(Difference);
54   end
55
56   for stepsize=1:(floor(DataFiles/2)-1)
57   Difference = 0;
58   Average=0;
59   currentPos = 1;
60   Steps = floor(DataFiles/(stepsize+1));
61   for l=1:Steps
62   Average(l)=mean(signal2f(currentPos:currentPos+stepsize));
63   currentPos=currentPos+stepsize+1;
64   end
65
66   for j=1:Steps-1
67   Difference(j)=(Average(j+1)-Average(j))^2;
68   end
69
70   AllanVar2f(stepsize)=0.5/(Steps-1)*sum(Difference);
71   end
72
73   %% 2
74   AllanVar2f1f=AllanVar2f1f';
75   AllanVar1f=AllanVar1f';
76   AllanVar2f=AllanVar2f';
77   timebase = 1;
78   for j=1:length(AllanVar2f1f)
79   time(j)=j*timebase;
80   end
81   % figure
82   % loglog(time,AllanVar)
83   % xlabel('Integration time [s]')
84   % ylabel('Allan variance [V]')
85
86   %------------ calculate and plot Allan deviation in LIA voltage ------------------
87   AllanDev2f1f = sqrt(AllanVar2f1f);
88   AllanDev1f = sqrt(AllanVar1f);
89   AllanDev2f = sqrt(AllanVar2f);
90   figure
91   loglog(time,AllanDev2f1f)
92   hold on
93   loglog(time,AllanDev1f)
94   loglog(time,AllanDev2f)
95   xlabel('Integration time [s]')
96   ylabel('Allan deviation [V]')
97   legend('2f1f','1f','2f')
98
99   %------------ plot time dependent LIA p-p voltage value with 0.6sec between measurements -----------
100  timeseries=(1:length(signal2f1f));
101  timeseries=timeseries*1;
102  figure
```

```matlab
103    plot(timeseries,signal2f1f)
104    hold on
105    plot(timeseries,signal1f)
106    plot(timeseries,signal2f)
107    xlabel('Measurement time [s]')
108    ylabel('LIA p-p signal [V]')
109    legend('2f1f','1f','2f')
110
111    %------------ calculate and plot Allan deviation in ppm, with 10ppm used as sample gas -----------
112    meanPP2f1f = mean(signal2f1f);
113    AllanDevPPm2f1f = 10*AllanDev2f1f/meanPP2f1f;
114    meanPP1f = mean(signal1f);
115    AllanDevPPm1f = 10*AllanDev1f/meanPP1f;
116    meanPP2f = mean(signal2f);
117    AllanDevPPm2f = 10*AllanDev2f/meanPP2f;
118    figure
119    loglog(time,AllanDevPPm2f1f)
120    hold on
121    loglog(time,AllanDevPPm1f)
122    loglog(time,AllanDevPPm2f)
123    xlabel('Integration time [s]')
124    ylabel('Allan deviation [%]')
125    legend('2f1f','1f','2f')
126    toc
```

216